Modifying Layered Perovskite Oxide for Photocatalysis

Haozhe Zhang

St Hilda's College

Trinity Term 2025

A thesis submitted for the degree of

DPhil in Inorganic Chemistry

Declaration

The work in this thesis was carried out at the Inorganic Chemistry Laboratory at the University of Oxford between October 2021 and March 2025 under the supervision of Prof. Shik Chi Edman Tsang. I confirm that all research described in this thesis is my own work unless otherwise stated. All the materials used in this thesis from other sources have been properly cited and fully acknowledged.

Dedication

To the four-year companionship during my PhD, whether in Manchester, Birmingham, London or Southampton.

Acknowledgement

I would like to express my deep gratitude to my supervisor Prof. Shik Chi Edman Tsang for providing me the opportunity to pursue a doctoral degree, giving me encouragement and trust throughout my research. I aspire to carry forward his legacy of optimism and perseverance as a profound tribute to honour his memory. And I will be forever grateful for his guidance and support, which I shall always remember with the deepest respect.

My sincere appreciation extends to Prof. Michael L. Neidig and Prof. Dermot O'Hare for their help on my thesis. It was my pleasure to collaborate with excellent researchers: Dr. Yiyang Li, Dr. Tatchamapan Yoskamtorn and Dr. Xuelei Pan.

And special thanks go to Tsang group members: Dr. Ping-Luen Ho, Dr. Yanjie Wang, Dorottya Szalay, Amy Radford and Mengqi Duan.

My study was funded by Chinese Scholarship Council of China's Ministry of Education, under People's Republic of China government. I greatly acknowledge them for long-term financial support.

The final and greatest thanks are given to my parents Mrs. Li Zhang and Mr. Zhenyu Zhang, also my grandparents. Thank you for everything.

Haozhe Zhang

23rd May 2025

Abstract

Perovskite has emerged as a noteworthy role in photocatalysis, demonstrating exceptional performance in water splitting, CO_2 reduction and organic pollutant degradation. Their intrinsic advantages, including tuneable band structures, high defect tolerance, and rich surface redox chemistry, position them as prime candidates for advancing photocatalytic reaction. Nevertheless, the full potential of perovskite-based systems remains underexplored, necessitating more investigations and modifications to understand its aptitude.

This thesis constructs an integrated ammonia energy cycle mediated by perovskite photocatalysts, delineating a closed-loop hydrogen economy encompassing three strategically linked phases: photocatalytic hydrogen generation from water splitting; photocatalytic ammonia synthesis for hydrogen storage and transportation; and on-demand hydrogen release through photocatalytic ammonia decomposition. Throughout this value chain, perovskite-based catalysts serve as the unifying platform, enabling an efficient interconversion between hydrogen and ammonia energy carriers.

The synthesised photocatalysts were characterised by Synchrotron X-ray diffraction, neutron powder diffraction, X-ray absorption spectroscopy, and X-ray pair distribution function. Subsequent contents correlate these structural insights with photochemical performance metrics, revealing mechanistic connections between crystallographic features and catalytic functionality.

Chapter 1 introduces the fundamental principles of layered perovskite materials along of various photocatalytic reactions. Chapter 2 outlines the experimental methodology, including catalyst characterisation techniques and catalytic activity evaluation

protocols. Chapter 3 investigates perovskite / reduced graphene oxide heterostructures for photocatalytic water splitting, with emphasis on interfacial charge transfer mechanisms. Chapter 4 elucidates the hydrazine-mediated photo-thermal decomposition of ammonia using protonated layered perovskites. Chapter 5 explores moiré-engineered 2D perovskite for enhanced ammonia synthesis efficiency.

List of Abbreviations

2D	2-Dimensional
AQE	Apparent Quantum Efficiency
CN	Coordination Number
CB	Conduction Band
DFT	Density Functional Theory
DI	Deionized
DRFITS	Diffuse Reflectance Infrared Fourier Transform Spectroscopy
EDX	Energy Dispersive X-ray Spectroscopy
EELS	Electron Energy Loss Spectroscopy
EPR	Electron Paramagnetic Resonance
EXAFS	Extended X-ray Absorption Fine Structure
FFT	Fast Fourier Transformation
GC	Gas Chromatography
GoF	Goodness of Fit
HAADF	High-angle Annular Dark-field
HER	Hydrogen Evolution Reaction
ICP-MS	Inductively Coupled Plasma-Mass Spectrometry
IR	Infra-Red
NMR	Nuclear Magnetic Resonance
NPD	Neutron Powder Diffraction
OER	Oxygen Evolution Reaction
PDF	Pair Distribution Function
rGO	Reduced Graphene Oxide
SEM	Scanning Electron Microscopy

SHE	Standard Hydrogen Electrode
STEM	Scanning Transmission Electron Microscopy
STE	Self-trapped Exciton
STH	Solar to Hydrogen
TBA	Tetra-butyl Ammonium
TEA	Tetra-ethyl Ammonium
TEM	Transmission Electron Microscopy
TGA	Thermogravimetric Analysis
TMA	Tetra-methyl Ammonium
TPA	Tetra-propyl Ammonium
TRPL	Time-resolved Photoluminescence
UV-Vis	Ultraviolet-Visible
VASP	Vienna ab initio Simulation Package
VB	Valence Band
XANES	X-ray Absorption Near-Edge Structures
XAS	X-ray Absorption Spectroscopy
XPS	X-ray Photoelectron Spectroscopy
XRD	X-ray Diffraction

List of Figures and Tables

Chapter 1

Chapter 2

Chapter 3

Chapter 5

Appendices

A) Appendices for Chapter 3

B) Appendices for Chapter 4

C) Appendices for Chapter 5

Table of Contents

Chapter 1 | Introduction

1.1 Layered perovskite oxide

Layered perovskite oxides are among the most intensive studied materials in solid state chemistry and physics as they exhibit lots of interesting fundamentally chemical and physical properties.[1] They can show the magnetic orderings ranging from ferromagnetic to antiferromagnetic;[2] They can have electronic structures ranging from insulating to metallic;[3] Moreover, they can demonstrate excellent performance in electro, thermal and photo-catalysis. As a result, layered perovskite materials have a wide range of application in electronic devices, magnetic materials, solar cells and so on.[4]

1.1.1 ABO_3 perovskite structure

General perovskites are binary metal oxides with chemical formula ABO_3, in which A-site cation is twelve-coordinated, and B-site cation is octahedrally-coordinated. As shown in Figure 1.1, the 3D network of perovskite is formed by linking corner-sharing BO_6 octahedra, and A-site cations fill the space between octahedral unit cells to balance the overall crystal charge. Importantly, varying the ionic radii could lead to distortion or collapsing of cubic structure of perovskite, because BO_6 octahedra would tilt to compensate for the non-ideal ratios of ionic size.

$$t = \frac{r\mathrm{A} + r\mathrm{O}}{\sqrt{2}\,(r\mathrm{B} + r\mathrm{O})} \quad \text{(Euqation 1.1)}$$

The Goldschmidt tolerance factor (t) is used to determine the phase and structural stability of a perovskite compound (Equation 1.1), where r_A, r_B and r_O are the radii of A-site, B-site and oxygen ions.[5] The tolerance factor is an important parameter for the designing of any new type of perovskites. When the value of Goldschmidt tolerance factor is 1.00, the perovskite structure has a perfectly cubic symmetry without any distortion. Octahedral

factor f_O ($f_O = r_B / r_O$) is also an important parameter for perovskite structure. It is thought that for the formation of cubic perovskites, f_O is in the range of $0.41 \leq f_O \leq 0.73$, which is necessary to evaluate the stability and distortion of BO_6 octahedra.[6] While values outside this range tend to induce octahedral tilting, coordination changes or defect formation that modify perovskite crystal symmetry.

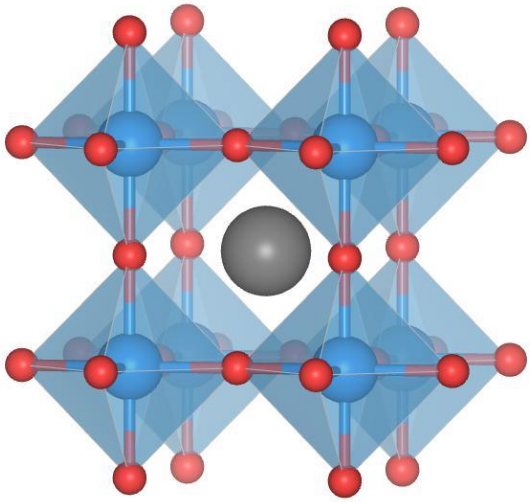

Figure 1.1: The cubic ABO_3 perovskite structure, in which the grey sphere represents the A-site cation, the blue spheres represent the B-site cations, and the red spheres represent the oxygen anions.

The Glazer notation is applied to denote the octahedral tilting in perovskite.[7] The sequence of symbols (*a*, *b* and *c*) corresponds to the crystallographic axes (i.e., first symbol indicates the tilting along [100] axis). When the symbols are identical, the perovskite structure has the same tilting amplitude. When the symbols are identical (for example $a^-a^-a^-$), it means the tilting amplitude about those axes is the same. Equal tilt amplitudes therefore produce equivalent distortions of the BO_6 octahedra along those directions and constrain the attainable space groups and lattice parameters. The superscripts represent zero tilting (0), in-phase tilting (+) and anti-phase tilting (-) of subsequent layers of octahedra. For example, $a^0a^0a^0$ is a cubic perovskite with $Pm\bar{3}m$

space group. While $a^0a^0c^+$ in Figure 1.2a is tetragonal with space group P4/*mbm*, where adjacent octahedra layers having in-phase rotation. Figure 1.2b shows $a^0a^0c^-$ with anti-phase rotation has space group I4/*mcm* in tetragonal symmetry as well.[8]

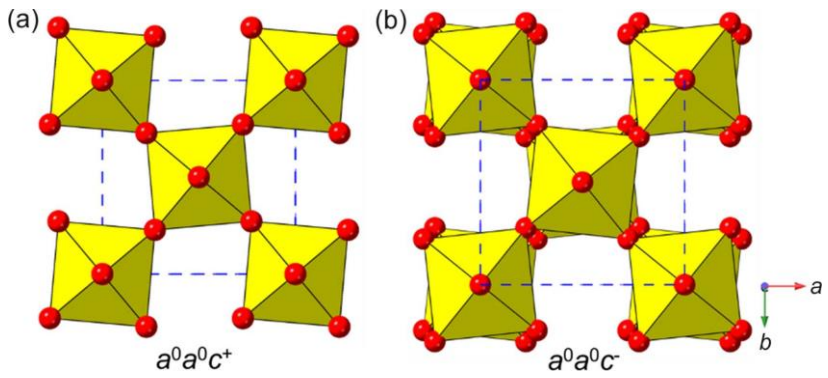

Figure 1.2: Tilted ABO_3 perovskite structure, in which the grey sphere represents the A-site cation, the blue octahedra represents BO_6 and the red spheres represent the oxygen anions. Figure reproduced from Reference [8].

1.1.2 Cation ordering in double perovskite

Partial cation substitution can take place either at A site or B site in perovskite, which is a normal approach for tailoring the perovskite properties. There are three orderings that can be envisioned for either the A or B-site cations: rock salt, columnar and layered ordering (Figure 1.3).[9][10] B-site cations favour rock salt ordering, because the oxygen anions remain chemically equivalent, and each oxygen anion is surrounded by one B and one B' cation. Furthermore, when radii difference between B and B' is effective, the anion is capable of shifting towards the smaller cation and away from the larger one (Figure 1.4 a). However, in layered ordering of B-site cations, there are three different anion environments (Figure 1.4 b), which means it violates Pauling's fifth rule of parsimony (if possible, all the same type anions should have the same environment).[10][11]

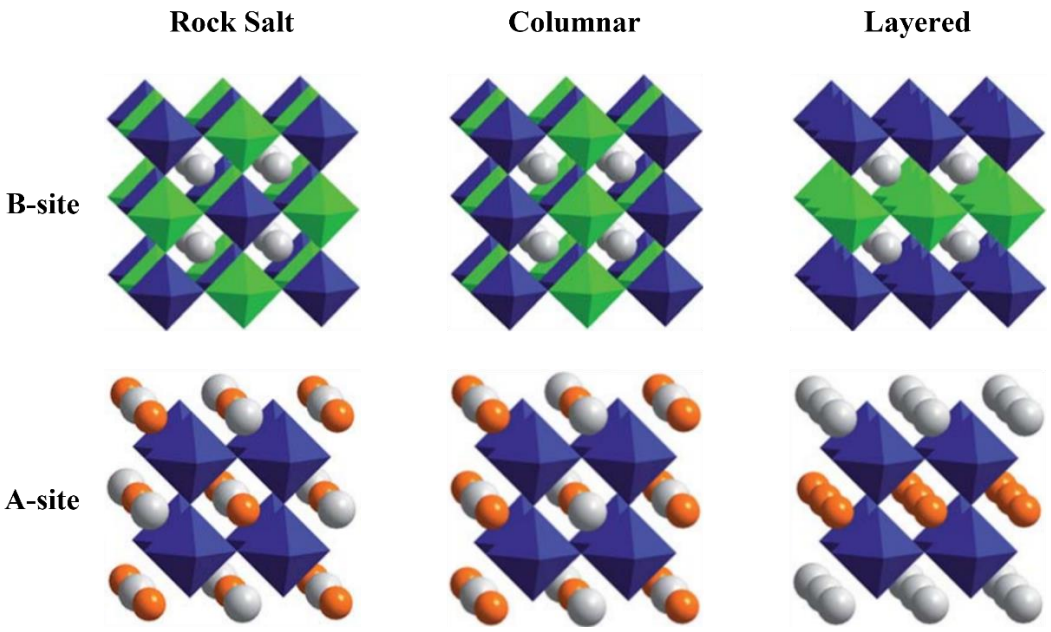

Figure 1.3: Cation ordering schemes in perovskite. From left to right: Rock Salt, Columnar and Layered, in which blue and green octahedra represents BO_6 and $B'O_6$, orange and white spheres represent A/A'-site cations. Figures reproduced from Reference [10].

In contrast to B-site cations, A-site cations favour layered ordering. Oxygen anions in rock salt ordering are coordinated with A and A'-site cations (Figure 1.4 c), remaining in a trans configuration, which means it is difficult for oxygen anions to shift in response to an A/A' size differential. However, in layered ordering, two-thirds of the anions are coordinated with two A and two A' cations in a cis configuration (Figure 1.4 d). Then they are free to displace if A and A' have different radii.[10] While rock salt and layered cases are dominant for B-site and A-site cation orderings, respectively, other types of cation ordering are known. For example, La_2CuSnO_6 with P4/*mmm* space group is a B-site layered ordering perovskite.[12] It is stabilised by a second order Jahn-Teller distortion of B-site cations and suitable tilting of octahedra. $NdSrMn^{3+}Mn^{4+}O_6$ with P4/*mmm* space group is a B-site columnar ordering perovskite, which is stabilised by first

order Jahn-Teller distortion of B-site cations.[13] There is also columnar ordering perovskite for A-site cation, which is $CaFeTiO_6$ with $P4_2/nmc$ space group. It is rare and stabilised by A/A' charge difference.[14]

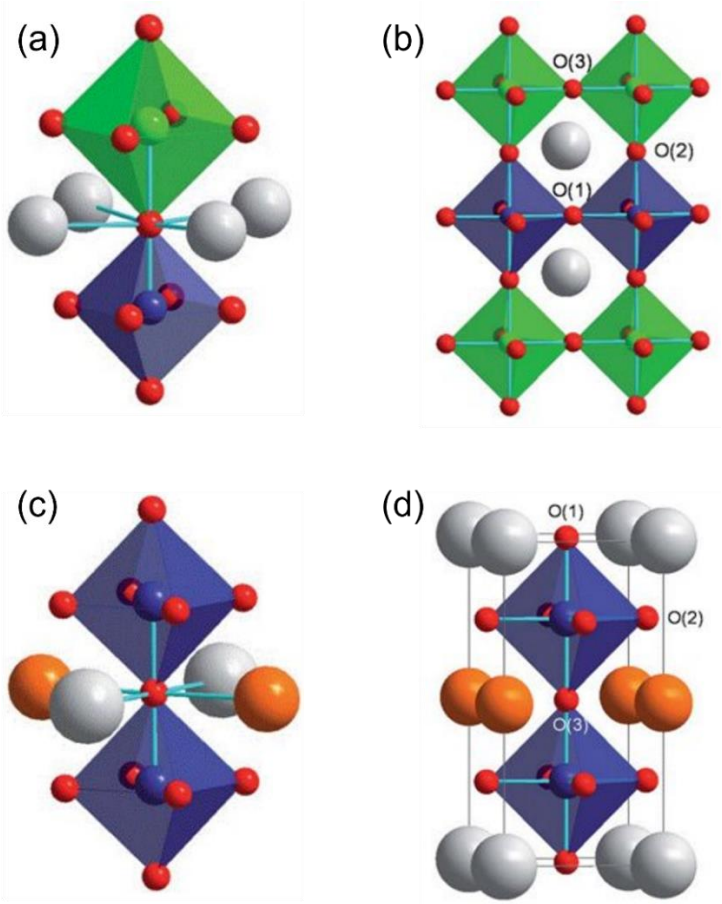

Figure 1.4: The oxygen anion environment in (a) B-site cation rock salt ordering, (b) B-site cation layered ordering, (c) A-site cation rock salt ordering and (d) A-site cation layered ordering, in which blue and green spheres represent B/B'-site cations, orange and white spheres represent A/A'-site cations, red spheres represent oxygen anions. Figures reproduced from Reference [10].

1.1.3 Layered double perovskite structure

Layered perovskite is a derivative of cubic perovskite ABO_3. These layered materials consist of massive 2D slabs of ABO_3 (octahedra layer) interleaved with A' cations. Generally, layered perovskite oxides can be classified as Ruddlesden–Popper, Dion–Jacobson and Aurivillius. Layered perovskite with Aurivillius phase has Bi_2O_2 at the interlayer space instead of organic or metal cations.[15] The difference between Ruddlesden–Popper and Dion–Jacobson perovskite is the displacement between octahedra slabs and the charge density at the interlayer space.

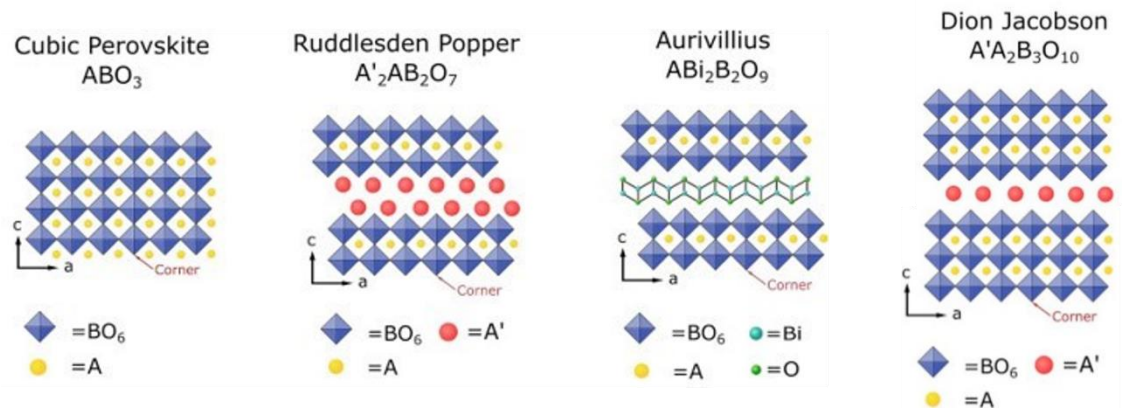

Figure 1.5: Crystal structure of cubic and layered perovskite. Figures reproduced from Reference [15].

When the layer stacking orientation corresponds to *c* axis (Figure 1.5), layered perovskite oxides can be described as $A_{n+1}B_nO_{3n+1}$ or $A'_2A_{n-1}B_nO_{3n+1}$ (Ruddlesden–Popper phase) and A'$(A_{n-1}B_nO_{3n+1})$ (Dion–Jacobson phase) and $(Bi_2O_2)A_{n-1}B_nO_{3n+1}$ (Aurivillius phase), where A' and A are usually alkali, alkali-earth and rare-earth metals, B is a transition metal such as Ti, Nb or Ta, n represents the number of BO_6 octahedra arranged perpendicular to the layers (thickness of each slab).[16][17] In the layered structure, adjacent octahedra slabs are weakly connected with each ither by electrostatic force, where interlayer cations A' are dispersed between them, holding the whole material in an electrically neutral state. Due to the weak interlayer bonds, A' cations can be exchanged

by other cations, leading to a flexible structure and wide application of this type of materials.[18]

1.1.4 Charge carrier dynamics in layered structure

Layered perovskite has a 'sandwich' system, where each octahedra layer acts as "wells" sandwiched between interlayer A'-site cations acting as 'barriers', constructing a natural multiple quantum-well structure (Figure 1.6a).[19][20][21][22][23][24] The generated excitons are confined within the octahedra slabs, surrounded with low-dielectric screening A'-site cations at interlayer. The dimensionality of layered perovskite can be changed by varying the thickness of octahedra slabs, modulating both the exciton binding energy and perovskite bandgap (Figure 1.6b). As the thickness of octahedra layer declines, the Coulombic attraction between excitons goes through both octahedral layers and interlayer, experiencing a significant dielectric change from high-dielectric octahedral layers to low-dielectric interlayer space. This dielectric mismatch reduces the screening of electron-hole Coulombic interaction, enhancing exciton binding energy and widening perovskite bandgap.[20][25][23][27]

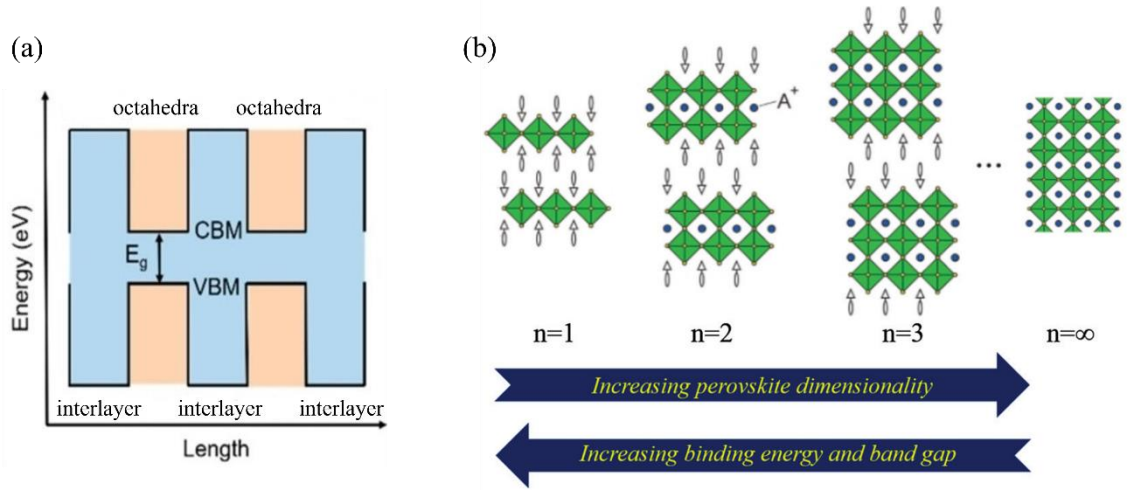

Figure 1.6: a) Quantum-well structure of layered perovskite, b) Layered perovskite with increasing dimensionality n. Figures reproduced from Reference [20].

Due to the strong excitonic properties and distortion in the inorganic framework of layered perovskite, its photoluminescence emissions may feature red-shifted broadened peaks (Figure 1.7a). This is because the coupling between the lattice vibration and charge carriers can generate a lattice distortion field, trapping the electron-hole pair as a small polaron, so called 'self-trapped exciton' (STE). Different energy state free exciton and STE can coexist with different energies lying within the bandgap (Figure 1.7b).[28] Thus, recombination will occur from multiple local minima surface, resulting a broadband emission below the bandgap. As shown in Figure 1.7c, multiple STE states give an inhomogeneous emission in the photoluminescence spectrum, because it takes longer time to emit for the deeper self-trapped states due to high lattice distortion.[29]

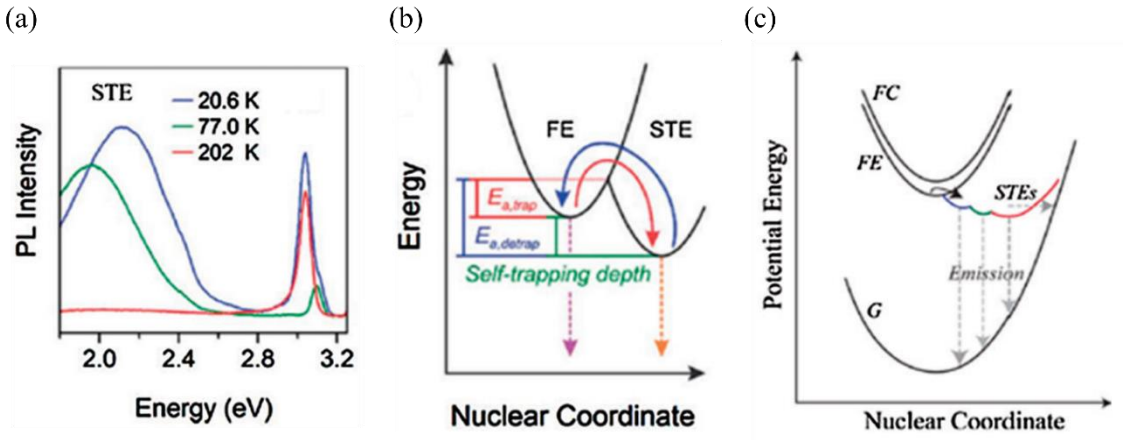

Figure 1.7: a) typical photoluminescence spectra of layered perovskite, revealing (at low temperatures) a broad emission band below the band gap, attributed to the emission from self-trapped excitons. b) Schematic representation of self-trapped excitons in layered perovskite. c) Schematic representation of the adiabatic potential curves of the ground state, free exciton state, free-carrier state, and various excited states. Figures reproduced from Reference [28][29].

1.2 Catalysis with light

The Swedish chemist Berzelius first coined the term “catalysis” in 1835. However, a suitable definition was provided much later by Ostwald in 1894: “Catalysis is the acceleration of a slow chemical process by the presence of a foreign material.”[30] Today, more than one hundred years later, we use catalysts to accelerate reaction by providing an alternative pathway with lower activation energy. Although the catalysts participate the reaction, it remains unchanged and can transform many molecules. Therefore, it only requires a small amount to facilitate the transformation of large quantities. During the past century, the progress of experimental techniques allowed the investigation in details of the interaction between adsorbate molecules and catalyst surface.[31]

Photocatalysis is a branch of catalysis where the photocatalysts accelerate the rate of a chemical reaction on exposure to light. Upon light illumination of a desired wavelength, the photon energy is absorbed by an electron (e^-) in the valence band, and it is excited to the conduction band. In this process, a hole (h^+) is created in valence band. It leads to the formation of photo-excitation state, and the excited electron-hole pair is generated and can participate in redox reactions.[32][33] However, the generated electron-hole pair can also recombine and release the energy in the form of light, heat or molecular vibration.[34][35] So, an ideal photocatalyst can separate the electron and hole, diffusing them to the catalyst surface where they can contact the reactant molecules.[36][37] Indeed, photocatalysts have been applied for wastewater treatment, antifogging, energy storage, etc. The photocatalytic fuel-forming and energy storage reactions will be discussed in detail in subsequent content.

1.2.1 Photocatalytic water splitting

H_2 gas is a carbon-free clean energy carrier that releases a significant amount of energy ($\Delta H° = -284$ kJ mol^{-1}) upon combustion, and water is the only product. It is also the key feedstock for industrial chemicals such as hydrogen peroxide, methanol and ammonia. Currently, most commercially available H_2 is derived from fossil fuels such as coal (black H_2) and natural gas (grey H_2), which means CO_2 emission is inevitable. Photocatalytic water splitting is a promising approach for sustainable H_2 production, utilising semiconductor photocatalysts to split water into H_2 and O_2 (Equation 1.2). This process requires a positive change in standard Gibbs free energy ($\Delta G° = 237$ kJ mol^{-1}).[38]

$$H_2O \rightarrow H_2 + \frac{1}{2}O_2 \quad \text{(Equation 1.2)}$$

$$2H^+ + 2e^- \rightarrow H_2 \quad \text{(Equation 1.3)}$$

$$H_2O + 2h^+ \rightarrow \frac{1}{2}O_2 + 2H^+ \quad \text{(Equation 1.4)}$$

In its half-cell reaction, excited electrons in conduction band need to reduce H^+ in the hydrogen evolution reaction (HER) shown in Equation 1.3. Its standard electrochemical potential is 0 V versus standard hydrogen electrode (SHE). While the holes in valence band will oxidise H_2O in the oxygen evolution reaction (OER) shown in Equation 1.4. It has standard electrochemical potential of +1.23 V against SHE. As a result, the conduction band and the valence band of a single light absorber photocatalyst need to be positioned to straddle these redox potentials (Figure 1.8a), enabling the simultaneously H_2 and O_2 production. In 1980, it was reported that TiO_2 and $SrTiO_3$ powdered materials can be used as catalysts for UV light-driven water splitting.[39][40][41][42] Since then, many different types of water splitting photocatalysts have been discovered.

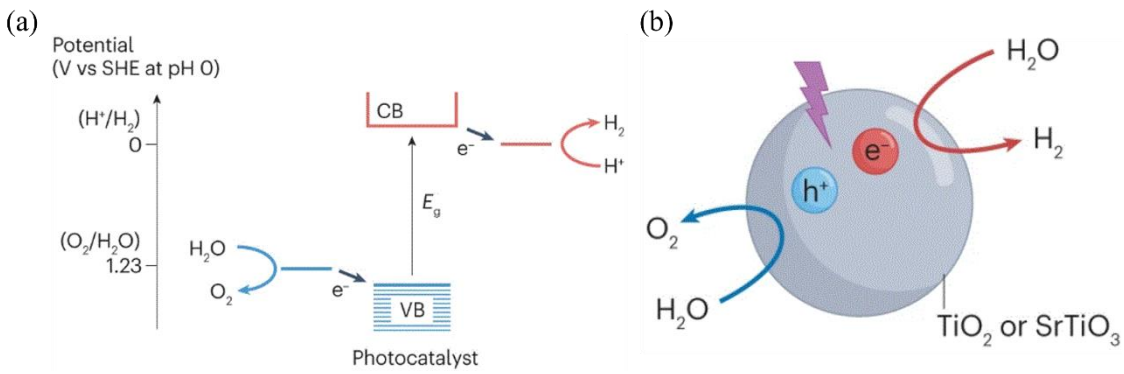

Figure 1.8: (a) Energy diagram for photocatalytic water splitting in a one-step photoexcitation system. CB, conduction band; VB, valence band. (b) Diagram showing the reactions during water splitting on a semiconductor photocatalyst. Figures reproduced from Reference [38].

The simplest photocatalyst for water splitting is a single semiconductor particle, driving HER and OER under light illumination (Figure 1.8b). However, few photocatalysts can split water into H_2 and O_2 without sacrificial reagents.[43][44] And most of them need the loading of appropriate nanoparticle co-catalyst for efficient H_2 production. Therefore, it is important to minimise the electron-hole pair recombination and increase its utilising efficiency. One of the strategies is doping another element in the wide-bandgap metal oxide. The dopants introduce donor or acceptor states in the bandgap of the semiconductor host, inhibiting the electron-hole pair recombination (Figure. 1.9A). Importantly, the dopant ions need to possess a similar size to the substituted ions in the photocatalyst.[38][45] Moreover, the overall charge needs to be balanced. $SrTiO_3$ doped with chromium or rhodium demonstrates improved performance in photocatalytic water splitting. When different concentration of chromium (Figure. 1.9B) or different noble metal (Figure. 1.9C) was doped in $SrTiO_3$ structure, the absorption in visible-light range increased, indicating the additional energy states were introduced into the $SrTiO_3$ band structure.[46][47]

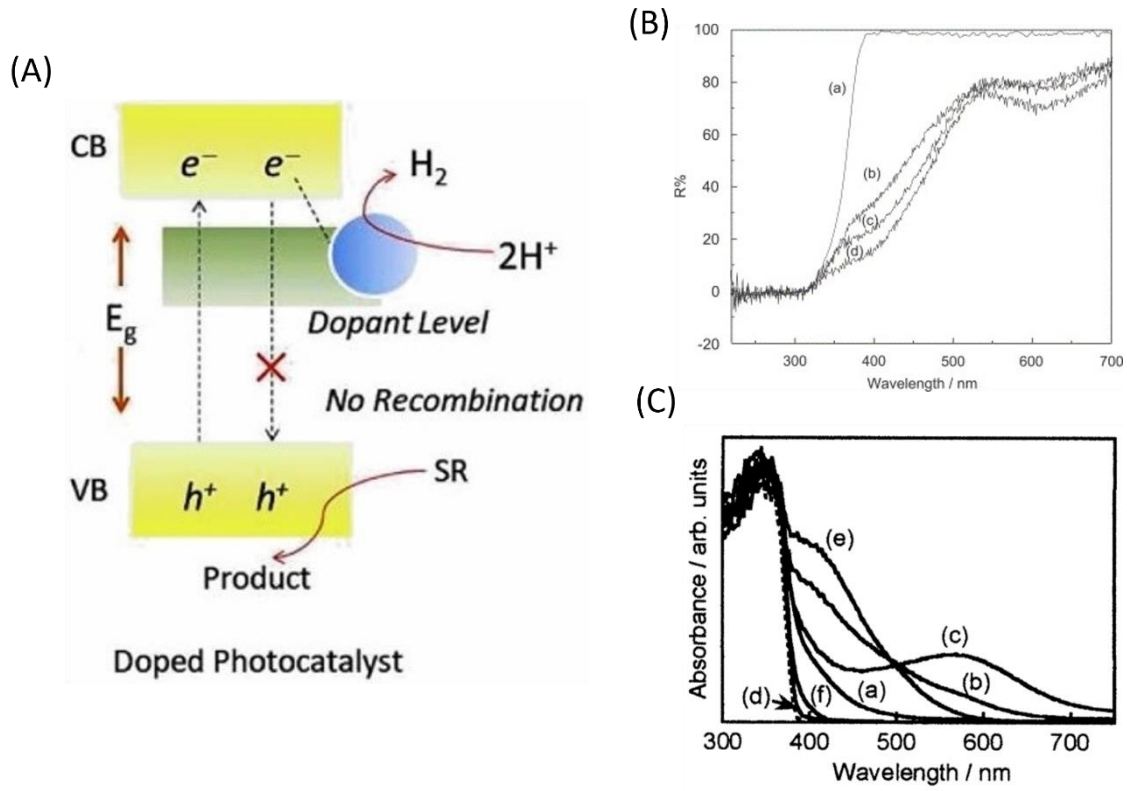

Figure 1.9: (A) Photocatalysts with heteroatom doping for water splitting. CB, conduction band; VB, valence band; SR, sacrificial reagent; E_g, bandgap. (B) UV–vis diffuse reflectance spectra of $SrTi_{1-x}Cr_xO_3$: a) non-doped $SrTiO_3$ and $SrTiO_3$-doped with chromium, b) 2%, c) 5%, and d) 10%. (C) Diffuse reflectance spectra of $SrTiO_3$:M(0.5%). M = a) Mn, b) Ru, c) Rh, d) Pd, e) Ir, and f) Pt. A broken line represents a spectrum of non-doped $SrTiO_3$. Figures reproduced from Reference [45][46][47].

Except using single component photocatalysts for water splitting, type II heterojunction nanocomposites using two semiconductors can significantly improve the photocatalytic performance by separating charge carriers (Figure 1.10a).[48] For instance, CdS/ZnS nanocomposites demonstrate a higher photocatalytic activity for water splitting compared with individual CdS and ZnS due to the isolation of electrons and holes in separated locations.[49] Although the type II heterojunction-type nanocomposites facilitate charge separation, photocatalytic ability of this system is weakened due to the migration of

electrons and holes to more electropositive conduction band and electronegative valence band potential attributed to the nature of charge transfer.

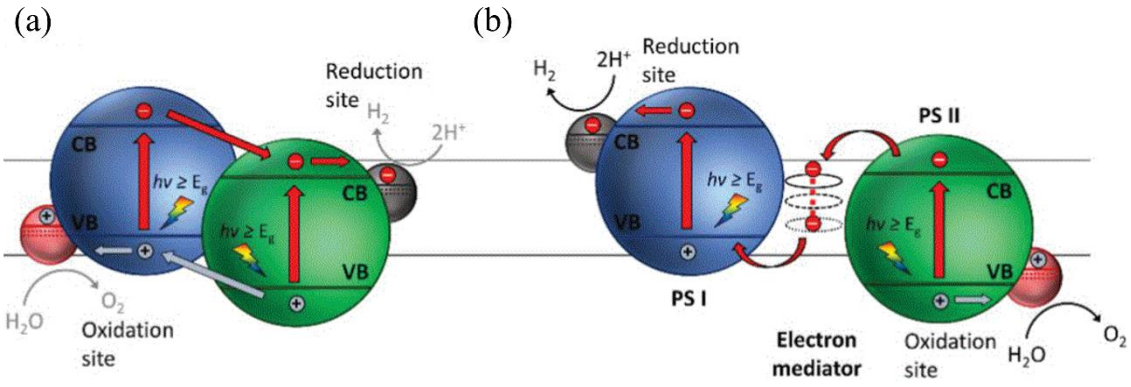

Figure 1.10: Schematic illustration of (a) type-II heterojunction photocatalytic system and (b) Z-scheme photocatalytic system. PS I, photosystem I; PS II, photosystem II. Figures reproduced from Reference [48].

Another photocatalytic system introduces an anisotropic configuration of two photocatalysts and an electron mediator known as the Z-scheme photocatalytic system, where performing water splitting through two-step photoexcitation process. This system achieves efficient photocatalytic water splitting through two isolated catalysts' synergy interaction. As shown in Figure 1.10b, one of them acts as the reduction site (photosystem I) while the other acts as oxidation site (photosystem II). In addition, an electron transport chain works as the mediator, facilitating the electron flow between these two photocatalysts. Unlike type II heterojunction semiconductor nanocomposites, there is a unique electron flow pattern enabled by electron-relaying channel introduced in the Z-scheme photocatalytic system. Upon photoexcitation, electrons from the valence band of both photosystem I and photosystem II are excited to the conduction band, leaving photogenerated holes in the valence band. Then, the electrons in photosystem II are transported by the mediator to recombine with the holes in the valence band of photosystem I through Ohmic contact. This distinct vectorial electron transfer mechanism

allows electrons and holes to remain in separate photocatalysts while retaining strong redox abilities. Consequently, photosystem II becomes a hole-rich photocatalyst for OER, while photosystem I accumulates electrons for HER. An early work was demonstrated by Abe et al. in 2001, in which anatase and rutile TiO_2 was used as photocatalysts, and IO_3^-/I^- redox couple as an ionic electron mediator.[50] Except aqueous iodine, divalent and trivalent Fe ions can also be used in the redox cycle system. Nishioka et al. designed a Z-scheme system for water splitting, where IrO_2-loaded TiO_2:Ta,N is combined with Ru/$SrTiO_3$:Rh in aqueous $FeCl_3$ solution.[51] Moreover, graphic carbon nitride is also possible for the construction of the Z-scheme water splitting system.[52][53]

However, most of laboratory-scale photocatalytic water splitting experiments are done by using photocatalyst powders suspended in water. This suspension system includes lots of limitation such as requiring additional energy for catalyst dispersion, difficulties in catalyst collection and so on. Therefore, photocatalytic panels and sheets have received significant interests in recent years. And it is possible to make sunlight absorption more effective. A large-scale prototype system for overall water splitting, covering an area of 100 m^2, has been developed utilising $SrTiO_3$:Al modified with a Rh/Cr co-catalyst for H_2 evolving and a Co co-catalyst for O_2 evolving.[54]

Catalysts	Light source	Irradiation Area (cm^{-2})	STH (%)	Ref.
g-C_3N_4	> 420 nm	1	0.06	[97]
$SrTiO_3$:Al	AM1.5 G	9	0.65	[98]
Ta_3N_5/$KTaO_3$	AM1.5 G	38.2	0.014	[99]
CdTe/In_2S_3	AM1.5 G	0.64	1.31	[100]
$MaPbI_3$/Pt	> 475 nm	0.25	0.81	[101]
CdS_2	AM1.5 G	2.25	2.2	[102]

Table 1.1: A summary of the performance and experimental parameters of reported photocatalytic overall water splitting.

This system demonstrated stable and safe performance, achieving an approximate solar-to-hydrogen (STH) efficiency of 0.76% over 1,600 hours with product gas collection and separation. Zhao et al. used a single-bed particle suspension 'baggie' reactor for overall photocatalytic water splitting with Al-doped $SrTiO_3/Rh_{2-y}Cr_yO_3$, reaching a STH value of 0.11%.[55] And Table 1.1 summarises STH efficiency values and detailed parameters of different water splitting systems.

1.2.2 Photocatalytic ammonia decomposition

Although H_2 is a green energy source without any carbon emission, there are still great challenges we need to face and put effort to tackle. For example, H_2 has low volumetric energy density and highly explosive nature, making its storage and transportation significantly difficult. A variety of possible H_2 storing approach has been reported, including liquid state storage, solid state storage and chemical state storage. Liquid H_2 has a high purity and energy density (70.8 kg/m^3), but intensive energy is required to bring and keep H_2 in liquid state. H_2 physically adsorbed on metal-organic framework is easy to release, however, the density of storage is low. While solid-state metal hydrides possess a high energy density, the release of H_2 is not convenient. Ammonia is a promising material for H_2 storage, which has a high energy density 106 kg/m^3 with H_2 content of 17.8%.[56] Moreover, ammonia can be liquified under 8 -10 bars pressure at room temperature, making mature storage and easy transportation.[57] Compared to other H_2 carriers like CH_3OH, HCOOH or cyclohexane, ammonia generates a carbon-free system.

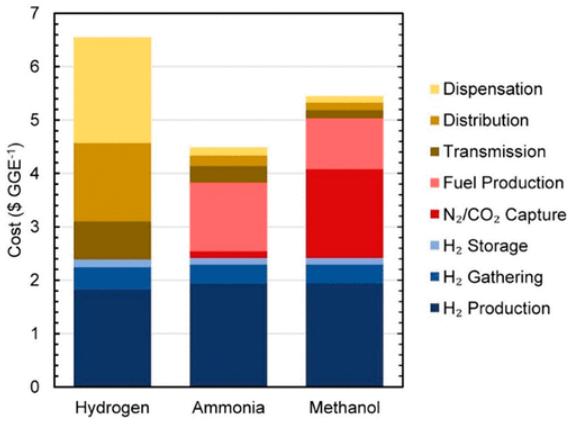

Figure 1.11: Source-to-tank cost comparison of carbon-neutral transportation fuels (GGE represents gasoline gallon equivalent). H_2 gathering indicates H_2 collection from production units. Figures reproduced from Reference [58].

Figure 1.11 compares the source-to-tank costs (energy consumption and associated costs incurred from the primary energy or feedstock source through to delivery into the vehicle fuel tank) of hydrogen, ammonia and methanol, breaking the total into production, collection, storage, transmission, distribution and dispensing components. CO_2 for carbon-based pathways is assumed to be supplied by direct air capture. And the direct air capture capital and operating costs fully included in the upstream (source-to-tank) cost accounting. Moreover, all fuels are modelled as being produced via carbon-neutral routes using renewable energy. Ammonia exhibits a lower cost compared to hydrogen and methanol, with decrease of 31% and 18%, respectively.[58] The high cost of hydrogen arises from expenses associated with its dispensation and distribution. The disadvantage of methanol is low volumetric H_2 density and CO_2 production that requires extra purification. So, methanol carries a larger lifecycle carbon burden, that applies similarly to all other carbon-containing fuels. On a source-to-tank basis, ammonia shows a clear economic advantage among these three fuels. Therefore, considering both volumetric hydrogen density and economic feasibility, ammonia emerges as a promising alternative for hydrogen storage. To extract H_2 from ammonia, catalytic ammonia decomposition is

important and has been extensively researched. The accepted conception is that NH_3 is first adsorbed at the active sites of metal catalysts, giving surface NH_3^*. Then via successive NH_3^* dehydrogenation, N^* and H^* atoms will be formed. Finally, recombinative desorption of N* and H* species leads to the release of N_2 and H_2 into the gas phase (Figure 1.12a).[59]

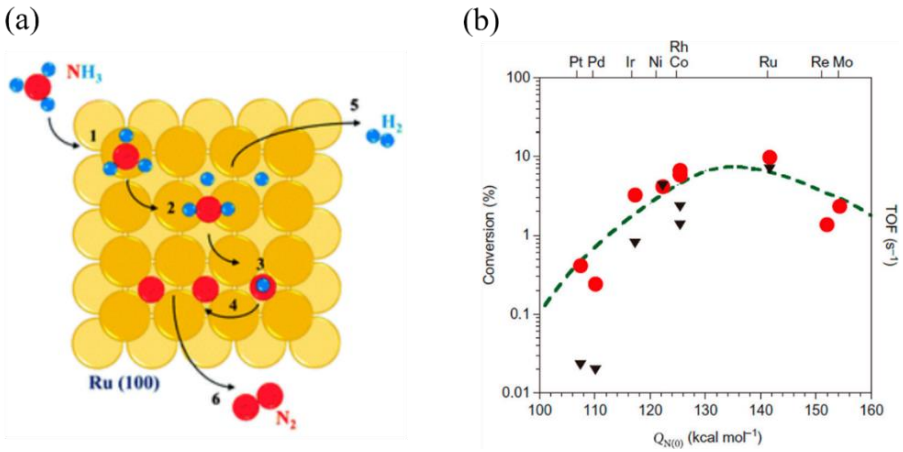

Figure 1.12: (a) Schematic representation of NH_3 decomposition reaction over Ru catalysts. (b) Ammonia conversion calculated from microkinetic modelling (circles, left axis) at 850 K for various transition-metal catalysts and experimental supported catalyst turnover frequencies (TOF) (triangles, right axis) at 850 K plotted against the nitrogen binding energies ($Q_{N(0)}$). The dotted line is calculated by assuming average interaction energies and a correlation between nitrogen and hydrogen binding energies to aid in determining the volcano maximum. Figures reproduced from Reference [60][61].

In Figure 1.12b, the term "theoretical ammonia conversion" refers to the single-pass conversion (%) predicted by the microkinetic reactor model that is parameterised with DFT-computed adsorption/activation energetics. The plotted conversion values are the modelled outlet conversions under the reactor conditions used for the simulation, and therefore represent a kinetic prediction that depends on the assumed temperature, pressure and residence time. [61]

To date, thermal-catalysis is favourable for generating H_2 from ammonia due to the high productivity and reliability, where Ru-based materials were found to be one of the most active and stabile catalysts towards ammonia decomposition among the single-metal catalysts (Figure 1.12b).[61][65][66] Ru/MgO (111) and Ru/γ-Al_2O_3 catalysts are good examples of thermal ammonia decomposition.[62][63] However, this approach encounters intensive thermal energy input. For instance, TiO_2 without any co-catalyst needs the temperature of 700 °C to achieve 100% ammonia conversion at an 80 ml/min NH_3 flow rate.[64] And most of metal-oxide/carbon-material supported Ru catalysts need above 500 °C temperature to give a high turnover frequency or a 100% conversion rate for ammonia decomposition.[67][68] Therefore, photocatalysis provides a green and eco-friendly approach to release H_2 from ammonia by utilising solar energy as the driving force. Photocatalytic ammonia decomposition in the aqueous phase often takes place in alkaline conditions. The photogenerated charge carriers will migrate to the photocatalyst surface to initiate a series of reactions with adsorbed species, resulting ammonia degradation. The oxidation and reduction of ammonia can only proceed when the potential of electron-hole pairs fall within the conduction band and valence band potentials. For aqueous-phase ammonia decomposition, various nitrogen-containing products may form due to their similar redox potentials, including N_2, NO, NO_2, NO_2^- or NO_3^-, which depends on the reaction conditions such as pH, temperature, O_2 concentration or sacrificial reagents. Therefore, effective photocatalytic ammonia decomposition requires that photogenerated electrons and holes on the semiconductor surface possess appropriate reduction and oxidation capabilities to interact with adsorbed species, leading to the formation of free radicals or various reaction products (Figure 1.13a).[69]

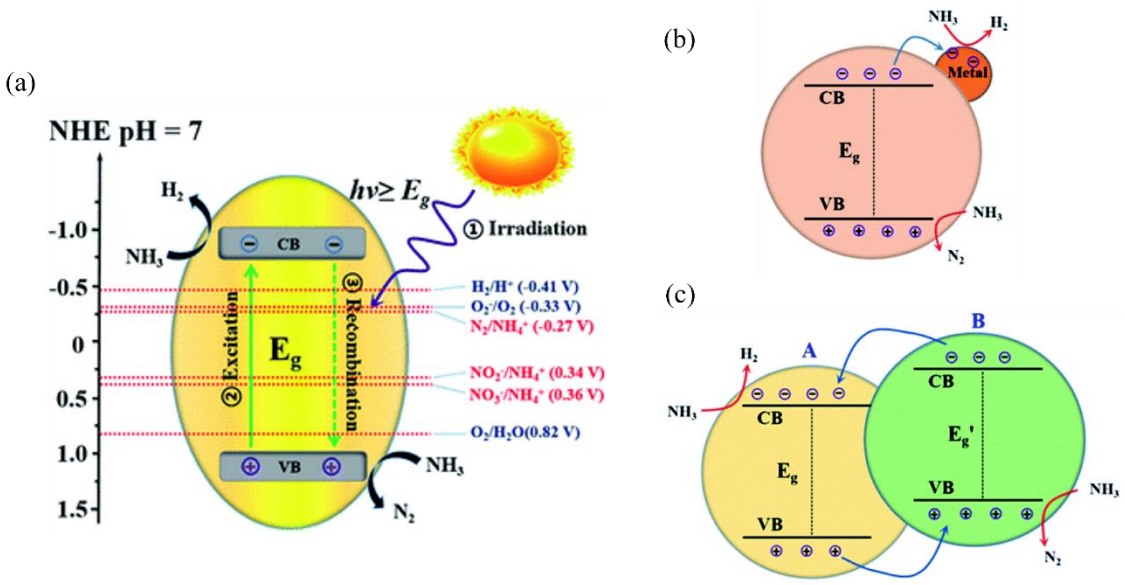

Figure 1.13: (a) The process of photocatalytic ammonia decomposition. (b) Metal-loading and (c) heterojunction building for enhanced photocatalytic ammonia decomposition performance. Figures reproduced from Reference [69].

Most of ammonia decomposition photocatalysts are obtained by metal-loading or constructing heterojunction with another semiconductor. As shown in Figure 1.13b, metal loading will give a heterogeneous nanostructure. It will introduce defect sites and high-speed charge transfer pathways, enhancing the photogenerated electron–hole pair migration and separation, facilitating reactant adsorption and product desorption.[69] TiO_2 has been reported as an active photocatalyst for ammonia decomposition in the aqueous ammonia solution.[70][71][72] As shown in Figure 1.14a, b, a variety of metal including Pt, Rh, Pd, Au, Ni and Cu were loaded on TiO_2 surface, in which Pt/TiO_2 shows the highest activity while Cu/TiO_2 is the worst. This is because when the metal with larger work function (i.e., lower Fermi level) is loaded on TiO_2 surface, photo-excited electrons will be more easily accepted from conduction band to promote ammonia decomposition (Figure 1.14b), indicating Pt has a strong electron extracting ability to separate photogenerated electron-hole pairs. Except modulating the Fermi level of TiO_2 photocatalyst, its performance for ammonia decomposition can also be improved by

adjusting the bandgap structure.[73] Different amount of Ce (from 0 to 1.4 wt.%) was doped into TiO_2 structure, in which 1.2 wt.% Ce/TiO2 demonstrates the best activity due to the most favourable conduction band minimum potential and maximally low bandgap energy.[72]

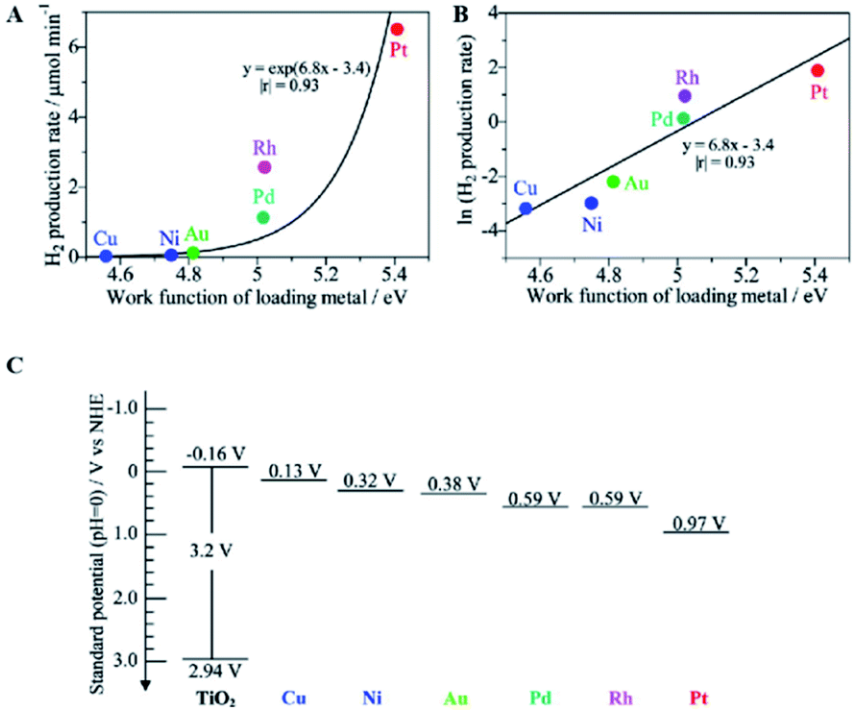

Figure 1.14: (A) The relationship between the hydrogen evolution rate for ammonia decomposition over the TiO_2 with different loading-metal samples and the work function of the corresponding bulk metal, (B) and the logarithmic plot. The tests were operated in a fixed-bed flow reactor with 0.6 g of catalysts and 1 mL/min ammonia flow rate. (C) The standard potentials for the band edge position of titanium oxide and the Fermi level of each loading metal. Figures reproduced from Reference [73].

The proposed mechanism was demonstrated for Pt/TiO_2 as shown in Figure 1.15a. Upon irradiation, TiO_2 generates electron–hole pairs, with the holes migrating to the surface and the electrons transferring to the Pt sites. The photogenerated holes facilitate the oxidation of adsorbed NH_3, forming amide radicals and protons. The amide radicals can further react to produce hydrazine, which subsequently forms diazene. Diazene

decomposes to N_2 and H_2 driven by repulsive interactions between the filled nitrogen lone-pair orbitals and the π-bonding orbital, which destabilise the N–N bond and facilitate H_2 elimination. Meanwhile, the photogenerated electrons at the Pt sites reduce protons, leading to hydrogen production.[73] Utsunomiya et al. applied density function theory (DFT) to help investigate ammonia decomposition over TiO_2 photocatalyst. It was found that the decomposition pathway via NH_2-NH_2 formation is more energetically favourable, where NH_2-NH_2 is generated by coupling of two NH_2 radicals or interaction between one NH_2 radical and one NH_3 molecule, as shown in the route 2 and 2' of Figure 1.15b. And their activation energies are 74.4 and 59.2 kcal mol^{-1}, respectively, which are much lower than the route 1 of Figure 1.15b with activation energy 235.7 kcal mol^{-1}.[71] Therefore, hydrazine molecule (N_2H_4) species act as a vital role in the pathway of photocatalytic ammonia decomposition. In contrast to this associative pathway for ammonia decomposition, Ru/GaN nanowire photocatalyst shows that after the intermediate NH_2^* stabilised on the catalyst surface, it will successively dehydrogenate to give N^*, instead of forming hydrazine species (Figure 1.15c).[74]

ZnO is also widely used in photocatalysis as its performance can be enhanced by tailoring the crystalline size, oxygen defects and surface area. Oxygen defect concentration in ZnO can severely influence the activity of ammonia decomposition. As the increased deep oxygen vacancy concentration in the structure of ZnO, there will be deep levels trapping the photo-excited electrons, making them unavailable for the photocatalytic reaction.[75] Moreover, ZnO and its heterojunction has also been used to decompose aqueous ammonia. TiO_2/ZnO is a good example, where photogenerated charge carriers are effectively separated.[76]

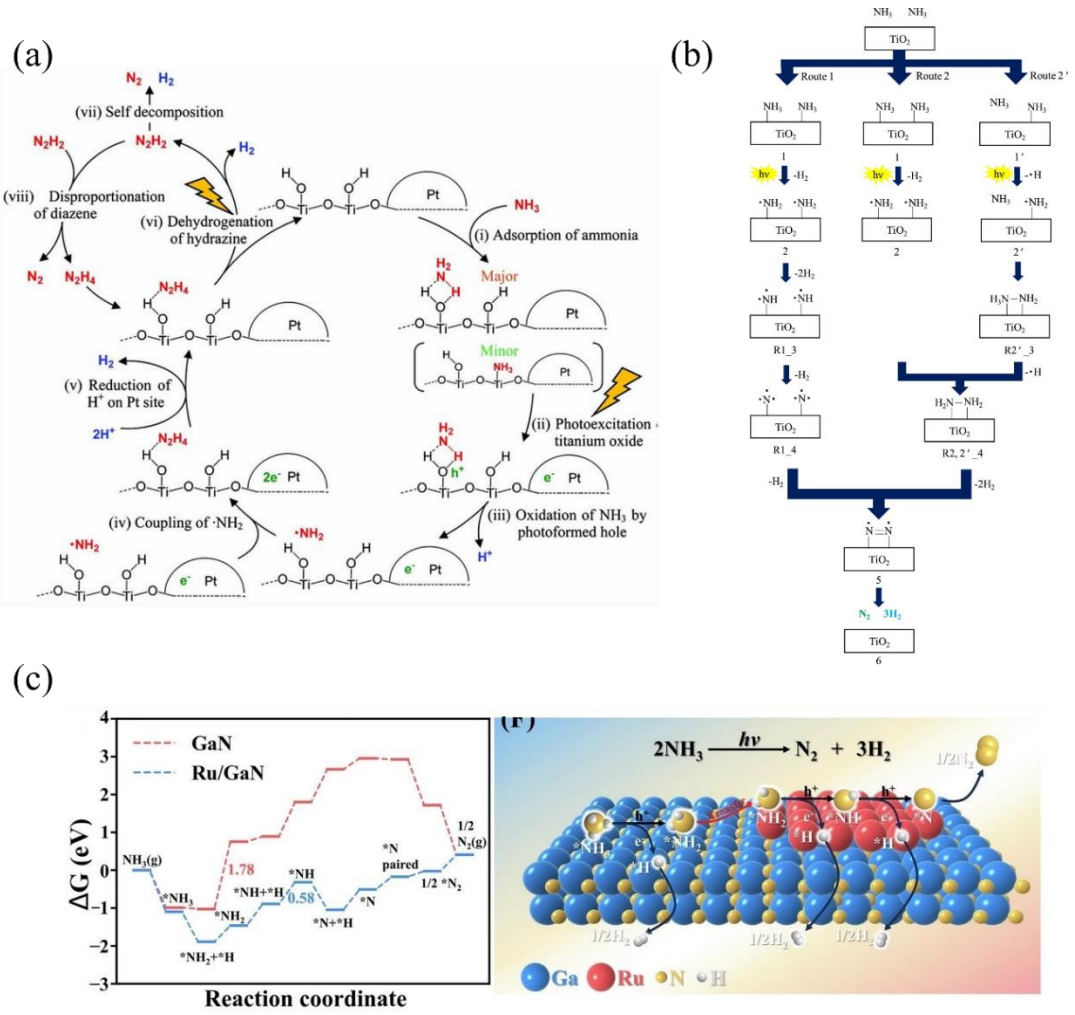

Figure 1.15: Proposed Mechanisms for photocatalytic decomposition of aqueous ammonia solution over (a) Pt/TiO_2 and (b) TiO_2. (c) Calculated free energy ΔG diagrams for NH_3 decomposition on GaN and Ru/GaN. Figures reproduced from Reference [73][71][74].

However, there are only few studies on the photocatalytic ammonia decomposition in the gas phase, especially in a closed system. Cu-Fe and Ru/Al_2O_3 show a good activity in the flow reactor.[77][78] The Cu-Fe antenna-reactor in a gas flow system under 470 nm LEDs with 7.63 W/cm^2 light intensity (Figure 1.16a) has 0.466 mmol $g^{-1}h^{-1}$ of ammonia decomposition activity, which is higher than the Ru-based thermo-catalyst activity at 623 K (0.435 mmol $g^{-1}h^{-1}$). The embedded correlated wave function theory was applied to calculate potential energy surfaces projected along minimum-energy paths (Figure 1.16b).

And it was found that dissociative adsorption of NH_3 and associative desorption of N_2 are two possible rate determine steps.[77] For gas-phase ammonia decomposition over Ru/Al_2O_3 in a flow reactor was utilised to study the proton poisoning effect (Figure 1.16c), which shows that higher H_2 pressure will lead to H* species adsorbed on the catalyst surface, blocking the active sites and decreasing the photocatalytic activity (Figure 1.16d).[78] When the catalytic reaction is carries in a closed system, the activity will be severely affected by the reaction equilibrium shift. As the decomposition of NH_3 increases the molecule number, the gradually increased pressure favours the reverse reaction, inhibiting the decomposition process. For instance, the photocatalytic gaseous ammonia decomposition was carried out in a closed batch reactor over Pt/TiO_2, where the H_2 evolution rate is only 217 μmol $g^{-1}h^{-1}$ compared to the activity of 650 μmol $g^{-1}h^{-1}$ in a gaseous ammonia flow system.[73]

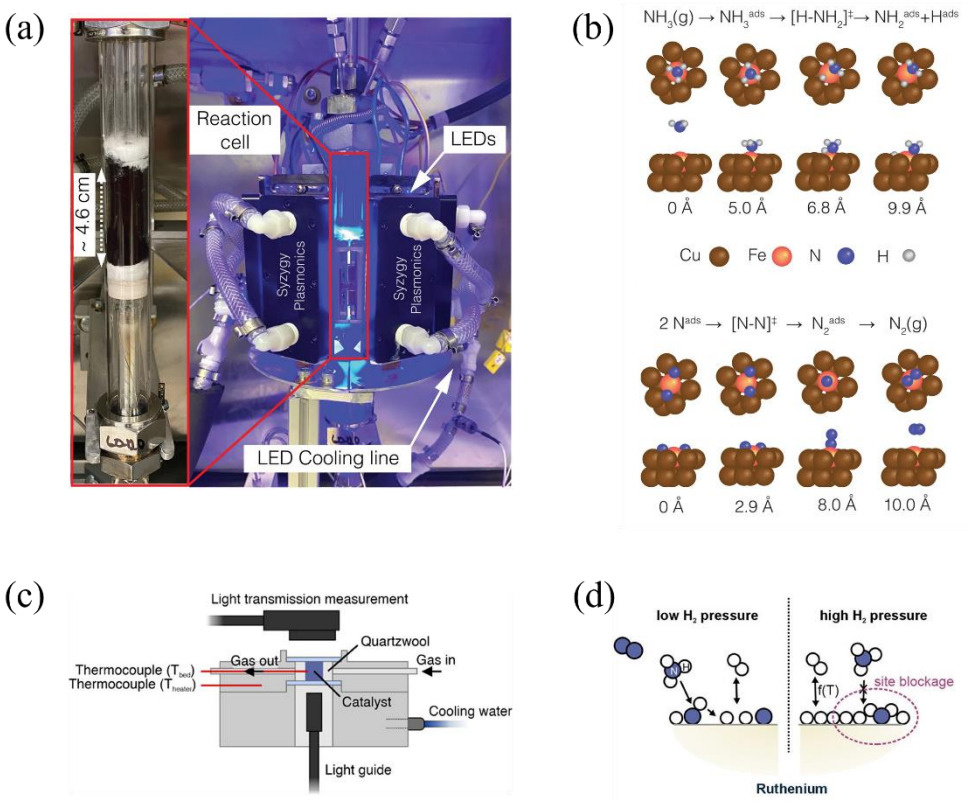

Figure 1.16: (a) The Harrick reaction chamber as a reaction cell with LEDs at 470 nm for gas phase ammonia decomposition in a flow system with Cu-Fe. (b) NH_3 dissociative

adsorption and associative desorption of N_2 pathway on a Cu-Fe antenna-reactor surface. (c) Gas-flow reactor with Ru/Al_2O_3 for photocatalytic ammonia decomposition. (d) H_2 dissociatively chemisorbs on Ru at high H_2 pressure, resulting in site blockage and decreased ammonia decomposition reaction rate. Figures reproduced from Reference [77][78].

1.2.3 Photocatalytic ammonia synthesis

Not only is ammonia a promising approach for H_2 storage, it is also crucial for the production of agricultural fertiliser, medical drugs and chemicals. Ammonia synthesis via Haber-Bosch process was one of the greatest inventions in the 20th century.[79] By directly converting abundant atmospheric nitrogen into ammonia, it contributes for 90% of the world's annual ammonia production.[80] And it has led to nearly a 400% increase in crop yields, ensuring a stable food supply for the global population.[81] However, this process operates at high temperature around 300 to 500 °C using iron-based catalysts to activate N_2. This harsh reaction conditions consume approximately 2% of the world's total energy and contribute around 1.4% of global CO_2 emissions annually.[82] Given the current energy crisis and the push for carbon neutrality, developing an efficient, green, and sustainable ammonia synthesis technology is important. Therefore, photocatalytic ammonia synthesis has attracted lots of attention in recent years. But there are great challenges we need to face for using N_2 in photocatalytic ammonia synthesis according to its inert properties. For example, an intensive N≡N triple bond energy is 941 kJ mol^{-1}, formed by filling six electrons in the bonding orbitals (Figure 1.17a). And its dissociation is significantly inhibited by the ultra-strong cleavage energy of the first bond (410 kJ mol^{-1}).[79]

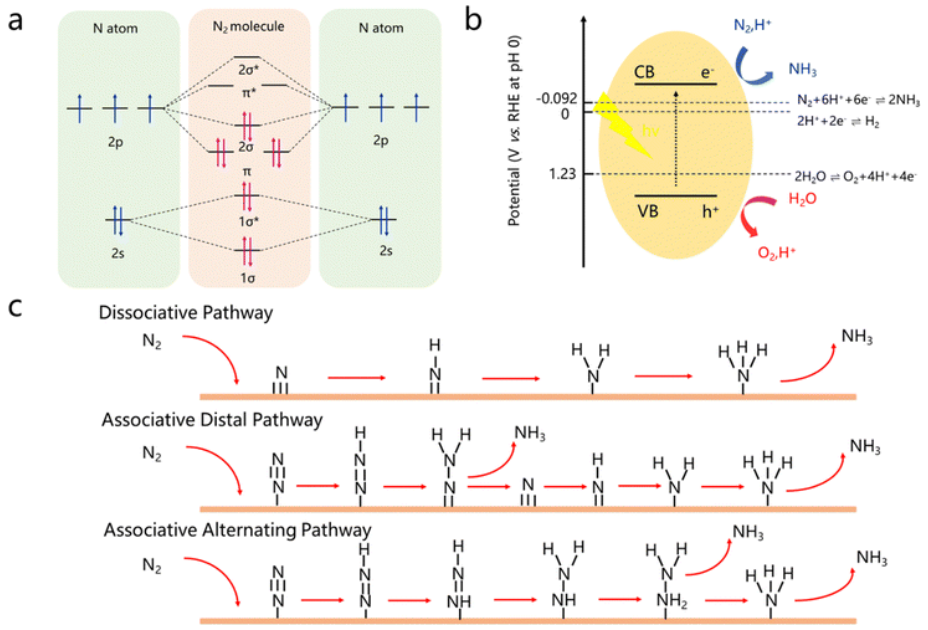

Figure 1.17: (a) N_2 molecular orbitals. (b) The reaction process and redox potentials (V *vs.* RHE at pH 0) of photocatalytic ammonia synthesis. (c) The reaction mechanism of the ammonia synthesis reaction. Figures reproduced from Reference [79].

As shown in Figure 1.17b, under light illumination, photogenerated electrons and holes can migrate to the catalysts surface to initiate N_2 reduction and H_2O oxidation reaction.[83] Unlike the dissociative Haber–Bosch mechanism, which requires high temperatures to break the N≡N triple bond, photocatalytic ammonia synthesis proceeds via an associative pathway in which N_2 is chemisorbed on the catalyst surface and stepwise hydrogenated to intermediates such as $*N_2H$ under mild conditions (Figure 1.17c). Then there are two possible pathways according to the hydrogenation sequence. In the distal associative pathway, the nitrogen atom positioned farther from the photocatalyst undergoes hydrogenation first, forming NH_3, followed by the hydrogenation of the second nitrogen atom to produce another NH_3 molecule. In contrast, the alternating pathway involves the stepwise, alternating hydrogenation of both nitrogen atoms, leading to the sequential release of two NH_3 molecules.[84] Based on the description above, photocatalysts for N_2

reduction to NH_3 need to absorb and activate inert N_2 molecules, allowing this thermodynamically uphill reaction to occur at a measurable rate.

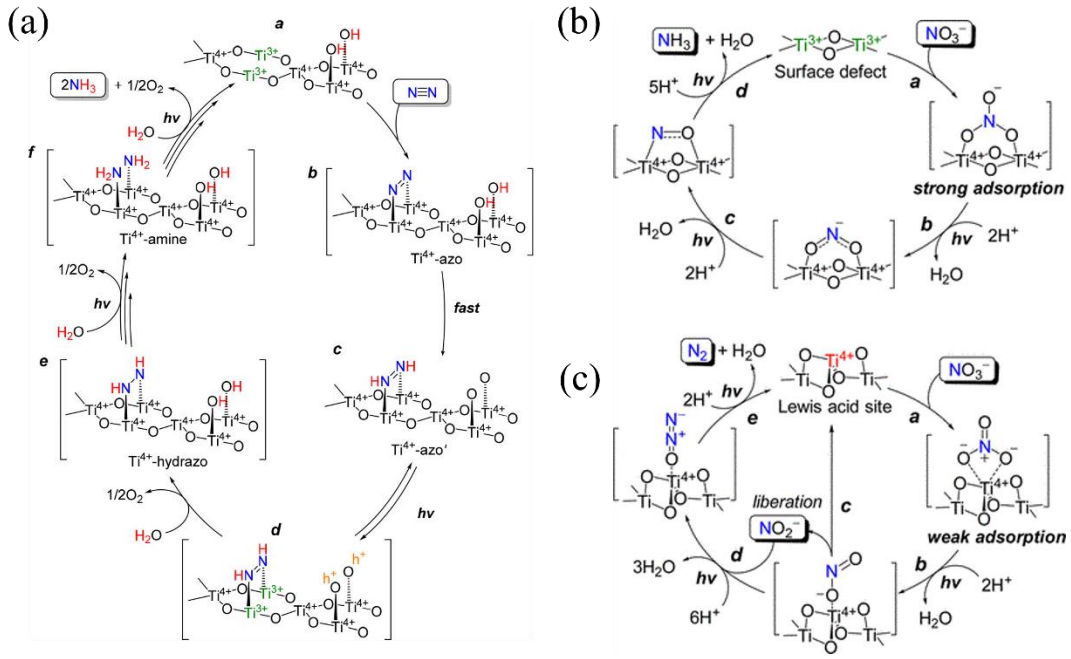

Figure 1.18: (a) Suggested mechanism for photocatalytic N_2 reduction over TiO_2 with oxygen vacancy; Proposed Mechanisms for Photocatalytic Reduction of NO_3^- on (b) surface defect and (c) Lewis-acid site of TiO_2. Figures reproduced from Reference [85][86].

Fe-doped TiO_2 shows activity for ammonia synthesis under UV irradiation, with small amount of N_2H_4 generation. This is because doping Fe in TiO_2 can facilitate the separation between photoexcited electron-hole pairs.[39] Besides, it has been reported that the surface oxygen vacancy on TiO_2 can help enhance the photocatalytic activity of ammonia synthesis. The commercial TiO_2 with large amount of oxygen vacancy under UV-light demonstrated a stable performance for ammonia synthesis over 48 hr. This is because Ti^{3+} created by oxygen vacancy serves as an adsorption site for N_2 and trapping sites for photo-generated electrons, facilitating the efficient conversion of N_2 to NH_3. As the reaction proceeded, electrons and protons were successively transferred to the adsorbed

N_2 molecules, whilst the active Ti^{3+} sites could be regenerated, thereby ensuring a sustained photocatalytic activity (Figure 1.18a).[85] Moreover, nitrate species can also be reduced to ammonia by TiO_2, in which the TiO_2 sample with a large amount of oxygen vacancy has a 97% selectivity for the nitrate-to-ammonia conversion under UV irradiation. As shown in Figure 1.18b, NO_3^- can be adsorbed onto the two adjacent Ti cations with a bidentate structure. The strongly adsorbed NO_3^- is reduced by photoexcited electrons and kept adsorbed strongly onto the surface defects, suppressing its liberation and inhibiting N_2 formation. Therefore, NH_3 is selectively produced on the surface defects. In contrast, NO_3^- is adsorbed onto the Lewis acid site of TiO_2 with a bridged structure (Figure 1.18c), where the coordination is much weaker. Thus, the intermediate liberation will promote N_2 production.[86]

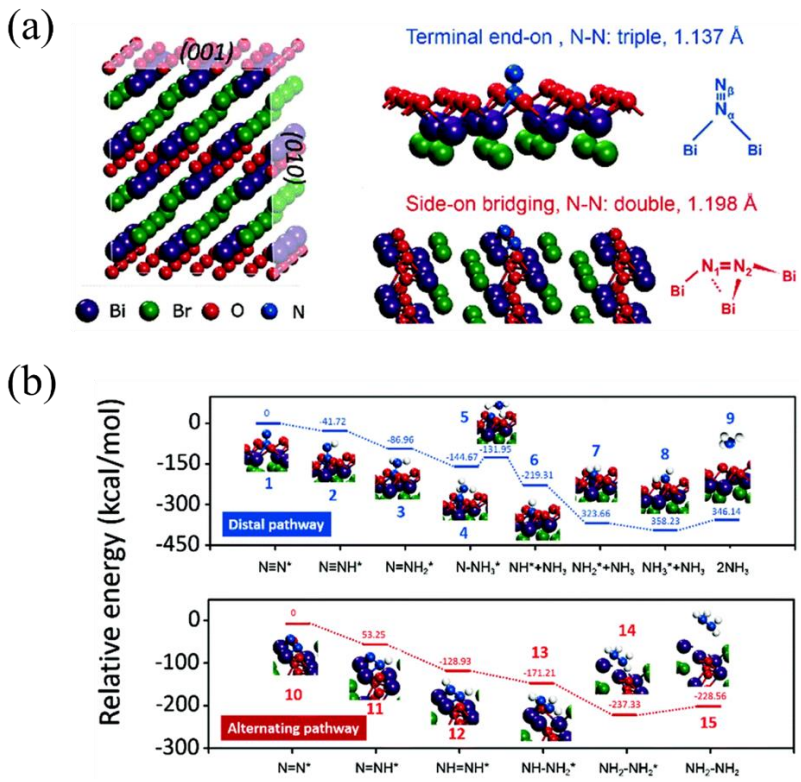

Figure 1.19: (a) The (001) and (010) facets of BiOCl. The terminal end-on adsorption mode and the side-on bridging adsorption mode of N_2 on (001) facets and (010) facets of

BiOCl, respectively. (b) The distal pathway and alternating pathway for N_2 fixation mediated on (001) and (010) facets. Figures reproduced from Reference [87].

Besides, bismuth-based materials have also attracted lots of attention due to its optical properties. BiOCl with surface oxygen vacancy has been investigated to obtain insights of NH_3 synthesis on different facets (010) and (001), where the N_2 molecule adsorbed on the oxygen vacancy site can be reduced to NH_3 via successive proton-assisted electron transfer steps. As shown in Figure 1.19a, the N_2 adsorption mode is influenced by the facets of BiOCl. On the oxygen vacancy site of the (001) facet, the N_2 molecule is adsorbed via a terminal end-on coordination mode, allowing an asymmetric distal pathway to NH_3 (Figure 1.19b). While the N_2 molecule adsorption on the (010) facet has a side-on bridging coordination geometry, generating a N_2H_4 molecule through an alternating pathway (Figure 1.19b).[87] This above mechanistic study clearly shows how different crystalline facets affect the photocatalytic ammonia synthesis.

1.3 Photocatalysis with layered perovskite oxide

Layered perovskite oxide exhibits excellent stability and possess conduction bands significantly more negative than the reduction potential of H^+ for photocatalytic water splitting, providing sufficient over potential for H_2 generation, particularly under UV-light irradiation. These materials are typically composed of earth-abundant elements and can be readily synthesised through the calcination of mixed simple oxide precursors, reducing production costs.[15] Due to their unique slab structure, which can accommodate different metal cations at the A or B sites, partial or complete substitution of these cations enables extensive compositional tuning. This flexibility allows for precise control and optimisation of their physicochemical properties, improving photocatalytic performance. More importantly, their layered structure promotes charge separation. In

conventional photocatalysts without a layered structure, photogenerated charge carriers must migrate long distances to reach the surface reaction sites (Figure 1.20a). In contrast, layered perovskite provides reaction sites within the interlayer space, effectively shortening the charge migration distance and reducing carrier recombination (Figure 1.20b).[18]

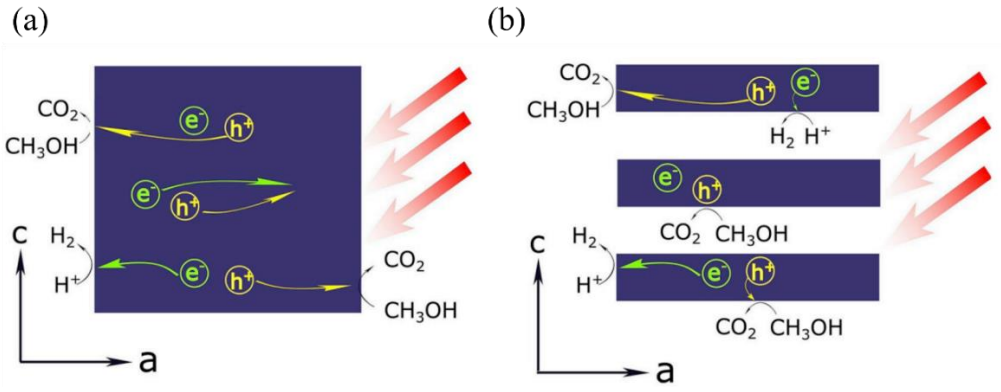

Figure 1.20: Schematic mechanisms of photocatalytic H_2 evolution over (a) non-layered materials and (b) layered perovskites from methanol solution (methanol as the sacrificial reagent). Figures reproduced from Reference [15].

And Table 1.2 demonstrates the photocatalytic activity of HER for various Dion-Jacobson phase layered perovskite.

Catalysts	Light source	Solution	Activity ($\mu molg^{-1}h^{-1}$)	Ref.
$RbTaTa_2O_7$	UV	Water	6.0	[103]
$RbPrTa_2O_7$	UV	Water	4.5	[103]
$RbNdTa_2O_7$	UV	Water	235.0	[103]
$HNdTa_2O_7$	UV	Water	6.0	[103]
$RbSmTa_2O_7$	UV	Water	53.0	[103]
$CsCa_2Ta_3O_{10}$	UV	Water	38.0	[104]
$NaCa_2Ta_3O_{10}$	UV	Water	61.0	[104]
$HCa_2Ta_3O_{10}$	UV	Water	13.0	[104]
$C_6H_{13}NH_3Ca_2Ta_3O_{10}$	UV	Water	551.5	[104]
$HPb_2Nb_3O_{10}$	> 420 nm	16% CH_3OH	3.2	[95]

Table 1.2: A summary of the performance of different Dion-Jacobson phase layered perovskite for overall photocatalytic water splitting.

Furthermore, their unique flexible layered nanostructure allows for convenient modification of micro-nanostructures and morphologies using "soft chemistry" approaches such as ion exchange, exfoliation, and self-assembly. These modifications can be achieved without altering the fundamental perovskite framework, offering additional strategies to enhance photocatalytic performance.

1.3.1 Ion-doping layered perovskite

Tuning bandgap is one of the most widely employed strategies to enhance light absorption and charge separation in semiconductor photocatalysts. The band structure of semiconductors is primarily determined by their chemical composition, crystal structure, grain size and superlattice arrangement. Among various band engineering techniques, ion doping is regarded as one of the most convenient and effective methods for improving photocatalytic performance of layered perovskite. Since doping introduces guest ions into the lattice, it can lead to structural distortion or defects. Therefore, to minimise disruption of the original crystal structure, the ionic radius of the dopant should be as close as possible to that of the substituted element. In layered perovskite oxide, Fe^{3+}, Ti^{4+}, W^{6+}, Cr^{3+}, Mo^{3+} and Ni^{2+} are commonly used to replace B-site cations, while nitrogen is often introduced as a substitute for oxygen. The effects of doping can be summarised as follows. (1) Electronic structure modification: doped metal cations introduce additional electronic states within the bandgap, acting as shallow traps for photogenerated electrons or holes, thereby promoting charge separation. (2) Enhanced light absorption: impurity levels introduced by doping can either facilitate inter-band excitation or hybridise with the original band structure, leading to a narrowed bandgap and improved visible-light

absorption. (3) Built-in electric fields: differences in valence states and ionic sizes between dopants and host atoms can induce internal electric fields, further facilitating charge separation.[88][89][90] Although the fundamental principles of ion doping remain consistent, the specific impact on photocatalytic performance varies depending on the intrinsic properties of the dopants and synthesis conditions. For example, Cr doped $HPbNb_3O_{10}$ layered perovskite shows an increase in H_2 evolution rate compared to undoped sample due to the hybridisation of Cr 3d and O 2p orbitals, allowing lower photon energy for electron excitation. When it comes to $KSrNb_3O_{10}$ layered perovskite, doped Cr provides a new energy state in the band structure by splitting of its 3d orbital which acts as a shallow hole trap and is beneficial for charge separation and enhancement of photocatalytic activity.[91][92] This band engineering difference is attributed to the position of valence band maximum in layered perovskite.

1.3.2 Co-catalyst loading layered perovskite

Co-catalyst is indispensable for layered perovskite to achieve efficient photocatalytic water splitting. Platinum is a widely used cocatalyst in photocatalysis and is typically deposited onto the external surface of photocatalysts via photo-deposition. The transfer of photogenerated electrons to Pt nanoparticles can effectively suppresses electron-hole recombination, significantly enhancing photocatalytic performance.[93] While the loading method plays a critical role in determining photocatalytic performance, as different deposition sites influence charge migration distances and recombination rates.[94] Thus, studying novel loading strategies to optimise the spatial distribution of co-catalysts is essential for enhancing charge carrier separation and enhancing the photocatalytic performance of layered perovskite. A highly effective strategy to reduce

charge transfer distance is the deposition of Pt at the interlayer space of layered perovskites. This approach eliminates the need for photogenerated carriers to migrate along the perovskite slabs to reach active reaction sites. $[Pt(NH_3)_4]Cl_2$ can be used as the precursor to disperse Pt nanoparticles within the interlayer region of $HPb_2Nb_3O_{10}$ perovskite. Because $[Pt(NH_3)_4]^{2+}$ ions can be intercalated into the interlayer space via ion exchange with interlayer H^+. Upon reduction, Pt nanoparticles are uniformly dispersed within the interlayer region, leading to a significant enhancement in photocatalytic activity. But when H_2PtCl_6 is used as the Pt precursor, the negatively charged $[PtCl_6]^{2-}$ ions cannot undergo ion exchange with interlayer H^+, resulting in Pt deposition exclusively on the external surface of $HPb_2Nb_3O_{10}$.[95] Besides Pt, other co-catalysts have also been extensively investigated for photocatalysis using layered perovskite. Ni co-catalyst was found to enhance the photocatalytic activity of $H_2La_{2/3}Ta_2O_7$ but had no obvious effect on $H_2SrTa_2O_7$. This difference arises from the distinct localisation of Ni species in the two materials. In $H_2La_{2/3}Ta_2O_7$, Ni^{2+} ions and small NiO clusters are intercalated into the interlayer space, where they can act as active sites for H_2 generation. However, in $H_2SrTa_2O_7$, NiO forms as large particles remaining exclusively on the external surface, failing to contribute to photocatalytic reaction.[96]

1.3.3 Exfoliating layered perovskite

Expanding the photocatalyst surface area is also a strategy for enhancing charge separation in photocatalysts. A larger surface area not only provides more active sites for the photocatalytic reaction but also correlates with smaller particle sizes, thereby shortening the migration distance of photogenerated carriers and reducing electron-hole recombination rates. For layered perovskites, an effective approach to increasing their specific surface area is exfoliation into ultrathin nanosheets. This method takes advantage of the intrinsic layered structure and ion-exchange properties of perovskites, increasing

the accessible surface area. The resulting 2D materials, with atomic-scale thickness and submicron lateral dimensions, exhibit improved photocatalytic performance compared to their bulk counterparts. Therefore, exfoliated layered perovskites have been widely applied in photocatalytic water splitting.[15][26]

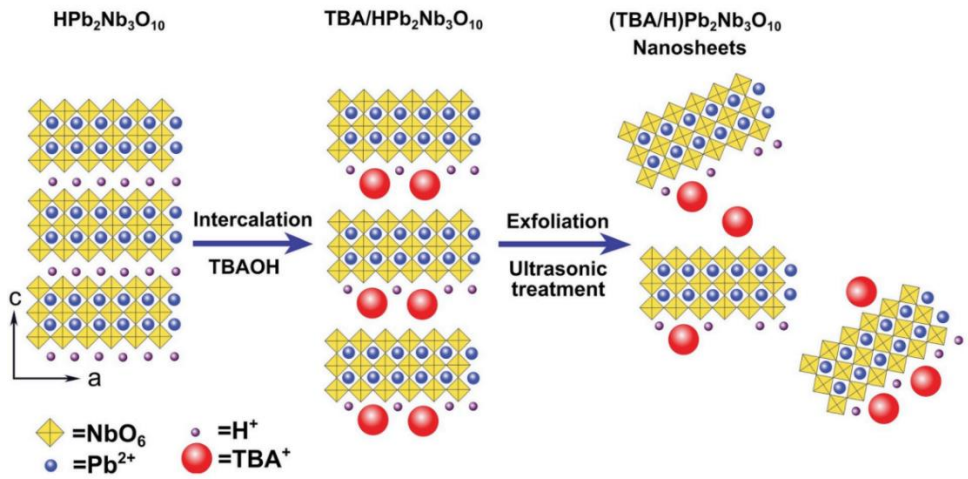

Figure 1.21: Intercalation and exfoliation of $HPb_2Nb_3O_{10}$ to obtain perovskite nanosheets. Figures reproduced from Reference [15].

As shown in Figure 1.21, perovskite nanosheets are prepared by exfoliating the protonated layered perovskite, which needs the intercalation of a large group such as tetrabutylammonium. By the acid-base reaction between tetrabutylammonium hydroxide (TBAOH) and H^+ at the interlayer, the interlayer space of layered perovskites can be swelled to the point of delamination and colloidal nanosheets can be collected. Besides, by applying the high-power ultrasonic waves, the interlayer water molecules can be heated and a large number of bubble clusters will be produced. These bubbles can generate intensive energy and introduce mechanical shear stress and turbulence, resulting an effective separation of $[Pb_2Nb_3O_{10}]$ octahedra slabs. Upon exfoliation, the surface area of $HPb_2Nb_3O_{10}$ is extended while the crystal structure maintains. As the large surface area is more accessible for co-catalyst loading, perovskite nanosheets of $HPb_2Nb_3O_{10}$ is more advantageous for photocatalysis than bulk $HPb_2Nb_3O_{10}$. And it has been shown that the

nanosheets give H_2 evolution activity three times as high as unexfoliated $HPb_2Nb_3O_{10}$ for water splitting under visible light.[96] Different modified layered perovskite nanosheets for water splitting are summarised in Table 1.3.

Nanosheet catalysts	Light source	Solution	Activity ($\mu molg^{-1}h^{-1}$)	Ref.
$HPb_2Nb_3O_{10}$	UV	20% CH_3OH	22.8	[105]
$Pt/HPb_2Nb_3O_{10}$	UV	20% CH_3OH	784.0	[105]
$BaNb_4O_{15}$	UV	Water	35.0	[106]
$NiO_X/BaNb_4O_{15}$	UV	Water	310	[106]
$Rh/N\text{-}Ca_2Ta_3O_{10}$	Full arc	20% CH_3OH	1660.0	[107]
$Ru/N\text{-}Ca_2Ta_3O_{10}$	Full arc	20% CH_3OH	715.0	[107]
$Pt/N\text{-}Ca_2Ta_3O_{10}$	Full arc	20% CH_3OH	700.0	[107]
$RhO_X/N\text{-}Sr_2Ta_3O_{10}$	Full arc	20% CH_3OH	1511.0	[108]
$RhO_X/N\text{-}Sr_2Ta_3O_{10}$	> 420nm	20% CH_3OH	1.4	[108]

Table 1.3: Summary of layered perovskite nanosheets for water splitting.

1.4 Aim of the thesis

Numerous countries worldwide are highly motivated to incorporate ammonia as a key component of future energy systems. As a result, they are actively working on establishing strategic roadmaps and advancing the necessary technologies to achieve this vision. Figure 1.22 demonstrates a sustainable route of ammonia application in the energy sector. First, H_2 is produced as the energy source by a green approach such as photocatalytic water splitting. Due to its highly explosive nature and low volumetric energy density, H_2 is then converted to NH_3 by photocatalytic ammonia synthesis, which makes safe storage and convenient transportation. In the utilisation site, the energy from NH_3 can be harvested directly to H_2 by photocatalytic ammonia decomposition. This route includes several photocatalytic technologies, which can effectively reduce the carbon emission and facilitate a green energy system in the future.

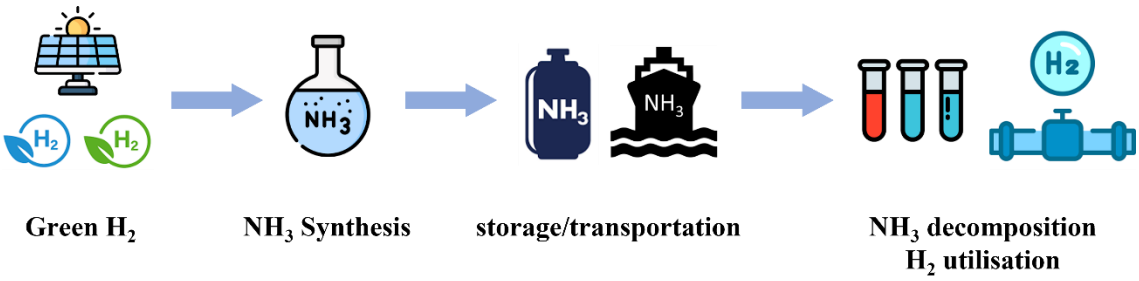

Figure 1.22: Production and application routes of ammonia.

Layered perovskite oxide possesses exceptional stability and tunability, especially the unique layered structure gives more possibilities to modify its chemical and physical properties. In my DPhil research, I chose this type of materials to investigate photocatalytic technologies in above ammonia application route, including water splitting, ammonia decomposition and ammonia synthesis. In various reaction scenarios, I adjusted the modifying strategies for layered perovskite to enhance its photocatalytic activity, and different characterisation techniques were used to understand the improvement of catalyst performance. In Chapter 3, perovskite nanosheets were integrated with reduced graphene oxide via an electrostatic-driven assembly approach. Then, various lanthanide elements including La, Pr and Nd were incorporated as A-site cations to further tune the nanocomposite electronic properties, achieving an increased photocatalytic activity for H_2 evolution from water splitting reaction. Density function theory simulations were applied to study the interaction between different elements present in the nanocomposites. Chapter 4 demonstrates a layered protonated perovskite, $HPrNb_2O_7$, as an efficient catalyst for ammonia decomposition under mild photo-thermal conditions. Upon exposure to NH_3 at elevated temperatures, $HPrNb_2O_7$ promoted the *in-situ* formation of hydrazine intermediates within its interlayer galleries, enabled by thermally generated oxygen vacancies and hydrogen bonding. Advanced characterisation techniques were applied to confirm the formation and stabilisation of hydrazine The stabilisation of

hydrazine intermediate promoted the associative mechanism, lowering the activation barrier. In Chapter 5, moiré engineering perovskite superlattice shows efficient photocatalytic ammonia synthesis under thermal assistance. The 2D Dion-Jacobson perovskite layers were precisely tuned by intercalating various tetra-alkyl ammonium cations, prolonging lifetime of localised charge carriers. This work demonstrates the integration of moiré engineering into photocatalysis, deepening the understanding of superlattice functionality and paving the way for designing efficient energy conversion systems under operational conditions.

1.5 Reference

1. Bhalla, A.S., Guo, R. and Roy, R., 2000. The perovskite structure—a review of its role in ceramic science and technology. *Materials research innovations*, *4*(1), pp.3-26.
2. Goodenough, J.B. and Longo, J.M., 1970. Crystallographic and magnetic properties of perovskite and perovskite-related compounds. *Landolt-Bornstein*, *4*, pp.126-314.
3. Pickett, W.E. and Singh, D.J., 1996. Electronic structure and half-metallic transport in the $La_{1-x}Ca_xMnO_3$ system. *Physical Review B*, *53*(3), p.1146.
4. Vasala, S. and Karppinen, M., 2015. A2B′ B ″O6 perovskites: a review. *Progress in solid state chemistry*, *43*(1-2), pp.1-36.
5. Goldschmidt, V.M., 1926. Die gesetze der krystallochemie. *Naturwissenschaften*, *14*(21), pp.477-485.
6. Kumar, A., Verma, A.S. and Bhardwaj, S.R., 2008. Prediction of formability in perovskite-type oxides. *Open Applied Physics Journal*, *1*, pp.11-19.
7. Glazer, A.M., 1972. The classification of tilted octahedra in perovskites. *Structural Science*, *28*(11), pp.3384-3392.
8. McNulty, J.A. and Lightfoot, P., 2021. Structural chemistry of layered lead halide perovskites containing single octahedral layers. *IUCrJ*, *8*(4), pp.485-513.
9. Anderson, M.T., Greenwood, K.B., Taylor, G.A. and Poeppelmeier, K.R., 1993. B-cation arrangements in double perovskites. *Progress in solid state chemistry*, *22*(3), pp.197-233.
10. King, G. and Woodward, P.M., 2010. Cation ordering in perovskites. *Journal of Materials Chemistry*, *20*(28), pp.5785-5796.

11. Pauling, L., 1929. The principles determining the structure of complex ionic crystals. *Journal of the american chemical society*, *51*(4), pp.1010-1026.
12. Anderson, M.T. and Poeppelmeier, K.R., 1991. Lanthanum copper tin oxide (La_2CuSnO_6): a new perovskite-related compound with an unusual arrangement of B cations. *Chemistry of Materials*, *3*(3), pp.476-482.
13. Caignaert, V., Millange, F., Hervieu, M., Suard, E. and Raveau, B., 1996. The manganite Nd0.5Sr0.5MnO3: A rare distortion of the perovskite. *Solid state communications*, *99*(3), pp.173-177.
14. Leinenweber, K. and Parise, J., 1995. High-pressure synthesis and crystal structure of CaFeTi2O6, a new perovskite structure type. *Journal of Solid State Chemistry*, *114*(1), pp.277-281.
15. Hu, Y., Mao, L., Guan, X., Tucker, K.A., Xie, H., Wu, X. and Shi, J., 2020. Layered perovskite oxides and their derivative nanosheets adopting different modification strategies towards better photocatalytic performance of water splitting. *Renewable and Sustainable Energy Reviews*, *119*, p.109527.
16. Grabowska, E., 2016. Selected perovskite oxides: Characterization, preparation and photocatalytic properties—A review. *Applied Catalysis B: Environmental*, *186*, pp.97-126.
17. Kanhere, P. and Chen, Z., 2014. A review on visible light active perovskite-based photocatalysts. *Molecules*, *19*(12), pp.19995-20022.
18. Takata, T., Tanaka, A., Hara, M., Kondo, J.N. and Domen, K., 1998. Recent progress of photocatalysts for overall water splitting. *Catalysis Today*, *44*(1-4), pp.17-26.

19. Calabrese, J., Jones, N.L., Harlow, R.L., Herron, N., Thorn, D.L. and Wang, Y., 1991. Preparation and characterization of layered lead halide compounds. *Journal of the American Chemical Society*, *113*(6), pp.2328-2330.
20. Hanmandlu, C., Singh, A., Boopathi, K.M., Lai, C.S. and Chu, C.W., 2020. Layered perovskite materials: key solutions for highly efficient and stable perovskite solar cells. *Reports on Progress in Physics*, *83*(8), p.086502.
21. Ahmad, S., Hanmandlu, C., Kanaujia, P.K. and Prakash, G.V., 2014. Direct deposition strategy for highly ordered inorganic organic perovskite thin films and their optoelectronic applications. *Optical Materials Express*, *4*(7), pp.1313-1323.
22. Ishihara, T., Takahashi, J. and Goto, T., 1989. Exciton state in two-dimensional perovskite semiconductor $(C_{10}H_{21}NH_3)_2PbI_4$. *Solid state communications*, *69*(9), pp.933-936.
23. Hong, X., Ishihara, T. and Nurmikko, A.V., 1992. Dielectric confinement effect on excitons in PbI 4-based layered semiconductors. *Physical Review B*, *45*(12), p.6961.
24. Muljarov, E.A., Tikhodeev, S.G., Gippius, N.A. and Ishihara, T., 1995. Excitons in self-organized semiconductor/insulator superlattices: PbI-based perovskite compounds. *Physical Review B*, *51*(20), p.14370.
25. Guo, Z., Wu, X., Zhu, T., Zhu, X. and Huang, L., 2016. Electron–phonon scattering in atomically thin 2D perovskites. *ACS nano*, *10*(11), pp.9992-9998.
26. Liu, X., Que, W., Xing, Y., Yang, Y., Yin, X., & Shao, J., 2016. New architecture of a petal-shaped Nb 2 O 5 nanosheet film on FTO glass for high photocatalytic activity. *RSC Advances*, *6*(12), 9581-9588.

27. Wu, X., Trinh, M.T. and Zhu, X.Y., 2015. Excitonic many-body interactions in two-dimensional lead iodide perovskite quantum wells. *The Journal of Physical Chemistry C*, *119*(26), pp.14714-14721.
28. Smith, M.D., Jaffe, A., Dohner, E.R., Lindenberg, A.M. and Karunadasa, H.I., 2017. Structural origins of broadband emission from layered Pb–Br hybrid perovskites. *Chemical science*, *8*(6), pp.4497-4504.
29. Hu, T., Smith, M.D., Dohner, E.R., Sher, M.J., Wu, X., Trinh, M.T., Fisher, A., Corbett, J., Zhu, X.Y., Karunadasa, H.I. and Lindenberg, A.M., 2016. Mechanism for broadband white-light emission from two-dimensional (110) hybrid perovskites. *The journal of physical chemistry letters*, *7*(12), pp.2258-2263.
30. Ertl, G., 2009. Wilhelm Ostwald: Founder of physical chemistry and Nobel laureate 1909. *Angewandte Chemie International Edition*, *48*(36), pp.6600-6606.
31. Roduner, E., 2014. Understanding catalysis. *Chemical Society Reviews*, *43*(24), pp.8226-8239.
32. Zhang, L., Zhang, J., Yu, H. and Yu, J., 2022. Emerging S-scheme photocatalyst. *Advanced materials*, *34*(11), p.2107668.
33. Chen, S., Hu, Y., Meng, S. and Fu, X., 2014. Study on the separation mechanisms of photogenerated electrons and holes for composite photocatalysts g-C_3N_4-WO3. *Applied Catalysis B: Environmental*, *150*, pp.564-573.
34. Xiao, M., Wang, Z., Luo, B., Wang, S. and Wang, L., 2019. Enhancing photocatalytic activity of tantalum nitride by rational suppression of bulk, interface and surface charge recombination. *Applied Catalysis B: Environmental*, *246*, pp.195-201.
35. Li, A., Chang, X., Huang, Z., Li, C., Wei, Y., Zhang, L., Wang, T. and Gong, J., 2016. Thin heterojunctions and spatially separated cocatalysts to simultaneously

reduce bulk and surface recombination in photocatalysts. *Angewandte Chemie*, *128*(44), pp.13938-13942.

36. Chen, F., Ma, T., Zhang, T., Zhang, Y. and Huang, H., 2021. Atomic-level charge separation strategies in semiconductor-based photocatalysts. *Advanced Materials*, *33*(10), p.2005256.
37. Chen, R., Pang, S., An, H., Zhu, J., Ye, S., Gao, Y., Fan, F. and Li, C., 2018. Charge separation via asymmetric illumination in photocatalytic Cu_2O particles. *Nature Energy*, *3*(8), pp.655-663.
38. Nishioka, S., Osterloh, F.E., Wang, X., Mallouk, T.E. and Maeda, K., 2023. Photocatalytic water splitting. *Nature Reviews Methods Primers*, *3*(1), p.42.
39. Schrauzer, G.N. and Guth, T.D., 2002. Photolysis of water and photoreduction of nitrogen on titanium dioxide. *Journal of the American chemical society*, *99*(22), pp.7189-7193.
40. Domen, K., Naito, S., Soma, M., Onishi, T. and Tamaru, K., 1980. Photocatalytic decomposition of water vapour on an NiO–SrTiO 3 catalyst. *Journal of the Chemical Society, Chemical Communications*, (12), pp.543-544.
41. Lehn, J.M., JP, S. and Ziessel, R., 1980. Photochemical water splitting continuous generation of hydrogen and oxygen by irradiation of aqueous suspensions of metal loaded strontium titanate.
42. Sato, S. and White, J.M., 1980. Photodecomposition of water over Pt/TiO2 catalysts. *Chemical Physics Letters*, *72*(1), pp.83-86.
43. Kudo, A. and Miseki, Y., 2009. Heterogeneous photocatalyst materials for water splitting. *Chemical Society Reviews*, *38*(1), pp.253-278.

44. Wang, Q. and Domen, K., 2019. Particulate photocatalysts for light-driven water splitting: mechanisms, challenges, and design strategies. *Chemical Reviews*, *120*(2), pp.919-985.

45. Suresh, R., Gnanasekaran, L., Rajendran, S. and Soto-Moscoso, M., 2023. Doped nanomaterials: application in hydrogen production via photocatalytic water splitting. *Fuel*, *348*, p.128528.

46. Liu, J.W., Chen, G., Li, Z.H. and Zhang, Z.G., 2006. Electronic structure and visible light photocatalysis water splitting property of chromium-doped SrTiO3. *Journal of Solid State Chemistry*, *179*(12), pp.3704-3708.

47. Konta, R., Ishii, T., Kato, H. and Kudo, A., 2004. Photocatalytic activities of noble metal ion doped SrTiO3 under visible light irradiation. *The Journal of Physical Chemistry B*, *108*(26), pp.8992-8995.

48. Ng, B.J., Putri, L.K., Kong, X.Y., Teh, Y.W., Pasbakhsh, P. and Chai, S.P., 2020. Z-scheme photocatalytic systems for solar water splitting. *Advanced science*, *7*(7), p.1903171.

49. QingáLu, G., 2009. Enhanced photocatalytic hydrogen evolution by prolonging the lifetime of carriers in ZnO/CdS heterostructures. *Chemical communications*, (23), pp.3452-3454.

50. Abe, R., Sayama, K., Domen, K. and Arakawa, H., 2001. A new type of water splitting system composed of two different TiO_2 photocatalysts (anatase, rutile) and a IO3−/I− shuttle redox mediator. *Chemical physics letters*, *344*(3-4), pp.339-344.

51. Nishioka, S., Yanagisawa, K.I., Lu, D., Vequizo, J.J.M., Yamakata, A., Kimoto, K., Inada, M. and Maeda, K., 2019. Enhanced water splitting through two-step

photoexcitation by sunlight using tantalum/nitrogen-codoped rutile titania as a water oxidation photocatalyst. *Sustainable Energy & Fuels*, *3*(9), pp.2337-2346.

52. Jo, W.K. and Natarajan, T.S., 2015. Influence of TiO_2 morphology on the photocatalytic efficiency of direct Z-scheme g-C_3N_4/TiO_2 photocatalysts for isoniazid degradation. *Chemical Engineering Journal*, *281*, pp.549-565.
53. Xue, W., Hu, X., Liu, E. and Fan, J., 2018. Novel reduced graphene oxide-supported $Cd_{0.5}Zn_{0.5}S$/g-C_3N_4 Z-scheme heterojunction photocatalyst for enhanced hydrogen evolution. *Applied Surface Science*, *447*, pp.783-794.
54. Nishiyama, H., Yamada, T., Nakabayashi, M., Maehara, Y., Yamaguchi, M., Kuromiya, Y., Nagatsuma, Y., Tokudome, H., Akiyama, S., Watanabe, T. and Narushima, R., 2021. Photocatalytic solar hydrogen production from water on a 100-m2 scale. *Nature*, *598*(7880), pp.304-307.
55. Zhao, Z., Goncalves, R.V., Barman, S.K., Willard, E.J., Byle, E., Perry, R., Wu, Z., Huda, M.N., Moulé, A.J. and Osterloh, F.E., 2019. Electronic structure basis for enhanced overall water splitting photocatalysis with aluminum doped $SrTiO_3$ in natural sunlight. *Energy & Environmental Science*, *12*(4), pp.1385-1395.
56. Makepeace, J. W., Wood, T. J., Hunter, H. M., Jones, M. O., & David, W. I., 2015. Ammonia decomposition catalysis using non-stoichiometric lithium imide. *Chemical Science*, *6*(7), 3805-3815.
57. Lan, R., Irvine, J. T., & Tao, S., 2012. Ammonia and related chemicals as potential indirect hydrogen storage materials. *International journal of hydrogen energy*, *37*(2), 1482-1494.
58. Zhao, Y., Setzler, B. P., Wang, J., Nash, J., Wang, T., Xu, B., & Yan, Y., 2019. An efficient direct ammonia fuel cell for affordable carbon-neutral transportation. *Joule*, *3*(10), 2472-2484.

59. Huang, X., Lei, K., Mi, Y., Fang, W., & Li, X., 2023. Recent progress on hydrogen production from ammonia decomposition: Technical roadmap and catalytic mechanism. *Molecules*, *28*(13), 5245.

60. García-García, F. R., Guerrero-Ruiz, A., Rodríguez-Ramos, I., Goguet, A., Shekhtman, S. O., & Hardacre, C., 2011. TAP studies of ammonia decomposition over Ru and Ir catalysts. *Physical Chemistry Chemical Physics*, *13*(28), 12892-12899.

61. Hansgen, D. A., Vlachos, D. G., & Chen, J. G., 2010. Using first principles to predict bimetallic catalysts for the ammonia decomposition reaction. *Nature chemistry*, *2*(6), 484-489.

62. Fang, H., Wu, S., Ayvali, T., Zheng, J., Fellowes, J., Ho, P. L., ... & Tsang, S. C. E., 2023. Dispersed surface Ru ensembles on MgO (111) for catalytic ammonia decomposition. *Nature Communications*, *14*(1), 647.

63. Karim, A. M., Prasad, V., Mpourmpakis, G., Lonergan, W. W., Frenkel, A. I., Chen, J. G., & Vlachos, D. G., 2009. Correlating particle size and shape of supported Ru/γ-Al_2O_3 catalysts with NH_3 decomposition activity. *Journal of the American Chemical Society*, *131*(34), 12230-12239.

64. Okura, K., Miyazaki, K., Muroyama, H., Matsui, T., & Eguchi, K., 2018. Ammonia decomposition over Ni catalysts supported on perovskite-type oxides for the on-site generation of hydrogen. *RSC advances*, *8*(56), 32102-32110.

65. Chen, C., Wu, K., Ren, H., Zhou, C., Luo, Y., Lin, L., ... & Jiang, L., 2021. Ru-based catalysts for ammonia decomposition: a mini-review. *Energy & Fuels*, *35*(15), 11693-11706.

66. Ganley, J. C., Thomas, F. S., Seebauer, E. G., & Masel, R. I., 2004. A priori catalytic activity correlations: the difficult case of hydrogen production from ammonia. *Catalysis Letters*, *96*, 117-122.

67. Yin, S. F., Xu, B. Q., Ng, C. F., & Au, C. T., 2004. Nano Ru/CNTs: a highly active and stable catalyst for the generation of COx-free hydrogen in ammonia decomposition. *Applied Catalysis B: Environmental*, *48*(4), 237-241.

68. Wang, L., Chen, J., Ge, L., Rudolph, V., & Zhu, Z., 2013. Difference in the cooperative interaction between carbon nanotubes and Ru particles loaded on their internal/external surface. *Rsc Advances*, *3*(31), 12641-12647.

69. Zhang, S., He, Z., Li, X., Zhang, J., Zang, Q., & Wang, S., 2020. Building heterogeneous nanostructures for photocatalytic ammonia decomposition. *Nanoscale Advances*, *2*(9), 3610-3623.

70. Obata, K., Kishishita, K., Okemoto, A., Taniya, K., Ichihashi, Y., & Nishiyama, S., 2014. Photocatalytic decomposition of NH_3 over TiO_2 catalysts doped with Fe. *Applied Catalysis B: Environmental*, *160*, 200-203.

71. Utsunomiya, A., Okemoto, A., Nishino, Y., Kitagawa, K., Kobayashi, H., Taniya, K., ... & Nishiyama, S., 2017. Mechanistic study of reaction mechanism on ammonia photodecomposition over Ni/TiO_2 photocatalysts. *Applied Catalysis B: Environmental*, *206*, 378-383.

72. Reli, M., Ambrožová, N., Šihor, M., Matějová, L., Čapek, L., Obalová, L., ... & Kočí, K., 2015. Novel cerium doped titania catalysts for photocatalytic decomposition of ammonia. *Applied Catalysis B: Environmental*, *178*, 108-116.

73. Yuzawa, H., Mori, T., Itoh, H., & Yoshida, H., 2012. Reaction mechanism of ammonia decomposition to nitrogen and hydrogen over metal loaded titanium oxide photocatalyst. *The Journal of Physical Chemistry C*, *116*(6), 4126-4136.

74. Li, J., Sheng, B., Chen, Y., Yang, J., Wang, P., Li, Y., ... & Zhou, B., 2024. Utilizing full-spectrum sunlight for ammonia decomposition to hydrogen over GaN nanowires-supported Ru nanoparticles on silicon. *Nature communications*, *15*(1), 7393.

75. Reli, M., Edelmannová, M., Šihor, M., Praus, P., Svoboda, L., Mamulová, K. K., ... & Kočí, K., 2015. Photocatalytic H_2 generation from aqueous ammonia solution using ZnO photocatalysts prepared by different methods. *International Journal of Hydrogen Energy*, *40*(27), 8530-8538.

76. Mohammadi, Z., Sharifnia, S., & Shavisi, Y., 2016. Photocatalytic degradation of aqueous ammonia by using TiO_2ZnO/LECA hybrid photocatalyst. *Materials Chemistry and Physics*, *184*, 110-117.

77. Yuan, Y., Zhou, L., Robatjazi, H., Bao, J. L., Zhou, J., Bayles, A., ... & Halas, N. J., 2022. Earth-abundant photocatalyst for H_2 generation from NH_3 with light-emitting diode illumination. *Science*, *378*(6622), 889-893.

78. Beck, A., Marlowe, J., Gordon, M. J., & Christopher, P., 2024. Is There a Discernible Photochemical Effect Beyond Heating for Visible Photon-Mediated NH_3 Decomposition over Ru/Al_2O_3?. *The Journal of Physical Chemistry C*, *128*(21), 8590-8600.

79. Shi, Y., Zhao, Z., Yang, D., Tan, J., Xin, X., Liu, Y., & Jiang, Z., 2023. Engineering photocatalytic ammonia synthesis. *Chemical Society Reviews*, *52*(20), 6938-6956.

80. Wang, L., Xia, M., Wang, H., Huang, K., Qian, C., Maravelias, C. T., & Ozin, G. A., 2018. Greening ammonia toward the solar ammonia refinery. *Joule*, *2*(6), 1055-1074.

81. Medford, A. J., & Hatzell, M. C., 2017. Photon-driven nitrogen fixation: current progress, thermodynamic considerations, and future outlook. *Acs Catalysis*, *7*(4), 2624-2643.

82. Zhang, S., Zhao, Y., Shi, R., Waterhouse, G. I., & Zhang, T., 2019. Photocatalytic ammonia synthesis: Recent progress and future. *EnergyChem*, *1*(2), 100013.

83. Chen, X., Li, N., Kong, Z., Ong, W. J., & Zhao, X., 2018. Photocatalytic fixation of nitrogen to ammonia: state-of-the-art advancements and future prospects. *Materials Horizons*, *5*(1), 9-27.

84. Shi, L., Yin, Y., Wang, S., & Sun, H., 2020. Rational catalyst design for N_2 reduction under ambient conditions: strategies toward enhanced conversion efficiency. *ACS Catalysis*, *10*(12), 6870-6899.

85. Hirakawa, H., Hashimoto, M., Shiraishi, Y., & Hirai, T., 2017. Photocatalytic conversion of nitrogen to ammonia with water on surface oxygen vacancies of titanium dioxide. *Journal of the American Chemical Society*, *139*(31), 10929-10936.

86. Hirakawa, H., Hashimoto, M., Shiraishi, Y., & Hirai, T., 2017. Selective nitrate-to-ammonia transformation on surface defects of titanium dioxide photocatalysts. *ACS catalysis*, *7*(5), 3713-3720.

87. Li, H., Shang, J., Shi, J., Zhao, K., & Zhang, L., 2016. Facet-dependent solar ammonia synthesis of BiOCl nanosheets via a proton-assisted electron transfer pathway. *Nanoscale*, *8*(4), 1986-1993.

88. Li, J., Jiang, J., Xu, Z., Liu, M., Tang, S., Yang, C., & Qian, D., 2018. Facile synthesis of Ag@ Cu_2O heterogeneous nanocrystals decorated N-doped reduced graphene oxide with enhanced electrocatalytic activity for ultrasensitive detection of H_2O_2. *Sensors and Actuators B: Chemical*, *260*, 529-540.

89. Niu, X., Yan, W., Zhao, H., & Yang, J., 2018. Synthesis of Nb doped TiO_2 nanotube/reduced graphene oxide heterostructure photocatalyst with high visible light photocatalytic activity. *Applied Surface Science*, *440*, 804-813.
90. Wang, M., Guo, P., Zhang, Y., Lv, C., Liu, T., Chai, T., ... & Zhu, T., 2018. Synthesis of hollow lantern-like Eu (III)-doped g-C_3N_4 with enhanced visible light photocatalytic perfomance for organic degradation. *Journal of hazardous materials*, *349*, 224-233.
91. Hu, Y., Guo, P., & Guo, L., 2012. Synthesis and photocatalytic properties of Cr-doped $KSr_2Nb_3O_{10}$ for hydrogen production. *International journal of hydrogen energy*, *37*(1), 1007-1013.
92. Hu, Y., Shi, J., & Guo, L., 2013. Enhanced photocatalytic hydrogen production activity of chromium doped lead niobate under visible-light irradiation. *Applied Catalysis A: General*, *468*, 403-409.
93. Nguyen, C. C., Nguyen, D. T., & Do, T. O., 2018. A novel route to synthesize C/Pt/TiO_2 phase tunable anatase–Rutile TiO_2 for efficient sunlight-driven photocatalytic applications. *Applied Catalysis B: Environmental*, *226*, 46-52.
94. Hu, Y., & Guo, L., 2015. Rapid Preparation of Perovskite Lead Niobate Nanosheets by Ultrasonic-Assisted Exfoliation for Enhanced Visible-Light-Driven Photocatalytic Hydrogen Production. *ChemCatChem*, *7*(4), 584-587.
95. Yoshimura, J., Ebina, Y., Kondo, J., Domen, K., & Tanaka, A., 1993. Visible light-induced photocatalytic behavior of a layered perovskite-type rubidium lead niobate, RbPb2Nb3O10. *The Journal of Physical Chemistry*, *97*(9), 1970-1973.
96. Shimizu, K. I., Itoh, S., Hatamachi, T., Kodama, T., Sato, M., & Toda, K., 2005. Photocatalytic water splitting on Ni-intercalated Ruddlesden− Popper tantalate $H_2La_{2/3}Ta_2O_7$. *Chemistry of materials*, *17*(20), 5161-5166.

97. Chen, X., Shi, R., Chen, Q., Zhang, Z., Jiang, W., Zhu, Y., & Zhang, T., 2019. Three-dimensional porous g-C3N4 for highly efficient photocatalytic overall water splitting. *Nano Energy*, *59*, 644-650.

98. Takata, T., Jiang, J., Sakata, Y., Nakabayashi, M., Shibata, N., Nandal, V., ... & Domen, K., 2020. Photocatalytic water splitting with a quantum efficiency of almost unity. *Nature*, *581*(7809), 411-414.

99. Wang, Z., Inoue, Y., Hisatomi, T., Ishikawa, R., Wang, Q., Takata, T., ... & Domen, K., 2018. Overall water splitting by Ta3N5 nanorod single crystals grown on the edges of KTaO3 particles. *Nature Catalysis*, *1*(10), 756-763.

100. Zhang, Y., Li, Y., Xin, X., Wang, Y., Guo, P., Wang, R., ... & Li, X., 2023. Internal quantum efficiency higher than 100% achieved by combining doping and quantum effects for photocatalytic overall water splitting. *Nature Energy*, *8*(5), 504-514.

101. Park, S., Chang, W. J., Lee, C. W., Park, S., Ahn, H. Y., & Nam, K. T., 2016. Photocatalytic hydrogen generation from hydriodic acid using methylammonium lead iodide in dynamic equilibrium with aqueous solution. *Nature Energy*, *2*(1), 1-8.

102. Wang, J., Zhang, Y., Jiang, S., Sun, C., & Song, S., 2023. Regulation of d‐band centers in localized CdS homojunctions through facet control for improved photocatalytic water splitting. *Angewandte Chemie International Edition*, *62*(35), e202307808.

103. Machida, M., Yabunaka, J. I., & Kijima, T., 2000. Synthesis and photocatalytic property of layered perovskite tantalates, RbLnTa2O7 (Ln= La, Pr, Nd, and Sm). *Chemistry of Materials*, *12*(3), 812-817.

104. Machida, M., Mitsuyama, T., Ikeue, K., Matsushima, S., & Arai, M., 2005. Photocatalytic property and electronic structure of triple-layered perovskite tantalates, MCa2Ta3O10 (M= Cs, Na, H, and C6H13NH3). *The Journal of Physical Chemistry B*, *109*(16), 7801-7806.

105. Compton, O. C., Carroll, E. C., Kim, J. Y., Larsen, D. S., & Osterloh, F. E., 2007. Calcium niobate semiconductor nanosheets as catalysts for photochemical hydrogen evolution from water. *The Journal of Physical Chemistry C*, *111*(40), 14589-14592.

106. Park, S., Song, H. J., Lee, C. W., Hwang, S. W., & Cho, I. S., 2015. Enhanced photocatalytic activity of ultrathin Ba5Nb4O15 two-dimensional nanosheets. *ACS applied materials & interfaces*, *7*(39), 21860-21867.

107. Ida, S., Okamoto, Y., Matsuka, M., Hagiwara, H., & Ishihara, T., 2012. Preparation of tantalum-based oxynitride nanosheets by exfoliation of a layered oxynitride, CsCa2Ta3O10–x N y, and their photocatalytic activity. *Journal of the American Chemical Society*, *134*(38), 15773-15782.

108. Ida, S., Okamoto, Y., Hagiwara, H., & Ishihara, T., 2013. Preparation and Photocatalytic Properties of Sr2−xBaxTa3O10−yNz Nanosheets. *Catalysts*, *3*(1), 1-10.

Chapter 2 | Experimental methods and techniques

2.1 Material synthesis

2.1.1 Materials and reagents

Rubidium carbonate (Rb_2CO_3, >99%), Caesium carbonate (Cs_2CO_3, >99%), Praseodymium oxide (Pr_6O_{11}, >99.996%), Neodymium nitrate hexahydrate (Nd_2O_3, >99.9%), Lanthanum oxide (La_2O_3, >99.96%), Niobium oxide (Nb_2O_5, >99.9%), graphene oxide (1 mg/mL), Nitric acid (HNO_3, 70 wt% in H_2O), Ammonium solution (NH_4OH, 35 wt% in H_2O), Tetramethylammonium hydroxide (TMAOH, ~25 wt% in methanol), Tetraethylammonium hydroxide (TEAOH, ~35 wt% in H_2O), Tetrapropylammonium hydroxide (TPAOH, ~25 wt% in H_2O), Tetrabutylammonium hydroxide (TBAOH, ~40 wt% in H_2O) and Poly (diallyldimethylammonium chloride) solution (MW <100000, 35 wt. %) and Methanol were purchased from Sigma-Aldrich Co. LLC. All of above chemical reagents were utilised directly without any further purification. Deionised water was used in this experiment.

2.1.2 Ceramic synthesis

All the pristine layered perovskite oxides discussed in this thesis were synthesised using conventional high-temperature ceramic methods. First, the starting reagents of metal oxide were dried at muffle furnace at 900 °C for 2 hours before being used. Then, stoichiometric amounts of the appropriate precursors (both metal oxides and carbonates) were thoroughly mixed using an agate mortar and pestle to ensure homogeneity. The resulting powders were then pressed into a pellet to minimise diffusion lengths and enhance grain-to-grain contact. Typically, the pellet needs to be initially heated at ~ 850 °C for 12 hours to decompose any carbonates. After this heating cycle, the samples were reground, re-pelletised, and subsequently heated at the target reaction temperature.

The temperature usually exceeded 1000 °C to overcome the substantial energetic barriers to solid-state diffusion.

2.1.3 Layered perovskite protonation

The pristine layered perovskites were stirred with 6 M of HNO_3 solution at 333 K for 7 days. The A' site cations in the interlayer space was replaced by protons. The collected powder samples were washed with deionised water until the pH = ~7. Then the resulting protonated product was dried for 48 h in a vacuum desiccator at room temperature.

2.1.4 Layered perovskite exfoliation

The as-prepared protonated perovskites were exfoliated with TBAOH. Typically, 0.1 g of protonated perovskite powder were added in 0.025 M of 100 ml TBAOH solution and stirred for 14 days. Additionally, the exfoliation process was under assistance of sonication every day. The separation from unexfoliated powder was performed by spontaneous precipitation for 1 day and the supernatant was used as the nanosheet suspension (concentration ~0.5 g/L). The perovskite nanosheets were washed with water several times and dried at room temperature.

2.1.5 Preparation of rGO/PDDA

60 mg of graphene oxide in 20 mL of deionised water was stirred with 800 μl of PDDA for 1 h. Then the solution was heated to 363 K under reflux for 12 hours. Solution was centrifuged at 12,000 rpm for 45 minutes, and the upper layer solution was removed. This step was repeated for several times to remove extra PDDA. Finally, the product was dried at 333 K for 24 h in a vacuum oven.

2.1.6 Synthesis of rGO/perovskite nanosheet nanohybrids

The typical procedure for nanohybrids was conducted as follows: 1 mg of rGO/PDDA was added in deionised water, then followed by the addition of 20 mL of perovskite nanosheet suspension under stirring. This procedure yielded flocculated sediment as a result of the electrostatic interaction of the perovskite nanosheet and rGO/PDDA. The resulting mixture was placed under UV light with continuous stirring to remove PDDA. Finally, the solid was washed with deionised water and collected by centrifugation at 12,000 rpm for 1 h.

2.1.7 Preparation of A'$PrNb_2O_7$ (A' = NH_4^+, TMA^+, TEA^+, TPA^+ or TBA^+)

The crystalline protonated $HPrNb_2O_7$ perovskites were stirred with 0.0025 M of 100 ml ammonium hydroxide solution [ammonium hydroxide (35 wt. % in H_2O), tetra-methyl ammonium hydroxide (25 wt. % in methanol), tetra-ethyl ammonium hydroxide (35 wt. % in H_2O), tetra-propyl ammonium hydroxide (25 wt. % in H_2O), or tetra-butyl ammonium hydroxide (25 wt. % in H_2O)] in H_2O with 5% methanol for 14 days with ultra-sonication assistance. Subsequently, only the material in supernatant was collected by a 12500 RPM high-speed centrifuge, and the collected samples needed to be very carefully washed by deionised water until pH = 7. Then the collected samples were dried for 48 h at 333K in a vacuum oven.

2.2 Material characterisation

2.2.1 Powder diffraction

Powder diffraction is a common approach to study the structure information of crystalline materials, including lattice type, lattice spacing and particle size. While an ideal crystal consists of an infinite, orderly array of atoms or molecules, where the entire structure can

be constructed by repeating a single unit cell through translational displacements. Because X-ray and neutron radiation has the wavelength comparable to interatomic distances, their interaction with a crystal can lead to elastic scattering by the atoms. In most directions, destructive interference occurs, diminishing the intensity of scattered waves and resulting in low-intensity regions in the diffraction pattern. However, in specific crystallographic directions, constructive interference takes place, producing distinct intensity maxima at those positions. The structural factor F_{hkl} (Equation 2.1) describes the total scattering contribution from all atoms in a unit cell, determining the amplitude of a diffraction peak. It is given by:

$$F_{hkl} = \sum_{1}^{N} f_{\mathrm{n}}\, e^{2\pi \mathrm{i}(hx_{\mathrm{n}}+ky_{\mathrm{n}}+lz_{\mathrm{n}})}\, e^{-B\sin^2\theta/\lambda} \quad \text{(Equation 2.1)}$$

where the sum is over all the atoms in the unit cell, f_{n} is the atomic form factor of the atom n (replaced with the scattering length, b_{n}, in neutron diffraction), h, k and l are the Miller indices of the diffraction plane, x_{n}, y_{n} and z_{n} are the atomic fractional coordinates of the atom n in the unit cell and B is the isotropic displacement parameter.[1][2] And the detected intensity is proportional to $|F_{hkl}|^2$.

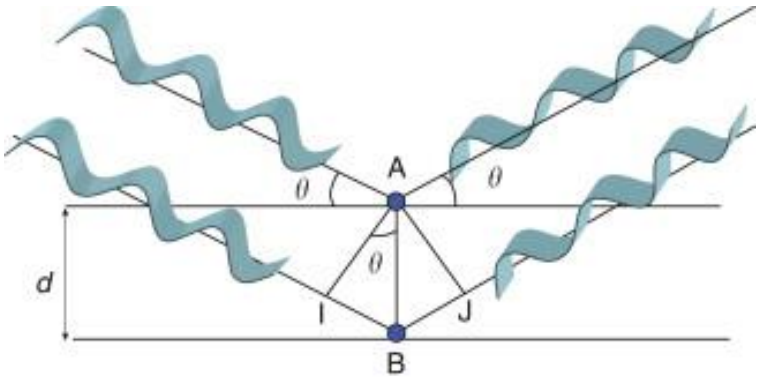

Figure 2.1: Illustration of the derivation of Bragg's Law, where θ is the incident angle. Figure reproduced from Reference [4].

While the peak positions in the diffraction pattern can be determined by Bragg's Law.[3] As shown in Figure 2.1, the path difference between the waves reflected off the two planes is given by $\Delta = BI + BJ$. For constructive interference to occur, this path difference must be an integer multiple, n, of the wavelength, where $\Delta = n\lambda$. Besides, we can also know that $n\lambda = 2d \sin\theta$. By this, we could obtain the Bragg equation (Equation 2.2):

$$n\lambda = 2d \sin\theta \quad \text{(Equation 2.2)}$$

X-ray diffraction

Laboratory-based X-ray diffraction (XRD) data were collected using a PANalytical Empyrean diffractometer equipped with a PIXcel1D detector. The instrument operates in Bragg-Brentano geometry and utilizes Cu Kα radiation. A Ge (111) monochromator is installed to ensure that only Cu Kα1 radiation is used. Measurements were conducted with 0.04 radian Soller slits. Some diffraction patterns were also collected using a PANalytical X'Pert PRO diffractometer (PANalytical, Cambridge, UK) with Cu Kα radiation (λ = 1.5148 Å, E = 8.048 keV). The designation Kα refers to X-ray generation resulting from an electronic transition from the L-edge (with quantum number n=2) to the K-edge (with quantum number n=1), corresponding to a 2p to 1s transition as dictated by the selection rule Δl = ±1. Additionally, Mo Kα radiation (λ = 0.7107 Å, E = 17.45 keV) may also be used. For sample preparation, the powder was loaded onto a lightly greased glass slide, which was then mounted in the flat-stage sample holder of the diffractometer.

Synchrotron X-ray diffraction

XRD using Cu Kα sources has a relatively low signal-to-noise ratio and, for highly symmetric materials, is primarily suitable for fingerprinting rather than detailed structural analysis. To perform Rietveld refinement on layered perovskite oxide, synchrotron XRD is required due to its significantly higher photon flux—several orders of magnitude

greater than that of laboratory-based diffractometers. Besides, the finer step size between individual data points in synchrotron XRD allows for a more detailed fitting profile with an increased number of refinable parameters. In this thesis, synchrotron XRD measurements were collected at beamline 01C2 at TLS National Synchrotron Radiation Research Centre, Taiwan, China. The energy of the incident X-ray was set at 28.5 keV, with a wavelength $\lambda = 0.43503$ Å. At the sample position, the expected photon flux is 1×10^{11} photon/sec/200 mA with an average energy resolution ($\Delta E/E$) of 1.6×10^{-4} and the focused beam size is about 0.9 mm × 0.2 mm. Synchrotron XRD data were obtained from the perovskite samples (loaded in 0.2 ~ 0.3 mm capillaries to minimize absorption and fluorescence interference from the heavy metal) using the MYTHEN 18K detector.

Neutron powder diffraction

Neutron powder diffraction (NPD) is also a technique for crystal structure determination, offering complementary information to XRD. The fundamental difference between the two methods lies in their scattering mechanisms: X-rays are scattered by the electron cloud of atoms, whereas neutrons are scattered by atomic nuclei. Each nucleus has a characteristic neutron scattering length, which varies both across the periodic table and among different isotopes of the same element. Unlike X-ray scattering, neutron scattering lengths do not follow a systematic trend with atomic number, making NPD particularly effective for precisely determining the positions and occupancies of light atoms. Another key advantage of NPD is that neutron scattering length is independent of scattering angle. As a result, high-angle diffraction peaks retain strong intensity, allowing for reliable extraction of structural information even at large scattering angles. Furthermore, because neutrons have a magnetic dipole moment, they interact with the magnetic moments in a material that exhibits magnetic ordering. As a result, neutrons are scattered by the

periodically arranged magnetic moments, providing a means to probe and determine the material's magnetic structure.

As shown in Figure 2.2, NPD measures the differential cross section $d\sigma/d\Omega$, representing the number of neutrons scattered per second at an angle 2θ into the solid angle $d\Omega$. The scattering cross section σ quantifies the strength of interaction between an incident neutron and a target nucleus. A larger cross section indicates a higher probability of interaction. It is measured in barns (1 barn = 10×10^{-28} m^2), representing the effective area presented by a nucleus to an incoming neutron.

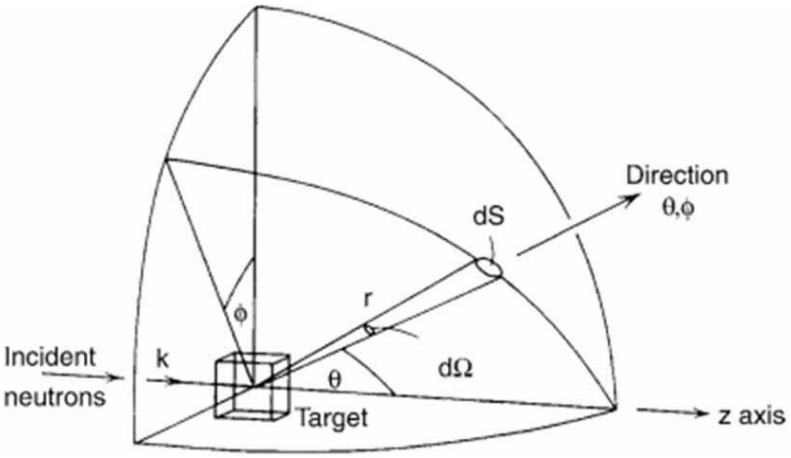

Figure 2.2: Geometry of the neutron scattering experiment. Figure reproduced from Reference [5].

At a pulsed neutron source like ISIS, neutrons are produced when high-energy protons, accelerated primarily in a proton synchrotron, collide with a heavy-metal target (e.g., Ta, W, or Pb). The time-of-flight (TOF) method is used to determine the neutron wavelength (λ) based on the total flight path (L) from the source (T = 0) to the sample (L_1) and then to the detector (L_2), as illustrated in Figure 2.3. Using the de Broglie relation ($\lambda = h/mv$) and the measurable values of T and L, the neutron wavelength λ is calculated as:

$$\lambda = \frac{h\mathrm{T}}{\mathrm{mL}} \quad \text{(Equation 2.3)}$$

where λ is in Å, T in μs, and L in meters. By combining Equation 2.3 with Bragg's law (Equation 2.2) where n = 1, we can derive the relationship between T and the interplanar spacing d_{hkl}:

$$d_{hkl} = \frac{\mathrm{T}}{505.56\mathrm{L}\sin\theta} \quad \text{(Equation 2.4)}$$

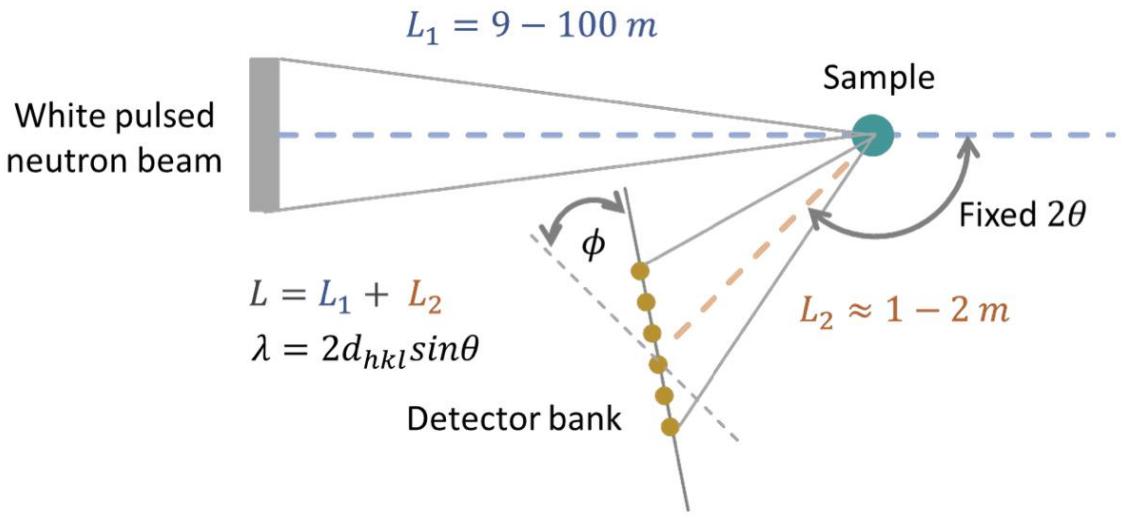

Figure 2.3: schematic diagram illustrating TOF instrumental configuration for NPD measurement. Neutrons with a broad range of energies (proportional to velocities) from a pulsed source are separated based on their time of arrival. This enables the measurement of various interplanar distances d_{hkl} at a fixed scattering angle 2θ. Figure reproduced from Reference [6].

All NPD data in this work were collected using the POLARIS instrument at the ISIS neutron and muon source. The POLARIS diffractometer has 5 detector banks, providing data over a combined *d*-spacing range of 0.2−40 Å.

Rietveld refinement

Rietveld refinement is a method that fits an entire diffraction pattern to a structural model by refining parameters through a least squares procedure.[7] In this approach, the calculated intensities are derived by using:

$$y_{calc,i} = \sum_{p} \left(S_p \sum_{s(p)} \left(\left| F_{calc,s,p,i} \right|^2 Corr_{s,p,i} \phi_{s,p,i} \right) \right) + Bkg_i \quad \text{(Equation 2.5)}$$

In above equation, the outer sum is taken over all crystalline phases *p* present, and S_p is a scaling factor that accounts for the different weight fractions of each phase. The inner sum is taken over all the Bragg reflections *s* of phase *p* that contribute to the intensity at position *i* in the powder diffraction pattern. The term $|F_{calc,s,p}|^2 Corr_{s,p,i}$ (where $Corr_{s,p,i}$ is a correction factor) provides the peak positions and intensities. The term $\Phi_{s,p,i}$ represents the peak profile, which is influenced by the sample's microstructure and instrumental factors. Finally, Bkg_i accounts for the background signal, arising from factors such as the sample environment and incoherent, inelastic, or thermal diffuse scattering.[8] Then the fitting procedure involves the minimising the sum of the squared differences between the observed and calculated intensities:

$$\sum_{i} \left(w_i \left(y_{obs,i} - y_{calc,i} \right)^2 \right) \rightarrow \text{Min} \quad \text{(Equation 2.6)}$$

where $y_{obs,i}$ and $y_{calc,i}$ are observed and calculated intensities, respectively, and w_i is a weighting factor obtaining by taking the reciprocal of $y_{obs,i}$. Herein, all Rietveld refinements were carried out using Topas Academic. The peak shapes were modeled with the symmetric Thompson-Cox-Hastings pseudo-Voigt function (TCHZ), while peak asymmetry was accounted for using a simple axial model. The background was fitted with a Chebyshev polynomial.[9][10] The quality of the fit between the observed and

calculated diffraction patterns was evaluated using the agreement factor (R_p), the weighted agreement factor (R_{wp}), and the goodness of fit (gof):

$$R_{\mathrm{p}} = \frac{\sum_i |y_{obs,i} - y_{calc,i}|}{\sum_i y_{obs,i}} \quad \text{(Equation 2.7)}$$

$$R_{\mathrm{wp}} = \sqrt{\frac{\sum_i \left(w_i \left(y_{obs,i} - y_{calc,i}\right)^2\right)}{\sum_i w_i y_{obs,i}^2}} \quad \text{(Equation 2.8)}$$

$$\mathrm{gof} = \frac{R_{\mathrm{wp}}}{R_{\mathrm{exp}}} \quad \text{(Equation 2.9)}$$

$$\text{and} \quad R_{exp} = \sqrt{\frac{N - P}{\sum_i w_i \, y_{obs,i}^2}} \quad \text{(Equation 2.10)}$$

where *N* is the number of data points and *P* is the number of parameters.

Pawley refinement

Pawley refinements were conducted by using the Topas Academic software. It enables the fitting of diffraction peaks without prior information of the crystal structure. Like Rietveld refinement, it employs a least square fitting procedure. However, instead of deriving intensities from a structural model, Pawley refinement treats them as refinable parameters. This could facilitate the precise determination of lattice parameters and enable the evaluation of different space groups for phases with unknown crystal structures.[11]

2.2.2 X-ray absorption spectroscopy

X-ray absorption spectroscopy (XAS) is a useful technique for probing the short-range order and local structure of materials.[12] This method involves tuning the photon energy to excite core electrons of a specific element within the material. When an incident X-ray with energy *E* is absorbed by an atom in the sample, it excites a core electron with binding energy E_0, generating a photoelectron with kinetic energy $E-E_0$. The absorption edges in

XAS are classified based on the principal quantum number n of the excited core electron. Specifically, transitions from core levels with $n = 1$, 2, and 3 correspond to the K, L, and M edges, respectively. The probability of these electronic transitions is governed by Fermi's Golden Rule, which describes the transition rates between quantum states under perturbation. Following core-level ionisation, the excited atom eventually relaxes as an electron from a higher-lying state fills the core hole. This relaxation process can result in the emission of either a fluorescent X-ray or an Auger electron, depending on the atomic number and electronic configuration of the element. This ejected photoelectron behaves as a quantum wave that propagates through the material. It undergoes scattering and interference due to interactions with neighboring atoms. The intensity and shape of the XAS spectrum are influenced by the local density of states (DOS) at the absorbing atom with energy $E-E_0$.

XAS spectrum is typically divided into three regions, each representing a separate spectroscopic technique. The pre-edge region corresponds to electronic transitions involving quadrupole or dipole-forbidden excitations, providing insight into the local electronic structure. The X-ray Absorption Near-Edge Structure (XANES) region is primarily used for determining the oxidation state and coordination geometry of the absorbing element. Then the Extended X-ray Absorption Fine Structure (EXAFS) region provides quantitative structural information by analysing the scattering of ejected photoelectrons, offering details on bond lengths, coordination numbers, and disorder effects in the local atomic environment. While the pre-edge and XANES regions are predominantly used for oxidation state determination, the EXAFS region is employed to characterize the local coordination environment surrounding the absorbing element.

Pre-edge and XANES regions

As the valence state of an element increases, the absorption edge position shifts to higher energies. The pre-edge feature in XAS arises from transitions of core electrons to vacant 3d states, and these transitions typically involve some hybridisation with the outer p orbitals of surrounding ligands. XANES features are attributed to electronic transitions from core levels to valence states, with the energy positions being sensitive to variations in the shielding of the nuclear charge, which is strongly influenced by the surrounding ligands. The determination of the valence state using either the pre-edge feature or XANES is typically accomplished by comparing the position of the feature to model compounds with known valence states. Valence state quantification can be performed through various methods, such as first derivative analysis, half-height intensity, integral methods, and linear combination fitting, by comparing the XAS data to those of reference compounds.

EXAFS regions

To transform EXAFS data from XAS spectra, the oscillation starting from the edge position needs to be extracted, and energy is converted to wavenumber k via:

$$\mathrm{k} = \sqrt{\frac{2m_e(E - E_0)}{\hbar}} \approx \sqrt{\frac{(E - E_0)}{3.81}} \quad \text{(Equation 2.11)}$$

where E-E_0 is the photo-electron kinetic energy, m_e is the rest mass of electron and ħ is the reduced Planck's constant. Then the oscillations are weighted by a power of k, typically k^2 or k^3, to generate the k-space EXAFS data, often referred to as χ(k). This k-space data is subjected to a Fourier transform to yield the R-space EXAFS data, which provides information about the coordination environment of the absorbing element in relation to the radial distance, expressed in angstrom Å.

EXAFS fitting

Based on scattering theory, χ(k) can be modelled as:

$$\chi(\mathrm{k}) = S_0^2 \sum_i N_i \frac{f_i(k)}{kR_i^2} e^{-\frac{2R_i}{\lambda(k)}} e^{-2k^2\sigma_i^2} \sin\left(2R_i k + \delta_i(k)\right) \quad \text{(Equation 2.12)}$$

where $f_i(k)$ is the scattering amplitude, $\lambda(k)$ is the photoelectron mean free path, and $\delta_i(k)$ is the phase shift. These three scattering functions depend on atomic number of the scattering element, which are are derived from the multiple scattering theory from which the EXAFS equation emanates and considered by EXAFS fitting software. S_0^2 is the amplitude reduction factor, N_i is the coordination number, R_i is the half-length of the scattering path, σ_i^2 is the Debye-Waller factor, k is the photoelectron wavenumber and $\delta_i(k)$ is the phase shift. The parameters N_i, R_i and σ_i can be assimilated to the peak height, peak position, and peak width of a Gaussian peak on data fitting. In the fitting procedure, the amplitude reduction factor is set as a fixed input parameter, determined through EXAFS analysis of a model compound. A global parameter is employed to refine the ΔE_0 , where the start of the EXAFS region is considered across the entire XAS spectrum. For each individual scattering path, three distinct parameters are used to refine the coordination number (N), radial distance (R), and displacement from the equilibrium position (σ, also known as the Debye-Waller factor). In cases where the fitting includes more parameters than allowed by the Nyquist criterion, specific constraints are applied to relate the parameters, ensuring that the Nyquist criterion is satisfied.

Analysis of the data was performed using the DEMETER software package. The data were normalised with a linear pre-edge and polynomial post-edge background subtracted from the raw $\ln(I_t/I_0)$ data using the Athena software. EXAFS fitting was performed using the Artemis software.[13] All the XAS data in this thesis were collected on the BL01B1

beamline at SPring-8 Japan or BL11B beamline at Shanghai Synchrotron Radiation Facility China.

2.2.3 X-ray photoelectron spectroscopy

X-ray photoelectron spectroscopy (XPS) is a characterization technique to determine the valence state of elements present on a material's surface. It provides information on hybridisation states and the bonding environment. Unlike Cu Kα X-rays, which have a higher energy of 8047.8 eV, XPS utilises Al Kα X-rays with a lower energy of 1486.6 eV, resulting in reduced penetration depth. This allows for the analysis of only the top few atomic layers of a material.[14] XPS is fundamentally based on the photoelectric effect. When X-ray photons interact with a material, electrons from the target elements absorb the energy, become excited, and are ejected as photoelectrons with non-zero kinetic energy. By measuring the kinetic energy of these emitted photoelectrons, the binding energy of specific elements in the sample can be determined using:

$$E_{binding} = E_{photon} - E_{kinetic} + \phi \quad \text{(Equation 2.13)}$$

where $E_{binding}$ is the binding energy of the specific element, E_{photon} is the energy of the X-ray photons (1486.7 eV for Al Kα X-ray), $E_{kinetic}$ is the measured kinetic energy of the electron, and Φ is the work function as a constant to correct for certain parameters.

In the experimental setup, a survey scan is performed by measuring the entire range of kinetic energy. XPS measurements are typically conducted under high vacuum conditions (~10^{-6} Pa) to ensure accurate detection of the kinetic energy of emitted photoelectrons,

preventing collisions with residual gas molecules in the chamber. This vacuum environment also helps protect the sensitive microchannel plates in the detectors from moisture.[15] In XPS spectra, each element exhibits a unique set of characteristic XPS peaks corresponding to its electron configuration. A peak is detected if the binding energy of a specific orbital is lower than 1486.7 eV, the energy of Al Kα X-rays. By correcting the intensity of each raw XPS peak using a relative sensitivity factor and normalising across all detected elements, the atomic composition of the sample can be quantified. However, a key limitation of this quantification method is the limited penetration depth of Al Kα X-rays, restricting its effectiveness for bulk material analysis. Fitting with Gaussian function is a common approach for XPS analysis. Raw XPS data often contain noise, making it difficult to accurately compare peak positions across different samples. By fitting the data with Gaussian function, the peak maxima can be determined more reliably, reducing the impact of noise and improving consistency in analysis. Additionally, peaks corresponding to different oxidation states may overlap, making it challenging to distinguish their contributions. Fitting these overlapping peaks allows for the quantification of the relative proportions of different oxidation states present in the sample.

2.2.4 Pair distribution function

The pair distribution function (PDF) method is based on the Debye scattering equation, first introduced by Debye in 1915.[16] In 1927, Zernicke and Prins highlighted the Fourier relationship between the atomic pair density in real space and the total scattering intensity in Q space.[17] With advancements in modern X-ray synchrotron facilities and spallation neutron sources, high fluxes of X-ray photons and neutrons can now be achieved. When combined with high energy, or short wavelength (λ), the high-Q region

becomes accessible (as Q is inversely proportional to λ), enabling high-quality Fourier transforms. The PDF $g(r)$ is defined as:

$$g(r) = \frac{1}{4\pi\rho_0 r^2 N}\sum_i\sum_{j\neq i}\delta(r - r_{ij}) \quad \text{(Equation 2.14)}$$

where ρ_0 represents the average number density of atoms, N is the total number of atoms, r_{ij} is the distance between atom i and atom j, $\delta(r - r_{ij})$ is the Dirac delta function which equals a single unit only when $r = r_{ij}$. In practice, the reduced atomic pair distribution function $G(r)$ is more commonly used:

$$G(r) = 4\pi r\rho_0|g(r) - 1| \quad \text{(Equation 2.15)}$$

And $G(r)$ can be calculated from the measured total scattering function $S(Q)$ via Fourier transformation:

$$G(r) = \frac{2}{\pi}\int_{Q_{min}}^{Q_{max}} Q|S(Q) - 1|\sin(Qr)dQ \quad \text{(Equation 2.16)}$$

where Q is the amplitude of the transferred momentum calculated by the difference between scattered wavevector and incident wavevector. $S(Q)$ is calculated by measured coherent scattering intensity $I^{coh}(Q)$:

$$S(Q) = 1 + \frac{I^{coh}(Q) - \sum c_i|f^i(Q)|^2}{|\sum c_i f^i(Q)|^2} \quad \text{(Equation 2.17)}$$

where c_i is the atomic concentration of the i^{th} element, $f^i(Q)$ is its atomic x-ray scattering factor (or neutron scattering length), and $I^{coh}(Q)$ is the coherent scattering intensity which can be directly collected from the experimentally measured total intensity $I(Q)$ when properly corrected for incoherent intensity, background noises, detector efficiency, multiple scattering, etc. By this, the relationship between measurable total scattering intensity $I(Q)$ and structural function $g(r)$ can be established.[18]

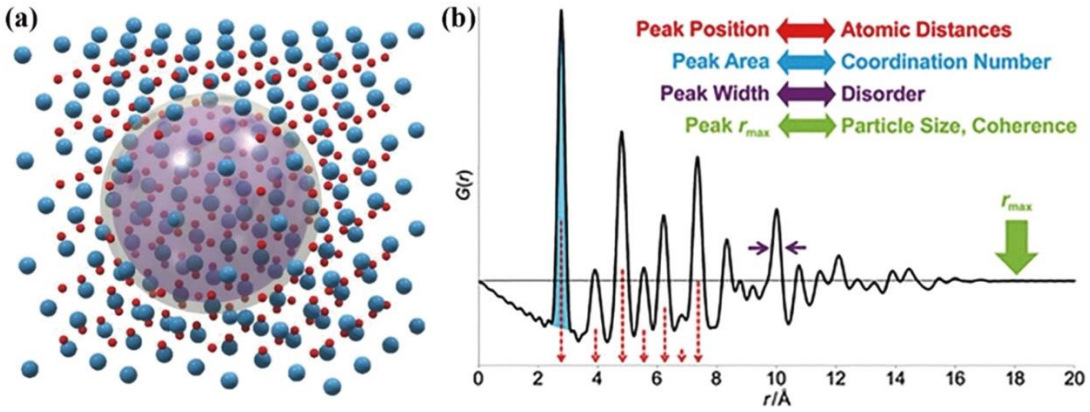

Figure 2.4: (a) Atom distribution of CeO_2 in real space, and a sphere centred at an atom with radius *r* and annulus thickness d*r*. (b) High-energy x-ray total scattering derived PDF in real space, *G*(*r*), provides real-space structure information. Figure reproduced from Reference [19][20].

As shown in Figure 2.4a, the quantity *R*(*r*)d*r* represents how many atoms can be found inside an annulus of thickness d*r* at a distance *r* from another particle. And *R*(*r*), which is the radial distribution function (RDF), can be expressed as:

$$R(r) = 4\pi r^2 \rho_0 g(r) \quad \text{(Equation 2.18)}$$

Figure 2.4b presents a typical PDF pattern *G*(*r*) for a material. As a real-space function, it provides structural information. The peak positions correspond to atomic pair distances, while the peak areas reflect the abundance of these pairs, weighted by their scattering power. Peak widths indicate the degree of disorder within the material, which may arise from structural disorder or atomic thermal vibrations. Additionally, the maximum distance at which peaks remain visible offers insight into the size of the coherent domain. In this thesis, all the PDF data was collected on BL08W at Spring-8, Japan.

2.2.5 Nuclear magnetic resonance spectroscopy

Nuclear Magnetic Resonance (NMR) provides information about the nuclear charge experienced by nuclei of NMR-active atoms with spin 1/2 (I = ½), such as ^{1}H and ^{13}C, which are key elements in organic chemistry. These nuclei possess two independent spin states, denoted by the spin quantum number $m_s = +1/2$ (spin-up) and $m_s = -1/2$ (spin-down). In the absence of a magnetic field, these states are degenerate, meaning the population of each state is equal, according to statistical mechanics. However, when exposed to a magnetic field, nuclei with spins aligned with the field become more energetically stable than those with spins opposing it, due to magnetic dipole interactions. This causes the degeneracy to break, resulting in an energy difference (ΔE) between the two states. This energy difference is proportional to the strength of the magnetic field B_0, described as:

$$\Delta E = \gamma \hbar B_0 \quad \text{(Equation 2.19)}$$

where γ is the gyromagnetic ratio for the nucleus and $\hbar$ is the reduced Planck's constant, which is summarised in Figure 2.5.

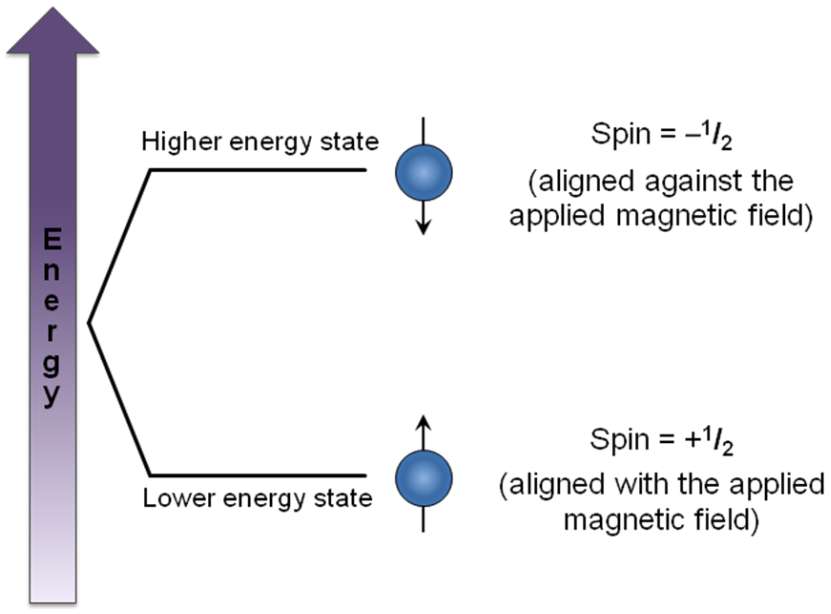

Figure 2.5: Magnetic field lifting degeneracy for nuclei with opposite spin. Figure reproduced from Reference [21].

Chemical shift is the resonant frequency of a certain NMR-active nucleus relative to a standard with the presence of a magnetic field, and is calculated in:

$$\delta = \frac{v_{sample} - v_{reference}}{v_{reference}} = \frac{1}{h}\frac{\Delta E_{sample} - \Delta E_{reference}}{\Delta E_{reference}} \quad \text{(Equation 2.20)}$$

where v_{sample} is the resonant frequency, ΔE_{sample} is energy difference due to presence of magnetic field for the sample, $v_{\text{reference}}$ and $\Delta E_{\text{reference}}$ represent those of the reference. Since the numerator is often in units Hz, and the denominator in units MHz, δ has the unit ppm (10^{-6}). Common references used for ^{1}H and ^{13}C tetramethyl silane, $Si(CH_3)_4$, while for other NMR-active nuclei there may be other reference compounds.

2.2.6 Electron paramagnetic resonance spectroscopy

Similar to NMR, the degeneracy of the spin of an unpaired electron can be broken in a magnetic field. The energy change ($m_s = +1/2 \leftrightarrow -1/2$) depends on the electron's magnetic moment (g-factor) and can be measured by varying the magnetic field under continuously irradiating with microwaves, which must have a much higher frequency than NMR.[22] The g-factor is characteristic of the chemical environment, and the signal strength provides information about the electron's concentration. This technique is particularly useful for studying electronic defects, such as the oxygen vacancy in the perovskite. The energy change is given by:

$$\Delta E = g\mu_B B_0 \quad \text{(Equation 2.21)}$$

where μ_B is the Bohr magneton.

2.2.7 Fourier-transform Infrared spectroscopy

Rather than shining monochromatic infrared radiation at each wavelength, Fourier-transform infrared (FT-IR) radiation simultaneously illuminates the sample with light composed of multiple frequencies and measures the amount of absorption at each frequency. This process is repeated across different sets of frequencies to gather more data points quickly over a short period. Then, an algorithm processes all the data points to reconstruct the absorption at each individual wavelength. This algorithm is a modified form of the Fourier transform, hence the technique is named FT-IR. The raw data before Fourier transformation is called an interferogram.[23] In this thesis, FT-IR spectroscopy was conducted in the range of 650-4000 cm^{-1} using a Nicolet iS 50 FT-IR spectrometry with an MCT/A detector at a resolution of 4 cm^{-1} in Wolfson Catalysis Centre at the University of Oxford.

2.2.8 Ultra-violet visible spectroscopy

Ultra-violet visible (UV-vis) spectroscopy utilises the ultraviolet and visible range of the electromagnetic spectrum for analytical purposes. It is relatively affordable and straightforward to perform, making it applicable in a variety of fields with the only requirement of the sample absorbing light in the UV-vis range. For solutions, absorbance is typically measured. While for solid samples, it is more common to measure the remission (including both specular reflection and diffusely back-scattered light). Electronic transitions in metals often fall within this energy range and can be examined using UV-vis spectroscopy. In the case of perovskite oxide, the common electronic transitions typically involve d–d transitions between the d-orbitals of transition metal ions, as well as possible oxygen 2p to metal 3d charge transfer transitions. Moreover, UV-vis spectroscopy can be used to determine the band gap of semiconductor materials through the Tauc plot:

$$(ahv)^{\gamma} = B(hv - E_g) \quad \text{(Equation 2.22)}$$

where α is the absorption coefficient of the material, h is the Planck's constant, v is the frequency of the electromagnetic radiation, B is the energy independent constant, and E_g is the energy of the band gap. While γ is the parameter denoting the nature of the transitions, where it equals to 2 for direct bandgap material and ½ for indirect bandgap material. All the UV-vis measurements were performed at Chemistry Teaching Laboratory, University of Oxford, using Shimadzu UV-2600 under diffuse reflectance mode, with barium sulphate pallet used as the white diffuse standard. The measurement is performed from 200 to 900 nm, with a sampling interval of 0.5 nm at 298 K. The slit width of the measurement is set at 5.0 nm and the wavelength of light source change from W halogen lamp to deuterium lamp was set to be 370.

2.2.9 Photoluminescence spectroscopy

Steady-state photoluminescence spectroscopy

Photoluminescence refers to the emission of light from a material upon photoexcitation. Typically, various relaxation processes can occur, with the excited electron and hole diffusing to the surface of the material, where they can participate in catalytic redox reactions. In addition, the electron-hole pairs can induce molecular motions such as vibrations or rotations within the structure of the material, or they may recombine radiatively to release light. Therefore, Steady-state photoluminescence (SSPL) spectroscopy is a useful technique for investigating the radiative recombination of excitons, helping to elucidate the electron transition behaviors in semiconductor materials.

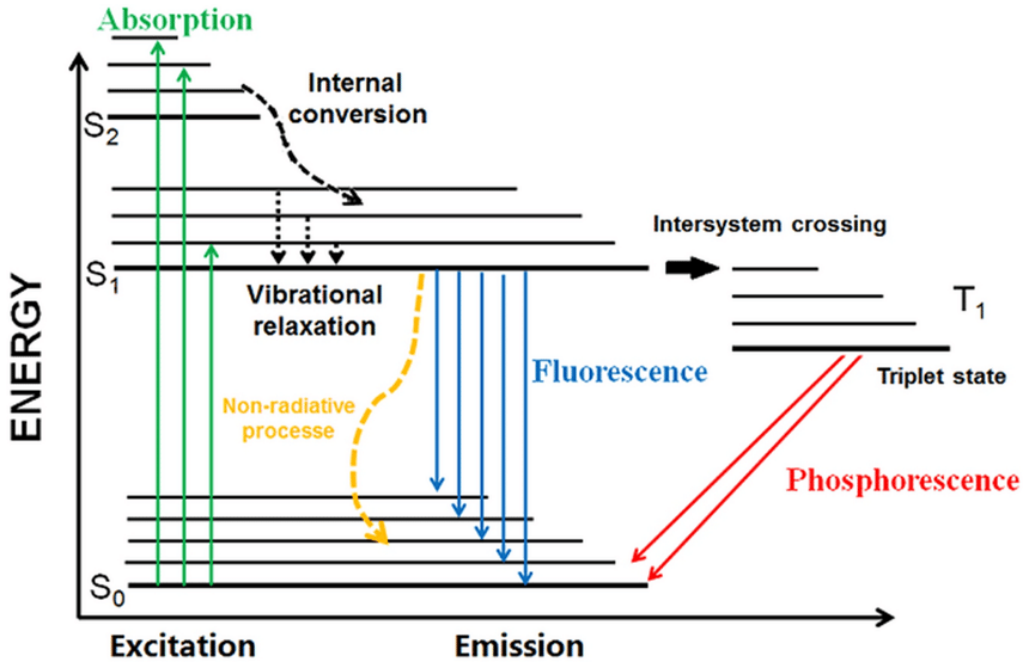

Figure 2.6: Jablonski diagram showing the light absorption, fluorescence, phosphorescence processes. S_0, S_1 and S_2 are arbitrary singlet states, while T_1 is arbitrary triplet states. Figure reproduced from Reference [24].

The Jablonski diagram is often used to explain the electron transition processes as shown in Figure 2.6. Upon photoexcitation, electrons are promoted to higher energy states ($S_0 \rightarrow S_2$), and they then undergo vibrational relaxation to the S_1 energy state. From here, the electron recombines with the hole in the S_0 ground state, releasing a photon in the process. This emission of light at a lower energy than the incident photon is termed fluorescence. Moreover, the electron may also undergo intersystem crossing to a triplet state T_1 via spin-orbit coupling, and it can recombine with the hole in the S_0 state and radiate a photon, which is known as phosphorescence. However, once the electron enters the triplet state T_1, it experiences a slow recombination process from triplet state T_1 to ground state S_0 due to the spin difference between these states. This spin mismatch makes the recombination process less probable. As a result, the phosphorescence emission tends to last longer. Its duration can range from microseconds to seconds, or even longer.[25]

SSPL spectroscopy can be conducted in three modes: excitation, emission, or simultaneous. In excitation mode, the detection wavelength is kept constant while the excitation wavelength is varied. In emission mode, the excitation wavelength is fixed, and the detected photon wavelength is altered. In simultaneous mode, the difference between the excitation and emission wavelengths is kept constant and both are adjusted simultaneously during the measurement. In this work, emission mode is used for SSPL spectroscopy of perovskite oxide. And all the SSPL data were obtained on Shimadzu RF-6000 spectrofluorophotometer at Chemistry Teaching Laboratory, University of Oxford. The excitation wavelength is 375 nm with emission wavelength monitored from 400 nm to 700 nm. Data interval was set to be 0.2 nm at a scan rate of 200 nm/min. The bandwidth of excitation and emission are set to be 10 nm. Samples were prepared at a concentration of 1mg/mL with deionised water as solvent at 298K.

Time-resolved photoluminescence spectroscopy

Time-resolved photoluminescence (TRPL) spectroscopy is an advanced spectroscopic technique used to study the dynamics and lifetime of photoluminescent processes with high time resolution. It is particularly useful for investigating the exciton lifetime in materials, such as photocatalysts, and it provides detailed insights into the temporal behavior of charge carriers following excitation, helping to understand processes like recombination, energy transfer, and material properties. In TRPL, a pulsed light source is used for excitation, and the emission is measured over time after the excitation pulse. And both the excitation wavelength and measured emission wavelength are selected to match the photoluminescence peaks of the material being studied, ensuring consistency with conventional SSPL measurements. Then, by recording the emission intensity as a function of time, the decay profile of the photoluminescence can be obtained, which

provides the information of exciton lifetime and is essential for evaluating the efficiency of charge carrier recombination.

The background-corrected TRPL data are normalized across all samples and then fitted to either a mono-exponential decay function:

$$y = A_1 e^{-x/\tau_1} \quad \text{(Equation 2.23)}$$

or a bi-exponential decay function:

$$y = A_1 e^{-x/\tau_1} + A_2 e^{-x/\tau_2} \quad \text{(Equation 2.24)}$$

which depends on the presence of one or two distinct exciton radiative recombination processes. In Equation 2.23 and 2.24, y represents the observed TRPL data, and x denotes the time elapsed since excitation. The parameters A_1, A_2, τ_1, and τ_2 are the fitting parameters, with τ_1 and τ_2 representing the lifetimes of the respective photoluminescence processes. The fitting errors are determined using the least squares method. The average lifetime of the sample is calculated using:

$$\tau_{avg} = \frac{A_1\tau_1 + A_2\tau_2}{A_1 + A_2} \quad \text{(Equation 2.25)}$$

All the TRPL results in this work were obtained from a bespoke photoluminescence setup in Department of Physics, University of Oxford. A Ti-Sapphire laser (λ = 266 nm, pulse duration = 150 fs, repetition rate = 76 MHz) is directed onto the sample. The diameter of the laser spot on the sample was ~ 200 μm, and its laser output power was 2 mW, resulting in a power density of 5000 mW/cm^2. A monochromator was employed to filter the signal before it was directed to a photomultiplier tube detector, which had an instrument response function width of 150 ps and was connected to a time-correlated counting module. The TRPL measurements were conducted in pulse-picking mode, where the recorded signals were selected by a pulse picker to allow for a sufficiently long decay

time of approximately 100 ns between consecutive signals. This ensured that all excited charge carriers had time to recombine and return to the ground state, while also preventing the accumulation of charge carriers in the sample.

2.2.10 Thermogravimetric analysis

Thermal analysis techniques, including thermogravimetric analysis (TGA), differential scanning calorimetry (DSC), and differential thermal analysis (DTA), provide information of the thermal stability, moisture content, volatile organic solvents, and decomposition temperatures of materials. TGA measures the change in mass of a sample as a function of temperature, with high precision, allowing for the detection of weight changes due to processes such as hydration, decomposition, or oxidation of powders. TGA is often performed in conjunction with DTA or DSC for complementary data. DSC measures the difference in heat flow between a sample and an inert reference over time and temperature, helping to identify endothermic processes (such as melting, glass transition, and evaporation) and exothermic processes (such as crystallization, oxidation, and specific heat capacity). DTA, on the other hand, records the temperature difference between a sample and a reference material as a function of time or temperature, providing key information like melting points, similar to DSC. These techniques are essential for understanding the thermal behaviours and stability of compounds. In this thesis, TGA was performed on a TA Instruments SDT Q600 under a constant air flow rate of 60 mL/min in Inorganic Chemistry Laboratory, University of Oxford. Sample of approximately 20 mg was added onto an alumina pan and heated from 30 °C to 900 °C at a rate of 5 °C / min[1].

2.2.11 Inductive coupled plasma mass spectrometry

Inductively coupled plasma mass spectrometry (ICP-MS) is a highly sensitive analytical technique that enables the quantification of specific elements at concentrations as low as parts per trillion (ppt). Samples are first digested in strong acid and then diluted to create a stable aqueous matrix. A plasma is generated by inductively heating argon gas with an electromagnetic coil, creating a medium rich in ions and electrons, making it electrically conductive. The sample is then introduced into a nebuliser, where an inert gas causes the liquid to aerosolise through supersonic expansion. The resulting argon plasma, which reaches temperatures up to 10,000 K, is used to vaporise, atomise, and ionise the sample, producing singly charged positive ions. These ions are then directed into a quadrupole mass spectrometer, which separates them based on their mass-to-charge (m/z) ratio using a varying magnetic field. ICP-MS can quantify specific elements at ultra-low concentrations and detect different isotopes of the same element. However, the technique is limited by mass-based interference, such as the overlap of sulphur (^{32}S) with oxygen (O_2) molecules (m = 32) present in the air, which can complicate the accurate quantification of certain elements. All the ICP-MS data were collected at Chemistry Teaching Laboratory, University of Oxford.

2.2.12 Temperature programmed reduction

NH_3 temperature programmed reduction (TPR) was measured on a Quantachrome ChemBET Pulsar TPR/TPD analyser with a cold trap in Inorganic Chemistry Department, University of Oxford. The detector current was set to 150 mA. About 50 mg of sample was degassed in a quartz cell at 473 K for 1 hour under helium gas. Then the TPR measurement was done from 298 K to 1073 K under NH_3 gas with flow rate 20 mL / min.

2.2.13 Scanning electron microscopy

Scanning electron microscope (SEM) is a widely used technique for imaging the microstructure and morphology of materials. In SEM, a low-energy electron beam is directed onto the sample, scanning its surface. As the beam interacts with the material, various interactions occur, resulting in the emission of photons and electrons from or near the sample's surface. To generate an image, the signals produced by electron–sample interactions are detected using different types of detectors, depending on the specific SEM mode employed.[26] In this thesis, SEM data was collected on Zeiss Merlin Compact Field Gun (FEG)-SEM with Gatan 3View for serial block face sectioning SEM in DUNN School, Sir William of Pathology, University of Oxford.

2.2.14 Transmission electron microscopy

Transmission electron microscopy (TEM) is a high-magnification imaging technique that visualises the transmission of an electron beam through a material. Because TEM uses electrons instead of light to illuminate the sample, it provides significantly higher resolution than optical imaging methods. Imaging contrast arises from the amplitude and phase changes in the transmitted electron beam, which are influenced by both the sample material and its thickness. To prepare samples for TEM imaging, nanoparticles are typically dried onto a copper grid coated with a thin carbon layer. Materials with higher electron densities than amorphous carbon are readily imaged, including most metals (e.g., Ag, Au, Cu, Al), oxides (e.g., silica, aluminium oxide, titanium oxide), and other nanoparticles such as polymers, carbon nanotubes, quantum dots, and magnetic nanoparticles.[27]

TEM is the preferred method for directly analysing particle size, grain size, size distribution, and morphology. And scanning transmission electron microscopy (STEM)

enhances spatial resolution by employing a rastering technique, where a focused electron beam scans across the sample. High-angle annular dark-field (HAADF) imaging further improves signal quality by enhancing counting statistics and reducing background noise from the transmitted beam.[28] With HADDF-STEM, a resolution of ~ 1 Å can be achievable. Additionally, FFT facilitate phase identification, structural and symmetry analysis, lattice parameter measurement, and the detection of defects and disorder in materials. All the STEM work in this thesis was done by Dr. Shuai Guo and Dr. Ping-Luen Ho.

2.2.15 Electron spectroscopy

Electron spectroscopy enables compositional mapping during imaging. Energy-dispersive X-ray spectroscopy (EDX) operates by detecting characteristic X-rays emitted during electronic relaxation transitions. The position of peaks in the spectrum identifies the elements present, while signal intensity correlates with their concentration. Electron energy loss spectroscopy (EELS), on the other hand, analyses inelastically scattered electrons (typically within a 5–100 mrad range). The energy loss of the electron beam corresponds to specific electronic transitions, providing insights into composition and electronic states. Similar to X-ray absorption techniques such as XANES and XAFS, EELS exhibits analogous spectral features known as electron loss near-edge structure (ELNES) and extended energy-loss fine structure (EXELFS).[29]

2.3 Product analysis

2.3.1 Gas chromatography

Chromatography is a separation technique that enables the isolation of individual components from a mixture. It is an essential tool across various branches of chemistry. Depending on the nature of the mixture, different chromatographic techniques are employed, such as gas chromatography (GC), liquid chromatography (LC), and column chromatography (CC), each utilising specialised equipment. In chromatography, the mixture is typically dissolved in a gaseous or liquid solvent, referred to as the mobile phase. This mobile phase carries the mixture through a stationary phase, which can take the form of a column, capillary tube, or sheet. Separation occurs due to the varying affinities of the components in the mobile phase toward the stationary phase, effectively counteracting the natural tendency toward disorder dictated by the second law of thermodynamics.

GC is particularly valuable in green energy research and catalytic fuel production, where it is used to separate and quantify gaseous molecules. The carrier gas (mobile phase) is selected based on the sample composition, with common choices including hydrogen, helium, and nitrogen. The stationary phase in GC typically consists of fused silica capillary columns with inner diameters around 100 μm and lengths of approximately 10 meters. Separation occurs as different gases, such as H_2, CO_2 and CH_4, which interact to varying degrees with the silica surface. And the most common detectors are the thermal conductivity detector (TCD) and the flame ionisation detector (FID).

The TCD operates by continuously measuring the thermal conductivity of the gas passing through it. It compares the conductivity of the samples stream to that of a reference stream containing only the pure carrier gas. The change in thermal conductivity relative to the

carrier gas generates a detectable signal at a specific retention time. Hydrogen and helium, due to their high thermal conductivities, are commonly used as carrier gases in conjunction with TCD. Since all organic and inorganic compounds exhibit non-zero thermal conductivity and are always lower than that of helium or hydrogen.[30] Therefore, TCD can effectively detect a wide range of substances. By plotting signal intensity against retention time, the peak position indicates the identity of the compound, while the peak area, obtained by integrating the signal over time, corresponds to its concentration. In this study, a TCD detector with helium as the carrier gas, coupled with an Agilent 7890 GC, was used to detect H_2 produced from photocatalytic water splitting and ammonia decomposition.

2.3.2 Selective ammonia electrode

The concentration of ammonia was determined by using a selective ammonia electrode, which detects ammonia molecules that permeate through the electrode membrane. This electrode features a hydrophobic, gas-permeable membrane that separates the sample solution from the electrode's internal filling solution, preventing liquid penetration while allowing dissolved ammonia to diffuse across the membrane. Equilibrium is reached when the partial pressure of ammonia is equal on both sides of the membrane. Since the partial pressure of ammonia is proportional to its concentration in solution, this relationship enables precise quantification. The potential of the electrode sensing element with respect to the internal reference element is described by the Nernst equation:

$$E = E_0 - S \log[\mathrm{NH_3}] \quad \text{(Equation 2.26)}$$

where E is the measured electrode potential, E_0 is the reference potential, S is the electrode slope, and $[NH_3]$ represents the ammonia concentration in solution. Before each

measurement, the pH of all standards and samples needs to be adjusted above 11 to ensure that ammonia remains in its gaseous form.[31] The electrode specifically responds to the partial pressure of dissolved ammonia gas, which correlates with ammonia concentration according to Henry's Law:

$$K_h = \frac{[NH_3]_{aqueous}}{P_{NH_3}} = 56 \text{ mol/L - atm } 298 \text{ K} \quad \text{(Equation 2.27)}$$

2.3.3 Catalytic test

Photocatalytic H_2 evolution experiments were performed under a 300 W xenon lamp (Sciencetech, Canada) as a light source and started from the room temperature. 20 mg of photocatalysts was dispersed in 10 mL of aqueous solution with 10 vol% methanol as a hole scavenger, and it was placed in an autoclave. The autoclave was evacuated and purged 10 times with Ar gas. The mixture then was irradiated under 250 rpm stirring speed for 1 h under 2 bar of 91 cm^3 Ar gas. The distance between light source and autoclave window was kept at 15 cm. The recycle experiments of the photocatalysts were measured over 4 h with four cycles. Each recycle was done by evacuating and purging with Ar gas, in order to remove the residual hydrogen gas in the autoclave. And then the photocatalytic measurement was repeated.

Photocatalytic NH_3 decomposition was carried out in an autoclave under a solar simulator ($1kW/m^{-2}$) as a light source. After placing the quartz loaded with photocatalysts in the autoclave, the autoclave was evacuated and purged 10 times with Ar gas. Then, the system was sealed with 6 bar of 240 cm^{-3} NH_3 gas rather than a continuous process. The temperature was controlled by two heating bars assembled in the autoclave prior to the light illumination. The irradiation power in the centre of the autoclave window was calculated to be 80 mW. After light illumination for 1 h, the gas sample was analysed

with a gas chromatograph (Agilent Technologies 7890B GC system) equipped with a thermal conductivity detector (TCD).

The photocatalytic NH_3 synthesis tests were carried out in a batch reactor equipped with two quartz windows. In a typical experiment, catalysts were first pre-treated under 473 K under Ar gas flow to remove adsorbed water molecules and ammonium cations. Then quartz loaded with photocatalysts and 10 mL of deionised water (NH_3 trap) in a glass lining (20 mm i.d. × 24 mm o.d. × 52 mm height) were both placed in the batch reactor. Continuous N_2 gas flow was purged after well-sealed to remove O_2. Then the batch reactor was pressurised with 6 bar of N_2-H_2 gas mixture (9:1 v/v). The reactor would then be allowed to heat up to certain elevated temperature. VeraSol solar simulator (AM 1.5G, 100 mW cm^{-2}, 1 sun) was then used to provide the simulated solar irradiation through the silica windows. The batch reactor was cooled down naturally to room temperature after reaction.

2.4 Density function theory calculation

The first principles calculations based on density function theory (DFT) were performed using the Vienna ab initio simulation package (VASP, version 5.44).[32] The Perdew-Burke-Ernzerhof (PBE) exchange-correlation functional within the generalized gradient approximation (GGA) was used to describe the exchange-correlation energy.[33] The plane wave cutoff energy was 450 eV. Geometries were converged to 10-7 eV in electric relaxation energy and 0.01 eV/Å in ion relaxation energy. A vacuum layer of 15 Å was used to avoid the periodic interactions. All the DFT modelling was performed by Dr. Yanjie Wang at CAS Key Laboratory of Nanosystem and Hierarchical Fabrication, National Centre for Nanoscience and Technology in Beijing, China.

2.5 Reference

1. Dinnebier, R. E., Leineweber, A., & Evans, J. S., 2018. *Rietveld refinement: practical powder diffraction pattern analysis using TOPAS*. Walter de Gruyter GmbH & Co KG.
2. Murrell, J., 2024. *The topochemical reduction of some complex iridium oxides* (Doctoral dissertation, University of Oxford).
3. Bragg, W. H., & Bragg, W. L., 1913. The reflection of X-rays by crystals. *Proceedings of the Royal Society of London. Series A, Containing Papers of a Mathematical and Physical Character*, *88*(605), 428-438.
4. Lindon, J. C., Tranter, G. E., & Koppenaal, D., 2016. *Encyclopedia of spectroscopy and spectrometry*. Academic Press.
5. Squires, G. L., 1996. *Introduction to the theory of thermal neutron scattering*. Courier Corporation.
6. Yoskamtorn, T., 2021. *Structural and dynamic studies of Zr-based metal-organic frameworks toward external stimuli* (Doctoral dissertation, University of Oxford).
7. Rietveld, H. M., 1969. A profile refinement method for nuclear and magnetic structures. *Applied Crystallography*, *2*(2), 65-71.
8. Dinnebier, R. E., Leineweber, A., & Evans, J. S., 2018. *Rietveld refinement: practical powder diffraction pattern analysis using TOPAS*. Walter de Gruyter GmbH & Co KG.
9. Coelho, A. A., Evans, J., Evans, I., Kern, A., & Parsons, S., 2011. The TOPAS symbolic computation system. *Powder Diffraction*, *26*(S1), S22-S25.
10. Thompson, P., Cox, D. E., & Hastings, J. B., 1987. Rietveld refinement of Debye–Scherrer synchrotron X-ray data from Al2O3. *Applied Crystallography*, *20*(2), 79-83.

11. Pawley, G. S., 1981. Unit-cell refinement from powder diffraction scans. *Applied Crystallography*, *14*(6), 357-361.
12. Grünert, W., & Klementiev, K., 2020. X-ray absorption spectroscopy principles and practical use in materials analysis. *Physical Sciences Reviews*, *5*(4), 20170181.
13. Ravel, B., & Newville, M. A. T. H. E. N. A., 2005. ATHENA, ARTEMIS, HEPHAESTUS: data analysis for X-ray absorption spectroscopy using IFEFFIT. *Synchrotron Radiation*, *12*(4), 537-541.
14. Chastain, J., & King Jr, R. C., 1992. Handbook of X-ray photoelectron spectroscopy. *Perkin-Elmer Corporation*, *40*(221), 25.
15. Held, G., Venturini, F., Grinter, D. C., Ferrer, P., Arrigo, R., Deacon, L., Scott, S., 2020. Ambient-pressure endstation of the Versatile Soft X-ray (VerSoX) beamline at Diamond Light Source. *Synchrotron Radiation*, *27*(5), 1153-1166.
16. Debye, P., 1915. Zerstreuung von röntgenstrahlen. *Annalen der Physik*, *351*(6), pp.809-823.
17. Zernike, F.T. and Prins, J.A., 1927. Die beugung von röntgenstrahlen in flüssigkeiten als effekt der molekülanordnung. *Zeitschrift für Physik A Hadrons and nuclei*, *41*(2), pp.184-194.
18. Wang, X., Tan, S., Yang, X.Q. and Hu, E., 2020. Pair distribution function analysis: Fundamentals and application to battery materials. *Chinese Physics B*, *29*(2), p.028802.
19. Ren, Y. and Zuo, X., 2018. Synchrotron X-ray and neutron diffraction, total scattering, and small-angle scattering techniques for rechargeable battery research. *Small Methods*, *2*(8), p.1800064.
20. Chapman, K.W., 2016. Emerging operando and x-ray pair distribution function methods for energy materials development. *MRS Bulletin*, *41*(3), pp.231-240.

21. Pavan M. V. Raja & Andrew R. Barron, https://chem.libretexts.org/Bookshelves/Analytical_Chemistry
22. Di Valentin, C., Pacchioni, G., Selloni, A., Livraghi, S. and Giamello, E., 2005. Characterization of paramagnetic species in N-doped TiO_2 powders by EPR spectroscopy and DFT calculations. *The Journal of Physical Chemistry B*, *109*(23), pp.11414-11419.
23. Ng, B.K.Y., 2024. *Modifying UiO-series metal-organic frameworks for fuel-forming photocatalysis* (Doctoral dissertation, University of Oxford).
24. Photophysics of fluorescent proteins, ibs Institut de Biologie Structural, France, https://www.ibs.fr/research/research-groups/dynamics-and-kinetics-of-molecular-processes-group-m-weik/pixel/photophysics-of-fluorescent/?lang=fr.
25. Tebyetekerwa, M., Zhang, J., Xu, Z., Truong, T. N., Yin, Z., Lu, Y., Nguyen, H. T., 2020. Mechanisms and applications of steady-state photoluminescence spectroscopy in two-dimensional transition-metal dichalcogenides. *ACS nano*, *14*(11), 14579-14604.
26. Mohammed, A., & Abdullah, A., 2018. Scanning electron microscopy (SEM): A review. In *Proceedings of the 2018 international conference on hydraulics and pneumatics—HERVEX, Băile Govora, Romania* (Vol. 2018, pp. 7-9).
27. Morajkar, P. P., & Naik, M. M. (Eds.)., 2023. *Advances in Nano and Biochemistry: Environmental and Biomedical Applications*. Elsevier.
28. Hungría, A. B., Calvino, J. J., & Hernández-Garrido, J. C., 2019. HAADF-STEM electron tomography in catalysis research. *Topics in Catalysis*, *62*(12), 808-821.
29. Hofer, F., Schmidt, F. P., Grogger, W., & Kothleitner, G., 2016. Fundamentals of electron energy-loss spectroscopy. In *IOP conference series: Materials science and engineering* (Vol. 109, No. 1, p. 012007). IOP Publishing.

30. Clarke, W., & Marzinke, M. (Eds.)., 2020. *Contemporary practice in clinical chemistry*. Academic Press.

31. Zheng, J., Lu, L., Lebedev, K., Wu, S., Zhao, P., McPherson, I. J., & Tsang, S. C. E., 2021. Fe on molecular-layer MoS_2 as inorganic Fe-S_2-Mo motifs for light-driven nitrogen fixation to ammonia at elevated temperatures. *Chem Catalysis*, *1*(1), 162-182.

32. Kresse, G., & Furthmüller, J., 1996. Efficiency of ab-initio total energy calculations for metals and semiconductors using a plane-wave basis set. *Computational materials science*, *6*(1), 15-50.

33. Perdew, J. P., Burke, K., & Ernzerhof, M., 1996. Generalized gradient approximation made simple. *Physical review letters*, *77*(18), 3865.

Chapter 3 | Tuning 2D perovskite-graphene composite for photocatalytic H_2 evolution from H_2O splitting

3.1 Abstract

The work in this chapter has already been published in *Sustainable Energy & Fuel* as "Tuning 2D perovskite-graphene composite for photocatalysis" with DOI: 10.1039/D4SE00630E.

Enhancing the photocatalytic activity of layered perovskite oxides through the integration of graphene-like materials offers a promising strategy for optimising solar energy conversion. The electron-rich nature and high conductivity of graphene make it an effective photosensitiser, significantly improving visible light harvesting. In this study, we report, for the first time, the assembly of ultrathin exfoliated Dion-Jacobson perovskite layers with reduced graphene oxide (rGO), forming a high-surface-area layered nanocomposite via a tailored electrostatic approach. To further tune the electronic properties of these perovskite-rGO composites, we incorporated different lanthanides as A-site cations in the Dion-Jacobson perovskites, specifically $LaNb_2O_7$ (LNO), $PrNb_2O_7$ (PNO), and $NdNb_2O_7$ (NNO). The resulting composites exhibited improved photocatalytic H_2 production, with rGO/NNO achieving the highest hydrogen evolution rate of 835 μmol/gh under light illumination, attributed to optimal interfacial interactions. Experimental and theoretical analyses suggest that hydrogen production is primarily governed by the charge density of the A-site cation within perovskite nanosheets, influencing charge transfer dynamics. This research provides valuable insights into photocatalytic mechanisms and paves the way for advanced solar energy conversion applications.

3.2 Introduction

To enhance the photocatalytic performance of layered perovskite oxides for hydrogen production, various strategies have been explored to modify their structure and properties. Wakayama et al. synthesized $Rb_2NdNb_2O_6N$ by nitriding $RbNdNb_2O_7$ with Rb_2CO_3, effectively narrowing the bandgap and improving light absorption.[1] Similarly, Ida et al. successfully exfoliated $CsCaTa_3O_{10-x}N_y$ into $CaTa_3O_{10-x}N_y$ nanosheets, leading to a substantial increase in HER under strong full-arc irradiation using 10 mg of catalysts.[2] Exfoliating layered perovskites into nanosheets has proven to be an effective approach for enhancing photocatalytic performance. This enhancement is primarily attributed to the increased surface area, which provides more active sites for the water-splitting reaction.[3][4] Additionally, the reduced size of the catalysts shortens charge carrier diffusion distances, facilitating their participation in the water-splitting process.[2]

However, challenges still remain, particularly the aggregation of perovskite nanosheets and the rapid recombination of charge carriers, which hinder their photocatalytic efficiency. To address the aggregation issue, Zhou et al. introduced a core-shell structure, dispersing perovskite nanosheets onto SiO_2 spheres. While this approach reduced aggregation, it also decreased the photocatalytic activity of H_2 evolution due to the light-scattering properties of SiO_2, which limited optimal light penetration.[5] In light of these, the development of nanocomposites integrating perovskite oxide nanosheets with photosensitisers is emerging as a promising strategy to further improve photocatalytic performance. The objective of these nanocomposites is to enhance light-harvesting capabilities and improve the stability of perovskite nanosheets. Carbon-based materials, known for their outstanding structural and electronic properties, have emerged as promising candidates for this purpose.[6][7] For instance, multi-walled carbon nanotubes

(MWCNTs), capable of sustaining high current densities (~10^9 A/cm^2),[8] have been used to synthesise perovskite-based nanocomposites. Shu et al. successfully anchored $CsPbBr_3$ quantum dots onto MWCNTs, achieving a threefold enhancement in photocatalytic CO_2 reduction performance.[9] Graphitic carbon nitride (g-C_3N_4), with a band gap of 2.7 eV and delocalised electrons under illumination, is another key material for forming heterostructures with perovskites.[10] Jiang et al. constructed a 2D-2D g-C_3N_4/$KCa_2Nb_3O_{10}$ heterojunction, demonstrating superior photocatalytic activity in tetracycline hydrochloride degradation.[11] Among conjugated carbon materials, graphene stands out as an exceptional supporting matrix for hybridization with perovskites due to its electron-rich characteristics, high electrical conductivity (15,000 $cm^2/V{\cdot}s$ at room temperature), and large surface area (2,600 m^2/g).[12] Li et al. synthesized a nanohybrid by integrating $Ca_2Nb_3O_{10}$ perovskite nanosheets with graphene, significantly enhancing photocatalytic activity due to efficient charge transfer and improved visible light absorption.[7] Similarly, Xian et al. reported that anchoring $CaTiO_3$ on graphene improved photocatalytic performance in methyl orange degradation.[13] Despite these advancements, the interfacial effects of layered perovskite-graphene composites in photocatalysis remain largely unexplored. Moreover, while perovskite-graphene nanohybrids are typically synthesised via hydrothermal methods, eliminating the need for high temperatures and prolonged reaction times. However, both perovskite nanosheets and graphene possess negative zeta potentials in water, which hinders their effective dispersion.[14][15]

In this work, we initially introduce a straightforward synthetic strategy to anchor perovskite nanosheets onto rGO, followed by an attempt to elucidate the advantageous interfacial effects during photocatalysis. We employ poly diallyl dimethylammonium chloride (PDDA), a UV light-sensitive mediator, on the rGO surface, which induces a

change in the zeta potential from -34.1mV (anionic) of rGO to 41.5 mV (cationic) at approximately pH 7. We found that the nanohybrids can be assembled effortlessly at room temperature within a brief reaction time of 10 minutes. This approach represents an efficient means of synthesising perovskite nanosheets and graphene nanocomposites under room temperature with reduced synthesis time (comparing with tradition hydrothermal approach for 48 hr under reflux), thereby addressing a significant gap in existing synthesis methodologies. Furthermore, through meticulous characterization using XRD via Simple Rietveld refinement, XPS, and XAS techniques with a synchrotron light source, as well as DFT calculations, we reveal a significant effect on bandgap reduction via lattice contraction and octahedra tilting in the layered perovskite. This effect is induced by increasing the charge density of lanthanide as A-site cations, even in the absence of rGO. Notably, the accumulated charge and the structural distortion at the rGO/perovskite interface could further amplify the distortion in octahedra. This accounts for the more subtle effect on bandgap reduction via the A-site cations. Our combination of experimental and theoretical studies provides a comprehensive understanding of charge dynamics at the interface of these layered composites. The findings of this study are particularly significant for advancing the field of layered perovskite oxide and graphene-analogous materials composites in photocatalysis.

3.3 Results and discussion

3.3.1 Material characterisation

Figure 3.1 illustrates the schematic representation of the fabrication process for the rGO/perovskite nanocomposite. To effectively anchor Dion-Jacobson layered perovskite onto rGO with a high surface area, we employed a two-step exfoliation strategy involving protonation and intercalation.

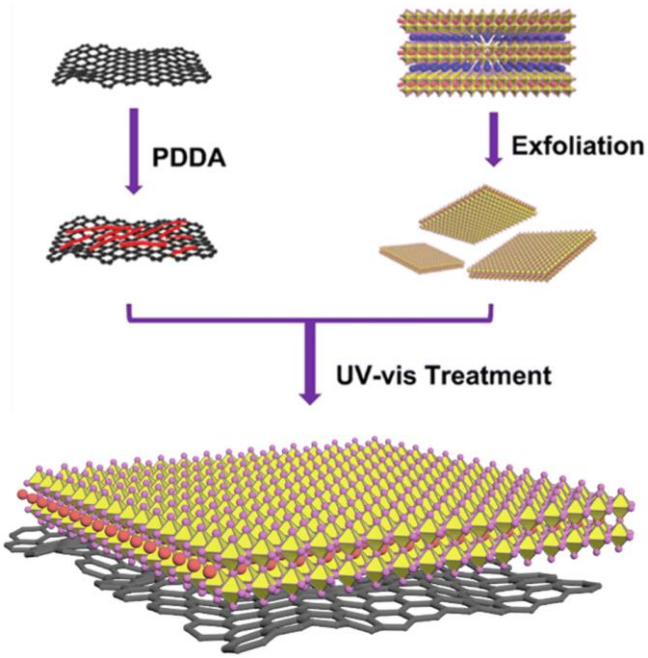

Figure 3.1: The overall synthetic approach towards nanohybrids of rGO and perovskite nanosheet.

We selected $RbLnNb_2O_7$ (Ln = La, Pr, and Nd) as the perovskite precursors, as confirmed by their XRD patterns in Figure 3.2. Additionally, we explored other lanthanide elements such as Ce, Pm, Sm, and Eu for the A-site. However, their tolerance factor values fell outside the optimal range of 0.925–0.955, preventing the formation of the desired layered structure. $RbLaNb_2O_7$ crystallizes in an orthorhombic structure with the *Imma* space group (ICSD = 75456; a = 5.4941 Å, b = 21.9901 Å, c = 5.4925 Å), while $RbPrNb_2O_7$ (ICSD = 238794; a = 5.4533 Å, b = 5.4503 Å, c = 21.9932 Å) and $RbNdNb_2O_7$ (ICSD =

258765; a = 5.4422 Å, b = 5.4297 Å, c = 21.9632 Å) adopt an orthorhombic structure with the *I2cm* space group.

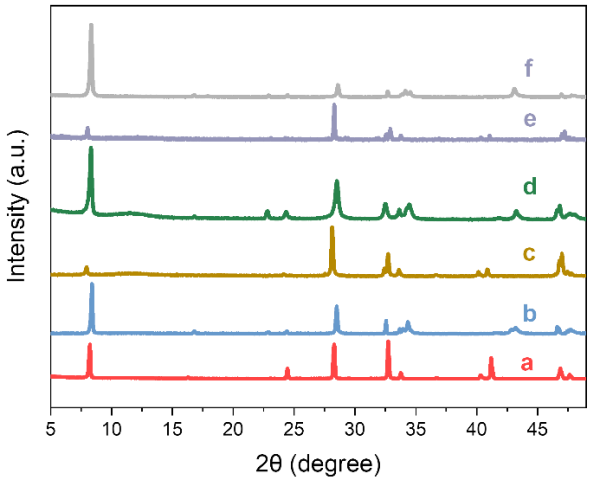

Figure 3.2: Powder XRD pattern of (a) $RbLaNb_2O_7$; (b) $HLaNb_2O_7$; (c) $RbPrNb_2O_7$; (d) $HPrNb_2O_7$; (e) $RbNdNb_2O_7$; (f) $HNdNb_2O_7$.

As shown in Figure 3.3, the protonation of $RbLnNb_2O_7$ leads to the formation of $HLnNb_2O_7$, causing the (001) diffraction peak to shift from 2θ = ~8.0° to 2θ = ~8.4°. This shift is attributed to the reduced interlayer distance, as H^+ has a smaller ionic radius compared to Rb^+.

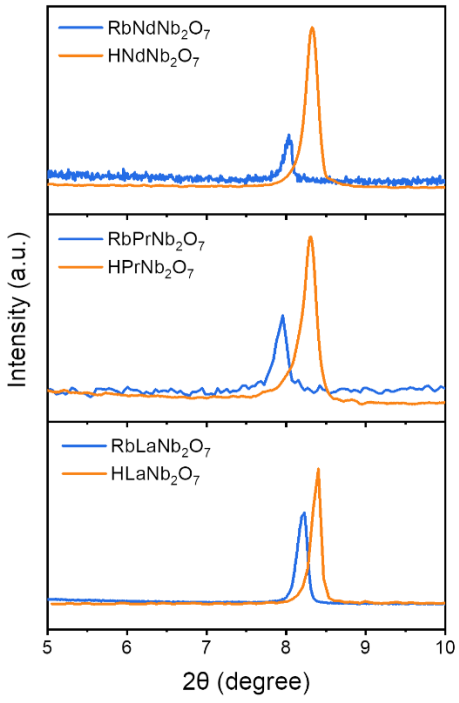

Figure 3.3: Diffraction peak (001) in XRD patterns of $RbLnNb_2O_7$ and $HLnNb_2O_7$. The blue peaks at 2θ = ~8.0° represent peak (001) of $RbLnNb_2O_7$ (Ln = La, Pr, Nd), and orange peaks at 2θ = ~8.4° represent peak (001) of $HLnNb_2O_7$. Thus, the (001) peak position can indicate the interlayer space of layered perovskite.

The XRD patterns also reveal substantial structural changes following protonation, indicating a transition to tetragonal symmetry with the *P4/mmm* space group. Detailed Rietveld refinement data are provided in Figure 3.4 a, b and c and Table 3.1, 3.2 and 3.3.

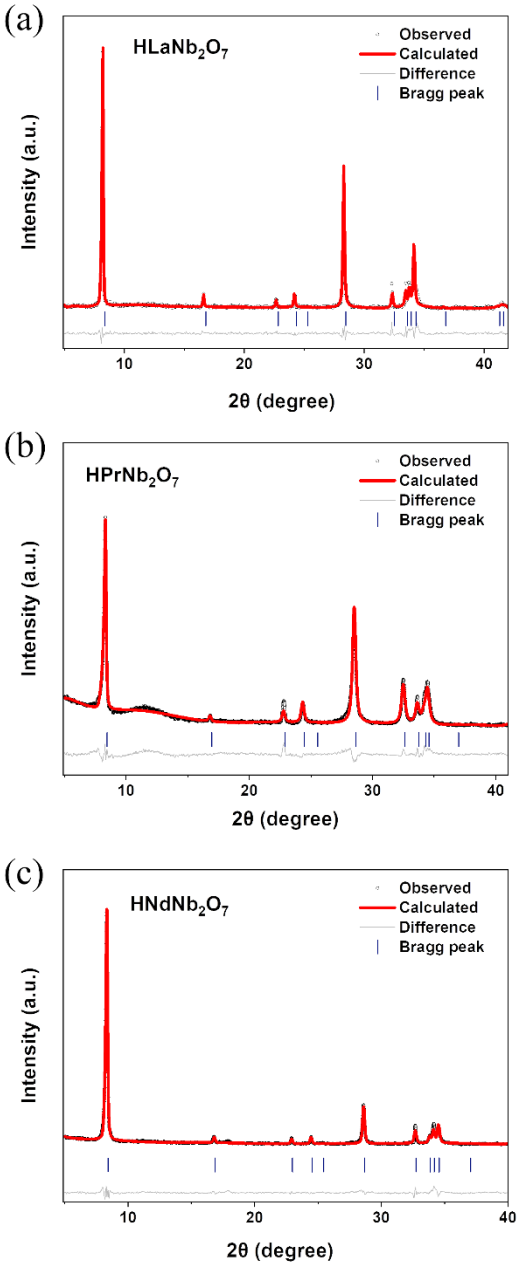

Figure 3.4: (a) Simple Rietveld refinement patterns of $HLaNb_2O_7$ with final reliability factor R*wp* = 14.69%, lattice parameters of *a* = 3.8918 *Å*, *c* = 10.5558 *Å*; (b) Simple Rietveld refinement patterns of $HPrNb_2O_7$ with final reliability factor R*wp* = 8.59%, lattice parameters of *a* = 3.8783 *Å*, *c* = 10.4490 *Å*; (c) Simple Rietveld refinement patterns of $HNdNb_2O_7$ final reliability factor R*wp* = 4.69%, lattice parameters of *a* = 3.8654 *Å*, *c* = 10.4848 *Å*.

Table 3.1: Refined structural parameters for XRD data of $HLaNb_2O_7$ layered perovskite.

Atom	Occupancy	x	y	z	$U_{iso}/Å^2$
H	1	0	0	0.5	0
La	1	0.5	0.5	0	0.001
Nb	1	0	0	0.2010	0.001
O	1	0	0.5	0.2266	0.01
O	1	0	0	0.3970	0.01
O	1	0	0	0	0.01

Table 3.2: Refined structural parameters for XRD data of $HPrNb_2O_7$ layered perovskite.

Atom	Occupancy	x	y	z	$U_{iso}/Å^2$
H	1	0	0	0.5	0
Pr	1	0.5	0.5	0	0.001
Nb	1	0	0	0.21594	0.001
O	1	0	0.5	0.1978	0.01
O	1	0	0	0.3971	0.01
O	1	0	0	0	0.01

Table 3.3: Refined structural parameters for XRD data of $HNdNb_2O_7$ layered perovskite.

Atom	Occupancy	x	y	z	$U_{iso}/Å^2$
H	1	0	0	0.5	0
Nd	1	0.5	0.5	0	0.001
Nb	1	0	0	0.2144	0.001
O	1	0	0.5	0.18976	0.01
O	1	0	0	0.3987	0.01
O	1	0	0	0	0.01

Then, the perovskite nanosheets were obtained through exfoliation along the (00*l*) planes using TBAOH solution. The XRD patterns of the resulting nanosheets are presented in Figure 3.5a, b and c. The exfoliated samples exhibit a significantly weakened (001) diffraction peak and a noticeable shift to lower angles, attributed to the intercalation of TBA^+ ions, which compensate for the negatively charged nanosheets. Furthermore, the (002) peaks at 16.84° for $HLaNb_2O_7$ (Figure 3.5a), 16.89° for $HPrNb_2O_7$ (Figure 3.5b), and 16.87° for $HNdNb_2O_7$ (Figure 3.5c) disappear after exfoliation. The absence of (00*l*) ($l \geq 2$) diffraction peak indicates the loss of the periodic layered structure of protonated perovskite following the exfoliation with TBAOH.

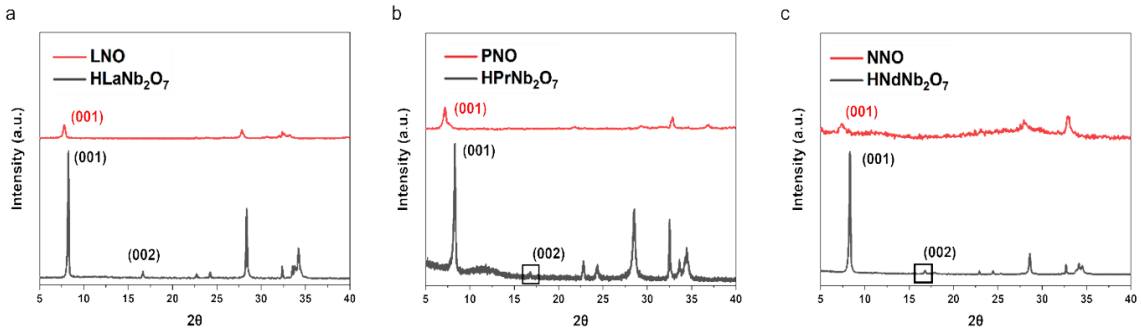

Figure 3.5: XRD pattern of (a) $HLaNb_2O_7$ and LNO; (b) $HPrNb_2O_7$ and PNO; (c) $HNdNb_2O_7$ and NNO.

The XRD patterns of $HLnNb_2O_7$ (black line) show a good material crystallinity, which also demonstrate a significantly reduced intensity of (001) peak with obvious shifts to lower angles. This is because the successful exfoliation reduced the crystallinity of layered perovskites, and TBA^+ intercalation can increase interlayer space and create disorder due to its bulky molecular size.

Further insights into the microstructure and morphology of the exfoliated NNO nanosheets were obtained using high-resolution TEM, HAADF-STEM, and SEM imaging. This observation is further corroborated by the SEM image (Figure 3.6), which

highlights the sheet-like nanostructure of NNO. Additionally, Figure 3.7 presents HAADF-STEM images of a monolayer NNO nanosheet, confirming its single-crystalline nature.

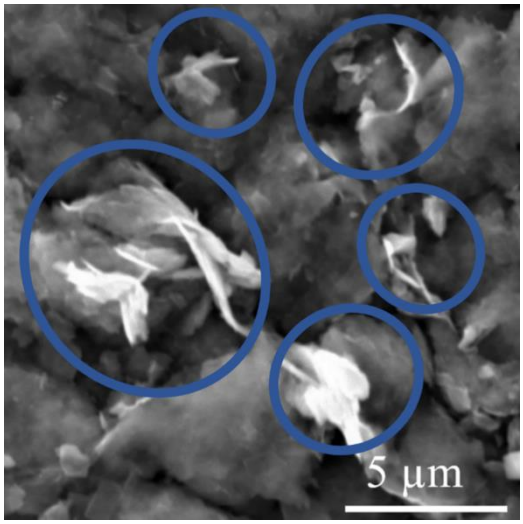

Figure 3.6: SEM image of NNO of the sheet-like structure, which is pointed out by blue circles.

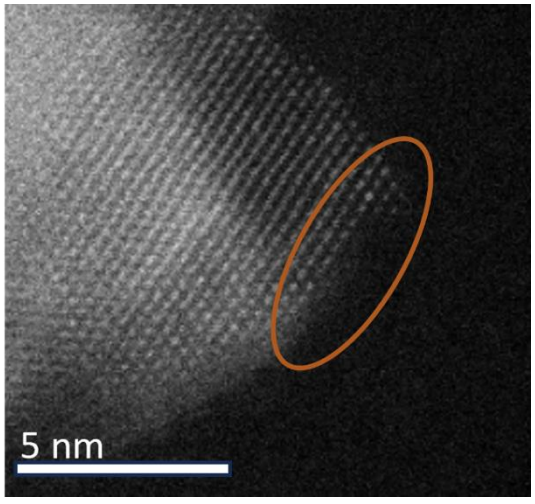

Figure 3.7: HADDF-STEM image of enlarged NNO monolayer showing a very crystalline structure. The damage edge of nanosheets is caused by the exfoliation process, which is pointed out by an orange circle.

The assembly of rGO/perovskite nanosheets is achieved through an electrostatically driven approach. As shown in Figure 3.8a, both perovskite nanosheets and graphene oxide possess negatively charged surfaces, with measured zeta potential values of −41.9 mV and −34.1 mV, respectively, at approximately pH 7. This electrostatic repulsion poses a challenge for direct assembly. To overcome this, graphene oxide is functionalised with PDDA, introducing positive charges that shift its zeta potential to 41.5 mV at pH 7 due to the presence of quaternary ammonium cations. It is crucial to note that perovskite nanosheets tend to restack in acidic environments due to proton interactions, necessitating the assembly process to be conducted at pH 7 or higher. Figure 3.8b illustrates the variation in zeta potential of perovskite nanosheets, rGO/PDDA, and graphene oxide across a pH range of 7 to 11. The perovskite nanosheets maintain a negative charge, while rGO/PDDA remains positively charged throughout this range, indicating that assembly can be effectively carried out under neutral and basic conditions. Following assembly, the composites are subjected to UV irradiation to facilitate the photochemical decomposition of PDDA into NH_4^+ and other soluble by-products, which was monitored using FTIR spectroscopy. As depicted in Figure 3.8c, no detectable FTIR signals were observed for perovskite nanosheets alone. In contrast, the rGO/PDDA/perovskite nanosheet composite exhibited prominent absorption peaks in the range of 1200 to 1300 cm^{-1}, corresponding to C–N stretching vibrations. However, after UV exposure, these peaks disappear, confirming the successful removal of PDDA and the formation of rGO/perovskite nanosheets in solution. A comparison of the self-assembly approach versus physical mixing is presented in Figure 3.8d. NNO suspensions remain well-dispersed in water due to their reduced thickness. However, when NNO suspension is mixed with rGO/PDDA, a precipitate rapidly forms within 10 minutes, indicating that NNO nanosheets have successfully anchored onto the rGO surface. Similar results are observed when exfoliated

PNO or LNO suspensions are mixed with rGO/PDDA. In contrast, when NNO is physically mixed with unmodified graphene oxide, no precipitation occurs, demonstrating that perovskite nanosheets cannot directly integrate with graphene at room temperature without prior surface modification.

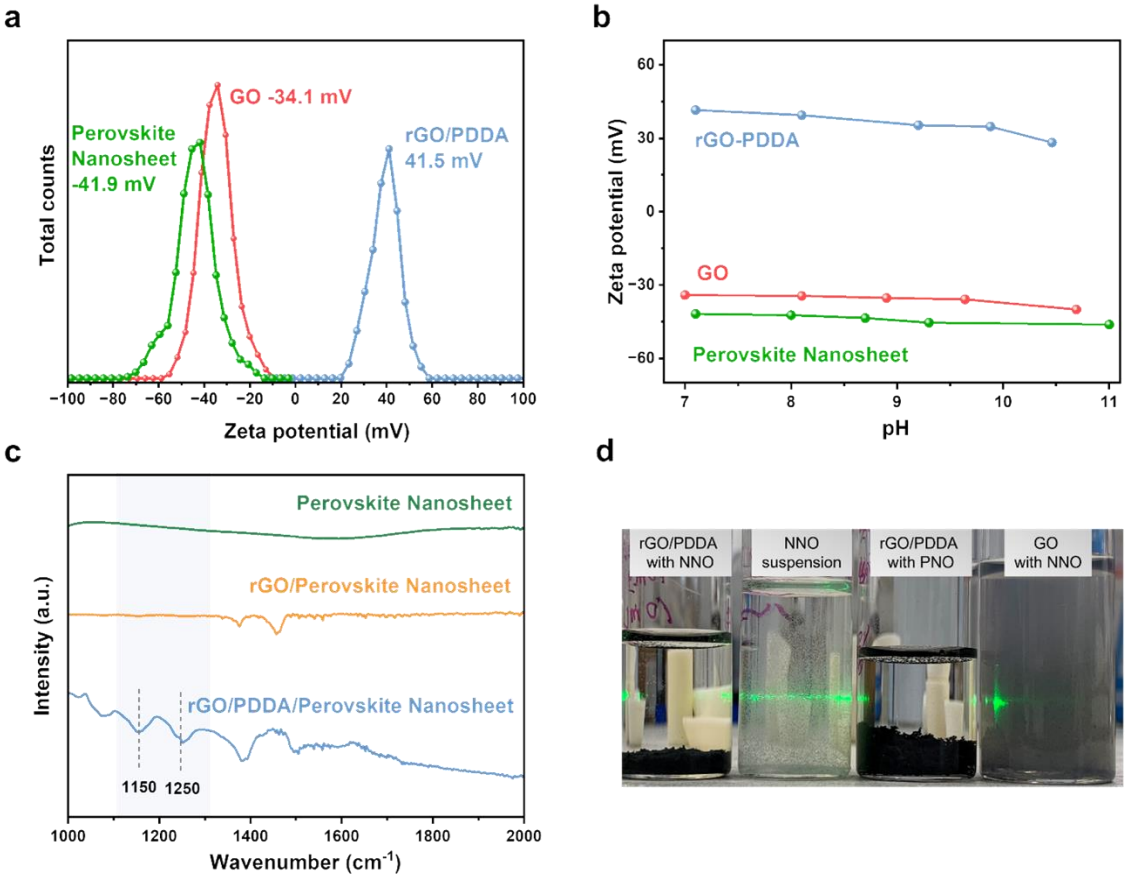

Figure 3.8: (a) Zeta potential of GO, rGO/PDDA and exfoliated perovskite nanosheet dispersed in deionized water at pH 7; (b) zeta potential diagram of GO, rGO/PDDA and exfoliated perovskite nanosheet as a function of pH in aqueous solution; (c) FT-IR spectra of exfoliated perovskite nanosheet, rGO/perovskite nanosheet and rGO/PDDA/perovskite nanosheet; (d) a photograph showing graphene, exfoliated perovskite nanosheet and nanohybrid suspension.

The formation of rGO/NNO nanohybrids is visually depicted in Figure 3.9a, as revealed by HAADF-STEM imaging. The image distinctly delineates the interface between rGO and NNO, with a selected region of the composite exhibiting well-defined crystal lattice fringes attributed to NNO. However, due to its ultrathin nature, the rGO region lacks discernible crystal lattice fringes. Notably, the interplanar spacing of approximately 0.388 nm (highlighted by the yellow arrow) corresponds to the (100) crystal plane of $HNdNb_2O_7$, strongly suggesting that the perovskite nanosheets are anchored onto the rGO surface via c-axis stacking.

Similarly, Figure 3.9d demonstrates that PNO is effectively anchored on the rGO surface, exhibiting a well-defined interface between the PNO and rGO regions. The rGO region retains its characteristic wrinkled 2D nanosheet morphology. In contrast, the PNO region displays distinct lattice fringes with an interplanar spacing of approximately 0.387 nm (marked by yellow arrows), corresponding to the (100) crystal plane of $HPrNb_2O_7$. To further analyse elemental distribution, a line scan was performed along the white arrow in Figure 3.9d, with the resulting profile shown in Figure 3.9e. In the rGO region, carbon signals dominate, while oxygen signals are relatively low. Conversely, in the PNO region, oxygen signals are significantly stronger, accompanied by the appearance of praseodymium signals. Although carbon signals decrease within this region, they do not completely vanish due to the presence of the carbon film coating on the copper grid. Further morphological characterisation is presented in Figure 3.9b, where the SEM image of rGO/NNO reveals its sheet-like structure. The corresponding energy dispersive EDX analysis, shown in Figure 3.9c, confirms the presence of carbon, oxygen, neodymium, and niobium within the nanohybrid. Additionally, EDX elemental mapping provides a visual representation of the homogeneous distribution of these elements across the rGO/NNO composite, further validating the successful integration of rGO with NNO.

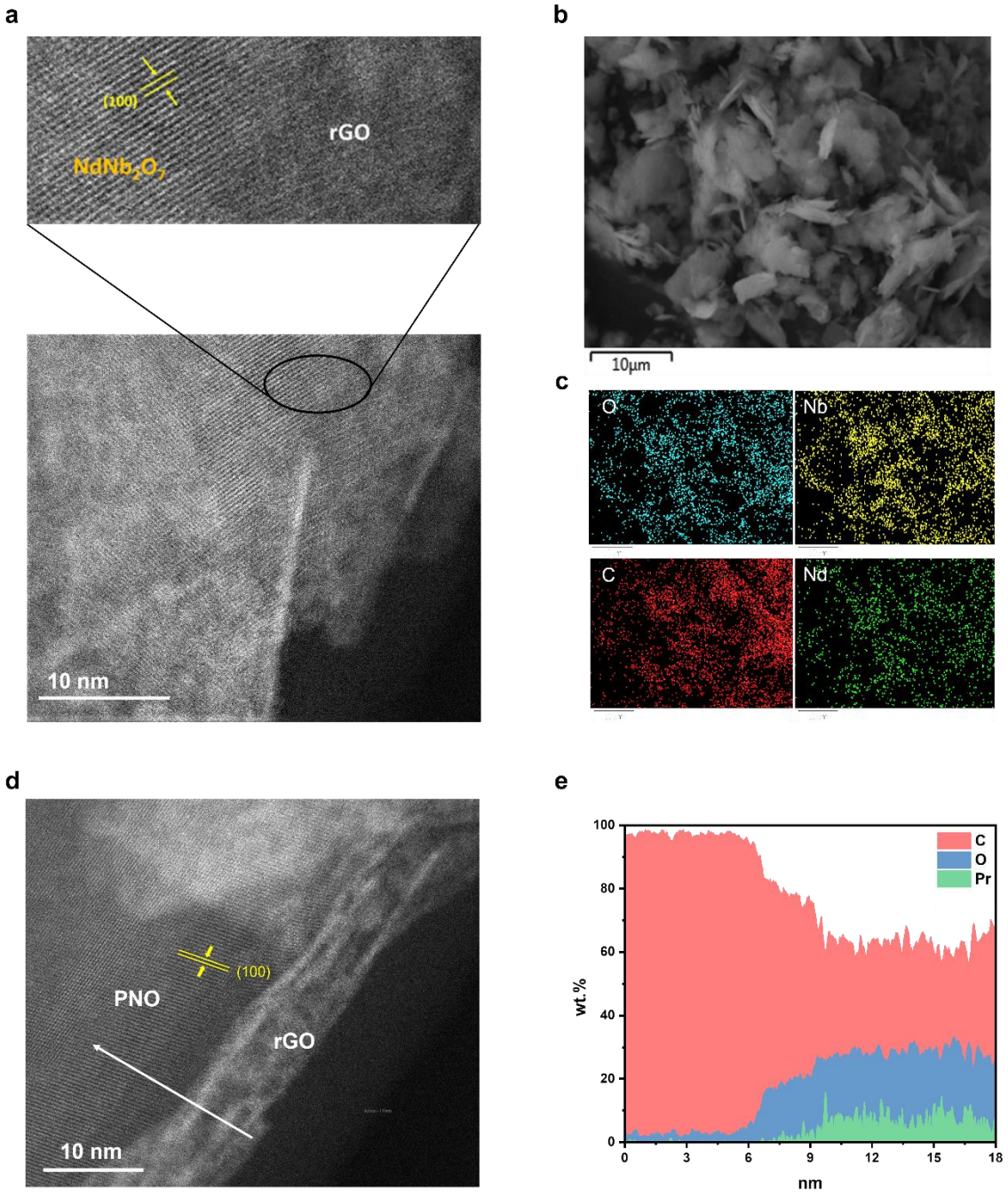

Figure 3.9: (a) HAADF-STEM images of rGO/NNO nanohybrid; (b) SEM images of rGO/NNO and the corresponding (c) EDX mapping of C, O, Nb and Nd elements; (d) HAADF-STEM images of rGO/PNO nanohybrid; (e) corresponding line profile in the white arrow range with C, O and Pr element signals.

The XPS survey spectra presented in Figure 3.10 confirm the presence of characteristic binding energy peaks corresponding to Nb 3d, Nb 3p, O 1s, and lanthanide elements (La 3d, Pr 3d, and Nd 3d). This observation verifies that the perovskite nanosheets maintain structural stability upon integration with rGO, without undergoing significant decomposition.

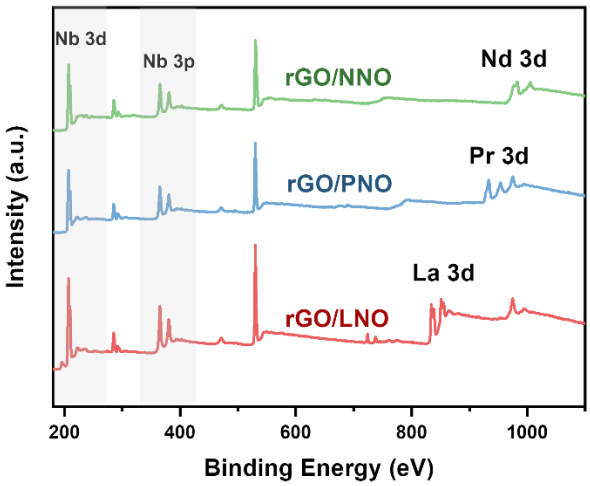

Figure 3.10: Overall XPS spectra of rGO/LNO, rGO/PNO and rGO/NNO

Additionally, XRD analysis (Figure 3.11) further supports the successful formation of rGO/LnNO nanohybrids, as no secondary phases or impurities are detected. The diffraction peaks around 26°, marked with a star, correspond to rGO, highlighting its incorporation into the hybrid structure.

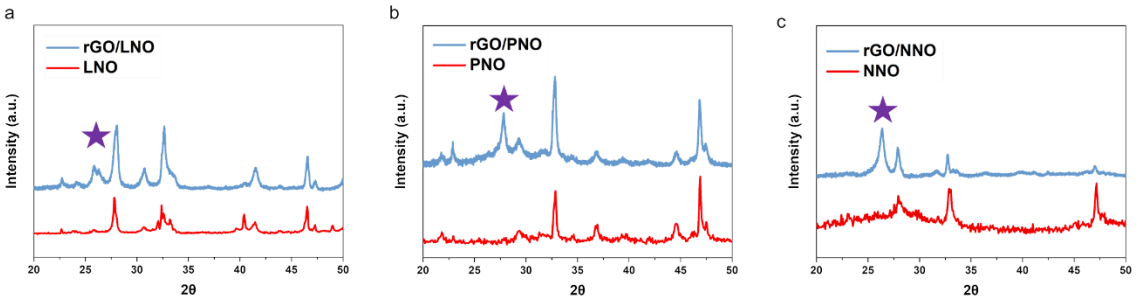

Figure 3.11: XRD patterns of (a) LNO and rGO/LNO; (b) PNO and rGO/PNO; (c) NNO and rGO/NNO.

To gain deeper insight into the structural properties of these composites, EXAFS analysis was performed. Figure 3.12 displays the Fourier-transformed EXAFS spectra of the Nb K-edge for rGO/LNO and rGO/NNO. The observed peaks at approximately 1.5 Å and 3.2 Å can be assigned to Nb–O and Nb–Nb scattering pathways, respectively. As summarised in Table 3.4, the average Nb–O coordination numbers for rGO/LNO, rGO/PNO, and rGO/NNO are determined to be 5.97, 5.98, and 5.77, respectively, within the margin of experimental uncertainty. These results confirm that the NbO_6 octahedral framework is largely preserved, albeit with minor structural distortions.

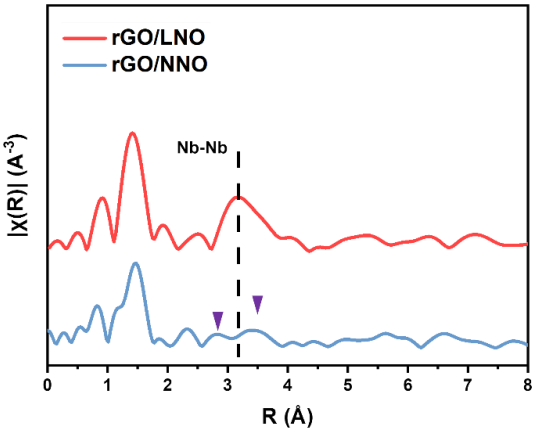

Figure 3.12: Fourier transformed EXAFS spectra for Nb K-edge of rGO/LNO and rGO/NNO.

Table 3.4: Structural parameters of the rGO/perovskite nanosheets extracted from the EXAFS fitting. CN is the coordination number; R(*Å*) is the average bond length of Nb-O; σ^2 is Debye-Waller factor. (S_0^2=0.61)

Sample	Scattering pair	CN	R(*Å*)	σ^2 ($10^{-3}Å^2$)	R factor
rGO/LNO	Nb-O	5.97 ± 0.37	2.05 ±0.006	3.0	1.46%
rGO/PNO	Nb-O	5.98 ± 0.70	2.04 ± 0.008	5.7	1.25%
rGO/NNO	Nb-O	5.77 ± 0.41	2.02 ± 0.006	2.3	2.90%

3.3.2 Photocatalytic performance

The photocatalytic performance of the synthesized samples was assessed by monitoring hydrogen evolution in a methanol solution under light irradiation. As shown in Figure 3.13, the crystalline layered perovskite $RbLnNb_2O_7$ exhibits minimal catalytic activity. Previous studies by Wakayama et al. have highlighted the challenges in enhancing the activity of $Rb_2NdNb_2O_6N$, even when loaded with 0.5 wt% Pt as a co-catalyst, which only resulted in a modest HER of 0.4 μmol/gh under a 300 W xenon lamp ($\lambda > 400$ nm).[1] The primary limitation is the inherently low surface area of these bulk crystalline materials, leading to a scarcity of active sites and, consequently, poor photocatalytic activity.

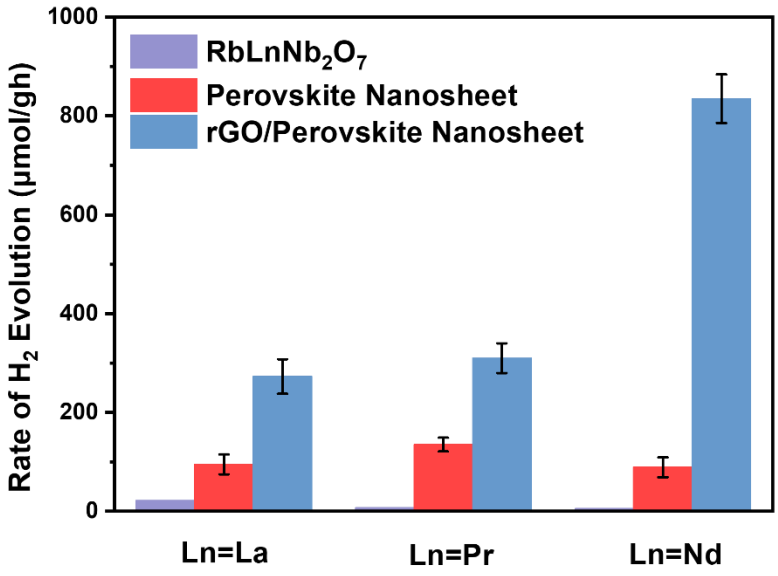

Figure 3.13: Photocatalytic hydrogen evolution rate over layered perovskite $RbLnNb_2O_7$, perovskite nanosheets and rGO/perovskite nanosheets.

However, following exfoliation, perovskite nanosheets exhibit a marked improvement in photocatalytic hydrogen evolution, primarily due to the enlarged surface area. Furthermore, the integration of rGO into the nanosheets further amplifies their photocatalytic activity (Figure 3.13). Notably, all rGO-based nanohybrids maintain

excellent stability over a three-hour reaction period, with no significant decline in HER (Figure 3.14). To rule out any non-photocatalytic hydrogen generation, control experiments were conducted in the absence of either light or catalyst, and no detectable hydrogen production was observed under these conditions.

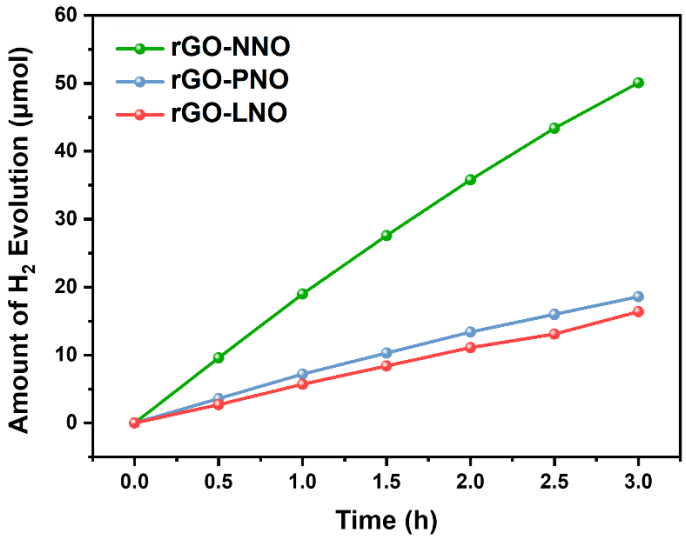

Figure 3.14: Photocatalytic H_2 evolution reaction in 3 hours over different nanocomposites.

To further investigate the role of TBAOH and PDDA, their effects on the photocatalytic activity of layered perovskite $RbLnNb_2O_7$ (Ln = La, Pr, and Nd) were examined. The results revealed that neither TBAOH nor PDDA contributed to any enhancement in catalytic performance. Additionally, a mechanical mixture of NNO and graphene oxide was tested, and no measurable improvement in HER was observed within experimental error (Figure 3.15). This suggests that graphene oxide and NNO do not establish a strong interfacial coupling, and the presence of graphene oxide likely obstructs or scatters incident light, further limiting its contribution to photocatalysis. This observation aligns with previous reports in which perovskite nanosheets were integrated with SiO_2 and rGO.[5][7]

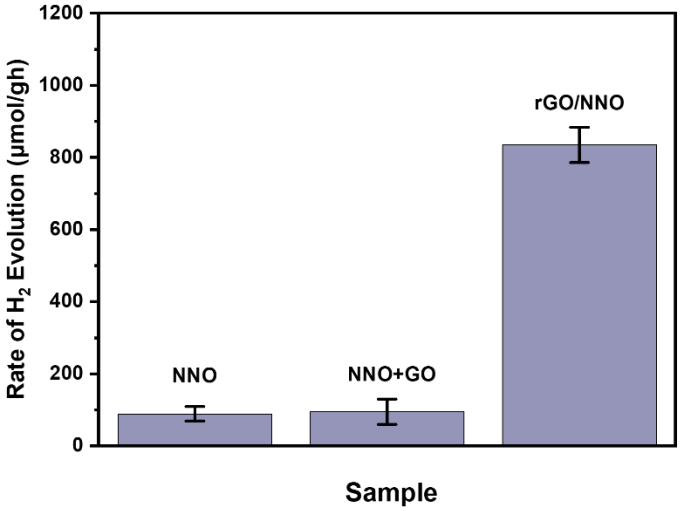

Figure 3.15: The HER of NNO, physically mixing of NNO and graphene oxide, electrostatic assembly NNO with rGO.

Interestingly, the enhancement in photocatalytic activity upon rGO incorporation is not solely dictated by the increase in surface area but is strongly dependent on the specific Ln element at the A-site. The rGO/PNO (310 μmol/gh) exhibits a slightly higher hydrogen evolution rate than rGO/LNO (273 μmol/gh), but rGO/NNO gives the highest photocatalytic activity (835 μmol/gh) (Figure 3.13), underscoring the critical influence of A-site cations on photocatalytic efficiency.

3.3.3 Structural distortion

Perovskite oxides have emerged as a versatile platform for tailoring catalytic performance due to their flexible chemical compositions, diverse crystal structures, and tuneable physicochemical properties. In most cases, the photocatalytic activity is intrinsically governed by the B-site cations and B–O bonding.[16][17] Our DFT-D3+U calculations (without SOC corrections) reveal that the total density of states (DOS) and partial density of states (pDOS) for both the valence band and conduction band of perovskite nanosheets near the Fermi level are predominantly influenced by oxygen 2p orbitals (valence band) and niobium 4d orbitals at the B site (conduction band) (Figure 3.16).[18]

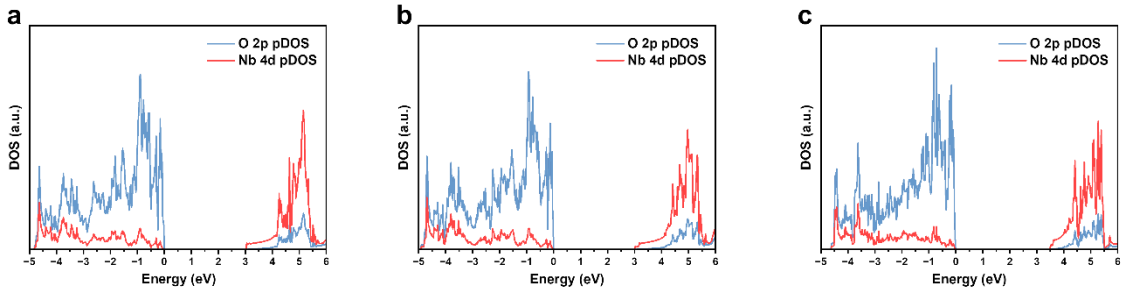

Figure 3.16: Calculated pDOS of (a) LNO (b) PNO and (c) NNO perovskite nanosheet by non-SOC DFT-D3+U method (4.0 eV Hubbard U Correction on Nb), and the calculated PNO bandgap (2.96 eV) is lower than that of LNO (3.02 eV), which aligns with our experimental results.

Surprisingly, despite their non-bonding nature, lanthanide (Ln^{3+}) cations at the A-site significantly impact catalytic behaviour. As demonstrated in Figure 3.17, Rietveld refinements of $HLaNb_2O_7$, $HPrNb_2O_7$, and $HNdNb_2O_7$ powders (without rGO) reveal a progressive lattice contraction and octahedral tilting, characterised by a decreasing O–Nb–O bond angle from its ideal 180°. This trend aligns with prior experimental and theoretical studies on Ln-containing perovskites, where the increasing charge density (+3 oxidation state/cation radius) of Ln^{3+} at the A-site induces Nb–O octahedral distortions

via electrostatic interactions, rather than direct involvement of their contracted f-electrons in the band structure.[19][20][21]

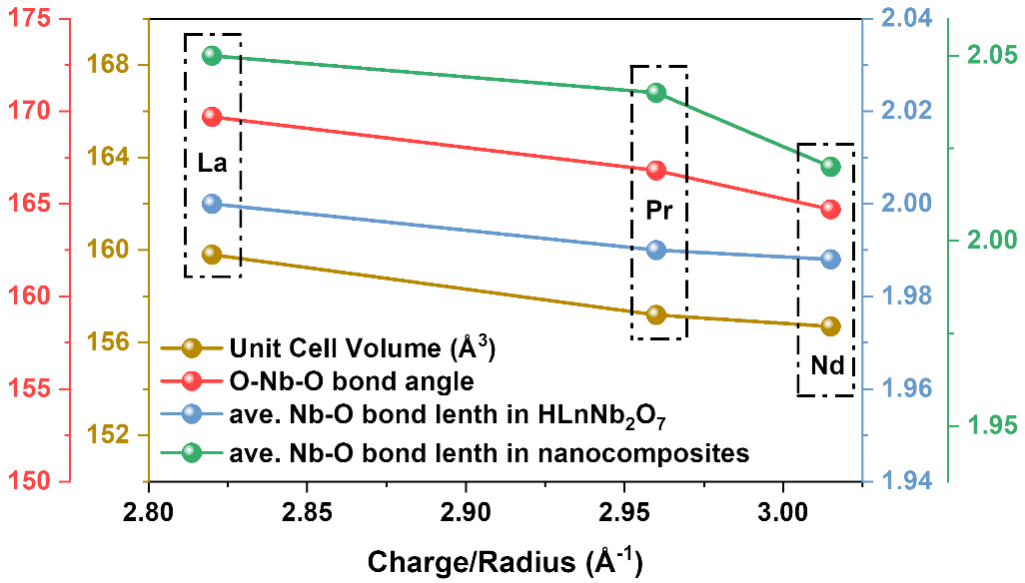

Figure 3.17: Average unit cell volume, O–Nb–O bond angle and Nb–O bond length of $HLaNb_2O_7$, $HPrNb_2O_7$, $HNdNb_2O_7$ and average Nb–O bond length of rGO/LNO, rGO/PNO, rGO/NNO against Ln^{3+} charge density at A site.

Both lattice contraction and octahedral tilting reduce the Nb–O–Nb bond angles, leading to bandgap narrowing, which enhances charge separation in photocatalysis. The measured bandgaps (Figure 3.18) corroborate this structural effect.

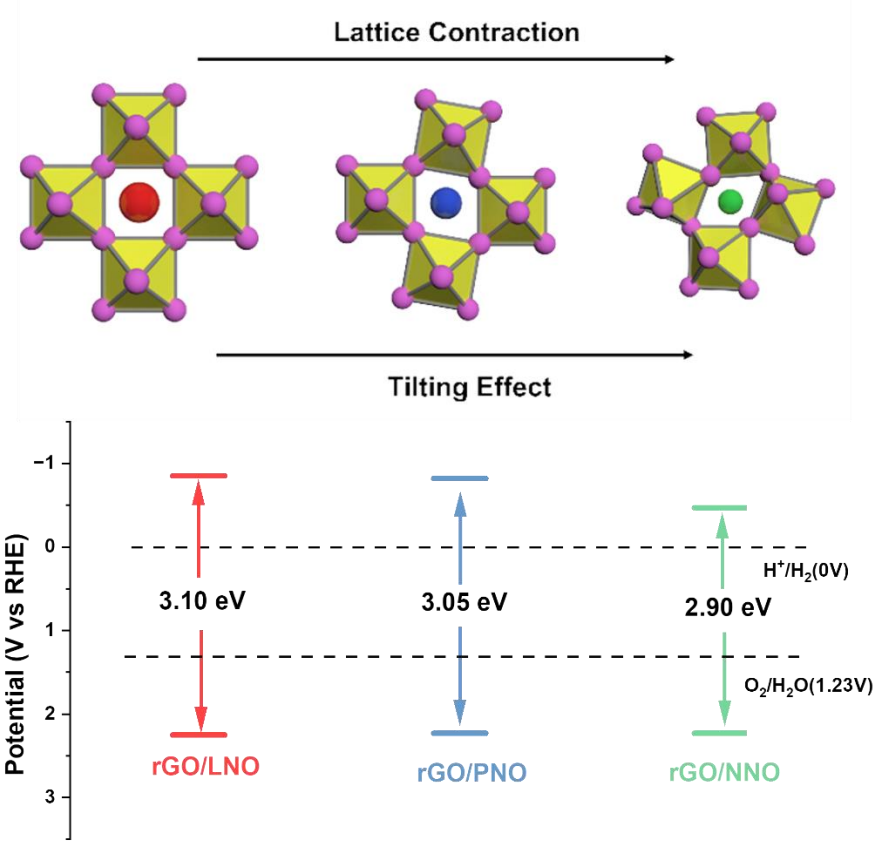

Figure 3.18: Band alignments of LNO, PNO, NNO with rGO derived from UV-vis and XPS measurements.

It is postulated that this reduction in Nb–O–Nb bond angle, caused by lattice distortions, stabilises the conduction band minimum, primarily associated with t_2g antibonding orbitals (Figure 3.19a), resulting in a lower excitation energy (Figure 3.19b and related references). However, the extent of structural change due to the A site prior to exfoliation and without rGO inclusion is relatively minimal.

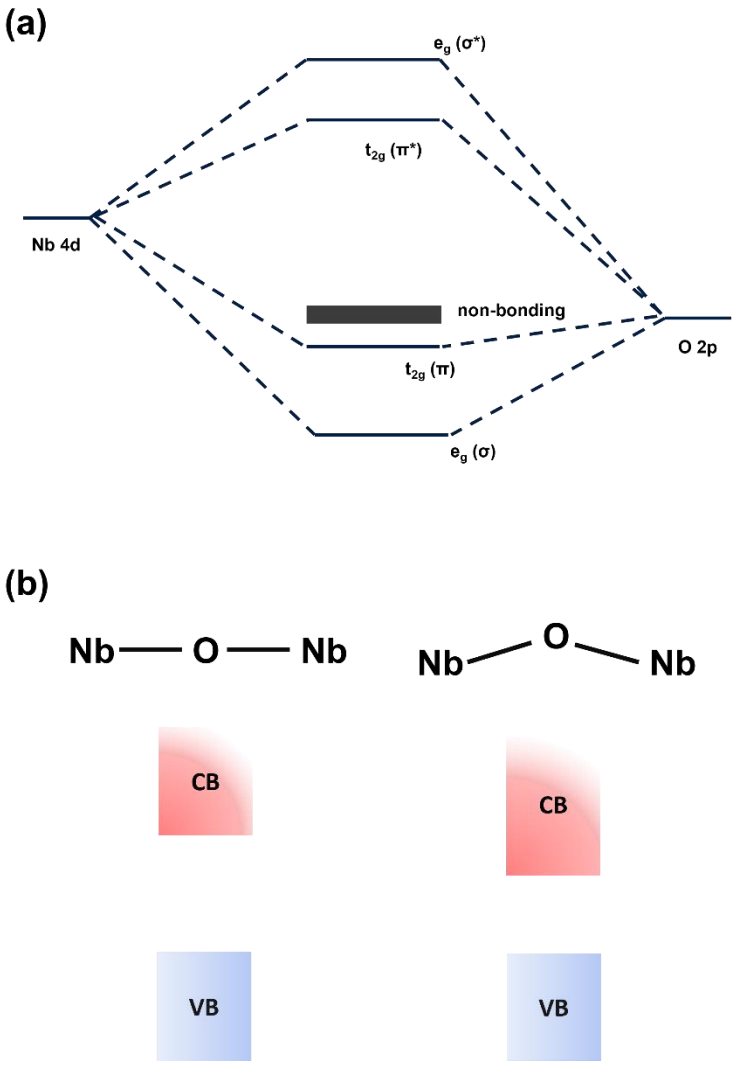

Figure 3.19: (a) Molecular orbital of NbO_6 in perovskite, which shows that O 2p non-bonding orbitals are VB maximum and Nb π antibonding represents CB minimum. (b) When Nb-O-Nb bond angle reduces, the bandgap shrinks because t_2g (π^*) is stabilized.[17]

Interestingly, as depicted in Figure 3.18, the introduction of graphene in the perovskite–graphene hybrid leads to the most pronounced reduction in Nb–O bond overlap, indicating that the graphene interface amplifies the octahedral tilting effect. Previous studies suggest that perovskite structures can undergo tilting due to both tensile and compressive interfacial strain.[22] During cooling to room temperature following UV-vis treatment (Figure 3.1), rGO would distort the perovskite nanosheets because it would expand in different directions.[23] This interfacial strain originates from the substantial difference in thermal expansion coefficients between rGO (-70×10^{-6} K^{-1}) and perovskite (7 to 9×10^{-6} K^{-1}).[24][25] As the A-site cation radius decreases, the perovskite's thermal expansion coefficient increases, further intensifying the interfacial strain effect. This phenomenon is consistent with EXAFS analysis (Figure 3.12), which reveals that rGO/NNO experiences greater structural distortion, as evidenced by the variation in Nb–Nb distances and a reduced Nb–O–Nb bond angle.[26] This would lead to continuous bandgap narrowing. Furthermore, it is hypothesised that rGO, acting as an electron photosensitiser, could inject additional charge density into the Nb–O octahedra at the interface, thereby alternating the O–Nb–O bond angle via electrostatic interactions and further reducing the bandgap. Such precise composite-layer engineering offers an effective strategy for tuning the electron-accepting capabilities of perovskite materials by leveraging A-site cations.

3.3.4 Charge dynamics

Density Functional Theory (DFT) calculations (Figure 3.20a, b and c) reveal a charge depletion on rGO and a corresponding charge accumulation on interfacial oxygen atoms within the layered perovskite structure at the interface. Notably, the charge density in rGO/NNO (Figure 3.20c) is significantly higher than that in rGO/PNO (Figure 3.20b) and rGO/LNO (Figure 3.20a). This suggests that the interfacial oxygen atoms within NbO_6 octahedra, particularly in NNO with its stronger electronegativity, are more efficient at trapping excited electrons from rGO.

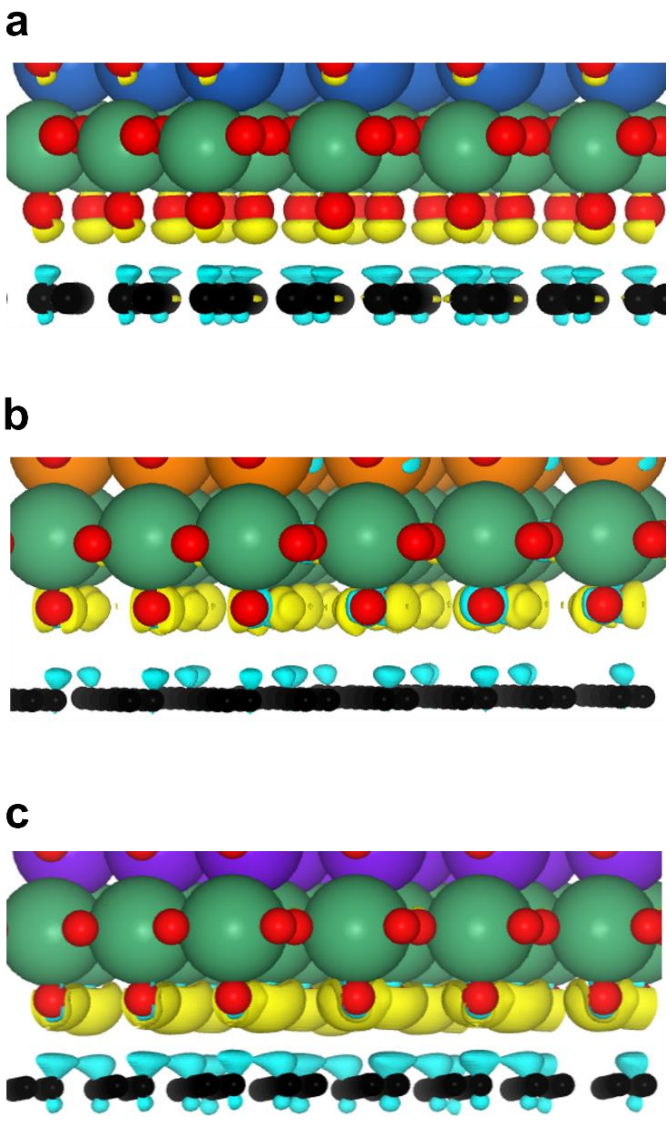

Figure 3.20: Differential charge distribution of modelled (a) rGO/LNO; (b) rGO/PNO; (c) rGO/NNO. The yellow and blue regions represent net electron accumulation and depletion, respectively. (La: blue; Pr: orange; Nd: purple; Nb: green; O: pink; C: black).

Using the Perdew–Burke–Ernzerhof (PBE) exchange–correlation functional within the generalized gradient approximation (GGA) framework, the calculated Bader charge on the interfacial oxygen quantifies the electron-accepting ability of the perovskite nanosheets.[27] The Bader charge analysis for the Ln series (Figure 3.21) reveals a progressive increase in electron transfer from rGO to the perovskites, corresponding to different Ln^{3+} cations at the interface. The electron transfer values are 0.56 |e| for rGO/GdNO, 0.54 |e| for rGO/NNO, 0.50 |e| for rGO/CeNO, 0.43 |e| for rGO/PNO, and 0.42 |e| for rGO/LNO.

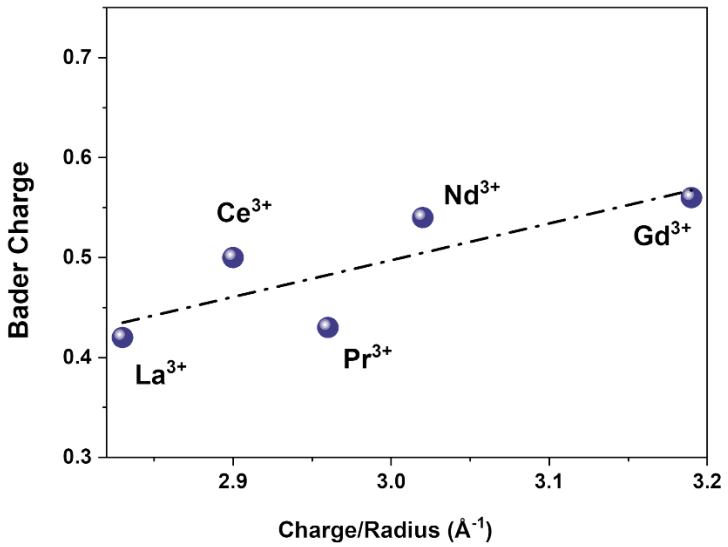

Figure 3.21: Calculated Bader Charge on oxygen atoms for rGO/LnNO in function of charge density of A-site cations.

Importantly, the DFT calculations indicate that the Ln 4f electrons of lanthanides do not contribute to band states, supporting the general consensus that 4f electrons remain highly localized around the Ln^{3+} nuclei and thus do not directly participate in H_2 evolution.

XPS measurements further confirm these findings. Figure 3.22e, f illustrates a negative binding energy shift of 0.29 eV (O 1s) and 0.31 eV (Nb 3d) in rGO/NNO, indicating an increased electron density at these sites. It is noteworthy that rGO/NNO exhibits a much larger shift compared to rGO/PNO (Figure 3.22c, d) and rGO/LNO (Figure 3.22a, b).

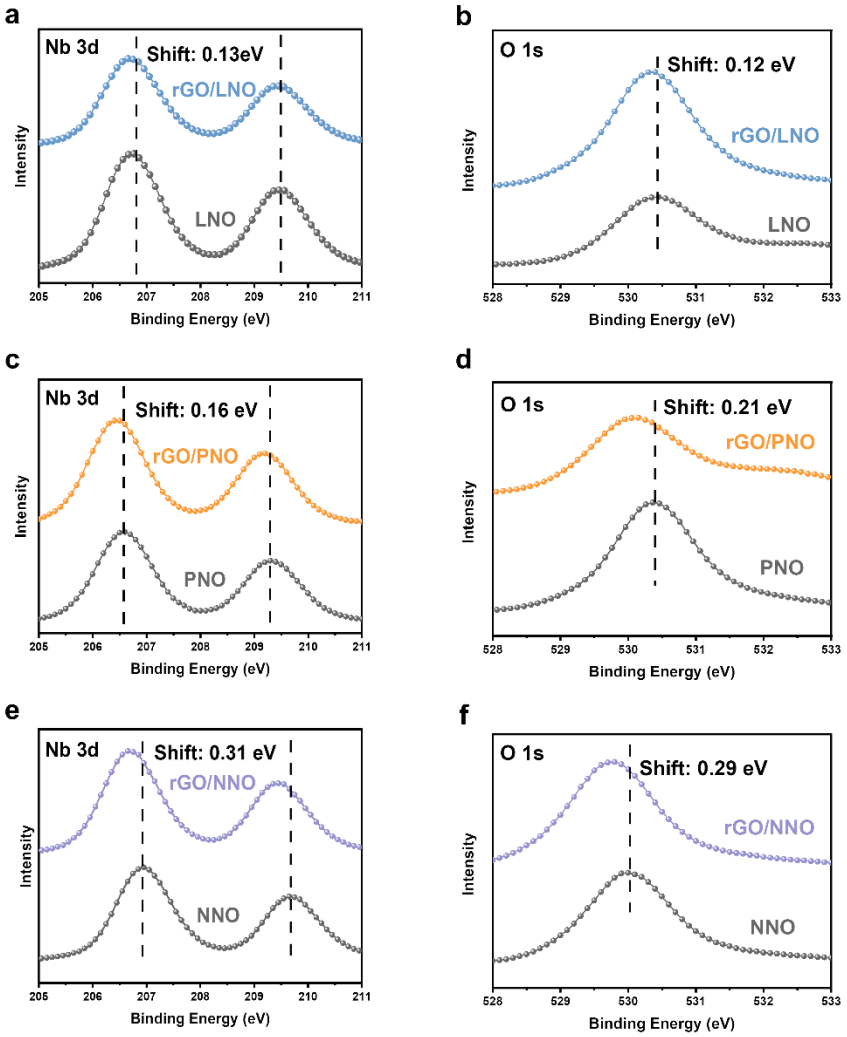

Figure 3.22: Corresponding shift in O 1s XPS spectra for (a) rGO/LNO; (c) rGO/PNO; (e) rGO/NNO; corresponding shift Nb 3d XPS spectra for (b) rGO/LNO; (d) rGO/PNO; (f) rGO/NNO with reference to adventitious C 1s (no shift).

Additionally, the C 1s spectra (Figure 3.23) reveal a more pronounced positive shift at the graphitic C_g–O interface in rGO/NNO (286.3 eV) compared to rGO/LNO (286.0 eV) and rGO/PNO (286.1 eV), reflecting the presence of more h^+ (holes) in this region. This is attributed to the efficient transfer of excited electrons through the C_g–O interface between NNO and rGO.[7] To minimize potential charging effects influencing peak shifts, all XPS spectra were referenced to adventitious C 1s, which is distinct from the C 1s of rGO (Figure 3.23).

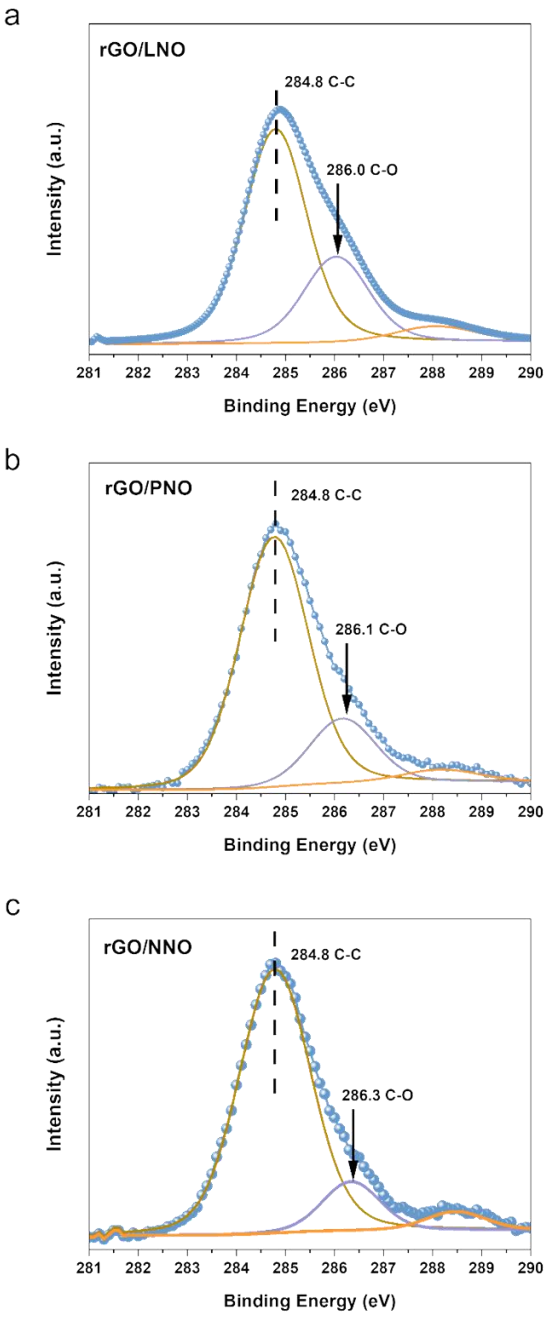

Figure 3.23: C 1s XPS of (a) rGO/LNO; (b) rGO/PNO and (c) rGO/NNO showing no change in adventitious C in C-C (284.8 eV).

However, ~ 286 eV of graphitic C1s region indicates the progressive shift to higher binding energy from rGO/ LNO to rGO/PNO and rGO/NNO due to increasing h^+ (holes) residence.[11][33][34] As excited electrons are transferred through the C_g-O interface between rGO and perovskite nanosheets.

Furthermore, the 3d spectra of lanthanides (La 3d, Pr 3d, and Nd 3d, shown in Figure 3.24) exhibit no detectable shift in their binding energies after incorporation with rGO, maintaining values of 834.5 eV (La 3d), 933.7 eV (Pr 3d), and 982.9 eV (Nd 3d). This confirms that the incorporation of rGO does not affect the electronic states of lanthanides, reinforcing the conclusion that the catalytic enhancement is primarily driven by interfacial charge transfer rather than direct lanthanide involvement.

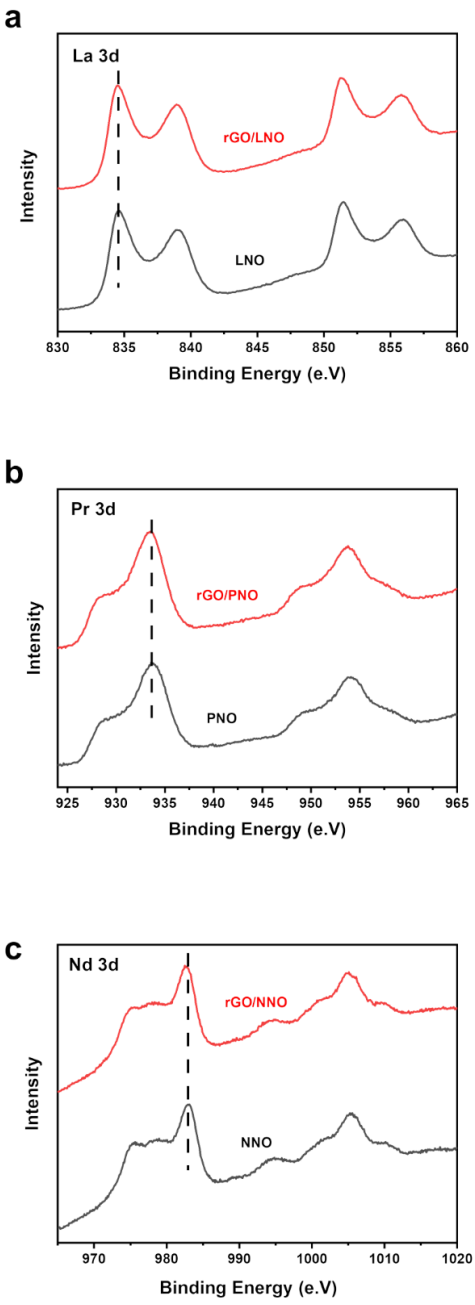

Figure 3.24: (a) La 3d XPS of LNO and rGO/LNO; (b) Pr 3d XPS of PNO and rGO/PNO; (c) Nd 3d XPS of NNO and rGO/NNO.

In LNO and rGO/LNO, the first peak of La 3d is found to be 834.5 eV. In PNO and rGO/PNO, the first peak of Pr 3d is found to be 933.7 eV. In NNO and rGO/NNO, the first peak of Nd 3d is found to be 982.9 eV. All these binding energies correspond to be the 3d of Ln^{3+} giving no barely change after incorporating with rGO.

Figure 3.25 presents the charge carrier dynamics in the nanohybrids upon light activation. TRPL spectroscopy reveals a rapid fluorescence intensity decay, indicating an efficient interfacial electron transfer from rGO to NNO in rGO/NNO. This results in a significantly shorter charge carrier lifetime compared to rGO/LNO and rGO/PNO, suggesting more effective charge separation.

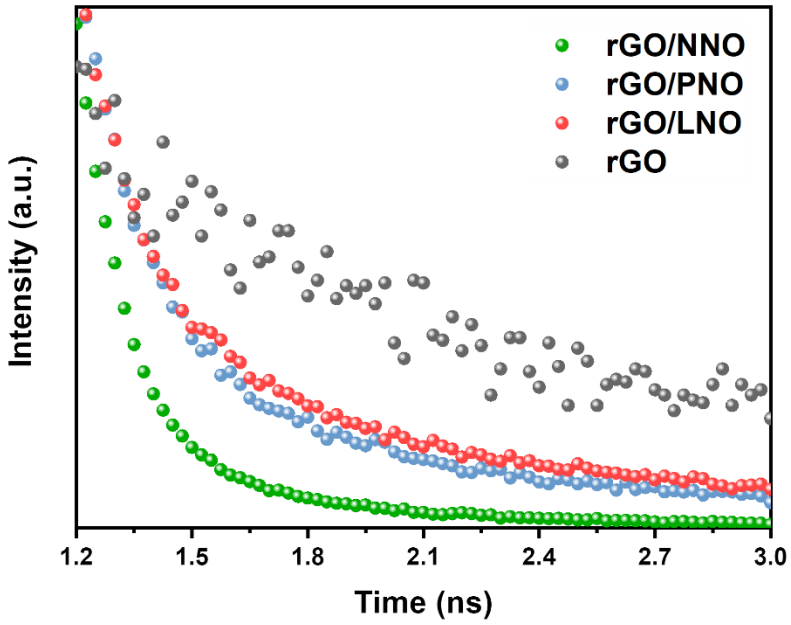

Figure 3.25: TRPL of rGO compared with substantial shorter lifetimes for nanohybrids.

As the electron-accepting ability of perovskite nanosheets increases (reflected in the higher Bader charge of interfacial oxygen atoms), rGO readily donates excited mobile electrons, thereby accelerating charge recombination and reducing exciton lifetime. Among them, NNO, which undergoes the most pronounced structural distortion, exhibits the highest electron-accepting capability. This enables it to capture a greater number of excited electrons from rGO, making it a highly efficient visible-light-driven photocatalyst, further enhancing its photocatalytic activity.[28]

To evaluate photocatalytic performance in the visible-light range, HER activity measurements of rGO/NNO were conducted under different wavelengths in the absence of a sacrificial reagent (Figure 3.26). Even at wavelengths beyond 550 nm and under low light intensity (15.7 mW), H_2 evolution activity was still observed. This result aligns with expectations, confirming that excited mobile electrons are effectively transferred from rGO to NNO in the nanohybrid structure.[7][29]

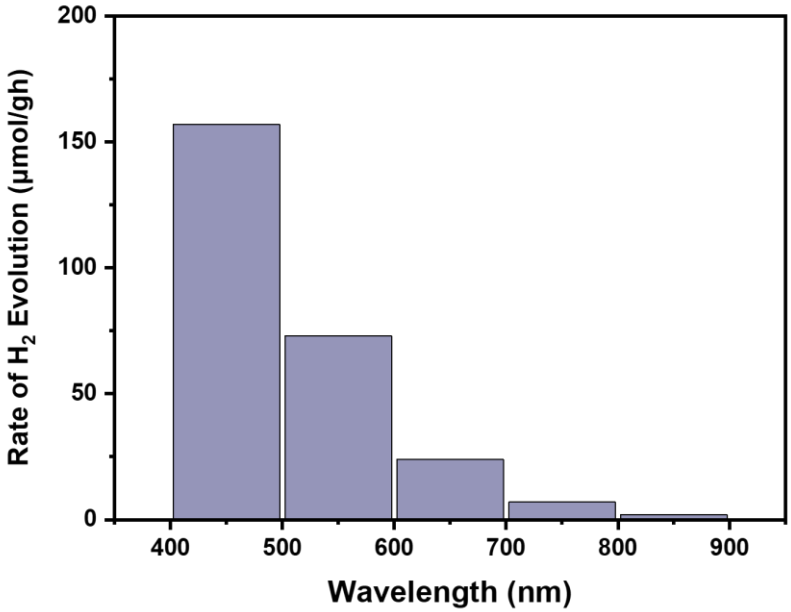

Figure 3.26: HER of rGO/NNO in deionized water under different wavelengths: 400-500 (7.9 mW), 500-600 (14.1 mW), 600-700 (15.7 mW) and 700-800 nm (15.7 mW). From 400 to 800 nm, rGO/NNO shows decent activity for water splitting. In the range from 400 to 500 nm, HER activity still gives 157 μmol/gh even though the light intensity is only set at 7.9 mW. Standard deviation is not provided as the measurements were not repeated.

The charge carrier lifetime was determined via biexponential function fitting of TRPL decay curves,[7][30] and the average lifetime was calculated based on the Equation 2.25. Additionally, SSPL spectra (Figure 3.27) confirm the Burstein–Moss effect in rGO/NNO, as evidenced by a blue shift in the emission peak. This shift results from a notable increase in charge carrier concentration,[9] leading to enhanced Nb–O lattice distortion and bandgap narrowing, influenced by Nd sites, as discussed previously.

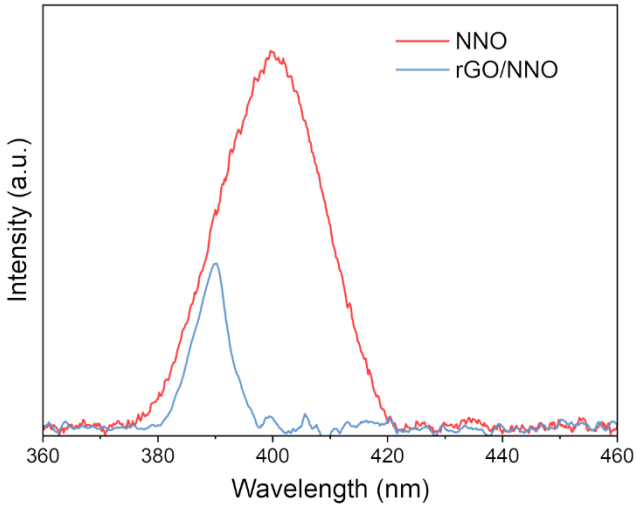

Figure 3.27: Steady-state fluorescence spectra with light excitation at 375nm at room temperature for NNO nanosheet which indicates the absorption maxima at 400nm while the absorption maxima at rGO/NNO shows a clear blue shift to 390nm. This is because all the states near CB are populated by the electrons transferred from rGO, triggering the Burstein-Moss shift in NNO.[9][35]

Furthermore, the observed photocatalytic activity trend correlates strongly with both the inverse exciton lifetime and the Bader charge on interfacial oxygen atoms (Figure 3.28), further substantiating the role of interfacial charge transfer in enhancing catalytic performance.

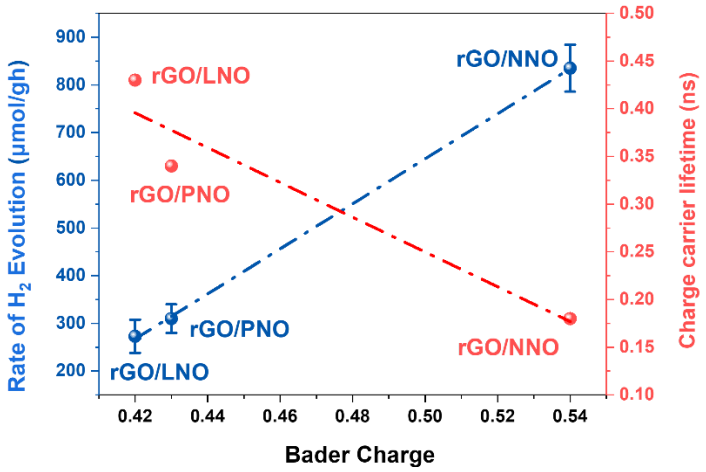

Figure 3.28: Inversed correlation of HER activity with average exciton lifetime of nanohybrids plotted against calculated Bader charge of interface oxygen atoms.

The above characterisations clearly demonstrate the critical role of optimising interfacial interactions between perovskite nanosheets and rGO in facilitating electron transfer. Efficient charge transfer not only enhances the screening effect but also reduces the binding energy of O 1s and Nb 3d, thereby further improving the photocatalytic performance.

In this process, rGO acts as a photosensitiser, supplying excited electrons to perovskite nanosheets and effectively extending their photocatalytic activity from UV-driven to visible-light-driven operation.[7][31][32] This distinct charge dynamic at the interface amplifies the A-site effect, inducing structural distortion in perovskite and providing a new strategy for tuning photocatalytic efficiency.

3.4 Conclusion

In summary, we have successfully integrated Dion–Jacobson perovskite nanosheets with rGO, utilising exfoliation and an electrostatic-driven assembly strategy to achieve a high surface area nanohybrid. These hybrids exhibit enhanced photocatalytic hydrogen evolution, primarily due to efficient interfacial electron transfer. The activity comparison with layered perovskite and other photocatalysts was shown in Table A3.1 (in Appendices) and Table 3.5, respectively.

Catalysts	Light source	Solution	Activity ($\mu molg^{-1}h^{-1}$)	Ref.
rGO/NNO	300W Xe lamp	10% CH_3OH	834.9	This work
Pt/TiO_2	400W Hg lamp	2.17M Na_2CO_3	1893.3	[36]
ZrO_2	400W Hg lamp	Water	72.0	[37]
Pt/ZrO_2	400W Hg lamp	0.94M $NaHCO_3$	120.0	[37]
CdS/WS/graphene	> 420nm	Water	1842.0	[38]
$MoS_2/CuInS_2$	300W Xe lamp	Water	202.0	[39]

Table 3.5: Performance comparison of rGO/NNO with other photocatalysts for H_2 evolution.

By modulating the A-site charge density, we demonstrate that lattice contraction and octahedral tilting at the interface can significantly alter the band structure of perovskite nanosheets. In particular, NNO, with its narrowed bandgap and lower conduction band minimum induced by structural distortion, effectively captures excited electrons from rGO, facilitating efficient charge separation for photocatalysis.

This synergistic interplay between A-site charge density and interfacial photosensitisation provides a powerful approach to tuning the electron-accepting properties of layered perovskites. Our findings establish fundamental design principles for the precise modulation of targeted band structures in perovskite-based photocatalysts.

3.5 Reference

1. H. Wakayama, K. Hibino, K. Fujii, T. Oshima, K. Yanagisawa, Y. Kobayashi, K. Kimoto, M. Yashima and K. Maeda., 2019. Synthesis of a layered niobium oxynitride, $Rb_2NdNb_2O_6N{\cdot}H_2O$, showing visible-light photocatalytic activity for H_2 evolution. *Inorg. Chem,* 58(9), 6161–6166.
2. S. Ida, Y. Okamoto, M. Matsuka, H. Hagiwara and T. Ishihara., 2012. Preparation of tantalum-based oxynitride nanosheets by exfoliation of a layered oxynitride, $CsCa_2Ta_3O_{10-x}N_y$, and their photocatalytic activity. *J. Am. Chem. Soc.,* 134(38), 15773–15782.
3. M. S. Khan, Z. Diao, M. Osada and S. Shen., 2020. Nitrogen doped ultrathin calcium/sodium niobate perovskite nanosheets for photocatalytic water oxidation, *Sol. Energy Mater. Sol. Cells*, 205, 110283.
4. M. Hojamberdiev, M. F. Bekheet, E. Zahedi, H. Wagata, Y. Kamei, K. Yubuta, A. Gurlo, N. Matsushita, K. Domen and K. Teshima., 2016. New Dion–Jacobson phase three-layer perovskite $CsBa_2Ta_3O_{10}$ and its conversion to nitrided $Ba_2Ta_3O_{10}$ nanosheets *via* a nitridation–protonation–intercalation–exfoliation route for water splitting, *Cryst. Growth Des.*, 16(4), 2302–2308.
5. H. Zhou, E. M. Sabio, T. K. Townsend, T. Fan, D. Zhang and F. E. Osterloh., 2010. Assembly of Core–Shell Structures for Photocatalytic Hydrogen Evolution from Aqueous Methanol, *Chem. Mater.,* 22(11), 3362–3368.
6. S. Acharya, S. Martha, P. C. Sahoo and K. Parida., 2015. Glimpses of the modification of perovskite with graphene-analogous materials in photocatalytic applications, *Inorg. Chem. Front.*, 2(9), 807–823.

7. D. Li, H. Zhao, L. Li, B. Mao, M. Chen, H. Shen, W. Shi, D. Jiang and Y. Lei., 2018. Graphene-sensitized perovskite oxide monolayer nanosheets for efficient photocatalytic reaction, *Adv. Funct. Mater.*, 28(52), 1806284.
8. V. Gupta and T. A. Saleh., 2011. Syntheses of carbon nanotube-metal oxides composites; adsorption and photo-degradation, *Carbon Nanotubes: Res. Appl.*, 17, 295–312.
9. M. Shu, Z. Zhang, Z. Dong and J. Xu., 2021. $CsPbBr_3$ perovskite quantum dots anchored on multiwalled carbon nanotube for efficient CO_2 photoreduction, *Carbon*, 182, 454–462.
10. X. Xu, G. Liu, C. Randorn and J. T. Irvine., 2011. g-C_3N_4 coated $SrTiO_3$ as an efficient photocatalyst for H_2 production in aqueous solution under visible light irradiation, *Int. J. Hydrogen Energy*, 36(21), 13501–13507.
11. D. Jiang, T. Wang, Q. Xu, D. Li, S. Meng and M. Chen., 2017. Perovskite oxide ultrathin nanosheets/g-C_3N_4 2D-2D heterojunction photocatalysts with significantly enhanced photocatalytic activity towards the photodegradation of tetracycline, *Appl. Catal., B*, 201, 617–628.
12. M. D. Stoller, S. Park, Y. Zhu, J. An and R. S. Ruoff., 2008. Graphene-based ultracapacitors, *Nano Lett.*, 8(10), 3498–3502.
13. T. Xian, H. Yang and Y. Huo., 2014, Enhanced photocatalytic activity of $CaTiO_3$-graphene nanocomposites for dye degradation, *Phys. Scr.*, 89(11), 115801.
14. Y.-S. Han, I. Park and J.-H. Choy., 2001. Exfoliation of layered perovskite, $KCa_2Nb_3O_{10}$, into colloidal nanosheets by a novel chemical process, *J. Mater. Chem.*, 11(4), 1277–1282.
15. A. H. Mevold, W.-W. Hsu, A. Hardiansyah, L.-Y. Huang, M.-C. Yang, T.-Y. Liu, T.-Y. Chan, K.-S. Wang, Y.-A. Su and R.-J. Jeng., 2015. Fabrication of gold

nanoparticles/graphene-PDDA nanohybrids for bio-detection by SERS nanotechnology, *Nanoscale Res. Lett.*, 10, 1–7.

16. L. Lu, S. Ni, G. Liu and X. Xu, Structural dependence of photocatalytic hydrogen production over La/Cr co-doped perovskite compound $ATiO_3$ (A = Ca, Sr and Ba), *Int. J. Hydrogen Energy*, 2017, 42(37), 23539–23547.
17. A. Kudo, H. Kato and S. Nakagawa., 2000. Water splitting into H_2 and O_2 on new $Sr_2M_2O_7$ (M = Nb and Ta) photocatalysts with layered perovskite structures: factors affecting the photocatalytic activity, *J. Phys. Chem. B*, 27(3), 571–575.
18. S. Di Tommaso, F. Giannici, A. Mossuto Marculescu, A. Martorana, C. Adamo and F. Labat., 2014. Toward tailorable surfaces: a combined theoretical and experimental study of lanthanum niobate layered perovskites, *J. Chem. Phys.*, 141, 024704.
19. R. Prasanna, A. Gold-Parker, T. Leijtens, B. Conings, A. Babayigit, H. G. Boyen, M. F. Toney and M. D. McGehee., 2017. Band Gap Tuning *via* Lattice Contraction and Octahedral Tilting in Perovskite Materials for Photovoltaics, *J. Am. Chem. Soc.*, 139(32), 11117–11124.
20. A. G. Bispo-Jr, A. J. de Morais, C. M. Calado, I. O. Mazali and F. A. Sigoli., 2022. Lanthanide-doped luminescent perovskites: a review of synthesis, properties, and applications, *J. Lumin.*, 252, 119406.
21. T. Hasegawa, T. Ueda, Y. Asakura and S. Yin., 2022. Cerium (III) Niobate Layered Perovskites: Abnormal Optical Absorption Modulations by Tuning of B-Site Composition and Perovskite Layer Charge Control, *Inorg. Chem.*, 61(50), 20636–20646.
22. H. S. Kim and N. G. Park., 2020. Importance of tailoring lattice strain in halide perovskite crystals, *NPG Asia Mater.*, 12(1), 78.

23. W. Pan, J. Xiao, J. Zhu, C. Yu, G. Zhang, Z. Ni, K. Watanabe, T. Taniguchi, Y. Shi and X. Wang., 2012. Biaxial compressive strain engineering in graphene/boron nitride heterostructures, *Sci. Rep.*, 2(1), 893.

24. S. Y. Ju, W. I. Lee and H. S. Kim., 2022, Enhanced Phase Stability of Compressive Strain-Induced Perovskite Crystals, *ACS Appl. Mater. Interfaces*, 14(35), 39996–40004.

25. A. Løken, S. Ricote and S. Wachowski., 2018. Thermal and chemical expansion in proton ceramic electrolytes and compatible electrodes, *Crystals*, 8(9), 365.

26. Z. Weng, L. Liu, Y. Hu, Y. Wei, P. Da, Z. Wu, Z. Mu, P. Xi and C. H. Yan., 2023. Significance of Engineering the MnO_6 Octahedral Units to Promote the Oxygen Reduction Reaction of Perovskite Oxides, *Adv. Mater.*, 25, 2311102.

27. T. Jaouen, P. Aebi, S. Tricot, G. Delhaye, B. Lépine, D. Sébilleau, G. Jézéquel and P. Schieffer., 2014. Induced work function changes at Mg-doped MgO/Ag (001) interfaces: Combined Auger electron diffraction and density functional study, *Phys. Rev. B: Condens. Matter Mater. Phys.*, 90(12), 125433.

28. P. Zhou, H. Chen, Y. Chao, Q. Zhang, W. Zhang, F. Lv, L. Gu, Q. Zhao, N. Wang, J. Wang and S. Guo., 2012. Single-atom Pt-I3 sites on all-inorganic Cs_2SnI_6 perovskite for efficient photocatalytic hydrogen production, *Nat. Commun.*, 12(1), 4412.

29. J. Tang, L. Brzozowski, D. A. Barkhouse, X. Wang, R. Debnath, R. Wolowiec, E. Palmiano, L. Levina, A. G. Pattantyus-Abraham, D. Jamakosmanovic and E. H. Sargent., 2010. Quantum dot photovoltaics in the extreme quantum confinement regime: the surface-chemical origins of exceptional air-and light-stability, *ACS Nano*, 4(2), 869–878.

30. Y. Yamamoto, T. Fukushima, Y. Suna, N. Ishii, A. Saeki, S. Seki, S. Tagawa, M. Taniguchi, T. Kawai and T. Aida., 2006. Photoconductive coaxial nanotubes of molecularly connected electron donor and acceptor layers, *Science*, 314(5806), 1761–1764.
31. Y. Zhang, N. Zhang, Z. R. Tang and Y. J. Xu., 2012. Graphene transforms wide band gap ZnS to a visible light photocatalyst. The new role of graphene as a macromolecular photosensitizer, *ACS Nano*, 6(11), 9777–9789.
32. G. Xie, K. Zhang, B. Guo, Q. Liu, L. Fang and J. R. Gong., 2013. Graphene-based materials for hydrogen generation from light-driven water splitting, *Adv. Mater.*, 25(28), 3820–3839.
33. Kim Y K, Park H. 2011. Light-harvesting multi-walled carbon nanotubes and CdS hybrids: Application to photocatalytic hydrogen production from water. *Energy Environ. Sci*., 4(3): 685-694.
34. An, J., Zhu, L., Wang, N., Song, Z., Yang, Z., Du, D., & Tang, H., 2013. Photo-Fenton like degradation of tetrabromobisphenol A with grapheneBiFeO3 composite as a catalyst. *Chemical engineering journal*, *219*, 225-237.
35. Zhu Q, Lu J, Wang Y, Qin F, Shi Z, Xu C., 2016. Burstein-moss effect behind Au surface plasmon enhanced intrinsic emission of ZnO microdisks. *Scientific Reports*. 6(1):36194.
36. Sayama, K. and Arakawa, H., 1997. Effect of carbonate salt addition on the photocatalytic decomposition of liquid water over Pt–TiO 2 catalyst. *Journal of the Chemical Society, Faraday Transactions*, *93*(8), pp.1647-1654.
37. Sayama, K. and Arakawa, H., 1993. Photocatalytic decomposition of water and photocatalytic reduction of carbon dioxide over zirconia catalyst. *The Journal of Physical Chemistry*, *97*(3), pp.531-533.

38. Xiang, Q., Cheng, F. and Lang, D., 2016. Hierarchical layered WS2/graphene‐modified CdS nanorods for efficient photocatalytic hydrogen evolution. *ChemSusChem*, *9*(9), pp.996-1002.
39. Yuan, Y.J., Chen, D.Q., Huang, Y.W., Yu, Z.T., Zhong, J.S., Chen, T.T., Tu, W.G., Guan, Z.J., Cao, D.P. and Zou, Z.G., 2016. MoS2 nanosheet‐modified CuInS2 photocatalyst for visible‐light‐driven hydrogen production from water. *ChemSusChem*, *9*(9), pp.1003-1009.

Chapter 4 | Hydrazine-mediated thermally assisted photocatalytic ammonia decomposition over layered perovskite

4.1 Abstract

The work in this chapter has already been published in *Advanced Science* as "Hydrazine-mediated thermally assisted photocatalytic ammonia decomposition over layered protonated perovskites" with DOI: 10.1002/advs.202511212.

The photocatalytic decomposition of ammonia presents an environmentally friendly approach to generate hydrogen, yet its practical application remains hindered by insufficient catalytic activity and incomplete mechanistic understanding. In this chapter, we demonstrate a protonated layered perovskite material, $HPrNb_2O_7$ (HPNO), exhibits remarkable catalytic performance for ammonia conversion under combined photo-thermal conditions. When subjected to ammonia exposure at moderately elevated temperatures, HPNO enables the generation and confinement of hydrazine intermediates within its interlayer structure, facilitated by thermally activated oxygen vacancies and hydrogen bonding. Comprehensive spectroscopic and structural analyses were employed to verify the formation and stabilisation of these reactive intermediates. Furthermore, thermal energy was found to extend the lifetime of photoinduced charge carriers while facilitating oxygen vacancy generation, thereby achieving a strong photo-thermal synergy. The stabilisation of hydrazine species promotes an associative reaction pathway, effectively reducing the activation energy barrier. This mechanism results in a significantly improved hydrogen production rate of 2277.6 μmol·g-1·h-1 at 200°C under simulated sunlight irradiation, achieved with a minimal Ru co-catalyst loading of 0.95 wt.%. These findings not only elucidate a reaction pathway mediated by hydrazine

intermediates but also establish protonated layered perovskites as a material platform for solar-driven ammonia conversion toward sustainable hydrogen production.

4.2 Introduction

Photocatalytic NH_3 decomposition has gained attention as a strategy for transforming NH_3 into H_2 and N_2 under solar-driven conditions with lower energy input. Transition metals like Ru and Ni, conventionally employed as active sites in thermal catalytic NH_3 decomposition, have been adapted for photocatalytic systems owing to their capacity to lower NH_3 activation barriers at reduced temperatures.[1] Despite these advancements, existing photocatalytic systems often rely on concentrated ammonia solutions (e.g., 15M) and high-intensity artificial light sources due to poor charge carrier separation and sluggish kinetics, limiting their practical scalability and environmental compatibility.[2-6] Moreover, achieved H_2 production rates remain unsatisfactory, and mechanistic details of the reaction pathways are still ambiguous. These limitations highlight the demand for designing highly active, solar-responsive photocatalysts and elucidating fundamental decomposition mechanisms. Most recently, the synergy of heat and charge carriers is highly promising for enabling a substantial reduction in the activation energy barrier of chemical process.[41]

Layered perovskite oxides have garnered attention as a versatile platform for photocatalysis owing to their structural flexibility and stability under operational conditions. Such materials can be modified through strategies including ion exchange, exfoliation, and doping. Their layered architecture features loosely bound octahedral slabs stabilised by interlayer cations, which balance charge neutrality while enabling tailored interlayer chemical environments through cation substitution. This structural

adaptability underpins their diverse functionalities and broad applicability in catalytic systems.[7-9]

In this study, we introduce a thermally-assisted photocatalytic NH_3 decomposition system utilising a protonated perovskite, $HPrNb_2O_7$ (HPNO). Under thermal activation in NH_3 atmosphere, HPNO promotes the generation and interlayer trapping of hydrazine intermediates via an associative dehydrogenation mechanism. These intermediates are stabilised through interactions with thermally induced oxygen vacancies within the layered structure. A combination of characterisation approaches, including NPD, operando DRIFTS, XPS, and PDF analysis, confirms the formation and spatial distribution of N_2H_4 species. Additionally, thermal energy is shown to facilitate oxygen vacancy and prolong charge carrier lifetimes, as validated by TRPL studies, thereby achieving photo-thermal synergy. This cooperative effect achieves an exceptional H_2 production rate of 2277.6 $\mu mol \cdot g^{-1} \cdot h^{-1}$ at 200°C under simulated sunlight with 0.95 wt.% Ru doping. Our findings not only reveal an unexplored hydrazine-mediated pathway but also highlight protonated layered perovskites as a tuneable and efficient material class for solar-driven hydrogen generation.

4.3 Results and discussion

4.3.1 Ru-doped protonated layered perovskite

The Dion-Jacobson layered perovskite $CsPrNb_2O_7$ (CPNO) was synthesized through a high-temperature solid-state reaction using stoichiometrically balanced precursors (Pr_6O_{11}, Nb_2O_5, and Cs_2CO_3). Protonated $HPrNb_2O_7$ (HPNO) was obtained by subjecting CPNO to a proton exchange process in concentrated HNO_3 at 60°C, effectively replacing interlamellar Cs^+ ions with H^+ (Figure 4.1).

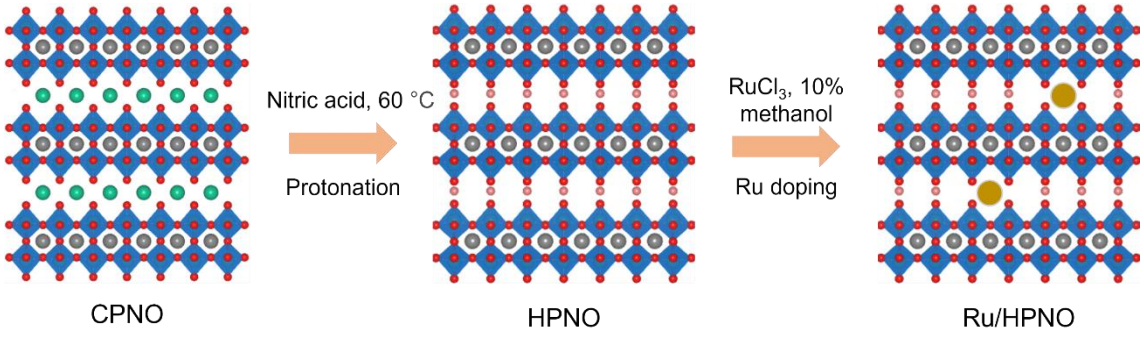

Figure 4.1: Schematic illustration of the Ru-doped HPNO catalyst preparation procedure.

Powder XRD analysis tracked the structural transformation during protonation, revealing a distinct shift of the (001) diffraction peak toward higher angles (from 7.7° to 8.4°), indicative of reduced interlayer spacing resulting from the smaller ionic radius of H^+ (Figure 4.2).

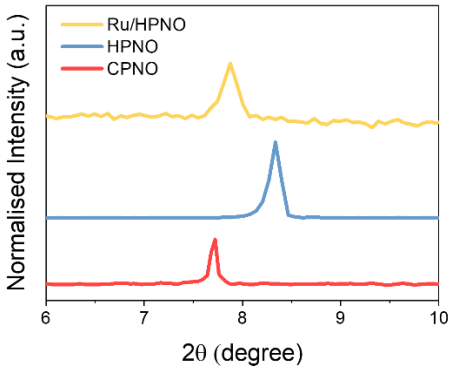

Figure 4.2: XRD patterns of layered perovskite $CsPrNb_2O_7$, HPNO and Ru-doped HPNO.

HAADF-STEM imaging confirmed the structural integrity of HPNO, displaying well-defined lattice fringes with a measured (010) plane spacing of 0.39 nm and minimal crystalline defects (Figure 4.3a). The single-crystalline nature of the material was further corroborated by sharp, ordered diffraction spots in the corresponding FFT image (Figure 4.3b).

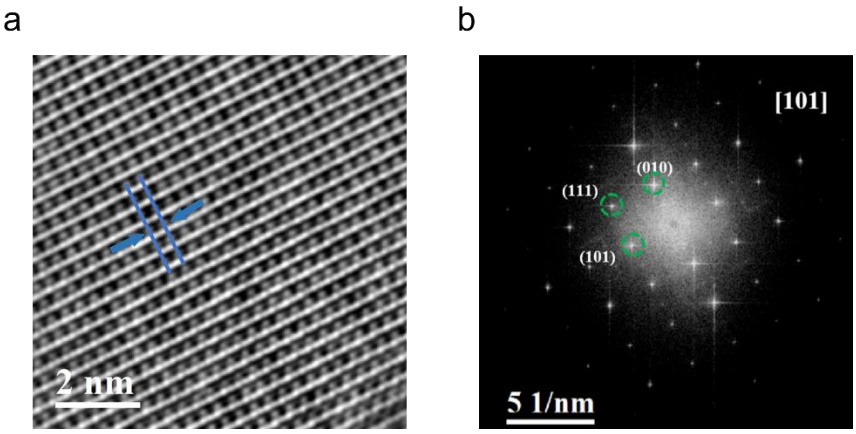

Figure 4.3: (a) HADDF-STEM images of HPNO. (b) Corresponding FFT of the STEM image.

To optimise the photocatalytic performance, Ru species were incorporated into the HPNO through a cation exchange strategy. Structural modifications induced by Ru integration were characterised by XRD analysis, where the (001) diffraction peak exhibited a systematic shift toward lower angles (Figure 4.2), signifying expansion of the interlamellar spacing due to Ru intercalation.[10] Materials with controlled Ru doping (0.95 wt.% and 3.04 wt.%) were systematically investigated, with ICP-MS confirming the precise metal incorporation ratios (Table 4.1 and Figure 4.4).

Synthetic conditions	3 wt. %	5 wt. %
ICP-MS	0.95 wt. %	3.04 wt. %

Table 4.1: Synthetic conditions and the observed Ru wt. % in HPNO perovskite.

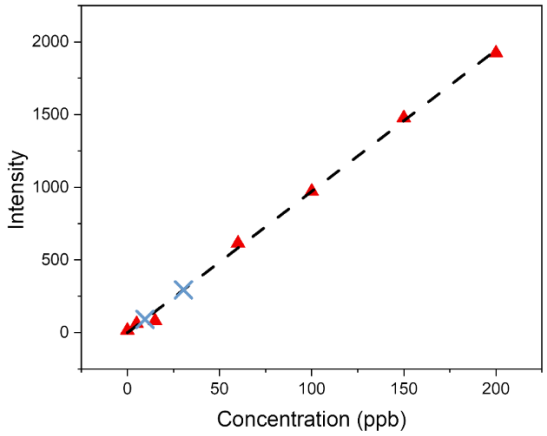

Figure 4.4: Calibration curve sued for Ru quantification by ICP-MS.

Notably, samples exceeding 3.04 wt.% Ru displayed an emergent diffraction feature at 38.3° (Figure 4.5), corresponding to the (100) plane of metallic Ru aggregates, confirming nanoparticle formation under high-loading conditions.

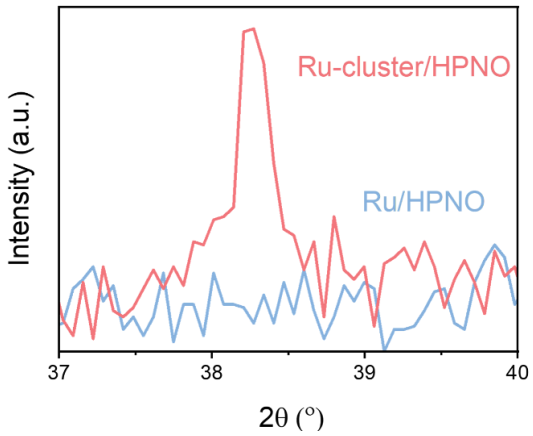

Figure 4.5: XRD patterns of Ru/HPNO and Ru-cluster/HPNO.

XPS analysis elucidated the chemical state evolution of Ru species. For low-loading samples (0.95–3.04 wt.%), the Ru $3p_{3/2}$ signal at 463.2 eV (Figure 4.6) aligns with Ru^{2+} species atomically dispersed within the lattice. Conversely, higher Ru concentrations induced a characteristic binding energy shift to 461.8 eV, indicative of metallic Ru^0 clusters,[11] demonstrating a critical threshold for Ru aggregation. These findings establish a structure-property correlation: optimal Ru^{2+} dispersion (<3.04 wt.%) is

stabilised through oxygen-mediated anchoring in the interlayer region, whereas excess loading triggers nanoparticle formation.

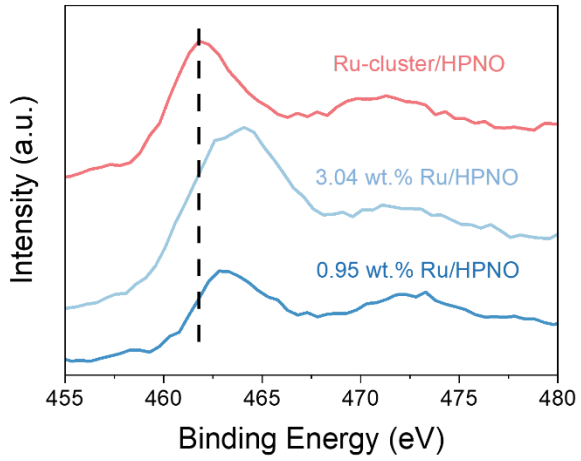

Figure 4.6: Ru 3p XPS spectra of Ru/HPNO and Ru-cluster/HPNO.

Elemental homogeneity in the 0.95 wt.% Ru/HPNO composite was verified by EDX mapping (Figure 4.7), revealing uniform spatial distribution of Pr, Nb, O, and Ru.

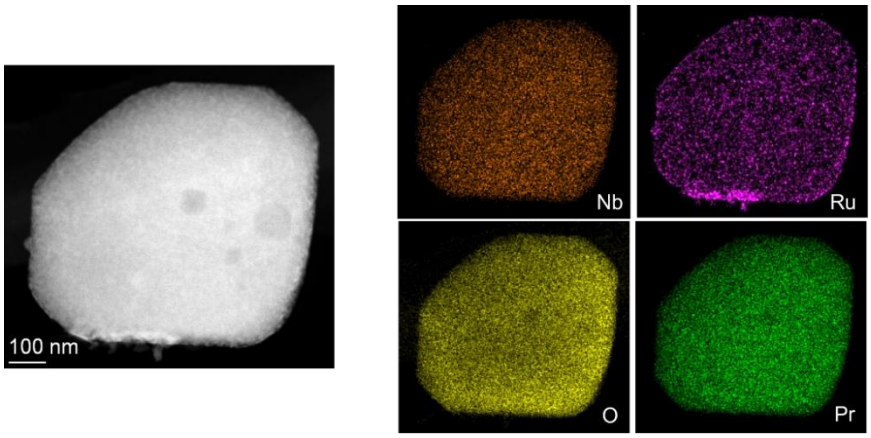

Figure 4.7: EDX mapping of Ru, Pr, O and Nb for 0.95 wt.% Ru/HPNO.

Optical characterisation via UV-Vis diffuse reflectance spectroscopy demonstrated progressive bandgap narrowing from 3.1 eV (CPNO) to 2.9 eV (HPNO) and 2.6 eV (Ru/HPNO), as derived from Tauc plot analysis (Figure 4.8), confirming enhanced light harvesting capacity through sequential material modifications.

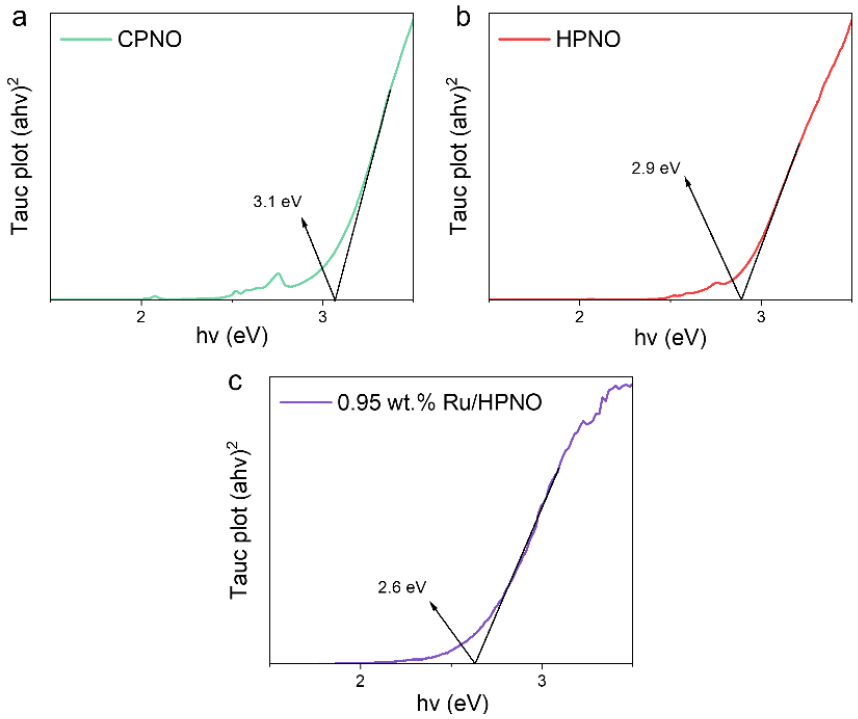

Figure 4.8: Tauc plot $(ahv)^2$ of (a) CPNO, (b) HPNO and (c) 0.95 wt. % Ru/HPNO.

4.3.2 Thermal-assisted photocatalytic ammonia decomposition

The catalytic efficiency for NH_3 decomposition was systematically evaluated in a sealed batch reactor under AM1.5G solar illumination. Catalyst pre-treatment involved thermal activation at 400 °C under Ar flow to eliminate surface-adsorbed contaminants. As depicted in Figure 4.9, Ru/HPNO exhibited a volcanic activity trend with Ru loading optimisation, achieving peak H_2 production at 0.95 wt.%. Excessive Ru loading (>3.04 wt.%) induced nanoparticle aggregation, likely diminishing active surface area through photon scattering effects and metal site occlusion, consistent with prior mechanistic studies.[11,12]

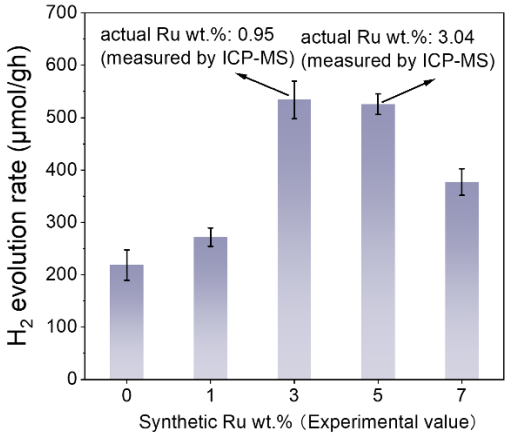

Figure 4.9: Photocatalytic ammonia decomposition activity over HPNO with different synthetic Ru wt.%.

Temperature-dependent studies (Figure 4.10) revealed progressive activity enhancement up to 200 °C, beyond which system equilibrium limited further improvement, particularly for unmodified HPNO. This plateau effect originates from thermodynamic constraints of NH_3 decomposition under elevated pressure in closed configurations.

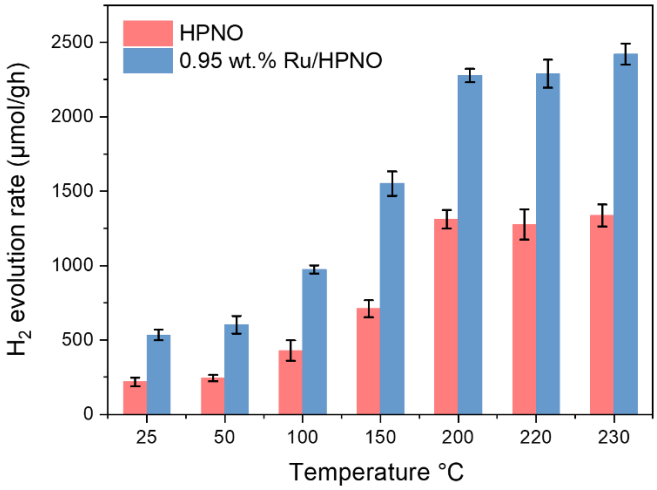

Figure 4.10: Photocatalytic ammonia decomposition activity over HPNO and 0.95 wt.% Ru/HPNO under different temperature.

Spectral responsivity analysis (Figure 4.11) confirmed the necessity of charge carrier generation, with complete activity cessation beyond 700 nm (IR region), validating the photocatalytic nature of the process.

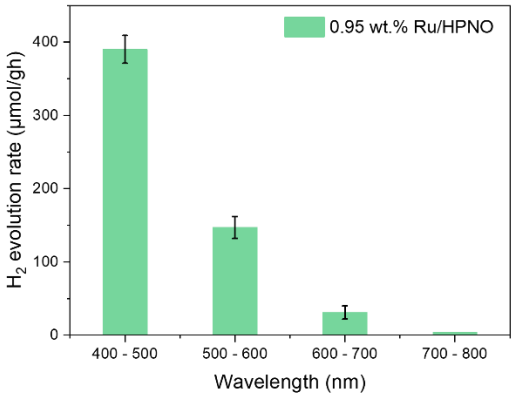

Figure 4.11: Photocatalytic ammonia decomposition activity over 0.95 wt.% Ru/HPNO under different wavelength of light source.

Long-term stability assessments across six operational cycles (Figure 4.12a) demonstrated exceptional durability. Post-reaction XRD analysis (Figure 4.12b) confirmed structural integrity preservation.

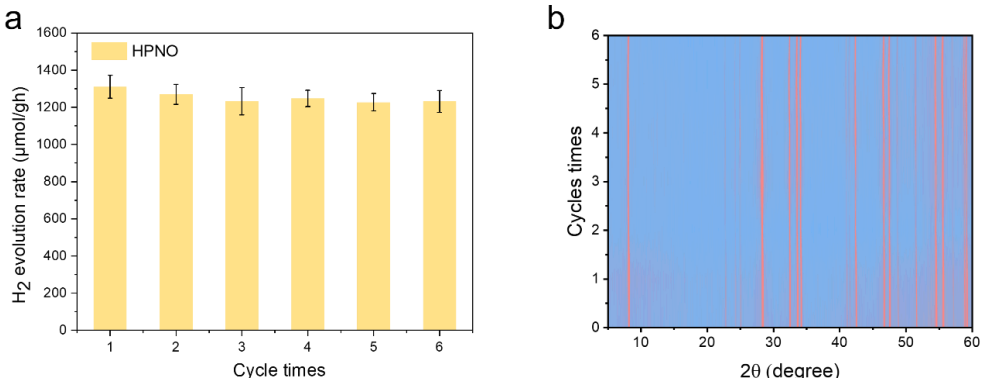

Figure 4.12: (a) The stability test of photocatalytic ammonia decomposition performance for HPNO at 200 °C for 1 hr with 6 cycle times. (b) XRD pattern of HPNO photocatalyst after 6 times of photocatalytic ammonia decomposition tests. The red colour represents the intensity of peaks.

Control experiments were established, where no H_2 generation under Ar atmosphere with illumination and no activity at 200°C / 6 bar NH_3 without photon input. Furthermore, a light-concentrated furnace was used to mimic a solar furnace (Figure 4.13), showing that stable and efficient ammonia decomposition activity at 200 ° C could be maintained solely by the concentrated light without any other external heating devices. A more exceptional activity of 10.3 mmol/gh was observed on 0.95 wt.% Ru/HPNO due to the high intensity of the concentrated light.

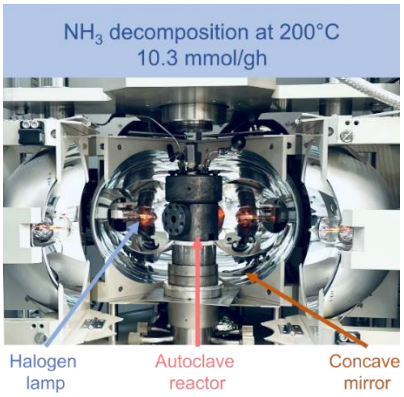

Figure 4.13: Photograph of a four-mirror floating-zone solar furnace from Crystal Systems used to mimic a solar concentrator to focus a light beam to provide both heat and photons to HPNO / Ru 0.95 wt. % without any other energy input from an electrical device.

Complementary thermal catalysis studies (Figure 4.14) revealed temperature-driven performance escalation across all catalysts. HPNO initiated NH_3 conversion at 400°C (43.4% at 550°C, weight hourly space velocity =30,000 $mL \cdot g_{cat}^{-1} \cdot h^{-1}$), while 0.95 wt.% Ru/HPNO achieved 80% conversion under identical conditions. Comparatively, CPNO exhibited limited activity (12.5% at 550°C), emphasising the synergistic enhancement from protonation and Ru integration.

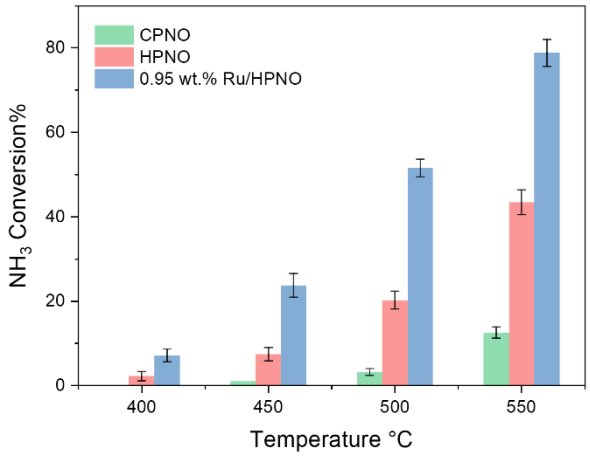

Figure 4.14: Ammonia conversion at different temperature over different perovskite catalysts, where weight hourly space velocity is 30,000 mL g_{cat}^{-1} h^{-1}.

The efficient separation of photogenerated charge carriers is recognised as a determinant in photocatalytic systems. To elucidate charge carrier dynamics under varying thermal conditions, TRPL spectroscopy was conducted across different temperatures (Figure 4.15a). Analysis of the TRPL decay profiles in Figure A4.1 in Appendices revealed two distinct components: a rapid bulk recombination phase and a slower decay process attributed to surface or interlayer recombination mechanisms. As illustrated in Figure 4.15b, the slow decay carrier lifetime exhibited a linear increase with rising temperature, suggesting thermal energy-mediated suppression of recombination through enhanced exciton delocalisation.[13-16] This thermally activated charge separation mechanism directly contributes to the observed photo-thermal synergistic enhancement in the NH_3 decomposition system.

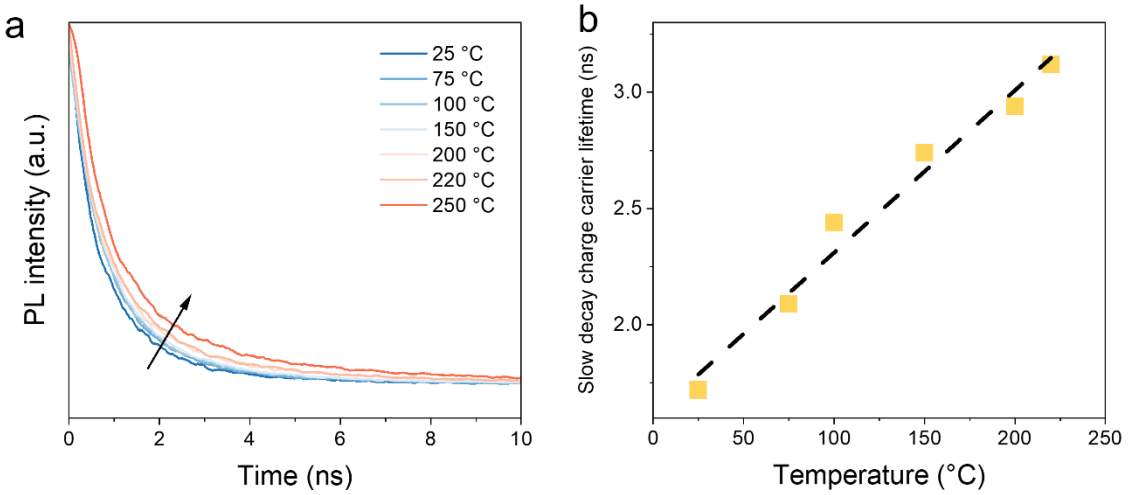

Figure 4.15: (a) TRPL spectra of HPNO under temperature from 25 °C to 250 °C, where the excitation wavelength is 430 nm. (b) Charge carrier lifetime versus temperature.

Complementary Arrhenius analysis was performed to quantify activation barriers under thermal catalytic conditions (Figure 4.16a). The calculated apparent activation energy (E_a) for HPNO measured 36.7 kJ/mol, which decreased by 19% to 29.9 kJ/mol following Ru incorporation, confirming the role of Ru sites as catalytic centres for NH_3 activation [11]. Remarkably, under photocatalytic conditions, Ea values were substantially reduced to 11.7 kJ/mol (HPNO) and 9.7 kJ/mol (Ru/HPNO) as shown in Figure 4.16b. This dramatic decrease in activation energy underscores the mechanistic divergence between photocatalytic and purely thermal reaction pathways, motivating deeper exploration of the light-driven NH_3 decomposition mechanisms in layered perovskite architectures.

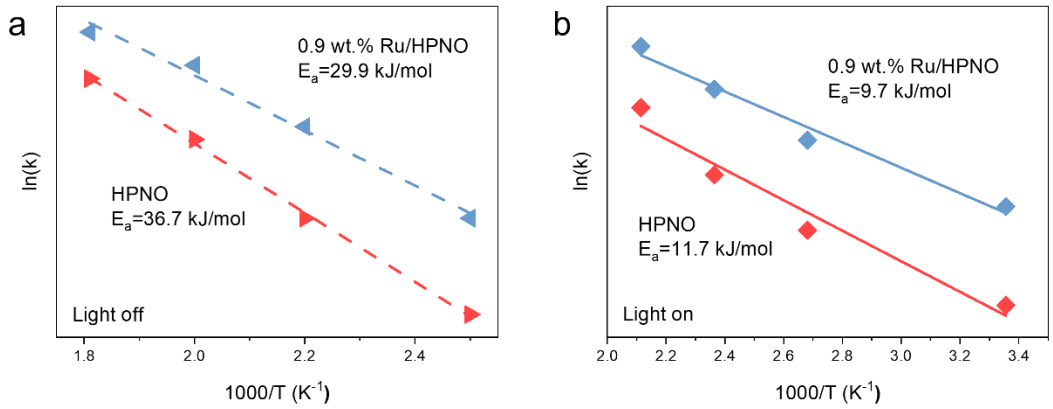

Figure 4.16: (a) Arrhenius plots of HPNO and 0.95 wt. % Ru/HPNO for thermal ammonia decomposition. (b) Arrhenius plots of HPNO and 0.95 wt. % Ru/HPNO for photocatalytic catalysis conditions.

4.3.3 Mechanistic investigations

To study the mechanistic basis of the observed photo-thermal enhancement and intermediate species involvement, systematic mechanistic investigations were conducted. Prior studies on Pt/TiO_2 based systems have suggested a photocatalytic NH_3 decomposition pathway wherein photogenerated holes oxidise adsorbed NH_3 to amide radicals and protons, subsequently forming hydrazine (N_2H_4) as a transient species prior to its decomposition into N_2 and H_2.[4] DFT calculations corroborate this associative mechanism *via* N_2H_4 intermediates, demonstrating a significantly lower activation barrier (~59.2 kcal·mol^{-1}) compared to dissociative pathways (~235.7 kcal·mol^{-1}).[17] Nevertheless, experimental validation of such intermediates remains scarce. In layered perovskite systems like HPNO, the interlamellar spaces may stabilise reactive intermediates through hydrogen bonding or defect interactions. To validate this hypothesis, a comprehensive suite of in situ characterisation methods was implemented to track intermediate formation, stabilisation, and transformation dynamics.

DRIFTS was employed to monitor NH_3 conversion processes on HPNO catalysts. Initial spectra collected under N_2 atmosphere at 25 °C showed no discernible vibrational features in the 800–2100 cm^{-1} region (Figure 4.17a). Upon NH_3 exposure, a distinct absorption band developed at 1623 cm^{-1}, assignable to the NH_3 bending vibration.[18] Subsequent analysis under thermal activation revealed progressive emergence of two additional bands at 1427 cm^{-1} and 948 cm^{-1} as temperatures approached 300°C, corresponding to characteristic H-N-H bending and N-N stretching modes of N_2H_4 intermediates.[13] Post-cooling N_2 purging eliminated NH_3-related signals while preserving N_2H_4 spectral features, demonstrating stable intermediate retention. Complementary temperature-resolved DRIFTS mapping (Figure 4.17b) tracked NH_3 depletion through intensity reduction of the N-H stretching band at 3320–3340 cm^{-1}, consistent with reaction

progression. Residual signals in this region were attributable to N_2H_4 N-H stretching, which gradually diminished at elevated temperatures due to intermediate decomposition.

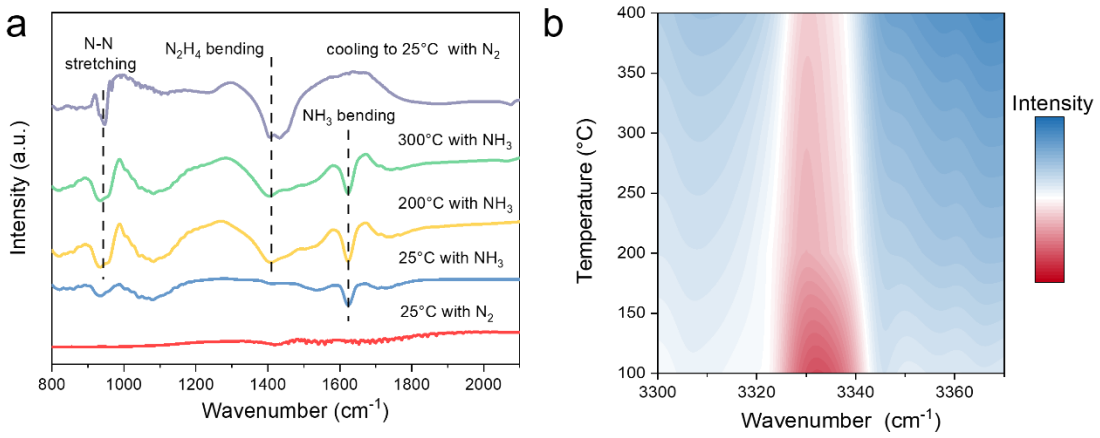

Figure 4.17: (a) DRIFTS study of hydrazine formation process, where HPNO is heated under NH_3 flow. (b) DRIFTS study of NH_3 decomposition under different temperature over HPNO.

In light of DRIFTS findings, XPDF analysis was conducted to investigate temperature-dependent structural evolution of the layered HPNO perovskite during NH_3 conversion. As illustrated in Figure 4.18, the characteristic Nb-O scattering peak at 1.9 Å exhibited broadening and intensity reduction at 100°C, indicative of lattice vibrational excitation and oxygen vacancy generation.[19-21] A partial recovery of this feature at 200°C was observed, correlated with NH_3 coordination to undercoordinated Nb centres through Lewis acid-base interactions.[22] XPDF refinement analysis (Figure A4.2 in Appendices) revealed that such interactions effectively replenish oxygen vacancies, restoring Nb-O coordination symmetry via $*NH_3$ compensation (Figure 4.19).[23] Above 300°C, renewed intensity attenuation coincided with desorption of N-coupled products (e.g., N_2H_4 or N_2), providing direct structural evidence for intermediate evolution within the layered framework.

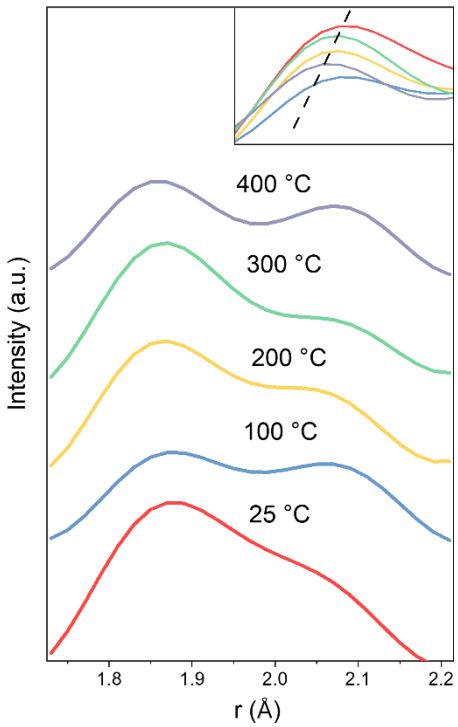

Figure 4.18: XPDF of Nb-O bond heated from 25 to 400 °C under ammonia gas.

Comparative XPDF studies of HPNO and CPNO quantified oxygen vacancy dynamics. HPNO demonstrated progressive vacancy formation with temperature-responsive structural adaptation, whereas CPNO maintained structural rigidity up to 400°C with minimal vacancy generation (Figure 4.19). This contrast underscores the critical role of interlayer Cs^+ cations in stabilising the perovskite lattice while impeding NH_3 interaction.

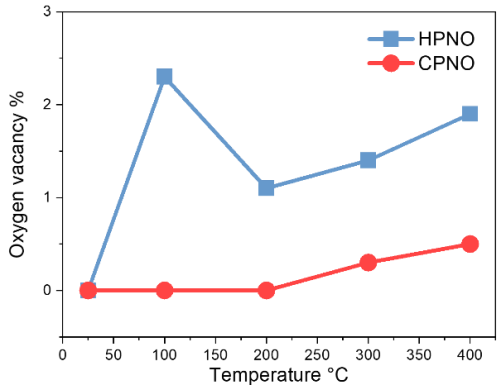

Figure 4.19: Oxygen vacancy variation as temperature increase under NH_3, which is determined by the refinement of XPDF.

Temperature-programmed surface reaction (TPSR) profiles (Figure 4.20a) corroborated these findings, showing significant NH_3 consumption by HPNO at 300°C through thermally activated vacancy creation, while CPNO exhibited negligible uptake due to restricted NH_3 accessibility. Kinetic analysis at 200°C (Figure 4.20b) further established oxygen vacancy formation as the rate-determining step preceding NH_3 adsorption and dehydrogenation.

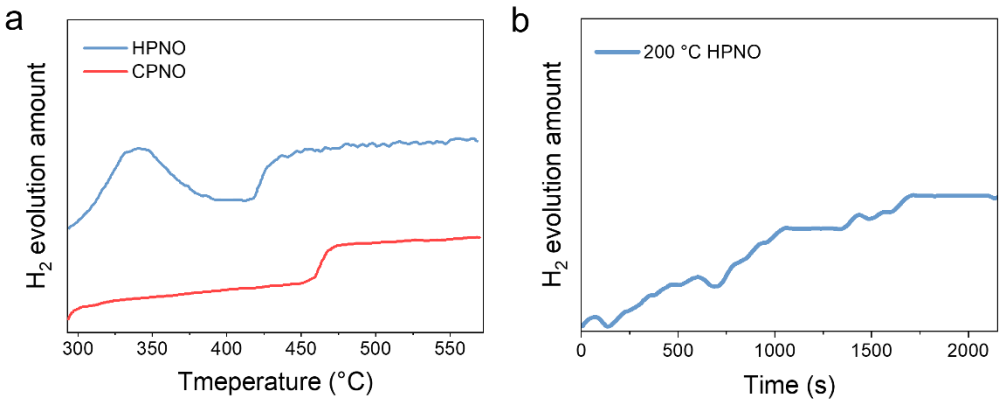

Figure 4.20: (a) TPSR of HPNO and CPNO at different temperature with NH_3 flow. (b) Ammonia consumption of HPNO at 200 °C at different time. (Instantaneous NH_3 consumption was represented by H_2 evolution amount at each time point under a fixed temperature)

Direct evidence of vacancy generation was obtained through EPR spectroscopy. NH_3-treated HPNO samples exhibited a characteristic EPR signal at $g \approx 2.005$ (Figure 4.21), corresponding to oxygen vacancies adjacent to Nb^{5+} centres.[24] Signal intensity progressively intensified with thermal activation up to 500°C, aligning with defect generation trends observed in XPDF and TPSR studies. Notably, a sharp signal enhancement accompanied by hyperfine splitting at 600°C suggests the formation of metastable vacancy clusters, potentially stabilised through nitrogen doping from decomposed NH_3 species.

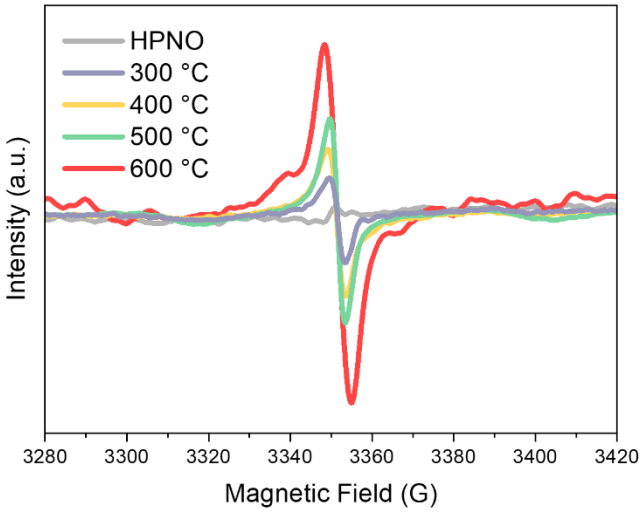

Figure 4.21: EPR pattern of HPNO after heated at different temperature with NH_3 flow.

Following the confirmation of N_2H_4 formation and stabilisation within HPNO under thermal activation, subsequent investigations focused on resolving the spatial distribution and local coordination of these intermediates. To capture immobilised N_2H_4 species, pristine HPNO underwent controlled NH_3 flow treatment at 300°C, a temperature optimised for intermediate retention. Consistent with prior DRIFTS observations, N_2H_4 intermediates generated at 300°C remained stabilised post-cooling and NH_3 purge. Comparative analyses extended to higher thermal regimes (600°C and 800°C) under identical NH_3 flow conditions, producing systematically labelled derivatives designated as HPNO-300, HPNO-600, and HPNO-800.

XRD characterisation revealed a progressive structural evolution across treated HPNO derivatives. The (001) diffraction peak shifted from 8.4° in pristine HPNO to 8.1° for HPNO-300, signalling interlayer expansion likely induced by N_2H_4 intercalation (Figure 4.22). HPNO-600 maintained structural similarity to HPNO-300, whereas HPNO-800 exhibited complete (001) peak disappearance, confirming framework collapse at extreme temperatures.[15]

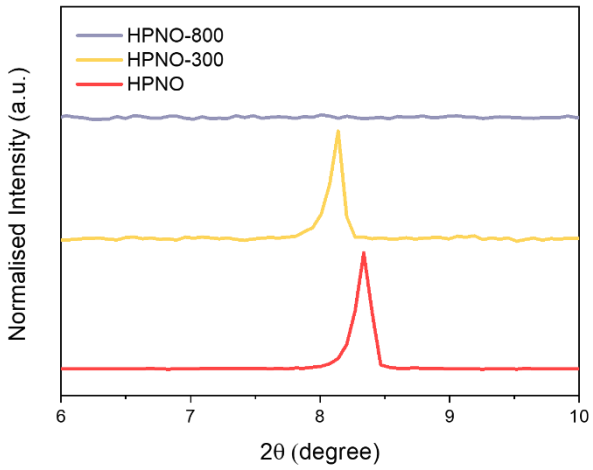

Figure 4.22: XRD pattern of HPNO, HPNO-300 and HPNO-800.

XPS analysis of HPNO-300 displayed a distinct N 1s peak at 399.7 eV, characteristic of N_2H_4 species (Figure 4.23b).[26-29] In contrast, HPNO-600 demonstrated N_3^--related peaks at 396.1 eV and residual N_2H_4 signals at 398.9 eV (Figure 4.23c), validating thermal decomposition thresholds and nitrogen substitution mechanisms.

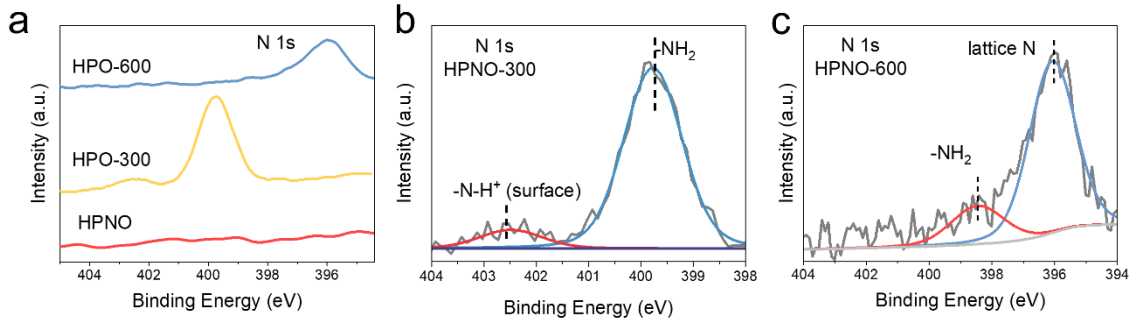

Figure 4.23: (a) N 1s XPS spectra of HPNO, HPNO-300 and HPNO-600. High resolution N 1s XPS spectra of (b) HPNO-300 and (c) HPNO-600. Grey line: raw data; Blue and Red line: fitted data.

Nb 3d spectra evolution further corroborated redox dynamics: pristine HPNO exhibited Nb^{5+} signatures at 209.8 eV ($3d_{3/2}$) and 207.1 eV ($3d_{5/2}$) (Figure 4.24a). HPNO-300 introduced additional Nb^{4+} peaks at 208.0 eV and 204.9 eV (Figure 4.24b). O 1s deconvolution identified three components in HPNO (Nb-O, -OH, H_2O; Figure 4.24c), with HPNO-300 showing a fourth defect-related peak at 531.8 eV,[24,30,31] aligning with XPDF and EPR observations.

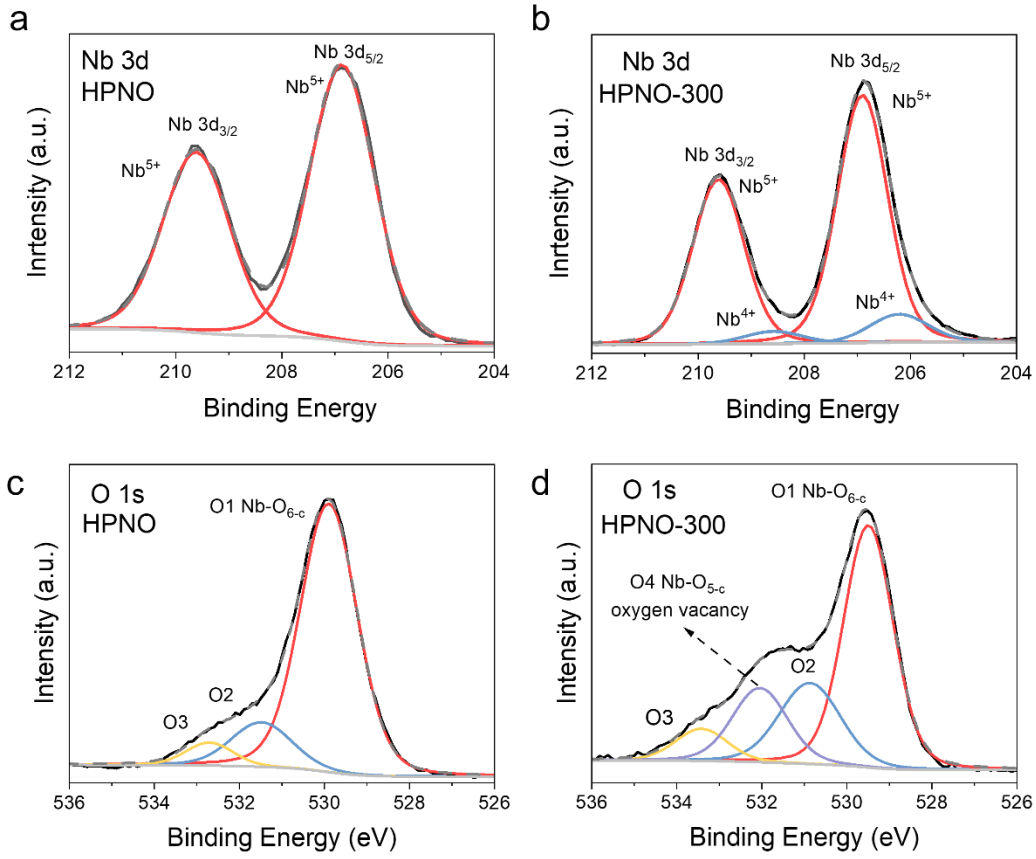

Figure 4.24: Nb 3d XPS spectra of (a) HPNO and (b) HPNO-300. O 1s XPS spectra of (c) HPNO and (d) HPNO-300.

TGA profiles differentiated intermediate states: HPNO-300 exhibited 2.5 wt.% mass loss from 400°C (N_2H_4 decomposition; Figure 4.25), while HPNO-600 gained 1.5 wt.% above 300°C (N_3^- → O^{2-} substitution). Both derivatives showed vacancy-driven mass loss beyond 550°C.

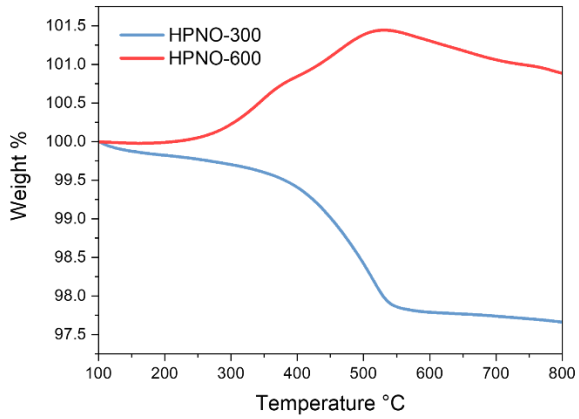

Figure 4.25: TGA curves under air flow for HPNO-300 and HPNO-600. Flow rate: 100 mL/min; ramp: 25 °C /min.

UV-vis spectroscopy with para-(dimethyl amino)benzaldehyde condensation confirmed N_2H_4 presence in HPNO-300 through dose-dependent absorption intensification at 400-450 nm (Figure 4.26).[32]

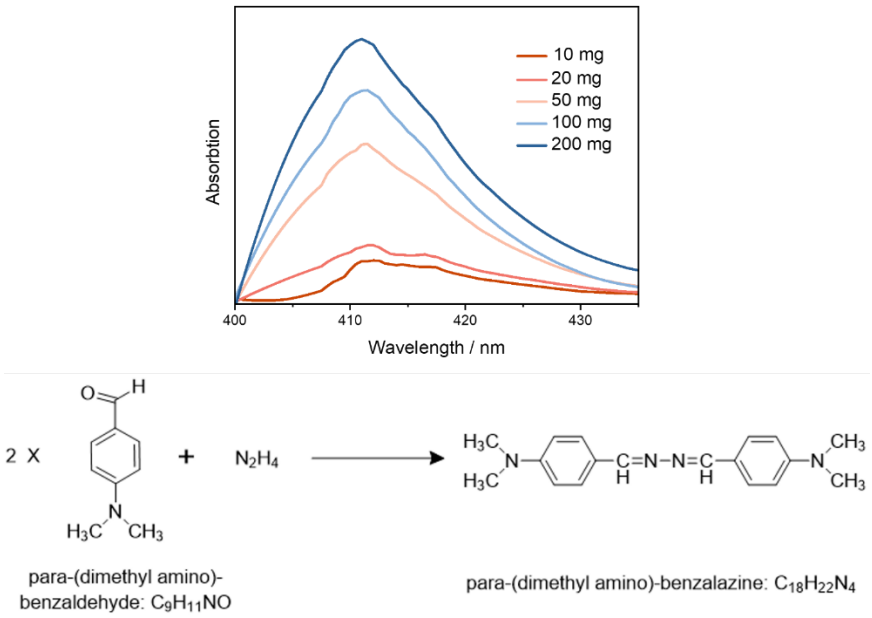

Figure 4.26: UV-vis absorption spectrum of *para*-(dimethyl amino)-benzaldehyde solution mixed with different amount of HPNO-300. Condensation reaction is between N_2H_4 and *para*-(dimethyl amino)-benzaldehyde. By the high-speed centrifuge, azine solution and HPNO-300 was well separated. Because no absorption was observed beyond 400 nm in UV-Vis spectrum of azine solution, which means HPNO-300 perovskite did not affect this absorption spectrum.

To further investigate the structure of intercalated HPNO-300, Rietveld refinement of XRD data was performed (Figure 4.27a), confirming a *P*1 space group with lattice parameters $a = 3.85151$ Å, $b = 3.86932$ Å, $c = 10.57143$ Å, and $\alpha = \beta = \gamma = 90°$, comprising corner-sharing NbO_6 octahedra arranged in double-layer slabs stacked along the *c*-axis. To precisely determine the location of light elements such as N and H, NPD was employed due to its high sensitivity to small atomic displacements and strong contrast for oxygen and nitrogen.[33] The NPD refinement of the *P*1 model (Figures 4.27b, c) confirmed that N_2H_4 molecules occupy the centre of the interlayer galleries, with a N-N distance of 0.14 nm, consistent with that in molecular N_2H_4.

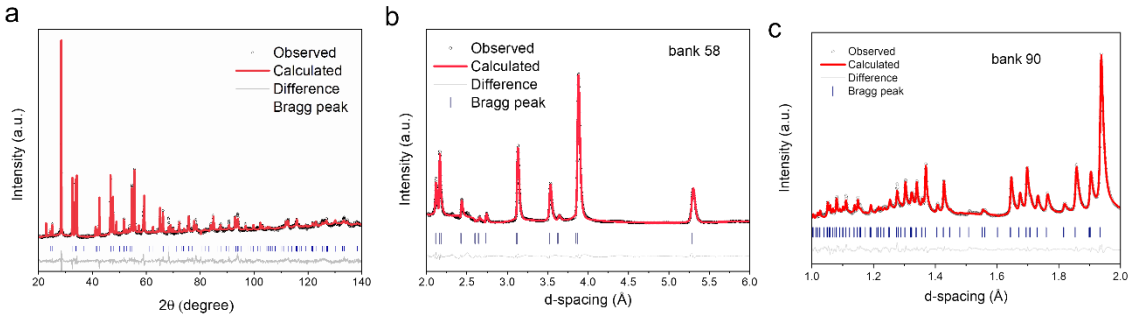

Figure 4.27: (a) XRD Rietveld refinement of HPNO at 298 K, R_{wp} = 9.6%. NPD joint Rietveld refinement of HPNO at 298 K, R_{wp} = 1.9%, at (b) bank 58 and (c) bank 90.

Hydrogen bonding interactions between the N-H groups of N_2H_4 and lattice oxygen atoms (Figure 4.28) slightly lengthen the N-H bond to 0.11 nm and compress the H-N-H bond angles to 101.8° and 100.5°, compared to free N_2H_4. This distortion arises from the restricted interlayer spacing and the altered lone pair-bond pair repulsion balance.

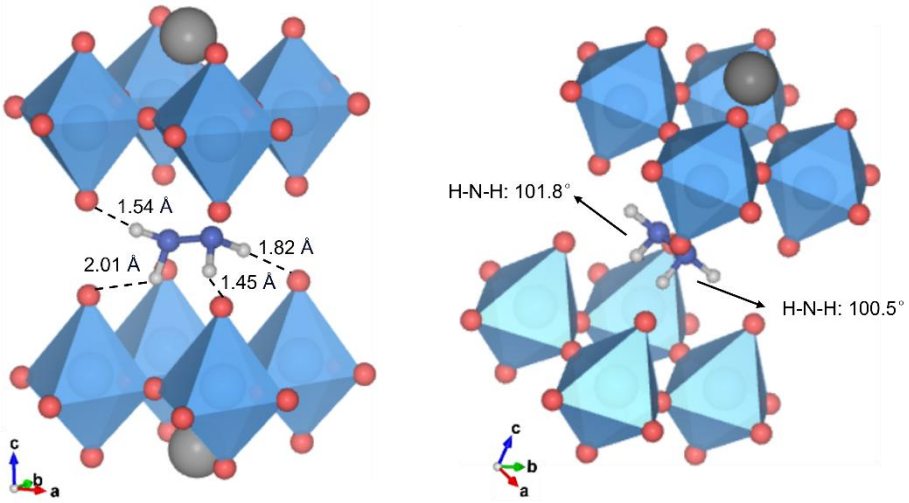

Figure 4.28: The refined structure of HPNO-300 (the proton between interlayer oxygen was hidden in order to give a more comprehensive view of N_2H_4). The dashed line represents the NH···O interaction.

HADDF-STEM images (Figure 4.29b) revealed the high crystallinity of HPNO-300, as indicated by the corresponding FFT pattern (Figure 4.29a) and well-defined lattice fringes.

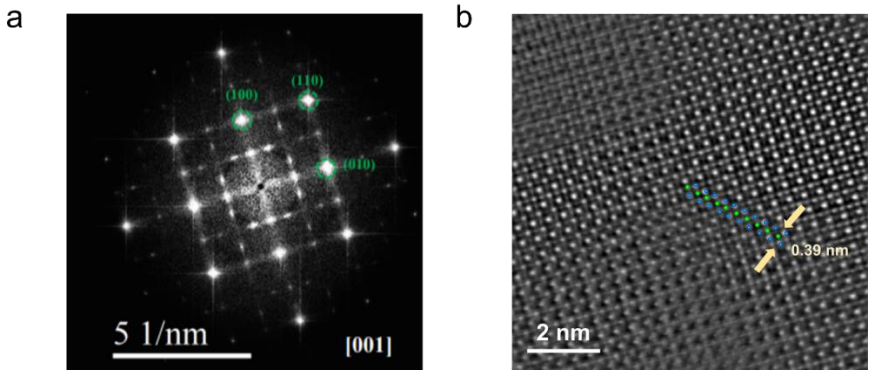

Figure 4.29: (a) FFT, (b) HADDF-STEM images of HPNO-300.

Additionally, SEM-EDX mapping (Figure 4.30) confirmed the homogeneous distribution of Pr, Nb, O, and N elements throughout the material.

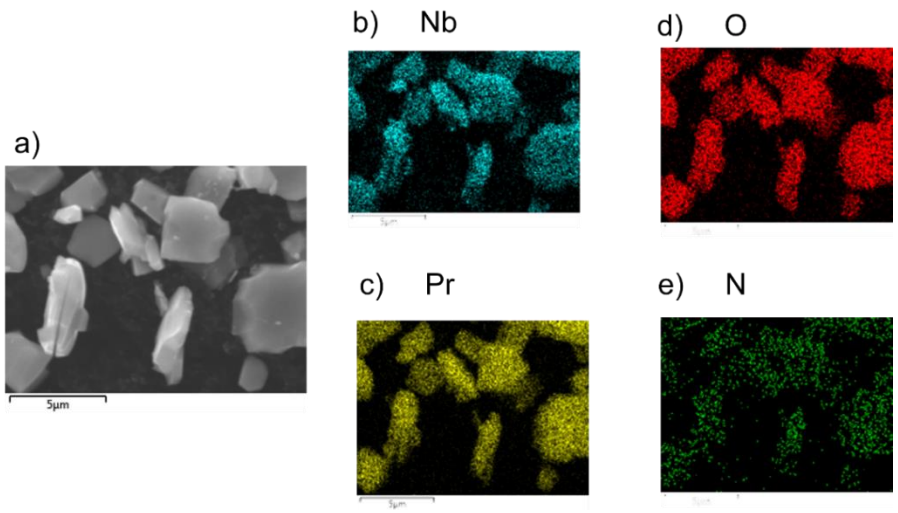

Figure 4.30: SEM images of HPNO-300 and the corresponding EDX mapping of Pr, Nb, O and N elements.

Complementary insights were obtained by the ^{14}N ssNMR spectroscopy. The NMR spectrum (Figure 4.31) gives a substantial pattern of spinning sidebands. These sidebands are caused by the anisotropic interactions, whose source can be quadrupolar coupling effects but as well as the spin-spin interactions with protons.[34,35] The breakdown of the ideal symmetry of the surroundings is due to the different NH···O interaction distance between N_2H_4 hydrogen and perovskite lattice oxygen (Figures 4.28).[36,37]

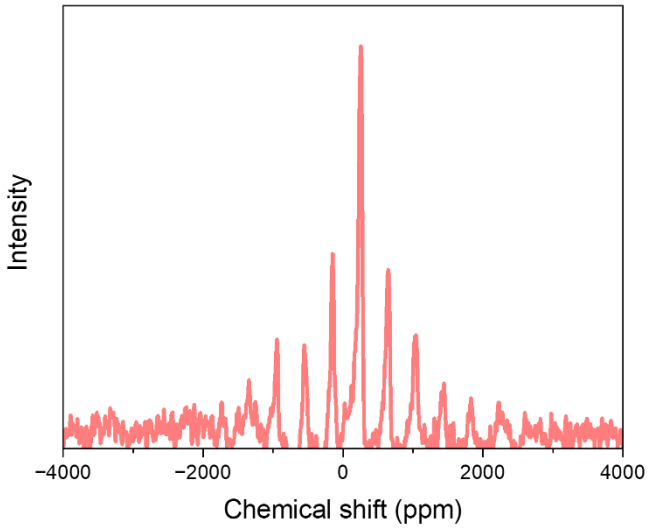

Figure 4.31: ^{14}N ssNMR spectrum of HPNO-300.

These results demonstrate that N_2H_4 occupies precisely defined but distorted sites within the layered framework, aligning with XRD and NPD evidence. Collectively, the data establish HPNO's capacity to selectively convert NH_3 to N_2H_4 under thermal activation, with stable interlayer confinement of the intermediate. Hydrogen bonding mediates this stabilisation, steering the reaction along an associative decomposition pathway. Such a mechanistic framework rationalises the superior performance of layered HPNO perovskites in photo-thermal catalytic NH_3-to-H_2 conversion.

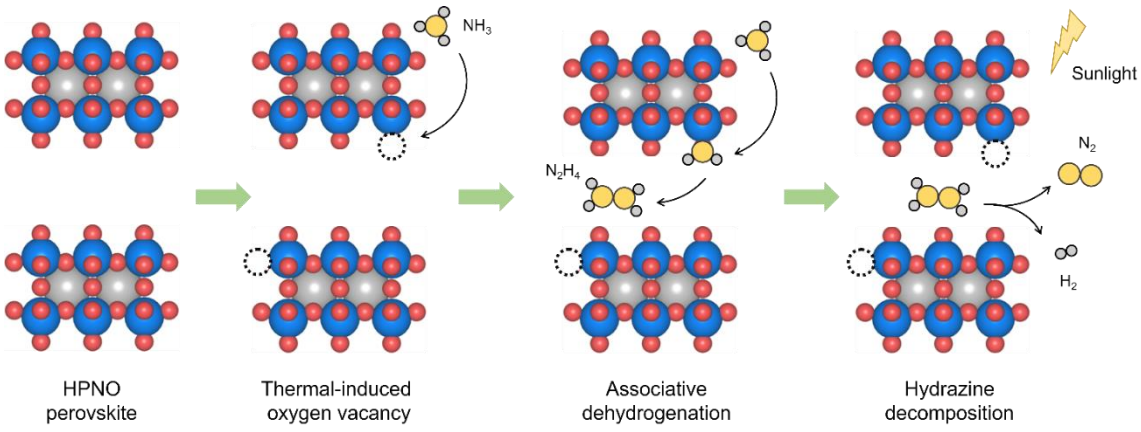

Figure 4.32: Schematic illustration of the photothermal NH_3 decomposition mechanism over the HPNO catalyst.

Figure 4.32 illustrates the proposed thermally-assisted photocatalytic NH_3 decomposition mechanism derived from these findings. Under thermal activation, oxygen vacancies are generated within HPNO. These vacancies act as active sites for the NH_3 decomposition process, where incoming NH_3 molecules adsorb onto these points to replenish these vacancy sites, as confirmed by XPDF analysis (Figure 4.18). The adsorbed $*NH_3$ intermediates subsequently undergo associative dehydrogenation, forming N2H4 as a reaction intermediate. NPD refinements (Figure 4.27b, c) reveal that the HPNO perovskite lattice effectively stabilises N_2H_4 within its layered structure. Under simulated solar irradiation, photoexcitation generates electron-hole pairs, which migrate to the catalyst surface to drive N_2H_4 decomposition. Concurrently, thermal input extends the lifetimes of photogenerated carriers, as demonstrated by TRPL measurements (Figure 4.15), synergistically boosting the overall ammonia decomposition activity.

4.4 Conclusion

In this work, we developed a protonated layered perovskite, HPNO, as an effective photocatalyst for NH_3 decomposition under mild conditions. We show that when exposed to NH_3 at elevated temperatures, hydrazine forms *via* an associative dehydrogenation route and becomes stably intercalated in the interlayer space of HPNO. This intermediate is stabilised by hydrogen bonding and interactions with thermally generated oxygen vacancies. A suite of characterisation methods confirms both the presence and local environment of the intercalated hydrazine species. Our findings also reveal that moderate heating prolongs photogenerated charge carrier lifetime and enhances vacancy creation, yielding the photo-thermal synergy. As a result, a H_2 evolution rate of 2277.6 μmol/gh is demonstrated in this system at 200 °C (Table 4.1).

Table 4.2: Thermally assisted photocatalytic NH_3 decomposition activity comparison.

Sample	Light Source	Power	Wavelength (nm)	Temperature (°C)	HER ($\mu molg^{-1}h^{-1}$)	Ref
Ru-HPNO	Solar simulator	0.08 W	400-1000	200	2277.6	This work
HPNO	Solar simulator	0.08 W	400-1000	200	1311.2	This work
Ce 1.2%, TiO_2	UV lamp	8 W	254	25	106.8	[5]
Pt 0.3%, TiO_2	Xe lamp	500 W	> 400	25	200.1	[3]
Pt/Fe TiO_2	Mercury arc	100 W	> 300	25	3.4	[38]
Pt/TiO_2 (A)	Xe lamp	300 W	200-2500	50	216.5	[4]
Ni-1.4-MCN	Xe lamp	300 W	> 420	52	35.6	[39]
Ru 0.5%, Fe_2O_3	LED	N/A	400-700	24	156.3	[40]

This study uncovers a distinct mechanistic pathway for NH_3 decomposition on layered perovskite and details the structure and interactions of the trapped hydrazine intermediate. These insights both deepen our understanding of NH_3 activation and highlight the promise of layered perovskites as robust, scalable platforms for solar-driven hydrogen generation.

4.5 Reference

1. Boisen, A., Dahl, S., Nørskov, J. K., & Christensen, C. H., 2005. Why the optimal ammonia synthesis catalyst is not the optimal ammonia decomposition catalyst. *Journal of Catalysis*, *230*(2), 309-312.
2. Yuan, Y., Zhou, L., Robatjazi, H., Bao, J.L., Zhou, J., Bayles, A., Yuan, L., Lou, M., Lou, M., Khatiwada, S. and Carter, E.A., 2022. Earth-abundant photocatalyst for H2 generation from NH3 with light-emitting diode illumination. *Science*, *378*(6622), pp.889-893.
3. Obata, K., Kishishita, K., Okemoto, A., Taniya, K., Ichihashi, Y. and Nishiyama, S., 2014. Photocatalytic decomposition of NH3 over TiO2 catalysts doped with Fe. *Applied Catalysis B: Environmental*, *160*, pp.200-203.
4. Yuzawa, H., Mori, T., Itoh, H. and Yoshida, H., 2012. Reaction mechanism of ammonia decomposition to nitrogen and hydrogen over metal loaded titanium oxide photocatalyst. *The Journal of Physical Chemistry C*, *116*(6), pp.4126-4136.
5. Reli, M., Ambrožová, N., Šihor, M., Matějová, L., Čapek, L., Obalová, L., Matěj, Z., Kotarba, A. and Kočí, K., 2015. Novel cerium doped titania catalysts for photocatalytic decomposition of ammonia. *Applied Catalysis B: Environmental*, *178*, pp.108-116.
6. Beck, A., Marlowe, J., Gordon, M.J. and Christopher, P., 2024. Is There a Discernible Photochemical Effect Beyond Heating for Visible Photon-Mediated NH3 Decomposition over Ru/Al2O3?. *The Journal of Physical Chemistry C*, *128*(21), pp.8590-8600.
7. Oshima, T., Ichibha, T., Oqmhula, K., Hibino, K., Mogi, H., Yamashita, S., Fujii, K., Miseki, Y., Hongo, K., Lu, D. and Maezono, R., 2020. Two-Dimensional Perovskite Oxynitride K2LaTa2O6N with an H+/K+ Exchangeability in Aqueous Solution

Forming a Stable Photocatalyst for Visible-Light H2 Evolution. *Angewandte Chemie International Edition*, *59*(24), pp.9736-9743.

8. Song, X., Wei, G., Sun, J., Peng, C., Yin, J., Zhang, X., Jiang, Y. and Fei, H., 2020. Overall photocatalytic water splitting by an organolead iodide crystalline material. *Nature Catalysis*, *3*(12), pp.1027-1033.
9. Oshima, T., Lu, D., Ishitani, O. and Maeda, K., 2015. Intercalation of highly dispersed metal nanoclusters into a layered metal oxide for photocatalytic overall water splitting. *Angewandte Chemie*, *127*(9), pp.2736-2740.
10. Oshima, T., Nishioka, S., Kikuchi, Y., Hirai, S., Yanagisawa, K.I., Eguchi, M., Miseki, Y., Yokoi, T., Yui, T., Kimoto, K. and Sayama, K., 2020. An artificial Z-scheme constructed from dye-sensitized metal oxide nanosheets for visible light-driven overall water splitting. *Journal of the American Chemical Society*, *142*(18), pp.8412-8420.
11. Fang, H., Wu, S., Ayvali, T., Zheng, J., Fellowes, J., Ho, P.L., Leung, K.C., Large, A., Held, G., Kato, R. and Suenaga, K., 2023. Dispersed surface Ru ensembles on MgO (111) for catalytic ammonia decomposition. *Nature Communications*, *14*(1), p.647.
12. Huang, J., Kang, Y., Liu, J., Yao, T., Qiu, J., Du, P., Huang, B., Hu, W., Liang, Y., Xie, T. and Chen, C., 2023. Gradient tungsten-doped Bi3TiNbO9 ferroelectric photocatalysts with additional built-in electric field for efficient overall water splitting. *Nature Communications*, *14*(1), p.7948.
13. Zheng, J., Lu, L., Lebedev, K., Wu, S., Zhao, P., McPherson, I.J., Wu, T.S., Kato, R., Li, Y., Ho, P.L. and Li, G., 2021. Fe on molecular-layer MoS2 as inorganic Fe-S2-Mo motifs for light-driven nitrogen fixation to ammonia at elevated temperatures. *Chem Catalysis*, *1*(1), pp.162-182.

14. Lin, C. H., Lin, H. S., Huang, C. C., Su, S. K., Lin, S. D., Sun, K. W., ... & Shen, J. L., 2009. Temperature dependence of time-resolved photoluminescence spectroscopy in InAs/GaAs quantum ring. *Applied Physics Letters*, *94*(18).
15. Okamoto, K., Niki, I., Scherer, A., Narukawa, Y., Mukai, T., & Kawakami, Y., 2005. Surface plasmon enhanced spontaneous emission rate of InGaN⁄GaN quantum wells probed by time-resolved photoluminescence spectroscopy. *Applied Physics Letters*, *87*(7).
16. Smith, M., Chen, G. D., Lin, J. Y., Jiang, H. X., Asif Khan, M., & Chen, Q., 1996. Time-resolved photoluminescence studies of InGaN epilayers. *Applied physics letters*, *69*(19), 2837-2839.
17. Utsunomiya, A., Okemoto, A., Nishino, Y., Kitagawa, K., Kobayashi, H., Taniya, K., ... & Nishiyama, S., 2017. Mechanistic study of reaction mechanism on ammonia photodecomposition over Ni/TiO_2 photocatalysts. *Applied Catalysis B: Environmental*, *206*, 378-383.
18. Nguyen, H. V. L., Gulaczyk, I., Kręglewski, M., & Kleiner, I., 2021. Large amplitude inversion tunneling motion in ammonia, methylamine, hydrazine, and secondary amines: From structure determination to coordination chemistry. *Coordination Chemistry Reviews*, *436*, 213797.
19. Hiley, C. I., Playford, H. Y., Fisher, J. M., Felix, N. C., Thompsett, D., Kashtiban, R. J., & Walton, R. I., 2018. Pair distribution function analysis of structural disorder by Nb5+ inclusion in ceria: Evidence for enhanced oxygen storage capacity from under-coordinated oxide. *Journal of the American Chemical Society*, *140*(5), 1588-1591.
20. Scavini, M., Coduri, M., Allieta, M., Brunelli, M., & Ferrero, C., 2012. Probing Complex Disorder in Ce1-x Gd x O2-x/2 Using the Pair Distribution Function Analysis. *Chemistry of Materials*, *24*(7), 1338-1345.

21. Osterbacka, N., & Wiktor, J., 2021. Influence of oxygen vacancies on the structure of BiVO4. *The Journal of Physical Chemistry C*, *125*(2), 1200-1207.

22. Qin, Q., Jang, H., Jiang, X., Wang, L., Wang, X., Kim, M. G., ... & Cho, J., 2024. Constructing interfacial oxygen vacancy and ruthenium Lewis acid-base pairs to boost the alkaline hydrogen evolution reaction kinetics. *Angewandte Chemie International Edition*, *63*(3), e202317622.

23. Wang, M., Zhao, G., Bai, X., Yu, W., Zhao, C., Gao, Z., ... & Zhang, N., 2023. Gradient concentration refilling of N stabilizes oxygen vacancies for enhanced Zn2+ storage. *Advanced Energy Materials*, *13*(38), 2301730.

24. Luo, D., Zhang, Z., Li, G., Cheng, S., Li, S., Li, J., Gao, R., Li, M., Sy, S., Deng, Y.P. and Jiang, Y., 2020. Revealing the rapid electrocatalytic behavior of ultrafine amorphous defective Nb2O5-x nanocluster toward superior Li-S performance. *ACS nano*, *14*(4), pp.4849-4860.

25. Josepha, E. A., Farooq, S., Mitchell, C. M., & Wiley, J. B., 2014. Synthesis and thermal stability studies of a series of metastable Dion-Jacobson double-layered neodymium-niobate perovskites. *Journal of Solid State Chemistry*, *216*, 85-90.

26. Liu, Z., Ou, J., Wang, H., You, X., & Ye, M., 2016. Synthesis and characterization of hydrazide-linked and amide-linked organic polymers. *ACS Applied Materials & Interfaces*, *8*(46), 32060-32067.

27. Awsiuk, K., Psarouli, A., Petrou, P., Budkowski, A., Kakabakos, S., Bernasik, A., ... & Raptis, I., 2011. Spectroscopic and microscopic examination of protein adsorption and blocking of non-specific binding to silicon surfaces modified with APTES and GOPS. *Procedia Engineering*, *25*, 334-337.

28. Gao, F. and Teplyakov, A.V., 2017. Monolayer of hydrazine facilitates the direct covalent attachment of C60 fullerene to a silicon surface. *Langmuir*, *33*(35), pp.8632-8639.
29. Rosenberger, L., Baird, R., McCullen, E., Auner, G., & Shreve, G., 2008. XPS analysis of aluminum nitride films deposited by plasma source molecular beam epitaxy. *Surface and Interface Analysis: An International Journal devoted to the development and application of techniques for the analysis of surfaces, interfaces and thin films*, *40*(9), 1254-1261.
30. Ma, H.S., Lee, M.K., Kim, B.H., Park, K.H., Park, J.J., Lee, S.H., Jeong, Y.G., Park, K.I., Jeong, C.K. and Lee, G.J., 2021. Role of oxygen vacancy defects in piezoelectric thermal stability characteristics of Mn-doped (K, Na, Li) NbO3 piezoceramics. *Ceramics International*, *47*(19), pp.27803-27815.
31. Onozato, T., Katase, T., Yamamoto, A., Katayama, S., Matsushima, K., Itagaki, N., Yoshida, H. and Ohta, H., 2016. Optoelectronic properties of valence-state-controlled amorphous niobium oxide. *Journal of Physics: Condensed Matter*, *28*(25), p.255001.
32. Ganesh, S., Khan, F., Ahmed, M.K., Velavendan, P., Pandey, N.K. and Mudali, U.K., 2012. Spectrophotometric determination of hydrazine with para-(dimethylamino) benzaldehyde in aqueous streams of purex process. *Int. J. Nucl. Energy Sci. Eng*, *2*(1).
33. Yang, M., Oró-Solé, J., Rodgers, J.A., Jorge, A.B., Fuertes, A. and Attfield, J.P., 2011. Anion order in perovskite oxynitrides. *Nature chemistry*, *3*(1), pp.47-52.
34. Steinadler, J., Krach, G., Schnick, W., & Bräuniger, T., 2024. Investigation of the Binary Nitrides YN, LaN and LuN by Solid-State NMR Spectroscopy. *Molecules*, *29*(23), 5572.

35. Ogg Jr, R. A., & Ray, J. D., 1957. Quadrupole relaxation and structures in nitrogen magnetic resonances of ammonia and ammonium salts. *The Journal of Chemical Physics*, *26*(5), 1339-1340.

36. Lim, A. R., & Yoon, M. B., 2023. Crystal growth, phase transition, and nuclear magnetic resonance of organic-inorganic hybrid perovskite NH2(CH3)2CdCl 3. *RSC advances*, *13*(37), 26015-26022.

37. Veinberg, S. L., Friedl, Z. W., Lindquist, A. W., Kispal, B., Harris, K. J., O'Dell, L. A., & Schurko, R. W., 2016. 14N Solid-State NMR Spectroscopy of Amino Acids. *ChemPhysChem*, *17*(23), 4011-4027.

38. Fuku, K., Kamegawa, T., Mori, K., & Yamashita, H. (2012). Highly Dispersed Platinum Nanoparticles on TiO_2 Prepared by Using the Microwave‐Assisted Deposition Method: An Efficient Photocatalyst for the Formation of H_2 and N_2 from Aqueous NH_3. *Chemistry–An Asian Journal*, *7*(6), 1366-1371.

39. Lin, J., Wang, Y., Tian, W., Zhang, H., Sun, H. and Wang, S., 2023. Macroporous carbon-nitride-supported transition-metal single-atom catalysts for photocatalytic hydrogen production from ammonia splitting. *ACS Catalysis*, *13*(17), pp.11711-11722.

40. Dzíbelová, J., Hejazi, S.H., Šedajová, V., Panáček, D., Jakubec, P., Baďura, Z., Malina, O., Kašlík, J., Filip, J., Kment, Š. and Otyepka, M., 2023. Hematene: A sustainable 2D conductive platform for visible-light-driven photocatalytic ammonia decomposition. *Applied Materials Today*, *34*, p.101881.

41. Li, J., Sheng, B., Chen, Y., Yang, J., Wang, P., Li, Y., Yu, T., Pan, H., Qiu, L., Li, Y. and Song, J., 2024. Utilizing full-spectrum sunlight for ammonia decomposition to hydrogen over GaN nanowires-supported Ru nanoparticles on silicon. *Nature communications*, *15*(1), p.7393.

Chapter 5 | Moiré-engineered perovskite for thermally assisted photocatalytic NH_3 synthesis

5.1 Abstract

The moiré superlattice has become a widely adopted strategy for engineering 2D materials owing to its capacity to precisely tailor interfacial architectures, thereby enabling fine control over electronic structures and charge carrier dynamics. However, the practical implementation of most superlattice systems remains constrained by the inherently weak interlayer coupling mediated by van der Waals interactions. In this study, we strategically employed tetra-alkyl ammonium cations to control the rotational alignment between 2D Dion-Jacobson perovskite layers, establishing robust interlayer coupling. High-resolution scanning transmission electron microscopy directly resolved moiré patterns, while selected area electron diffraction provided precise twist angle quantification. Crucially, time-resolved photoluminescence spectroscopy revealed exceptional temperature resilience of charge carrier trapping at the 45° twist configuration, and lattice strain is minimised to preserve a large moiré periodicity of ~2.8 nm. This optimal 45°-twisting configuration endows the 2D perovskite with record photocatalytic NH_3 production activity (34.2 mmol $g^{-1}h^{-1}$ at 473 K), attributed to the prolonged lifetime of localised charge carriers. This work showcases the example of integrating moiré engineering into photo-thermal catalysis, fundamentally reshaping our understanding of superlattice functionality and unlocking the potentials for designing energy conversion systems under operational conditions.

5.2 Introduction

Perovskites have emerged as notable materials in photocatalysis, demonstrating exceptional performance in water splitting, CO_2 reduction and organic pollutant degradation.[1] Their intrinsic advantages, including tuneable band structures, high defect tolerance, and rich surface redox chemistry, position them as prime candidates for advancing photocatalytic NH_3 synthesis.[2-9] Nevertheless, the full potential of perovskite-based systems in NH_3 photoproduction remains underexplored, necessitating more investigations and modifications to understand its aptitude. Most recent, moiré superlattice engineering attracts great interests, as it opens avenues for property modulation in perovskite. For instance, moiré superlattice could induce periodic potential landscapes, fundamentally altering the electronic band structures and the charge carrier dynamics.[10-14] However, a critical challenge persists: most experimentally observed moiré effects, particularly those governing electron transport phenomena, are confined to cryogenic environments (< 10 K).[10, 15, 16] This limitation originates from the weak van der Waals interactions in conventional superlattice systems,[17] which yield thermally fragile charge carrier localisation. Unlike van der Waals superlattice materials, perovskite possesses strong ionic bonding networks that enable robust interlayer coupling,[18-20] effectively broadening moiré-induced band splitting while resisting thermal decoherence. Therefore, it would allow the moiré engineering to operate under ambient photocatalytic conditions. Unfortunately, the application of moiré superlattice in photocatalysis remains as an unexplored territory, with no reported studies specifically targeting NH_3 synthesis. Thermal energy input further enhances the performance, with the NH_3 evolution rate increasing to 34.2 mmol g^{-1} h^{-1}. In this work, we precisely tuned the interlayer twist angle in 2D perovskite A'$PrNb_2O_7$ via strategic intercalation of A'-site cations with varying steric bulk, from ammonium (NH_4^+) to tetra-alkyl species: tetra-

methyl ammonium (TMA^+), tetra-ethyl ammonium (TEA^+), tetra-propyl ammonium (TPA^+), and tetra-butyl ammonium (TBA^+). High-angle annular dark-field scanning transmission electron microscopy (HAADF-STEM) combined with FFT analysis resolved the twist angle value and moiré pattern periodicity across the series. Notably, 45° twisted configuration, perovskite magic angle, exhibits a unique electronic confinement effect, significantly extending charge carrier lifetime. Moreover, its reduced lattice strain facilitates bandgap narrowing, improving the light harvesting abilities. As a result, the 45° twisting 2D perovskite demonstrates an exceptional activity of photocatalytic NH_3 synthesis. Our work pioneers moiré engineering in photocatalysis, establishing a platform for solar-driven NH_3 synthesis under practical conditions.

5.3 Results and discussion

5.3.1 Moiré superlattice in 2D perovskite

The Dion-Jacobson phase perovskite $CsPrNb_2O_7$ was firstly synthesised through a conventional solid-state reaction. Stoichiometric mixtures of Pr_6O_{11}, Nb_2O_5, and Cs_2CO_3 were calcined under optimised thermal conditions to obtain the layered precursor. As demonstrated in our previous studies, subsequent proton exchange treatment using concentrated acid can convert $CsPrNb_2O_7$ into $HPrNb_2O_7$ while preserving structural integrity.[21] This protonated derivative exhibits a high crystallinity, evidenced by HAADF-STEM (Figure 5.1a) and the corresponding fast Fourier transform (FFT) images (Figure 5.1b). The observed interplanar spacing of 0.37 nm aligns with the (101) crystallographic plane of $HPrNb_2O_7$ perovskite, confirming a highly ordered 2D layered stacking. Building upon this, we developed a systematic cation intercalation strategy to engineer moiré superlattices.

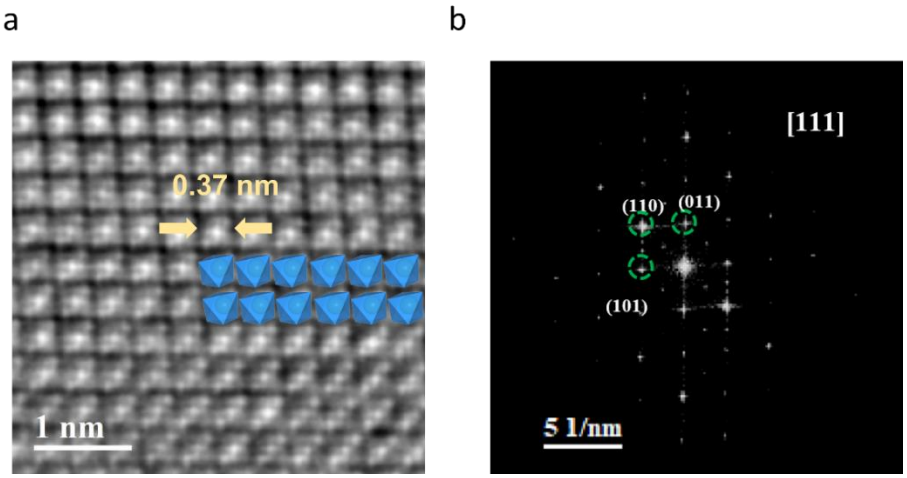

Figure 5.1: (a) HAADF-STEM of $HPrNb_2O_7$ perovskite. (b) Corresponding FFT pattern of $HPrNb_2O_7$ perovskite.

As illustrated in Figure 5.2, a series of quaternary ammonium cations (NH_4^+, TMA^+, TEA^+, TPA^+, and TBA^+) were introduced into the interlayer galleries of $HPrNb_2O_7$ via acid-base interactions. Subsequently, the 2D perovskite samples were isolated from the supernatant using a high-speed centrifuge operating at 12,500 rpm. This process yielded a family of tailored 2D perovskites: $NH_4PrNb_2O_7$, $(TMA)PrNb_2O_7$, $(TEA)PrNb_2O_7$, $(TPA)PrNb_2O_7$, and $(TBA)PrNb_2O_7$.

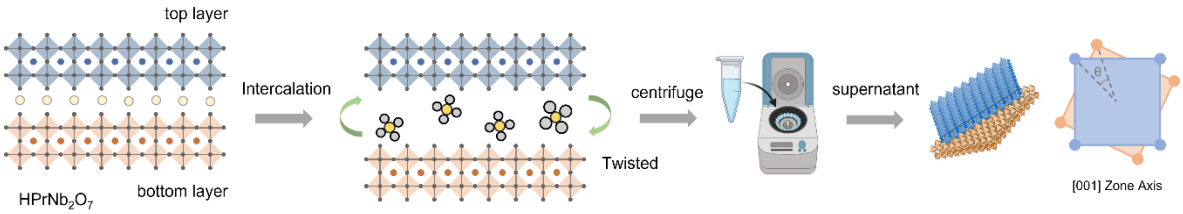

Figure 5.2: Schematic illustration of twist 2D perovskite preparation procedure.

The structural consequences of increasing alkyl chain length in intercalated ammonium cations are clearly evidenced by X-ray diffraction (XRD) analysis. As demonstrated in Figure 5.3a, the (001) diffraction peak systematically shifts toward left, progressing from 7.9° to 3.7° as the cation size expands. This contrasts with the original $HPrNb_2O_7$ material from our previous work, which exhibited a (001) peak at 8.4°. The continuous leftward peak displacement directly correlates with interlayer expansion, providing conclusive evidence of successful cation intercalation through acid-base interactions.[22-24] Then, N 1s X-ray photoelectron spectroscopy (XPS) was used to monitor the chemical states of intercalated ammonium cations within the perovskite framework. A shift to a lower binding energy (BE) was observed with increasing alkyl chain length (Figure 5.3b), a trend attributable to the enhanced electron-donating inductive effect of bulkier alkyl groups.[25-27]

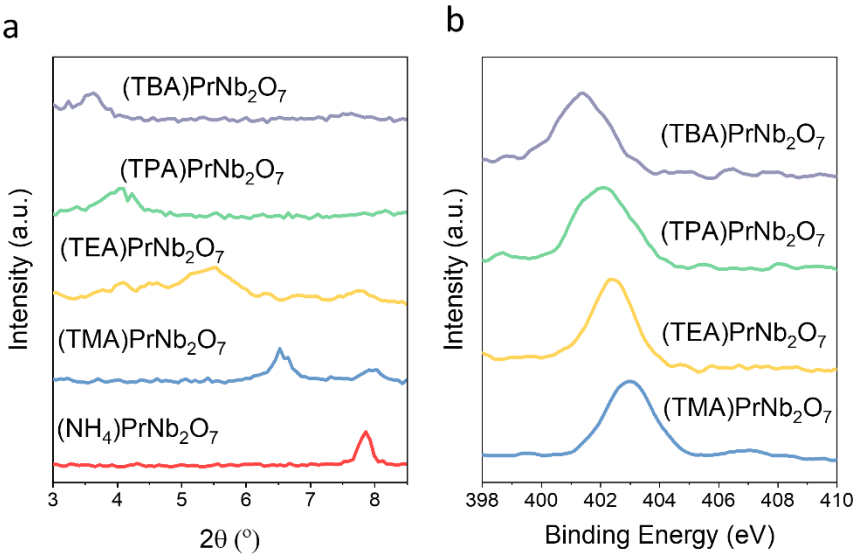

Figure 5.3: (a) XRD pattern and (b) N 1s XPS of different ammonium-cation intercalated perovskite.

In contrast, NH_4^+ incorporated perovskite gives a N 1s signal at 401.7 eV, accompanied by a broadened peak width (Figure 5.4). This peak broadening originates from heterogeneous hydrogen bonding interactions (N-H···O) between NH_4^+ and lattice oxygen atoms, which create discrete chemical environments for nitrogen atoms.[28-30]

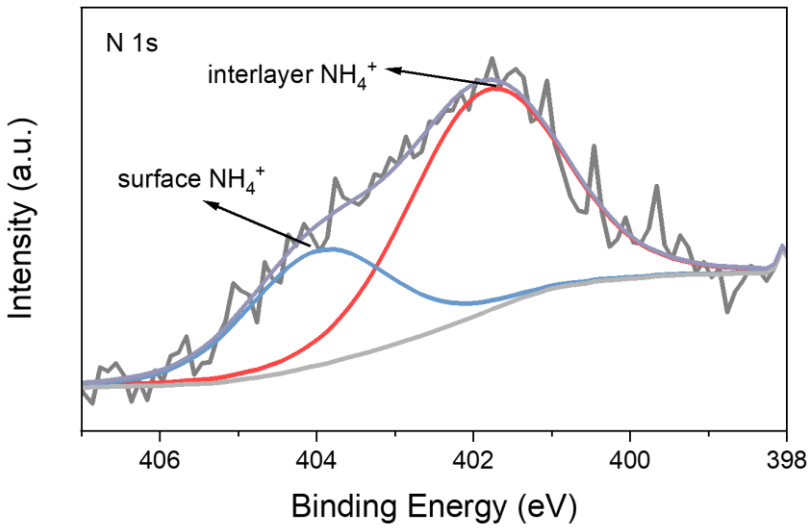

Figure 5.4: N 1s XPS of $(NH_4)PrNb_2O_7$.

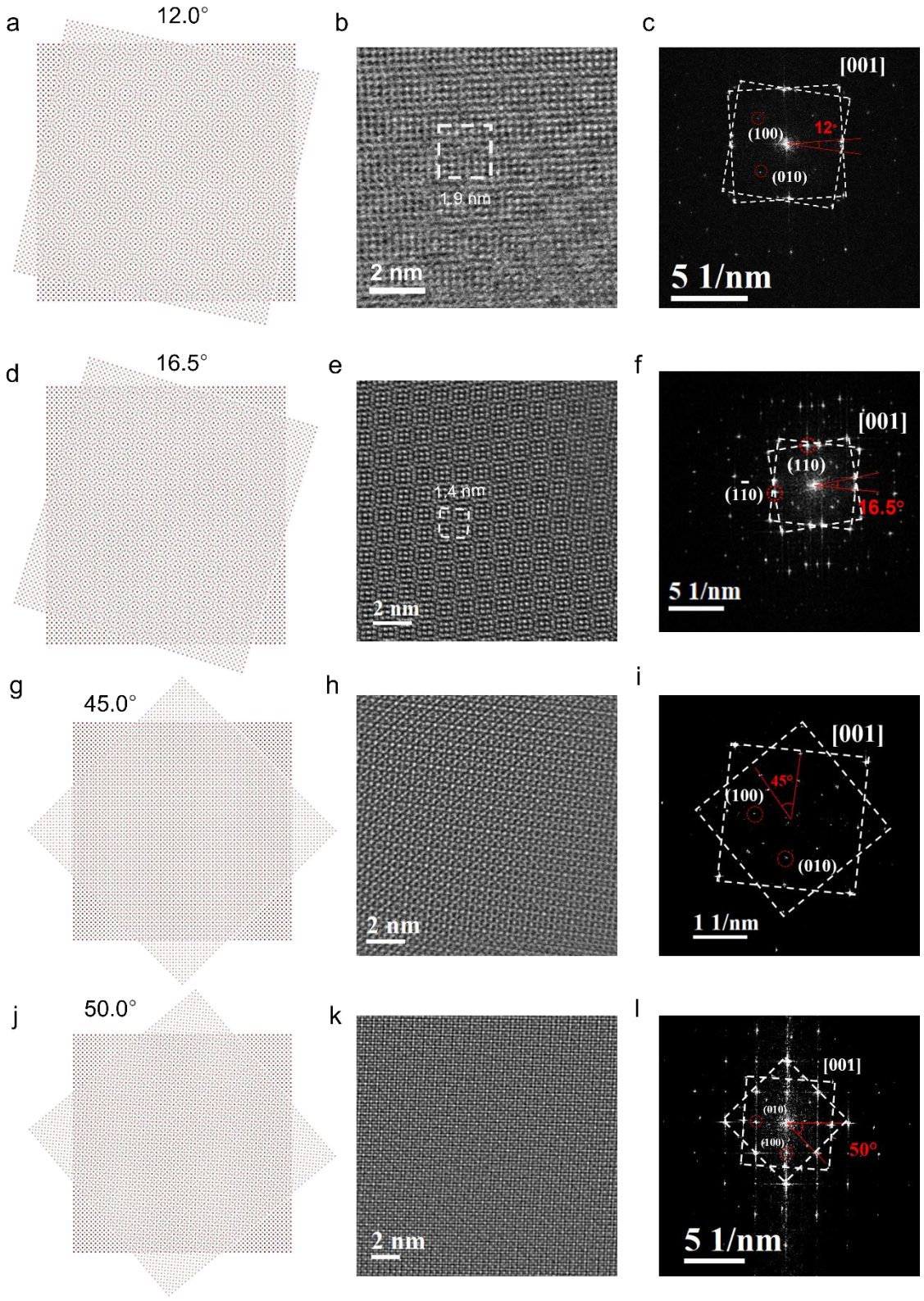

Figure 5.5: (a) Structure model, (b) HAADF-STEM and (c) FFT images of (TEA)$PrNb_2O_7$ 2D perovskite with 12° twist angle. (d) Structure model, (e) HAADF-STEM and (f) FFT images of (TPA)$PrNb_2O_7$ 2D perovskite with 16.5° twist angle. (g)

Structure model, (h) HAADF-STEM and (i) FFT images of (TMA)$PrNb_2O_7$ 2D perovskite with 45° twist angle. (j) Structure model, (k) HAADF-STEM and (l) FFT images of (TBA)$PrNb_2O_7$ 2D perovskite with 50° twist angle.

As the NbO_6 octahedra slabs and tetra-alkyl ammonium cations are stacked along the [001] zone axis, we applied HAADF-STEM coupled with FFT to probe the structural evolution of these angle-engineered 2D perovskite materials. As shown in Figure 5.5c,f, FFT images of (TEA)$PrNb_2O_7$ and (TPA)$PrNb_2O_7$ clearly show two sets of diffraction spots, giving twist angle values of 12° and 16.5°, respectively. In addition, the rotation between the perovskite lattice with small twist angle (θ < 20°) generates square moiré patterns,[10] where the quare moiré pattern periodic length d is determined by the rotation angle θ between the two lattices as:

$$d = \frac{a}{\sqrt{2 - 2\cos\theta}} \quad \text{(Equation 5.1)}$$

where a is the lattice constant of the ordered stacking 2D perovskite (0.39 nm of $HPrNb_2O_7$).[31, 32] The characteristic square moiré patterns can be clearly visualised in the HAADF-STEM images (Figure 5.5b,e), where the moiré pattern periodicity lengths are measured as 1.9 nm (12° twist angle) and 1.4 nm (16.5° twist angle). These experimental values exhibit exceptional agreement with theoretical predictions from Equation 5.1 (1.86 nm and 1.36 nm, respectively). In contrast, structural analysis reveals distinct moiré characteristics under large twist. As evidenced by FFT patterns (Figure 5.5i,l), (TMA)$PrNb_2O_7$ and (TBA)$PrNb_2O_7$ exhibit significantly larger twist angles of 45° and 50°, respectively. Unlike the small twist angle, these configurations produce more complex moiré morphologies in HAADF-STEM images (Figure 5.5h,k), where square moiré patterns no longer exist.[10, 33] This structural transition coincides

with the breakdown of the moiré periodicity-length equation (Equation 5.1), suggesting altered lattice coupling mechanisms beyond simple rigid rotation at high twist angles. To confirm the spatial uniformity of these twist configurations, we conducted HAADF-STEM scans together with the corresponding FFT images across the [001] zone axis at various regions (Figure A5.1 – A5.4 in Appendices). All measured regions consistently reproduced the respective twist angles for each composition, confirming homogeneous interlayer registry throughout the samples. Notably, control experiments with $(NH_4)PrNb_2O_7$ showed neither discernible twist angles in FFT patterns nor moiré patterns in HAADF-STEM images (Figure A5.5 in Appendices), highlighting the critical role of alkylammonium chain in driving interlayer rotation.

5.3.2 Photocatalytic performance of ammonia synthesis

The photocatalytic nitrogen fixation performance was systematically evaluated in a sealed batch reactor with simulated solar irradiation (AM1.5G, 100 mW cm^{-2}) using a N_2/H_2 mixture under a pressure of 6 bar. To minimise operational cost, we deliberately kept the H_2 fraction as low as practicable. Although higher H_2 fractions can improve reaction rates, they also increase the operating expenses, raise the risk of catalyst over-reduction and hydrogen poisoning, and impose stricter safety and ventilation requirements. Conversely, excessively low H_2 fractions may be insufficient to drive detectable ammonia formation at room temperature due to sluggish hydrogenation kinetics. For example, an initially tested 9.5:0.5 (v/v) N_2/H_2 mixture exhibited negligible ammonia synthesis activity at ambient conditions. However, when the N_2:H_2 ratio is increased to 9:1 (v/v), measurable ammonia production is observed, while cost, handling complexity, and safety risks remain comparatively low. Therefore, 9:1 (v/v) N_2/H_2 ratio enhanced the surface hydrogenation steps without incurring the large cost and safety penalties associated with substantially H_2 feeds.

Prior to testing, all catalysts were pre-treated at 473 K under an Ar flow to remove the surface-adsorbed ammonium and water species.

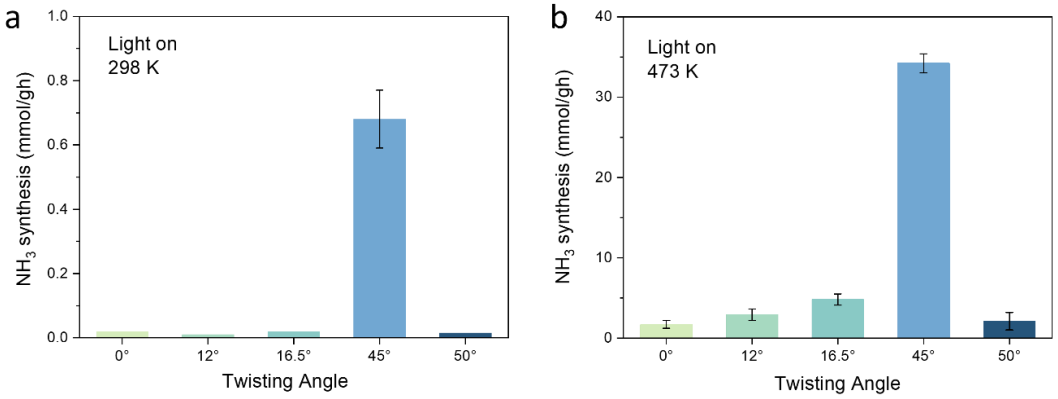

Figure 5.6: Photocatalytic activity of NH_3 synthesis over different twisted 2D perovskite under light illumination at (a) 298 K and (b) 473 K.

As shown in Figure 5.6, twist-angle dependence of NH_3 production across the 2D perovskite is illustrated, labelled with their interlayer rotation: 0° [$(NH_4)PrNb_2O_7$], 12° [$(TEA)PrNb_2O_7$], 16.5° [$(TPA)PrNb_2O_7$], 45° [$(TMA)PrNb_2O_7$], and 50° [$(TBA)PrNb_2O_7$]. At 298 K, only 45°-twisted 2D perovskite exhibits catalytic activity, with an NH_3 production rate of ~0.7 mmol $g^{-1}h^{-1}$. As temperature increasing to 473 K, NH_3 synthesis activity across all twisted 2D perovskite is universally enhanced, with the 45°-twisted system achieving an excellent activity of 34.2 mmol $g^{-1}h^{-1}$.

Our temperature-dependent analysis of the 45°-twisted 2D perovskite (Figure 5.7a) highlights the importance of thermal activation. Moreover, experiments under light-off conditions shows a contrast: while thermal energy alone enables modest NH_3 production (7.3 mmol $g^{-1}h^{-1}$ at 473 K), coupling with solar simulator irradiation increases the yield fivefold to 34.2 mmol $g^{-1}h^{-1}$, which reals a photo-thermal synergy for NH_3 synthesis. For the 45°-twisted 2D perovskite catalyst, we evaluated its stability over five cycles (Figure 5.7b) and observed no significant loss in activity.

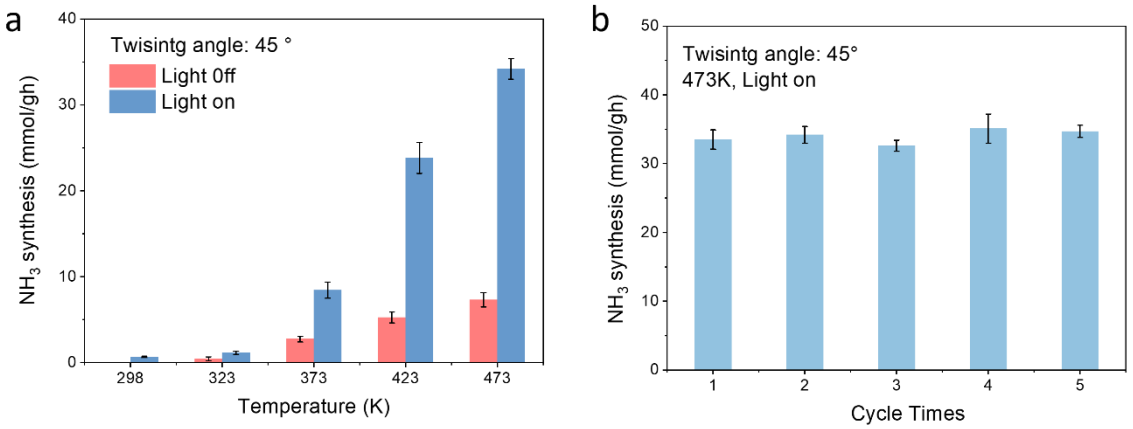

Figure 5.7: (a) Photocatalytic activity of NH_3 synthesis over 45°-twisted 2D perovskite under different catalytic condition. (b) Activity stability test of 45°-twisted 2D perovskite.

HAADF-STEM and FFT images were acquired to further investigate the material structures before and after the photocatalytic reaction (Figure A5.6 in Appendices). The results showed that the layers stayed firmly at 45°, confirming the structural stability of the catalyst. In addition, XRD analysis (Figure A5.7 – A5.11 in Appendices) was performed over all the twisted 2D perovskite, confirming that the crystal structure remained intact throughout the test, and ICP-MS analysis (Figure 5.8a) reveals that Pr wt.% in the twisted 2D perovskite remains unchanged before and after the reaction, demonstrating the catalyst's robustness. Controlled experiments under an Ar atmosphere showed no detectable NH_3 formation under light illumination at 473 K for any of the twisted 2D perovskites, confirming that NH_3 production arises exclusively from the N_2 and H_2 gas mixture. To demonstrate that the enhanced activity is due to twist-angle tuning, we compared it with $CsPrNb_2O_7$, which features a well-ordered [001] stacking. After pre-treating $CsPrNb_2O_7$ with either $(NH_4)OH$ or (TMA)OH, we ran five NH_3 production test cycles (Figure 5.8b). In both cases, only trace amounts of NH_3 were detected, showing that the ammonium cations themselves do not contribute directly to the photocatalytic activity.

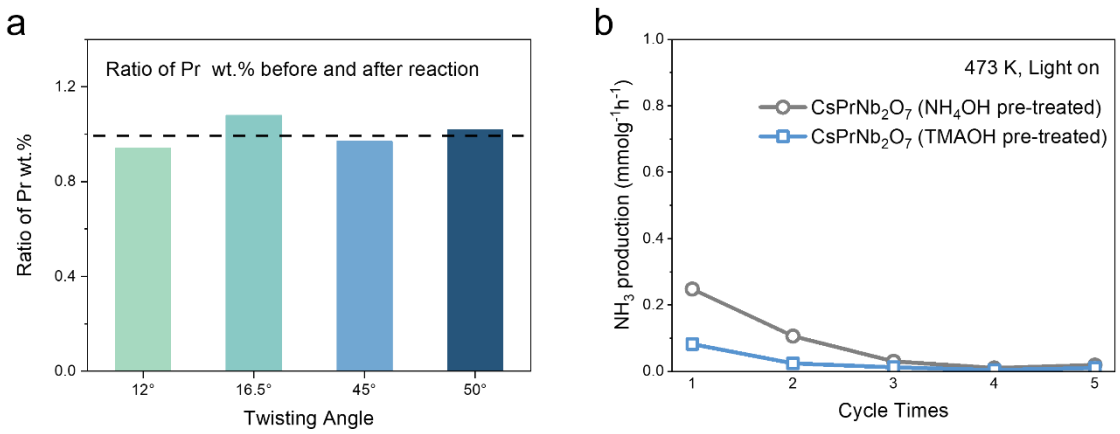

Figure 5.8: (a) The ratio of Pr wt.% in twisted 2D perovskite before and after the photo-thermal NH_3 synthesis test. Standard derivatives were not provided because ICP-MS measurements were not repeated. (b) NH_3 production at 473 K under solar simulator over 50 mg of $CsPrNb_2O_7$ perovskite, which was pre-treated with $(NH_4)OH$ and TMAOH, respectively.

Furthermore, a light-concentrated furnace was used to mimic a solar furnace, showing that stable and efficient NH_3 synthesis activity at 473 K could be maintained solely by the concentrated light without any other external heating devices. A more exceptional activity of 54.4 mmol $g^{-1}h^{-1}$ was observed on 45° twisted 2D perovskite due to the high intensity of the concentrated light. Compared to other catalysts reported for NH_3 synthesis, the 45°-twisted $(TMA)PrNb_2O_7$ stands out with exceptional activity at moderately elevated temperatures (Figure 5.9).

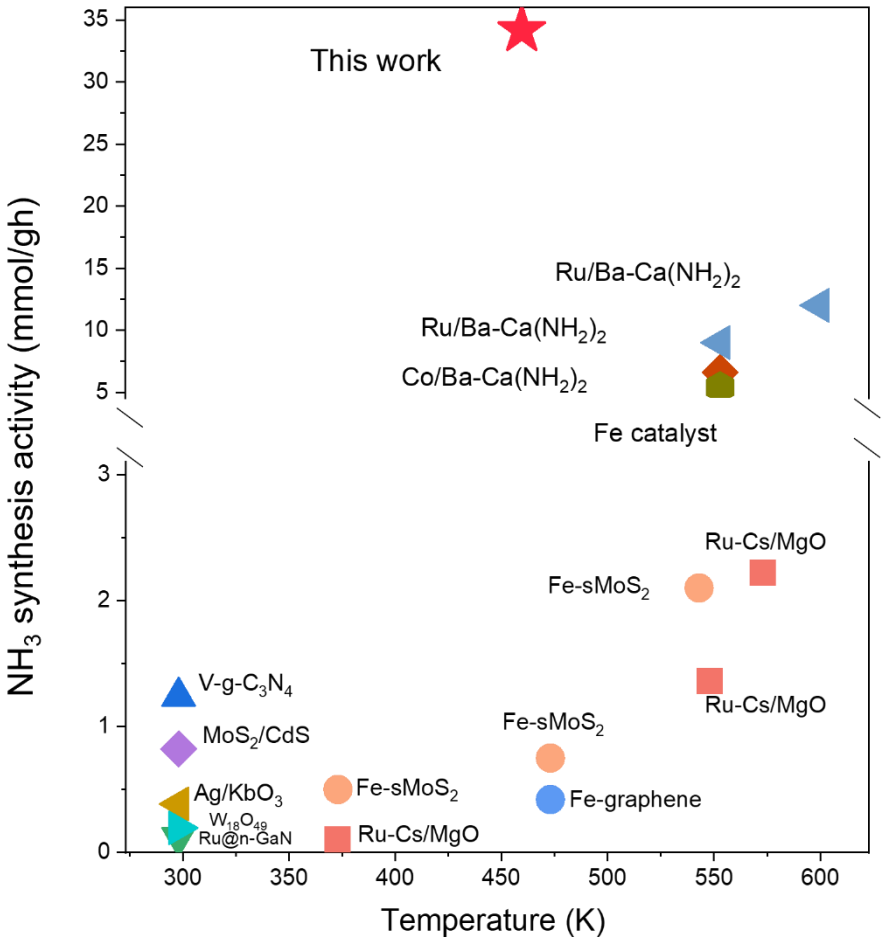

Figure 5.9: NH_3 synthesis activity comparison between this work and reported material. All the condition details are summarised in Table 5.1.

Catalysts	Light source	Reactant	Activity ($mmolg^{-1}h^{-1}$)	Ref.
$TMAPrNb_2O_7$(473K)	Solar simulator	H_2, N_2	34.2	This work
V-g-C_3N_4	> 420nm	H_2O, N_2	1.2	[54]
Fe-graphene(473K)	200-600 nm	H_2O, N_2	0.4	[55]
MoS_2/CdS	420-780 nm	H_2O, N_2	0.8	[56]
Ru@n-GaN	290-380 nm	H_2, N_2	0.1	[57]
$W_{18}O_{49}$	300W Xe lamp	H_2O, N_2	0.2	[58]
Fe-sMoS_2(543K)	70W W lamp	H_2O, N_2	2.1	[36]
Ag/$KNbO_3$	> 420nm	H_2O, N_2	0.4	[2]
Ru-Cs/MgO(550K)	Prizmatix LED	H_2, N_2	2.1	[59]
Co/Ba-Ca$(NH_2)_2$(573K)	N/A	H_2, N_2	6.6	[60]
Fe catalyst	N/A	H_2, N_2	5.4	[60]

Table 5.1: Comparison of photocatalytic ammonia synthesis with materials in other literatures.

To monitor *in situ* NH_3 formation, we performed DRIFTS on the 45°-twisted 2D perovskite catalyst. Under a N_2 and H_2 atmosphere at 295 K (Figures 5.10a and 5.10b), no NH_3-related bands were observed between 1000 and 1350 cm^{-1}. As the temperature rose under light illumination, distinct peaks emerged at 1097, 1201, 1274, 1307, and 1467 cm^{-1}, corresponding to -NH_2 twisting, adsorbed *NH_3, -NH_2 wagging, adsorbed *NH_3, and δ(H-N-H) bending modes, respectively.[34-36]

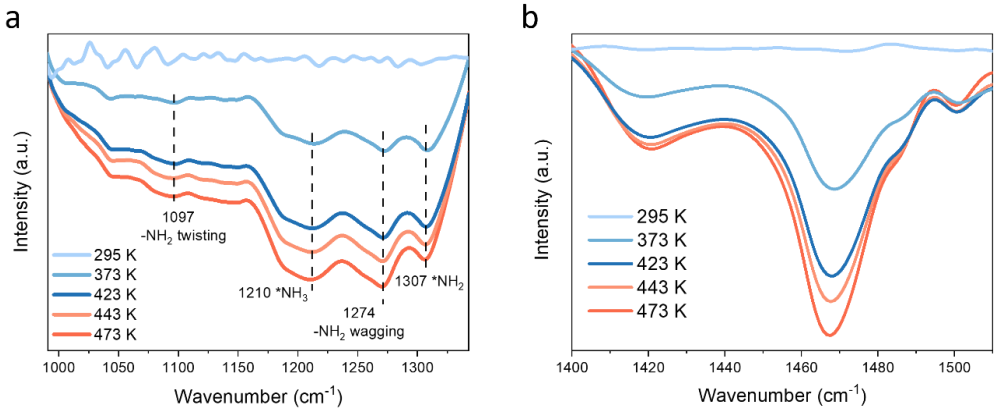

Figure 5.10: DRFITS of 45°-twisted 2D perovskite with N_2-H_2 gas mixture (9:1 v/v) under light illumination at different temperature.

In contrast, $CsPrNb_2O_7$ shows no significant signals until it was held at 473 K for 30 minutes (Figure 5.11). These results underscore how twist-angle engineering dramatically enhances the catalyst's ability to activate and convert N_2 under mild conditions.

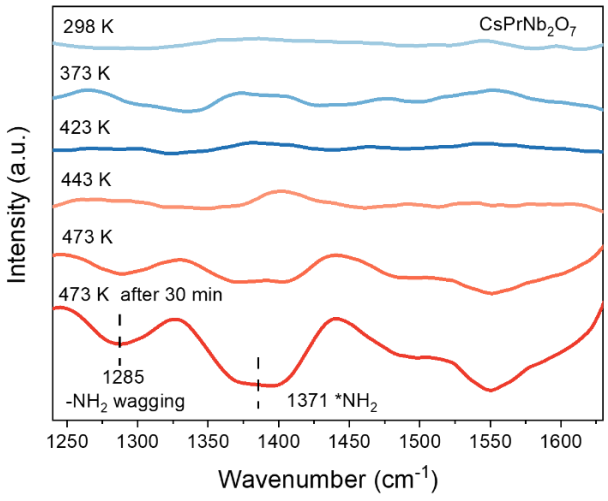

Figure 5.11: DRFITS of $CsPrNb_2O_7$ with N_2-H_2 gas mixture (9:1 v/v) under light illumination at different temperature.

It is widely accepted that separation of the photogenerated charge carriers plays a vital role in photocatalysis. Therefore, time-resolved photoluminescence (TRPL) spectroscopy was applied to investigate the photogenerated charge carrier dynamics. Two decay components could be identified by fitting the TRPL spectra in Figure A5.12 – A5.14 in Appendices: a fast recombination attributed to bulk recombination and a slower component associated with surface recombination processes.[37, 38] Twisted 2D perovskite at 298 K was first studied (Figure 5.12a), where 45° twisted 2D perovskite exhibits the longest exciton lifetime (Figure 5.12b).

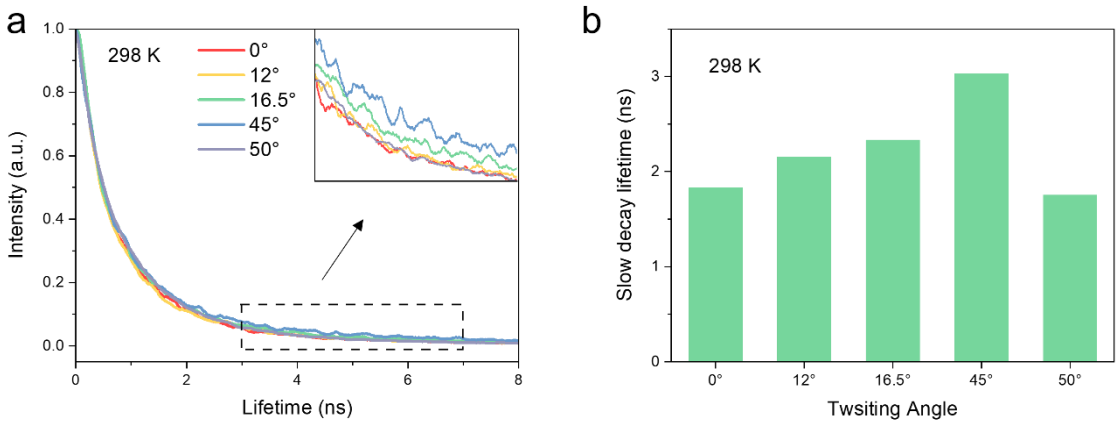

Figure 5.12: (a) TRPL spectra of different twist angle 2D perovskite at 298 K. (b) Charge carrier lifetime changes as perovskite twist angle variation at 298 K.

Early studies have proposed that exciton lifetime in superlattice is strongly correlated to the moiré pattern periodicity, where the photogenerated charge carriers can be trapped by the induced moiré potential.[10, 18, 39, 40] In the 45°-twisted 2D perovskite, the moiré pattern shifts from the square shape seen at 12° or 16.5° (Figure 5.13b, c) to a rhombic

network with a 2.8 nm moiré pattern periodicity (Figure 5.13a), which is more than six times the orderly stacking 2D perovskite lattice constant (~0.39 nm).[41]

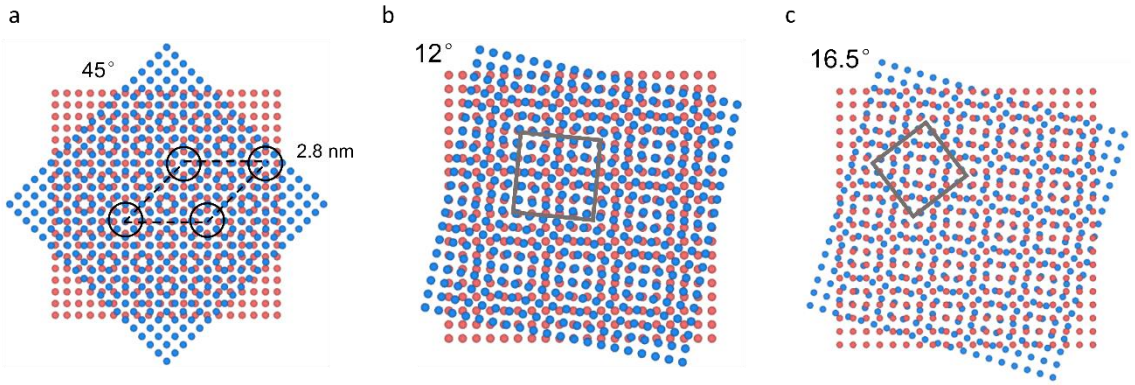

Figure 5.13: Moiré patterns in (a) 45°, (b) 12°, and (c) 16.5° twisted 2D perovskite.

As shown in Figure 5.14.a, the 45°-twisted 2D perovskite has the largest real-space moiré period, corresponding to a smaller mini-Brillouin zone in momentum space thus an extensive folding of the original band structure.[42, 43] This zone folding could generate a dense ladder of moiré minibands whose individual dispersions become progressively flatter, creating deep potential wells that trap charge carriers within the moiré supercell.[44] The stronger localisation would inhibit nonradiative recombination pathways, markedly extending exciton lifetimes.[18] Moreover, the bottom-top layer coupling is also crucial for the moiré exciton localisation. 45° twist angle has the shortest interlayer distance among the twist angle perovskite (Figure 5.14b).[45] This is because TMA^+ cations have shorter alkyl chain length, where the smaller size and higher charge density would strongly assembly the NbO_6 perovskite slabs. Therefore, this can yield more localised charge carrier density in the twisted layer structure due to a stronger interlayer anion coupling. Furthermore, in contrast to van der Waals superlattice materials like transition metal dichalcogenides or graphene, twisted 2D perovskite in this work contains alkyl ammonium cations at interlayer, which providing addition means in tuning

moiré excitons.[18] Compared to 0.9 nm distance between top-layer Nb and bottom-layer Nb in the 45°-twisted perovskite structure, TMA^+ cation with only a 0.3 nm radius can rotate freely at interlayer, modulating the moiré potentials to further separate photoexcited electrons and holes.

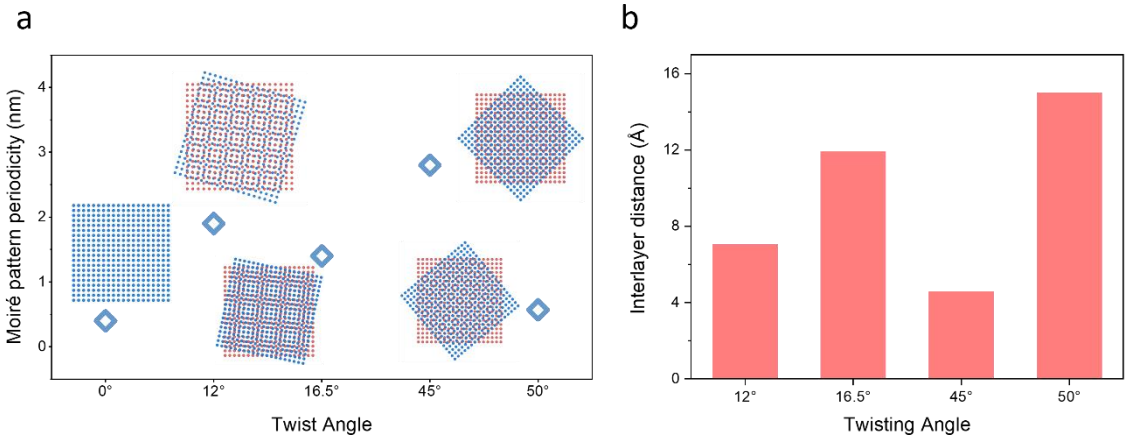

Figure 5.14: (a) Moiré patterns periodicity varies with the twist angle. (b) Interlayer distance for different twist angle (intercalated ammonium cations) estimated by the Bragg's Law.

To probe the charge carrier dynamics at a higher temperature, we performed TRPL measurements at 473 K (Figure 5.15a). All twisted perovskite samples exhibited prolonged charge carrier lifetimes under this condition (Figure 5.15b). Then we measured the charge carrier lifetime in the 45°-twisted 2D perovskite over a temperature range of 298 K to 523 K using TRPL (Figure 5.15c, d). At first, the average lifetime rose as the temperature increased, indicating that input thermal energy promotes charge mobility, likely facilitating electron interlayer tunnelling, thereby suppressing recombination. However, above approximately 500 K, thermal fluctuations are sufficient to disrupt the long-range moiré superlattice, collapsing the periodic potential and sharply reducing the moiré exciton lifetime.[46]

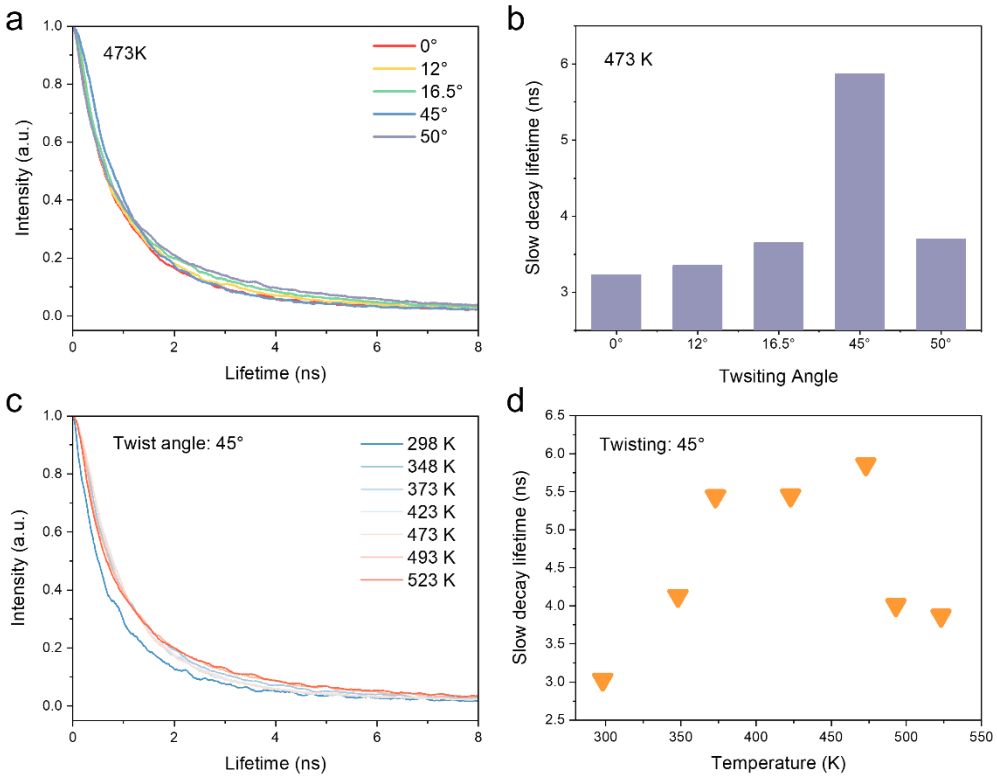

Figure 5.15: (a) TRPL spectra of different twist angle 2D perovskite at 473 K. (b) Charge carrier lifetime changes as perovskite twist angle variation at 473 K. (c) TRPL spectra of 45° twist angle 2D perovskite at different temperature. (d) Charge carrier lifetime changes with temperature for 45° twist angle 2D perovskite.

Interestingly, a blue shift of the emission is observed in the normalised steady-state photoluminescence (SSPL) spectra of the 45°-twisted 2D perovskite as the temperature increases in a pseudo-colour plot (Figure 5.16a). And the blue shift of the PL peak is as large as about 100 meV from 298 K to 498 K. The possible origin of this band gap shift is the photo-induced band filling. The blue shift of the optical band gap is a consequence of the charge carriers filling of the densities of states, as schematically shown in Figure 5.16b. As the moiré potential localised the charge carrier, the low-energy state miniband would be saturated. Therefore, carriers have to fill band edge states, with a consequent blue shift of the transition energy.[47] Moreover, the partial quenching on the peak intensity as temperature increase in Figure 5.16a aligns with our TRPL study (Figure 5.15c, d), in which the electron-hole pair recombination is inhibited and lifetime is prolonged at elevated temperature.

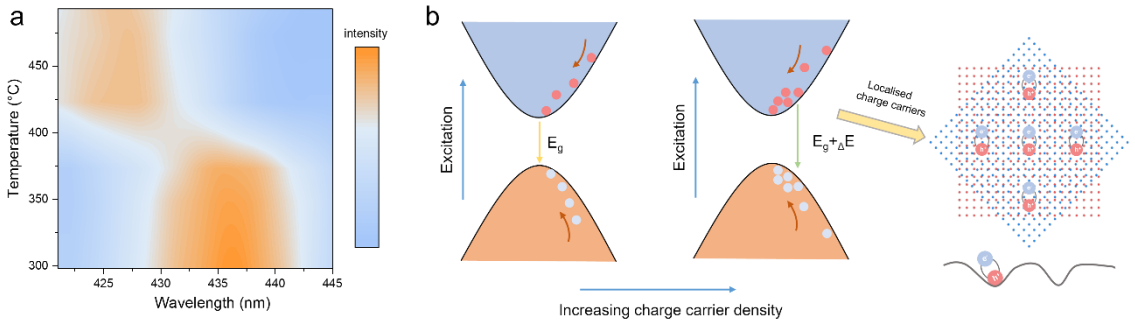

Figure 5.16: (a) Temperature dependent SSPL spectra of 45° twist angle 2D perovskite from 298 K to 498 K. (b) Schematic of the mechanism for the blue shift of the photoluminescence as a result of band filling.

It is well known that twist angle between interlayer could trigger substantial lattice strain effect.[48, 49] Therefore, X-ray absorption spectroscopy (XAS) is employed to understand the nature of structural variation of the twisted 2D perovskite materials. First,

X-ray absorption near-edge structure (XANES) at Nb K-edge (Figure 5.17) shows all the twist angle perovskite has higher near-edge absorption energies than NbO_2, but as same as that of Nb_2O_5. It suggests that Nb^{5+} remain its valence state at various twist angle.

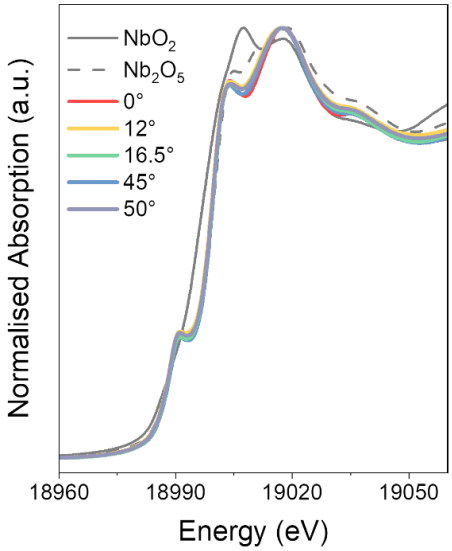

Figure 5.17: Comparison of Nb K-edge XANES spectra for NbO_2, Nb_2O_5 and the twist-angle perovskite materials.

The Fourier transformed extended X-ray absorption fine structure (EXAFS) spectra (Figure 5.18a) of twisted perovskite depicts peak components between 1.1 – 2.0 Å and 2.7 – 4.0 Å as a result of the Nb-O and Nb-Nb scattering pair, respectively.[50] It is worth to note that in the sample of 0° twisted perovskite [$(NH_4)PrNb_2O_7$], the peak assigned to Nb-O shows a reduced intensity with a peak-width broadening and the peak assigned to Nb-Nb experience a splitting. This is because the intercalated NH_4^+ cations can interact with the perovskite oxygen, where the NH···O interaction severely distorts the NbO_6 octahedra. We could observe that as the twist angle increasing, the peak position of Nb-Nb shifts from 3.3 Å (12° twist angle) to 3.1 Å (45° twist angle). It means that 45° twist angle 2D perovskite experienced less structural distortion induced by the atomic reconstruction. Because the large twist angle superlattice materials have larger area of the

AB stacking region (metal vertically mismatches in Figure 5.18c) than the AA stacking region (metal vertically stacks in Figure 5.18d), while the AA stacking regions have much higher energy in its local energy landscape than AB stacking.[51] Therefore, small twist angle perovskite (12° and 16.5°) tends to reshape by increasing the area of the AB stacking regions, experiencing locally inhomogeneous strains which triggers the structural distortion.[48] But large twist angle perovskite (45° and 50°) does not have to. The fitting in the EXAFS region (Figure A5.15 in Appendices) helps to unveil the trend of distortion. As shown in Figure 5.18b, 45° twisted 2D perovskite has the shortest Nb-O bond length around 2.02 Å, indicating less effective structural distortion.

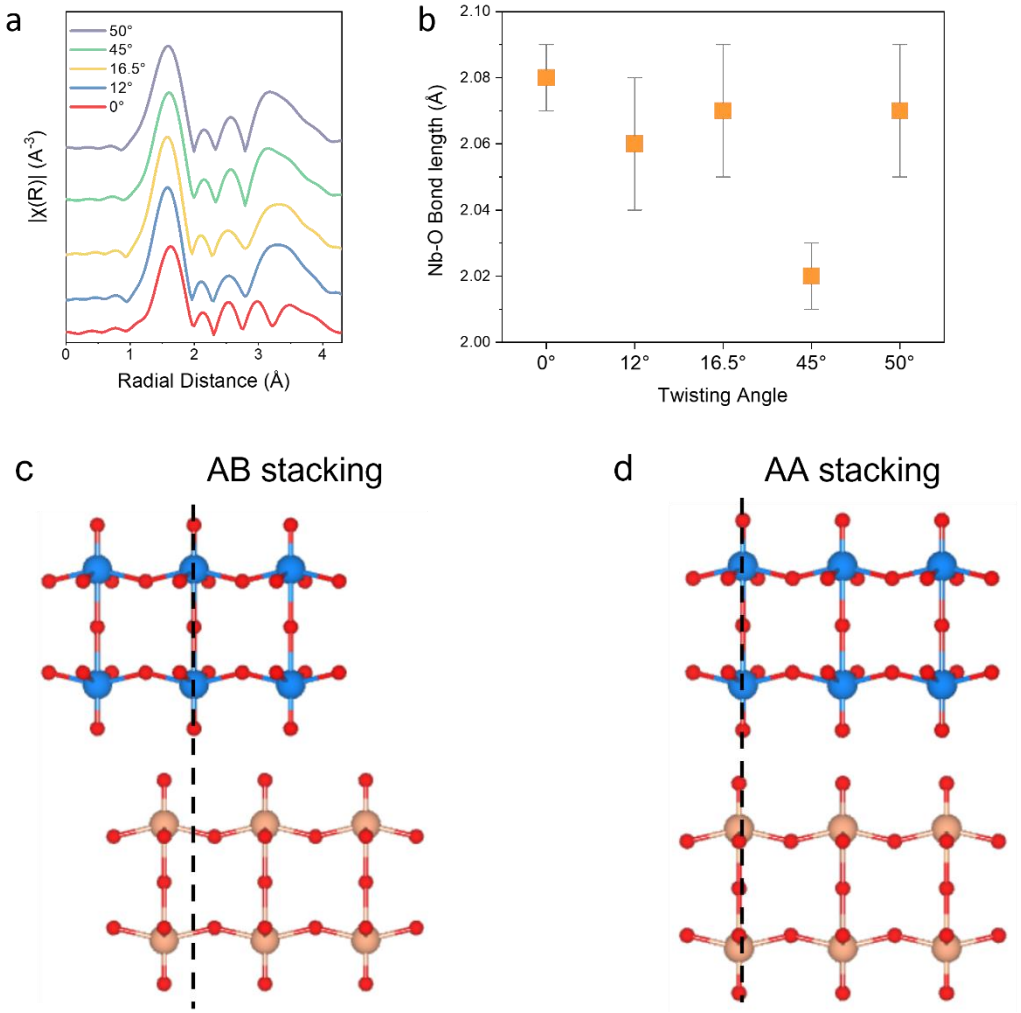

Figure 5.18: (a) Fourier transformed EXAFS spectra at Nb K-edge of different twist angle perovskite. (b) Fourier transformed EXAFS fitting results of the Nb-O length for different twist angle perovskite. Demonstrating graphs of (c) AB stacking and (d) AA stacking in twisted 2D perovskite.

The inhomogeneous strain in superlattice materials could lead to a spatial modulation of the phonon-exciton coupling, collective vibrations, and electronic wavefunctions.[48] Especially, such induced structural distortion and reconstruction could augment the band gap of perovskite.[52, 53] By tauc plot and valence band XPS (Figure A5.16, A5.17 in Appendices), we demonstrate the band alignments of different twist angle perovskite (Figure 5.19a). As shown in Figure 5.19b, 45° twisted 2D perovskite has the smallest bandgap of 2.86 eV, further improving the efficiency of photon energy utilisation to improve the photocatalytic performance.

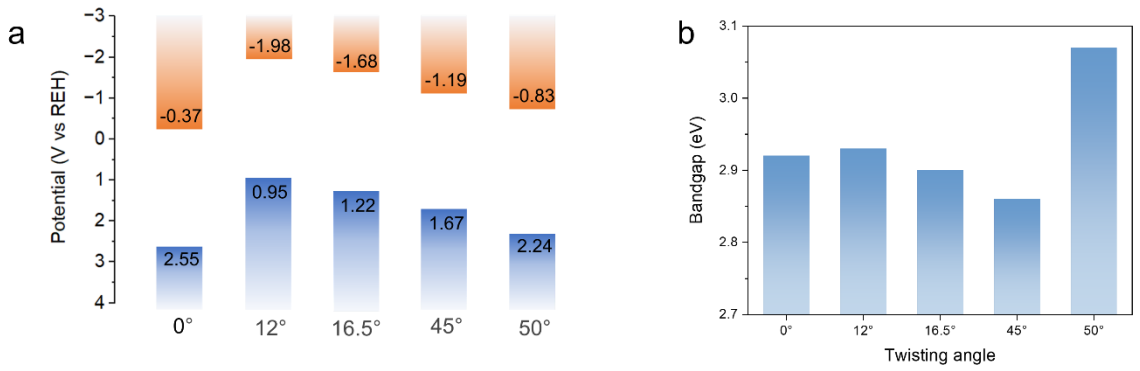

Figure 5.19: (a) Band alignment of different twist angle perovskite. (b) Bandgap value for different twist angle perovskite.

5.4 Conclusion

In this study, we successfully employed tetra-alkyl ammonium cations to precisely control the twist angle between adjacent 2D perovskite layers, enabling the formation of a robust moiré superlattice. At a 45^{o} twist, recognised as the “magic angle”, the resulting superlattice exhibited a large periodicity of ~2.8 nm, which created deep potential wells for effective trapping of photogenerated charge carriers. This configuration significantly prolonged carrier lifetimes, suppressed recombination pathways, and enhanced charge separation. Strong electrostatic coupling between layers further stabilised the 45^{o} superstructure, maintaining its integrity even under elevated temperatures and operational conditions. Moreover, the absence of energetically unfavourable AA-stacked regions at the 45^{o} twist minimised inhomogeneous strain, resulting in reduced structural distortion and a narrower bandgap. These synergistic effects culminated in an outstanding photocatalytic NH_3 production rate of 34.2 mmol g^{-1} h^{-1} at 473 K, surpassing previously reported systems and demonstrating the critical role of moiré engineering in enhancing photocatalytic performance. To the best of our knowledge, this work represents the first successful integration of moiré superlattice engineering into thermal-assisted photocatalysis, offering new insights into the design of high-performance catalysts for sustainable energy applications. The findings not only establish a clear structure-property-performance relationship but also open promising avenues for the development of advanced materials capable of efficient energy conversion and chemical synthesis under practical conditions.

5.5 Reference

1. Kumar, A., A. Kumar, and V. Krishnan., 2020. Perovskite oxide based materials for energy and environment-oriented photocatalysis. *Acs catalysis*, 10(17): p. 10253-10315.
2. Xing, P., Wu, S., Chen, Y., Chen, P., Hu, X., Lin, H., ... & He, Y., 2019. New application and excellent performance of Ag/KNbO3 nanocomposite in photocatalytic NH3 synthesis. *ACS Sustainable Chemistry & Engineering*, *7*(14), 12408-12418.
3. Xing, P., Zhang, W., Chen, L., Dai, X., Zhang, J., Zhao, L., & He, Y., 2020. Preparation of a NiO/KNbO3 nanocomposite via a photodeposition method and its superior performance in photocatalytic N2 fixation. *Sustainable Energy & Fuels*, *4*(3), 1112-1117.
4. Zhang, H., Li, X., Su, H., Chen, X., Zuo, S., Yan, X., ... & Yao, C., 2019. Sol–gel synthesis of upconversion perovskite/attapulgite heterostructures for photocatalytic fixation of nitrogen. *Journal of Sol-Gel Science and Technology*, *92*, 154-162.
5. Tao, R., Li, X., Li, X., Shao, C., & Liu, Y., 2020. TiO 2/SrTiO 3/gC 3 N 4 ternary heterojunction nanofibers: gradient energy band, cascade charge transfer, enhanced photocatalytic hydrogen evolution, and nitrogen fixation. *Nanoscale*, *12*(15), 8320-8329.
6. Mansingh, S., Sultana, S., Acharya, R., Ghosh, M. K., & Parida, K. M., 2020. Efficient photon conversion via double charge dynamics CeO2–BiFeO3 p–n heterojunction photocatalyst promising toward N2 fixation and phenol–Cr (VI) detoxification. *Inorganic Chemistry*, *59*(6), 3856-3873.

7. Li, X., He, C., Dai, D., Zuo, S., Yan, X., Yao, C., & Ni, C., 2020. Nano-mineral induced nonlinear optical LiNbO3 with abundant oxygen vacancies for photocatalytic nitrogen fixation: boosting effect of polarization. *Applied Nanoscience*, *10*, 3477-3490.
8. Zhang, C., Chen, G., Lv, C., Yao, Y., Xu, Y., Jin, X., & Meng, Q., 2018. Enabling nitrogen fixation on Bi2WO6 photocatalyst by c-PAN surface decoration. *ACS Sustainable Chemistry & Engineering*, *6*(9), 11190-11195.
9. Zhou, S., Zhang, C., Liu, J., Liao, J., Kong, Y., Xu, Y., & Chen, G., 2019. Formation of an oriented Bi 2 WO 6 photocatalyst induced by in situ Bi reduction and its use for efficient nitrogen fixation. *Catalysis Science & Technology*, *9*(20), 5562-5566.
10. Zhang, S., Jin, L., Lu, Y., Zhang, L., Yang, J., Zhao, Q., ... & Huang, L., 2024. Moiré superlattices in twisted two-dimensional halide perovskites. *Nature Materials*, *23*(9), 1222-1229.
11. Que, Z. X., Li, S. Z., Huang, B., Yang, Z. X., & Zhang, W. B., 2024. Ultra-flat bands at large twist angles in group-V twisted bilayer materials. *The Journal of Chemical Physics*, *160*(19).
12. Bistritzer, R., & MacDonald, A. H., 2011. Moiré bands in twisted double-layer graphene. *Proceedings of the National Academy of Sciences*, *108*(30), 12233-12237.
13. Wu, F., Lovorn, T., Tutuc, E., & MacDonald, A. H., 2018. Hubbard model physics in transition metal dichalcogenide moiré bands. *Physical review letters*, *121*(2), 026402.

14. Zhao, X. J., Yang, Y., Zhang, D. B., & Wei, S. H., 2020. Formation of bloch flat bands in polar twisted bilayers without magic angles. *Physical review letters*, *124*(8), 086401.
15. Cao, Y., Fatemi, V., Fang, S., Watanabe, K., Taniguchi, T., Kaxiras, E., & Jarillo-Herrero, P., 2018. Unconventional superconductivity in magic-angle graphene superlattices. *Nature*, *556*(7699), 43-50.
16. Choi, J., Hsu, W. T., Lu, L. S., Sun, L., Cheng, H. Y., Lee, M. H., ... & Chang, W. H., 2020. Moiré potential impedes interlayer exciton diffusion in van der Waals heterostructures. *Science advances*, *6*(39), eaba8866.
17. Halbertal, D., Klebl, L., Hsieh, V., Cook, J., Carr, S., Bian, G., ... & Basov, D. N., 2023. Multilayered atomic relaxation in van der Waals heterostructures. *Physical Review X*, *13*(1), 011026.
18. Zhang, L., Zhang, X., & Lu, G., 2021. Predictions of moiré excitons in twisted two-dimensional organic–inorganic halide perovskites. *Chemical Science*, *12*(17), 6073-6080.
19. Zhu, X., Xu, Z., Zuo, S., Feng, J., Wang, Z., Zhang, X., ... & Yang, D., 2018. Vapor-fumigation for record efficiency two-dimensional perovskite solar cells with superior stability. *Energy & Environmental Science*, *11*(12), 3349-3357.
20. Yang, Y., Gao, F., Gao, S., & Wei, S. H., 2018. Origin of the stability of two-dimensional perovskites: a first-principles study. *Journal of Materials Chemistry A*, *6*(30), 14949-14955.
21. Zhang, H., Wang, Y., Niu, W., Yoskamtorn, T., Luo, M., Tayler, R., ... & Tsang, S. C. E., 2024. Tuning 2D perovskite–graphene layered composite for photocatalysis. *Sustainable Energy & Fuels*, *8*(15), 3362-3371.

22. Tian, Y., Zhang, X., Zhao, K., Miao, X., Deng, T., Fan, W., ... & Xue, J., 2024. High-entropy hybrid perovskites with disordered organic moieties for perovskite solar cells. *Nature Photonics*, *18*(9), 960-966.
23. Zhao, R., Zhang, L., Wang, C., & Yin, L., 2017. Tetramethyl ammonium cation intercalated layered birnessite manganese dioxide for high-performance intercalation pseudocapacitor. *Journal of Power Sources*, *353*, 77-84.
24. Ida, S., Okamoto, Y., Matsuka, M., Hagiwara, H., & Ishihara, T., 2012. Preparation of tantalum-based oxynitride nanosheets by exfoliation of a layered oxynitride, CsCa2Ta3O10–x N y, and their photocatalytic activity. *Journal of the American Chemical Society*, *134*(38), 15773-15782.
25. Santos, A. R., Blundell, R. K., & Licence, P., 2015. XPS of guanidinium ionic liquids: a comparison of charge distribution in nitrogenous cations. *Physical Chemistry Chemical Physics*, *17*(17), 11839-11847.
26. Tompkins, F. K. T., Parker, L. G., Fogarty, R. M., Seymour, J. M., Gousseva, E., Grinter, D. C., ... & Lovelock, K. R., 2024. Controlling and predicting alkyl-onium electronic structure. *Chemical Communications*, *60*(77), 10756-10759.
27. Cabarcos, O. M., Shaporenko, A., Weidner, T., Uppili, S., Dake, L. S., Zharnikov, M., & Allara, D. L., 2008. Physical and electronic structure effects of embedded dipoles in self-assembled monolayers: Characterization of mid-chain ester functionalized alkanethiols on Au {111}. *The Journal of Physical Chemistry C*, *112*(29), 10842-10854.
28. Tian, G., Ling, D., Zhang, D., & Wang, Q., 2024. Reversible NH4+ intercalation/de-intercalation with phosphate promotion effect in tunnel (NH4) 0.25 WO3. *Chemical Engineering Journal*, *482*, 149160.

29. Yang, D., Song, Y., Zhang, M. Y., Qin, Z., Liu, J., & Liu, X. X., 2022. Solid–Liquid Interfacial Coordination Chemistry Enables High-Capacity Ammonium Storage in Amorphous Manganese Phosphate. *Angewandte Chemie International Edition*, *61*(37), e202207711.
30. Šetka, M., Calavia, R., Vojkůvka, L., Llobet, E., Drbohlavová, J., & Vallejos, S., 2019. Raman and XPS studies of ammonia sensitive polypyrrole nanorods and nanoparticles. *Scientific reports*, *9*(1), 8465.
31. Yankowitz, M., Xue, J., Cormode, D., Sanchez-Yamagishi, J. D., Watanabe, K., Taniguchi, T., ... & LeRoy, B. J., 2012. Emergence of superlattice Dirac points in graphene on hexagonal boron nitride. *Nature physics*, *8*(5), 382-386.
32. Hu, C., Wu, T., Huang, X., Dong, Y., Chen, J., Zhang, Z., ... & Shi, Z., 2022. In-situ twistable bilayer graphene. *Scientific Reports*, *12*(1), 204.
33. Shen, J., Dong, Z., Qi, M., Zhang, Y., Zhu, C., Wu, Z., & Li, D., 2022. Observation of moiré patterns in twisted stacks of bilayer perovskite oxide nanomembranes with various lattice symmetries. *ACS applied materials & interfaces*, *14*(44), 50386-50392.
34. Li, J., Sheng, B., Chen, Y., Yang, J., Wang, P., Li, Y., ... & Zhou, B., 2024. Utilizing full-spectrum sunlight for ammonia decomposition to hydrogen over GaN nanowires-supported Ru nanoparticles on silicon. *Nature communications*, *15*(1), 7393.
35. Zhang, Y., Peng, X., Tian, H. R., Yang, B., Chen, Z. C., Li, J., ... & Xie, S. Y., 2024. Fullerene on non-iron cluster-matrix co-catalysts promotes collaborative H2 and N2 activation for ammonia synthesis. *Nature Chemistry*, *16*(11), 1781-1787.

36. Zheng, J., Lu, L., Lebedev, K., Wu, S., Zhao, P., McPherson, I. J., ... & Tsang, S. C. E., 2021. Fe on molecular-layer MoS2 as inorganic Fe-S2-Mo motifs for light-driven nitrogen fixation to ammonia at elevated temperatures. *Chem Catalysis*, *1*(1), 162-182.
37. Li, Y., Zhou, H., Cai, S., Prabhakaran, D., Niu, W., Large, A., ... & Tsang, S. C. E., 2024. Electrolyte-assisted polarization leading to enhanced charge separation and solar-to-hydrogen conversion efficiency of seawater splitting. *Nature Catalysis*, *7*(1), 77-88.
38. Li, Y., Duan, M., Wu, S., Taylor, R. A., & Tsang, S. C. E., 2025. Harnessing Solar Energy for Ammonia Synthesis from Nitrogen and Seawater Using Oxynitride Semiconductors. *Advanced Energy Materials*, 2406160.
39. Shabani, S., Halbertal, D., Wu, W., Chen, M., Liu, S., Hone, J., ... & Pasupathy, A. N., 2021. Deep moiré potentials in twisted transition metal dichalcogenide bilayers. *Nature Physics*, *17*(6), 720-725.
40. Lin, Q., Fang, H., Kalaboukhov, A., Liu, Y., Zhang, Y., Fischer, M., ... & Xiao, S., 2024. Moiré-engineered light-matter interactions in MoS2/WSe2 heterobilayers at room temperature. *Nature Communications*, *15*(1), 8762.
41. Zhang, S., He, D., Huang, P., & Wang, F., 2021. Moiré pattern at graphene/Al (111) interface: Experiment and simulation. *Materials & Design*, *201*, 109509.
42. Wang, X., Xu, C., Aronson, S., Bennett, D., Paul, N., Crowley, P. J., ... & Yasuda, K., 2025. Moiré band structure engineering using a twisted boron nitride substrate. *Nature Communications*, *16*(1), 178.
43. Shi, B., Qi, P., Jiang, M., Dai, Y., Lin, F., Zhang, H., & Fang, Z., 2021. Exotic physical properties of 2D materials modulated by moiré superlattices. *Materials Advances*, *2*(17), 5542-5559.

44. Kalt, H., & Klingshirn, C. F., 2019. *Semiconductor Optics 1: Linear Optical Properties of Semiconductors*. Springer Nature.
45. Aly, A. E. M., & Nasr, A., 2014. Theoretical Study of One-Intermediate Band Quantum Dot Solar Cell. *International Journal of Photoenergy*, *2014*(1), 904104.
46. Bagchi, S., Johnson, H. T., & Chew, H. B., 2020. Rotational stability of twisted bilayer graphene. *Physical Review B*, *101*(5), 054109.
47. Fang, H. H., Adjokatse, S., Shao, S., Even, J., & Loi, M. A., 2018. Long-lived hot-carrier light emission and large blue shift in formamidinium tin triiodide perovskites. *Nature communications*, *9*(1), 243.
48. Li, L., Chen, J., Hu, L., Qiu, Z., Zou, Z., Liu, R., ... & Cong, C., 2025. Moiré collective vibrations in atomically thin van der Waals superlattices. *Nature Communications*, *16*(1), 4117.
49. He, F., Zhou, Y., Ye, Z., Cho, S. H., Jeong, J., Meng, X., & Wang, Y., 2021. Moiré patterns in 2D materials: a review. *ACS nano*, *15*(4), 5944-5958.
50. Chen, Z., Ye, Y., Feng, X., Wang, Y., Han, X., Zhu, Y., ... & Zhang, J., 2023. High-density frustrated Lewis pairs based on Lamellar Nb2O5 for photocatalytic non-oxidative methane coupling. *Nature Communications*, *14*(1), 2000.
51. Susarla, S., Naik, M. H., Blach, D. D., Zipfel, J., Taniguchi, T., Watanabe, K., ... & Raja, A., 2022. Hyperspectral imaging of exciton confinement within a moiré unit cell with a subnanometer electron probe. *Science*, *378*(6625), 1235-1239.
52. Zhang, S., Ma, K., Yuan, B., Yang, J., Lu, Y., Sun, D., ... & Dou, L., 2024. Deterministic Synthesis of a Two-Dimensional MAPbI3 Nanosheet and Twisted Structure with Moiré Superlattice. *Journal of the American Chemical Society*, *146*(40), 27861-27870.

53. Yaakob, M. K., Zulkafli, N. M. A., Kasim, M. F., Mamat, M. H., Mohamad, A. A., Lu, L., & Yahya, M. Z. A., 2021. Structural phase instability, mixed-phase, and energy band gap change in BiFeO3 under lattice strain effect from first-principles investigation. *Ceramics International*, *47*(9), 12592-12599.
54. Dong, G., Ho, W. and Wang, C., 2015. Selective photocatalytic N 2 fixation dependent on gC 3 N 4 induced by nitrogen vacancies. *Journal of Materials Chemistry A*, *3*(46), pp.23435-23441.
55. Lu, Y., Yang, Y., Zhang, T., Ge, Z., Chang, H., Xiao, P., Xie, Y., Hua, L., Li, Q., Li, H. and Ma, B., 2016. Photoprompted hot electrons from bulk cross-linked graphene materials and their efficient catalysis for atmospheric ammonia synthesis. *ACS nano*, *10*(11), pp.10507-10515.
56. Sun, B., Liang, Z., Qian, Y., Xu, X., Han, Y. and Tian, J., 2020. Sulfur vacancy-rich O-doped 1T-MoS2 nanosheets for exceptional photocatalytic nitrogen fixation over CdS. *ACS applied materials & interfaces*, *12*(6), pp.7257-7269.
57. Li, L., Wang, Y., Vanka, S., Mu, X., Mi, Z. and Li, C.J., 2017. Nitrogen photofixation over iii‐nitride nanowires assisted by ruthenium clusters of low atomicity. *Angewandte Chemie International Edition*, *56*(30), pp.8701-8705.
58. Zhang, N., Jalil, A., Wu, D., Chen, S., Liu, Y., Gao, C., Ye, W., Qi, Z., Ju, H., Wang, C. and Wu, X., 2018. Refining defect states in W18O49 by Mo doping: a strategy for tuning N2 activation towards solar-driven nitrogen fixation. *Journal of the American Chemical Society*, *140*(30), pp.9434-9443.
59. Li, X., Zhang, X., Everitt, H.O. and Liu, J., 2019. Light-induced thermal gradients in ruthenium catalysts significantly enhance ammonia production. *Nano Letters*, *19*(3), pp.1706-1711.

60. Kitano, M., Inoue, Y., Sasase, M., Kishida, K., Kobayashi, Y., Nishiyama, K., Tada, T., Kawamura, S., Yokoyama, T., Hara, M. and Hosono, H., 2018. Self‐organized ruthenium–barium core–shell nanoparticles on a mesoporous calcium amide matrix for efficient low‐temperature ammonia synthesis. *Angewandte Chemie International Edition*, *57*(10), pp.2648-2652.

Chapter 6 | Conclusion and Future Perspective

6.1 Conclusion

This thesis shows various modifying strategies of layered perovskite for different photocatalytic reactions. Layered perovskite, photocatalytic H_2 evolution, NH_3 decomposition and NH_3 synthesis were introduced in Chapter 1. Experimental techniques including synthesis approaches, structural characterisation and activity test were provided in Chapter 2. These two chapters provided contextual information for the research Chapter 3, 4 and 5.

In Chapter 3, Dion–Jacobson perovskite nanosheets integrating with rGO were demonstrated by utilising exfoliation and an electrostatic-driven assembly strategy, achieving a high surface area nanohybrid. These nanohybrids gives an efficient activity of photocatalytic H_2 evolution from water splitting, attributed to the efficient interfacial charge transfer between rGO and perovskite nanosheets. By EXAFS and Rietveld refinement on XRD, perovskite nanosheets shows that the band structure can be tuned by the A-site charge density due to lattice contraction and octahedral tilting. This synergy between A-site charge density and interfacial photosensitisation provides a powerful approach to tuning the electron-accepting properties of layered perovskite. We believe this finding could establish fundamental design principles for the targeted band structure modulation in perovskite-based photocatalysts.

In Chapter 4, a protonated layered perovskite $HPrNb_2O_7$ acts as an effective photocatalyst for NH_3 decomposition under mild conditions. And N_2H_4 forms *via* an associative dehydrogenation route and becomes stably intercalated in its interlayer space, which is evidenced by the refinement on XPDF and NPD. Moreover, photogenerated charge

carrier lifetime could be prolonged by induced moderate heating, yielding the photo-thermal synergy. This work uncovers a distinct mechanism for NH_3 decomposition over layered perovskite, detailing the structure and interactions between the trapped N_2H_4 intermediate and perovskite framework.

In Chapter 5, various tetra-alkyl ammonium cations were employed to precisely control the twist angle between adjacent 2D perovskite layers, enabling the formation of a robust moiré superlattice. 45^o twist is recognised as the "magic angle", the resulting superlattice exhibited a large periodicity of ~2.8 nm, in which the photogenerated charge carriers could be deeply trapped in the potential wells, prolonging carrier lifetimes and suppressing recombination pathways. Moreover, by evidence of EXAFS fitting, the 45^o twist minimised inhomogeneous strain, giving reduced structural distortion and a narrower bandgap. These synergistic effects culminated in an outstanding photocatalytic NH_3 production rate, demonstrating the critical role of moiré engineering in enhancing photocatalytic performance. This study provides insights into the high-performance catalysts designing for sustainable energy applications.

6.2 Future Perspective

Based on the findings presented in this thesis, future research may provide a complement and extension to this current work.

6.2.1 Catalytic testing

More comprehensive catalytic measurements will be needed to study the catalyst performance described in above chapters. For the NH_3 decomposition system, systematic H_2 and N_2 rate tests should be performed across an extended temperature range, under variable initial pressures and feed compositions (e.g., different NH_3 partial pressure within inert gas Ar). Also, long-term photocatalytic tests within the flow fixed-bed reactor could help kinetic studies, revealing the activation energy. Complementary hydrogen–deuterium exchange experiments can also be operated to investigate the role of perovskite interlayer protons, demonstrating whether it contributes to hydrogen evolution or not. For instance, a deuterated analogue ($DPrNb_2O_7$) can be synthesised via repeated D_2O exchange of $HPrNb_2O_7$. Then the NH_3 decomposition reaction was conducted on this material under light irradiance, coupled with mass spectrometry to detect H_2, D_2 or HD gas evolution. For the thermally assisted photocatalytic NH_3 synthesis catalysts, activity can be further studied under different N_2/H_2 ratios, evaluating the catalytic performance and H poisoning under various H_2 concentration.

6.2.2 Mechanistic studies

Clearly, Ru incorporation significantly can enhance photocatalytic activity of NH_3 decomposition, highlighting promising directions for future research and catalyst optimisation. To advance the understanding of function of interlayer Ru atoms within HPNO, future systematic work for studying the Ru chemical environment by XAS (both

XANES and EXAFS) and microscopic techniques would be expected, which could further unveil the improvement by Ru doping.

Besides, the mechanistic details for the pathway of NH_3 synthesis over twisted 2D perovskites remain incomplete. The future work should couple *in situ* techniques with DFT calculation to resolve how moiré engineering affects the photocatalytic performance. *In situ* XAS (Nb K-edge) across twisted angles under N_2/H_2 gas mixture at elevated temperature will reveal changes in local coordination and oxidation state, while *in situ* ambient-pressure XPS can identify surface intermediates and adsorption geometries (side-on or end-on) under catalytic conditions. Isotopically labelled studies (e.g., $^{15}N_2$) combined with mass spectrometry will help distinguish associative from dissociative NH_3 synthesis pathways. And DFT calculations can be employed to study the band structure, especially the band flattening induced by the moiré superlattice. In addition, the charge carrier localisation can be studied by the charge density of the lowest energy exciton in twisted 2D perovskite. Meanwhile, the reaction pathways for the catalytic process can also be established by DFT simulations.

6.2.3 Industrial scales

Building on layered protonated perovskite and moiré-engineered 2D perovskite (Chapter 4 and 5), industrial-scale development of ammonia decomposition or synthesis technologies need to tackle two core challenges: materials design and process engineering. Key priorities include developing cost-efficient synthetic routes to mass-produce catalysts with consistent structural features, and designing reactor configurations that retain lab-scale activity and stability under industrial conditions.

In addition, techno-economic assessments with performance metrics including turnover frequency, attrition thresholds, energy efficiency, and catalyst lifetime, are critical to

prioritise catalytic systems for scale-up testing. Early integration of these economic and durability criteria will enable researchers to focus on catalytic systems that are not only lab-active but also commercially viable and de-risked for demonstration.

Appendices

A) Appendices for Chapter 3

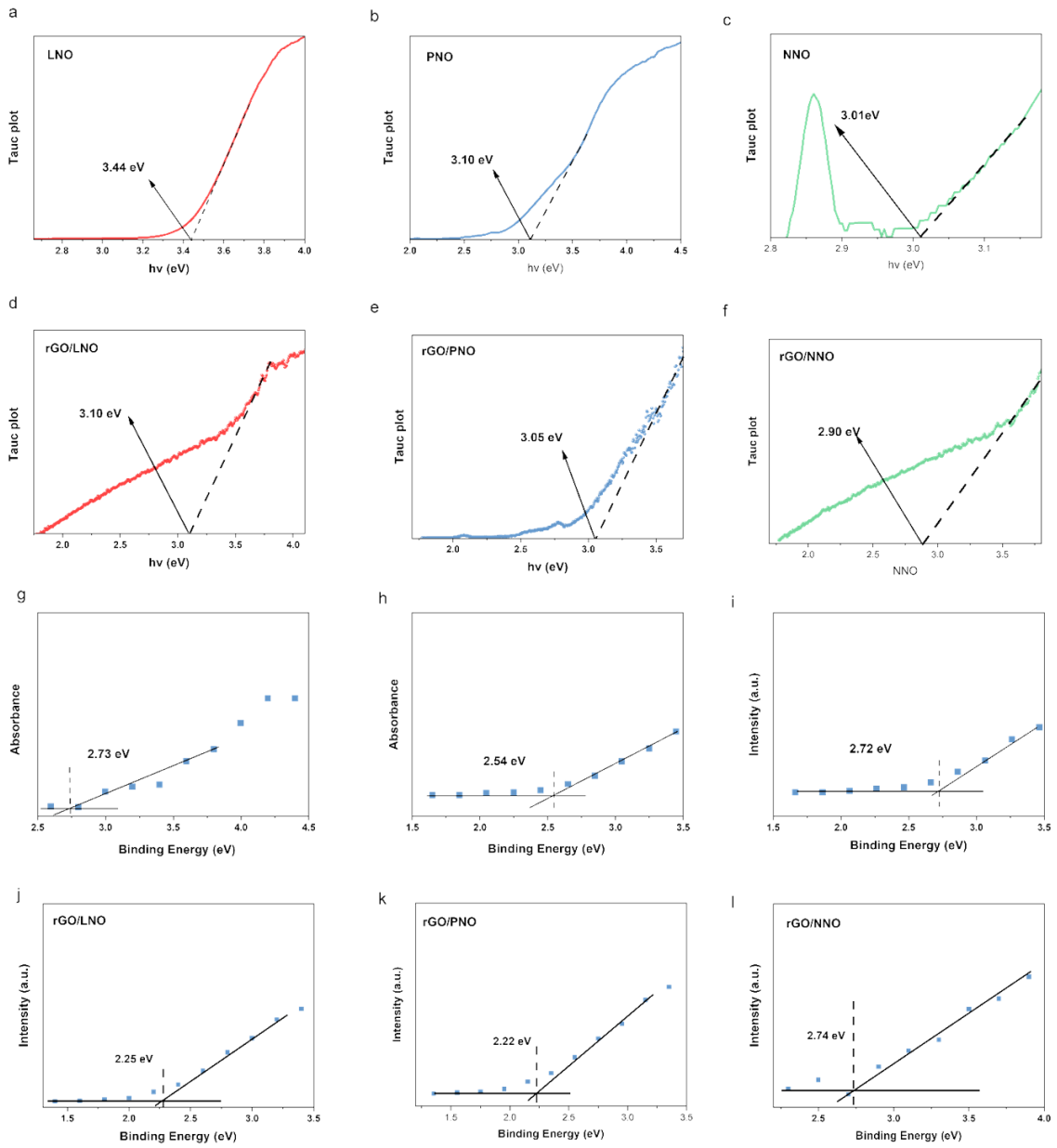

Figure A3.1: Tauc plot $(F(R)*hv)^{1/2}$ of a) LNO, b) PNO, c) NNO, d) rGO/LNO, e) rGO/PNO, f) rGO/NNO; Valence band XPS of g) LNO, h) PNO, i) NNO, j) rGO/LNO, k) rGO/PNO, l) rGO/NNO.

Table A3.1: Performance comparison of rGO/NNO with previously reported layered perovskite photocatalysts.

Photocatalyst	HER µmol/gh	AQE	Ref
rGO/NNO	834.9 (>400 nm)	0.30% (400-500 nm)	This work
$NaLaTiO_{4-x}N_y$	~70 (>420 nm)	0.17% (400-500 nm)	[1]
$[Pb_8I_8(H_2O_3)][O_2C(CH_2)_4CO_2]_4$	~140 (solar simulator)	0.067% (450 nm)	[2]
Bi_3TiNbO_9	435.6 (>300 nm)	0.26% (365 nm)	[3]
$Rb_2NdNb_2O_7$	0.4 (>400 nm)	-	[4]
$Ca_2Ta_3O_{9.7}N_{0.2}$ nanosheet	4.7 (>420 nm)	-	[5]
$rGO/Ca_2Nb_3O_{10}$	820.8 (>400 nm)	-	[6]

$$AQE = \frac{Number\ of\ reacted\ electrons}{Number\ of\ incident\ photons} \times 100\% = \frac{2 \times Number\ of\ evolved\ H2\ molecules}{Photon\ Flux \times S \times t}$$

Where, S is the irradiation area, t is the photoreaction time

1. Xu, X., Wang, R., Sun, X., Lv, M. and Ni, S., 2020. Layered perovskite compound NaLaTiO4 modified by nitrogen doping as a visible light active photocatalyst for water splitting. *Acs Catalysis*, *10*(17), pp.9889-9898.
2. Song, X., Wei, G., Sun, J., Peng, C., Yin, J., Zhang, X., Jiang, Y. and Fei, H., 2020. Overall photocatalytic water splitting by an organolead iodide crystalline material. *Nature Catalysis*, *3*(12), pp.1027-1033.
3. Huang, J., Kang, Y., Liu, J.A., Chen, R., Xie, T., Liu, Z., Xu, X., Tian, H., Yin, L., Fan, F. and Wang, L., 2023. Selective Exposure of Robust Perovskite Layer of Aurivillius-Type Compounds for Stable Photocatalytic Overall Water Splitting. *Advanced Science*, *10*(23), p.2302206.
4. H. Wakayama, K. Hibino, K. Fujii, T. Oshima, K. Yanagisawa, Y. Kobayashi, K. Kimoto, M. Yashima and K. Maeda, 2019. Synthesis of a layered niobium oxynitride, $Rb_2NdNb_2O_6N{\cdot}H_2O$, showing visible-light photocatalytic activity for H_2 evolution, *Inorg. Chem.*, 58(9), 6161–6166.
5. S. Ida, Y. Okamoto, M. Matsuka, H. Hagiwara and T. Ishihara, 2012. Preparation of tantalum-based oxynitride nanosheets by exfoliation of a layered oxynitride, $CsCa_2Ta_3O_{10-x}N_y$, and their photocatalytic activity, *J. Am. Chem. Soc.*, 134(38), 15773–15782.
6. D. Li, H. Zhao, L. Li, B. Mao, M. Chen, H. Shen, W. Shi, D. Jiang and Y. Lei, 2018. Graphene-sensitized perovskite oxide monolayer nanosheets for efficient photocatalytic reaction, *Adv. Funct. Mater.*, 28(52), 1806284.

B) Appendices for Chapter 4

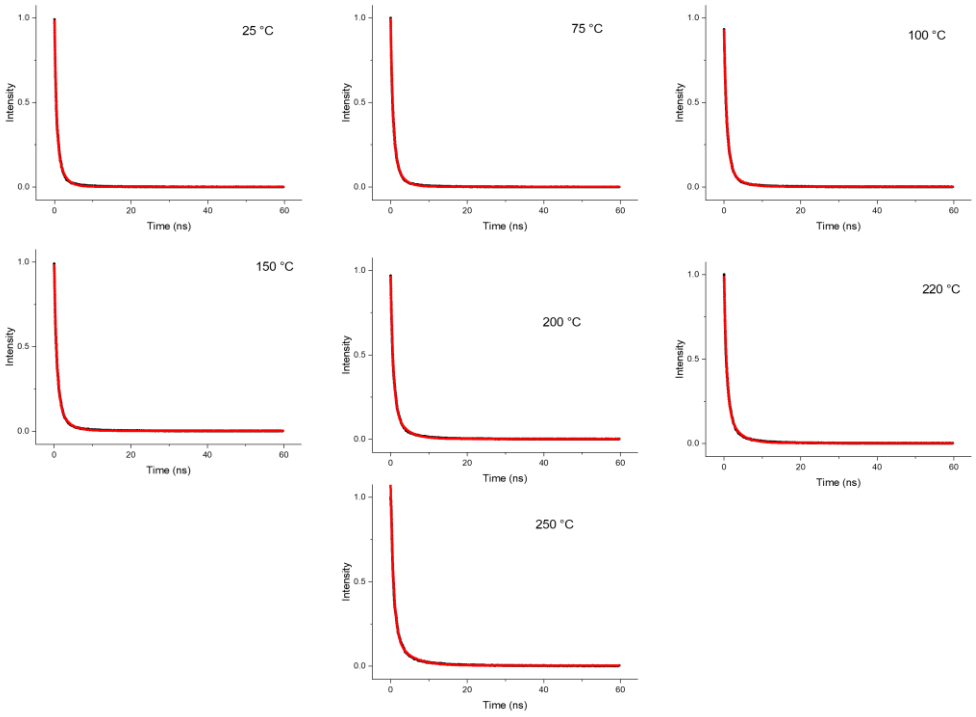

Figure A4.1: Exponential fittings of the TRPL spectra. The TRPL spectra were fitted using a biexponential decay function.

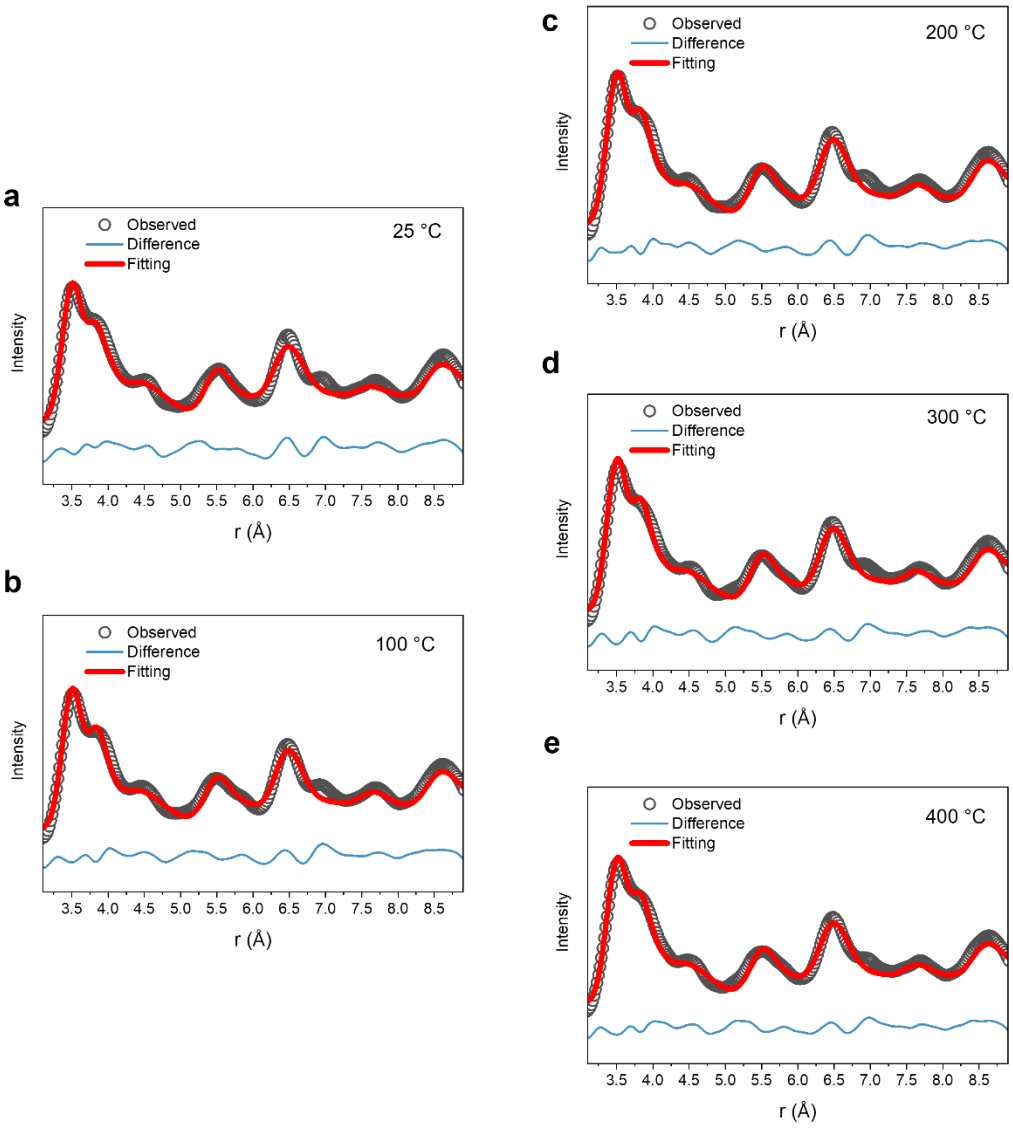

Figure A4.2: PDF refinement of $HPrNb_2O_7$ under NH_3 with increased temperature. Rw value: (a) 17.8%; (b) 17.9%; (c)18.7; (d)17.2%; (e) 16.1%.

C) Appendices for Chapter 5

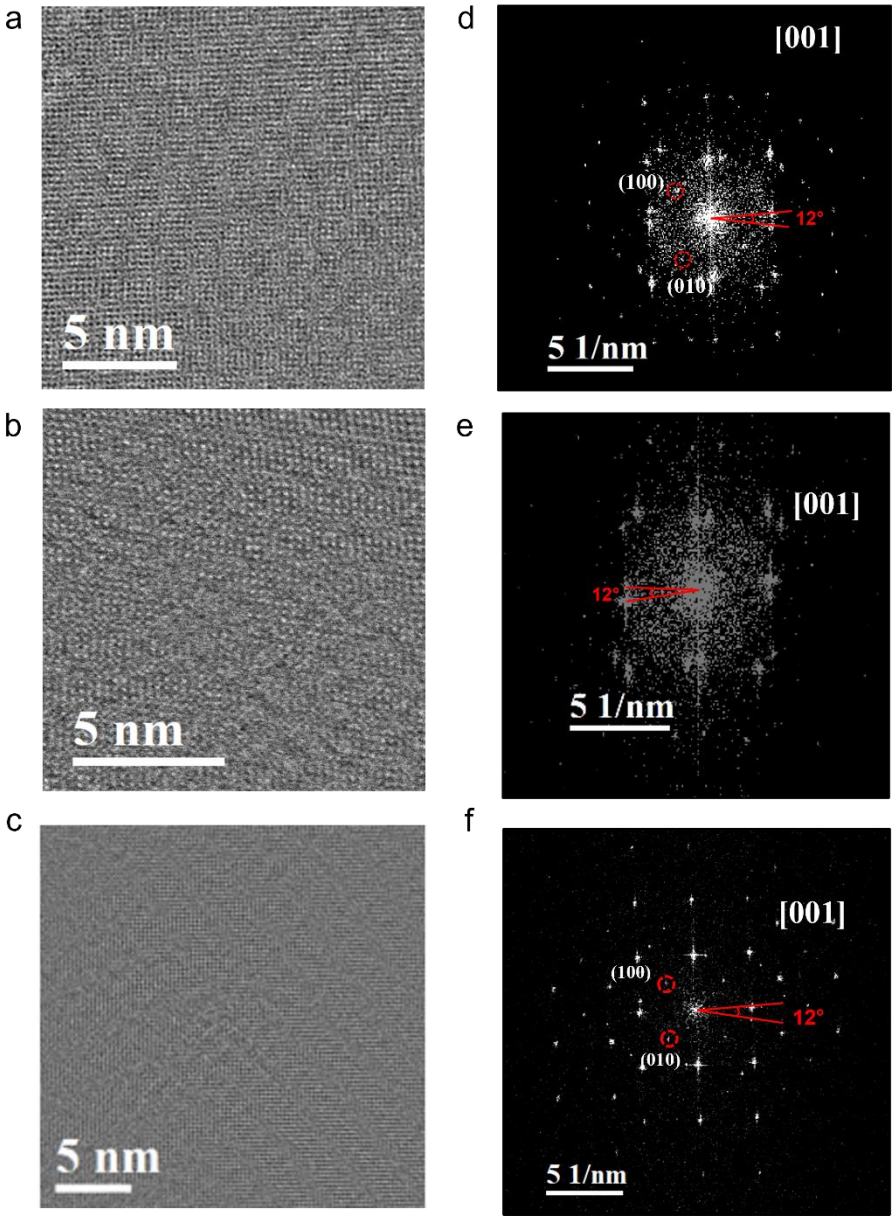

Figure A5.1: (a - c) HAADF-STEM images of (TEA)$PrNb_2O_7$ and the corresponding (d - f) FFT images.

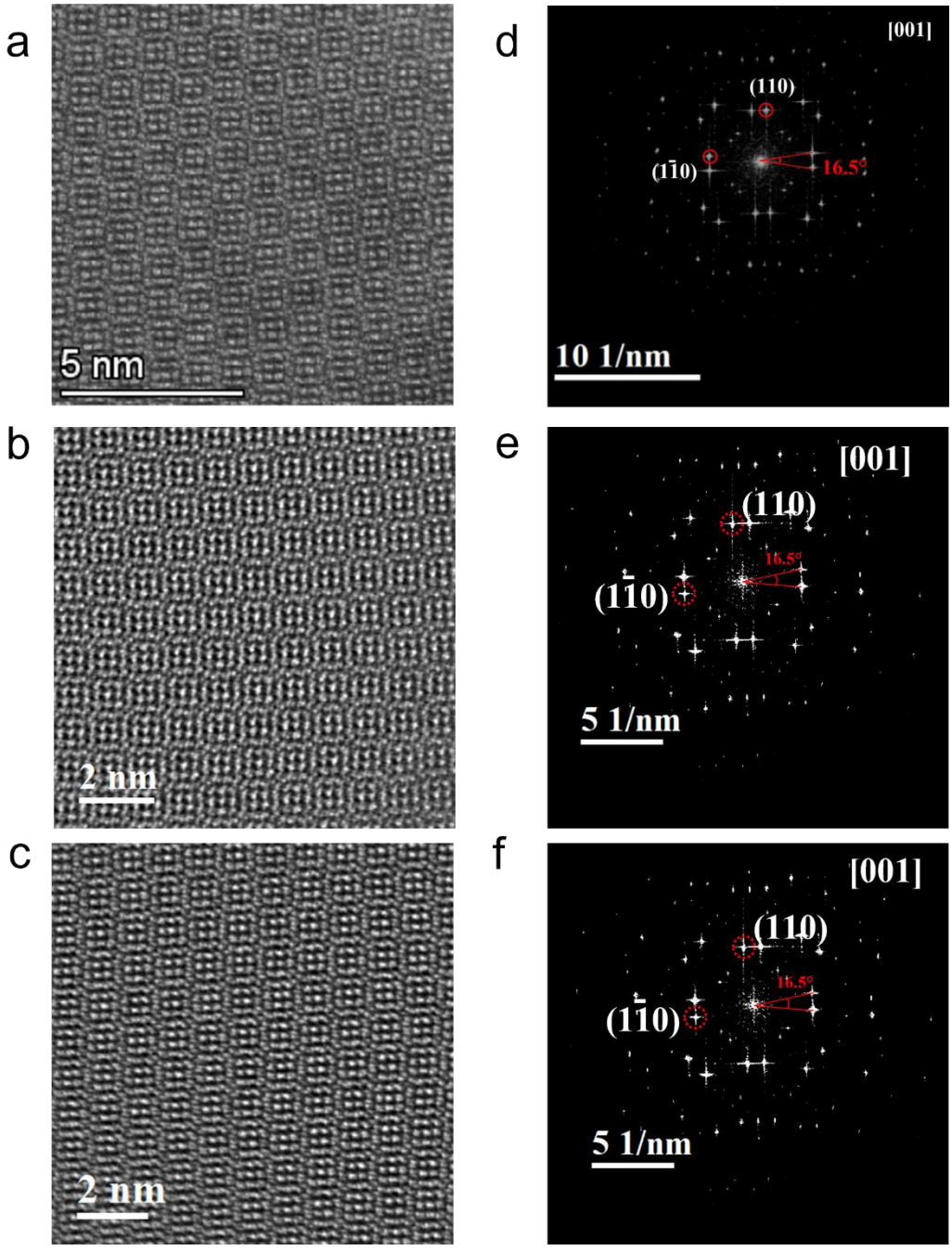

Figure A5.2: (a - c) HAADF-STEM images of (TPA)$PrNb_2O_7$ and the corresponding (d - f) FFT images.

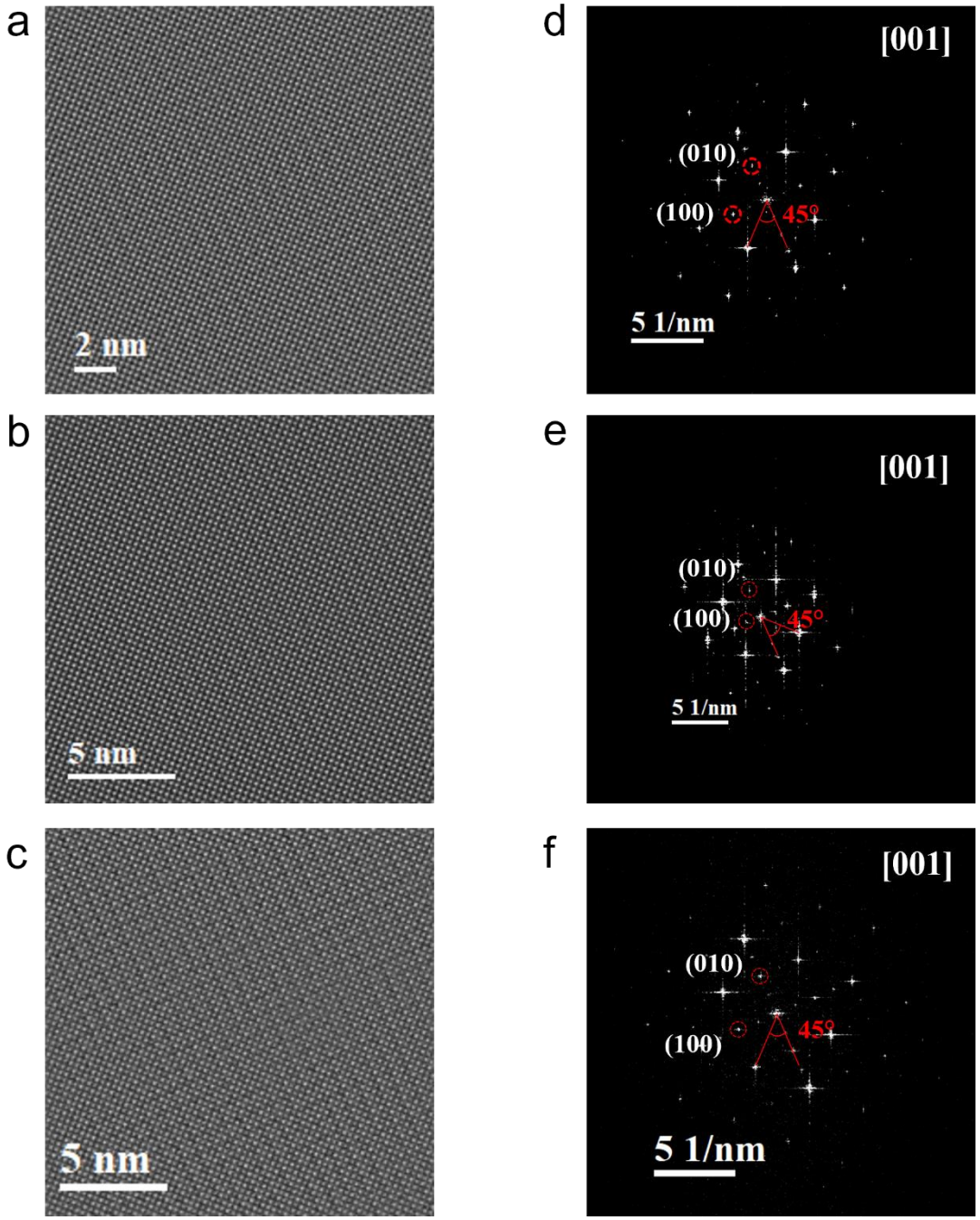

Figure A5.3: (a - c) HAADF-STEM images of (TMA)$PrNb_2O_7$ and the corresponding (d - f) FFT images.

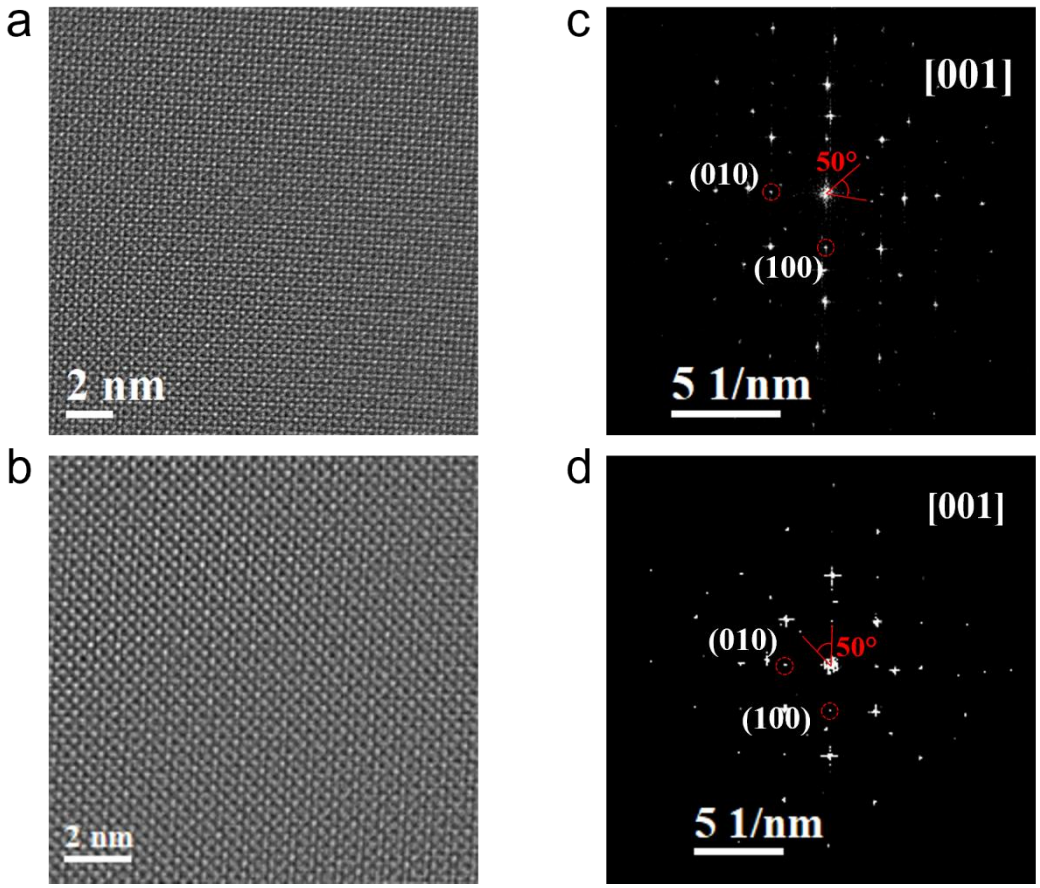

Figure A5.4: (a, b) HAADF-STEM images of (TBA)$PrNb_2O_7$ and the corresponding (c, d) FFT images.

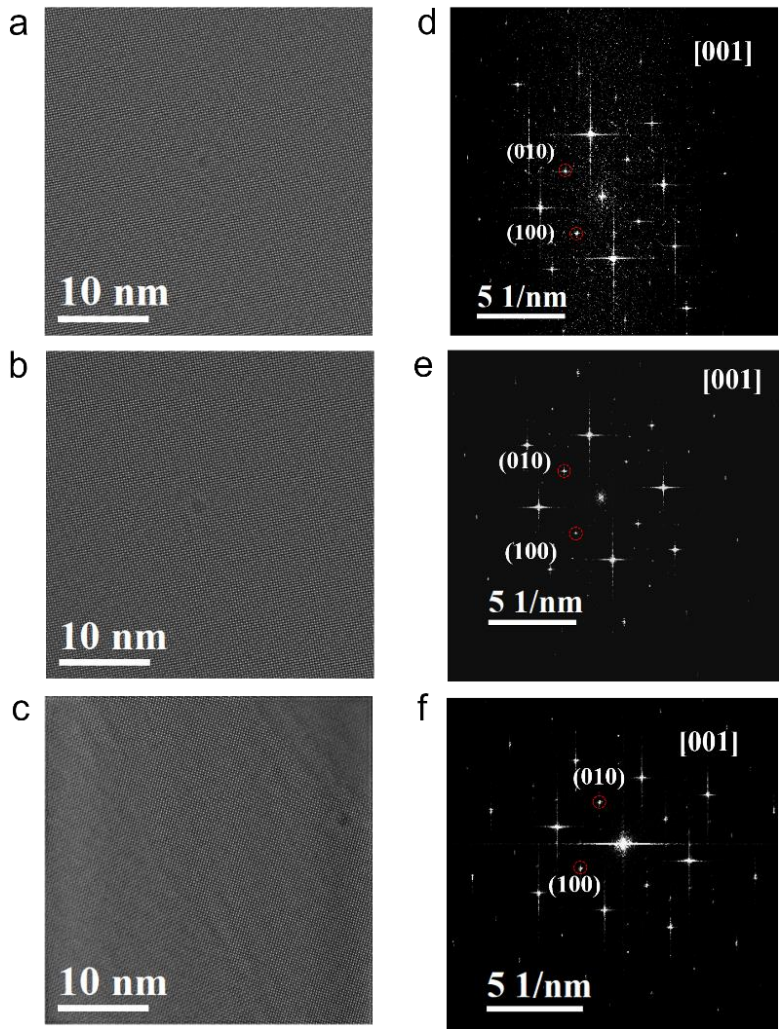

Figure A5.5: (a - c) HAADF-STEM images of $(NH_4)PrNb_2O_7$ and the corresponding (d - f) FFT images.

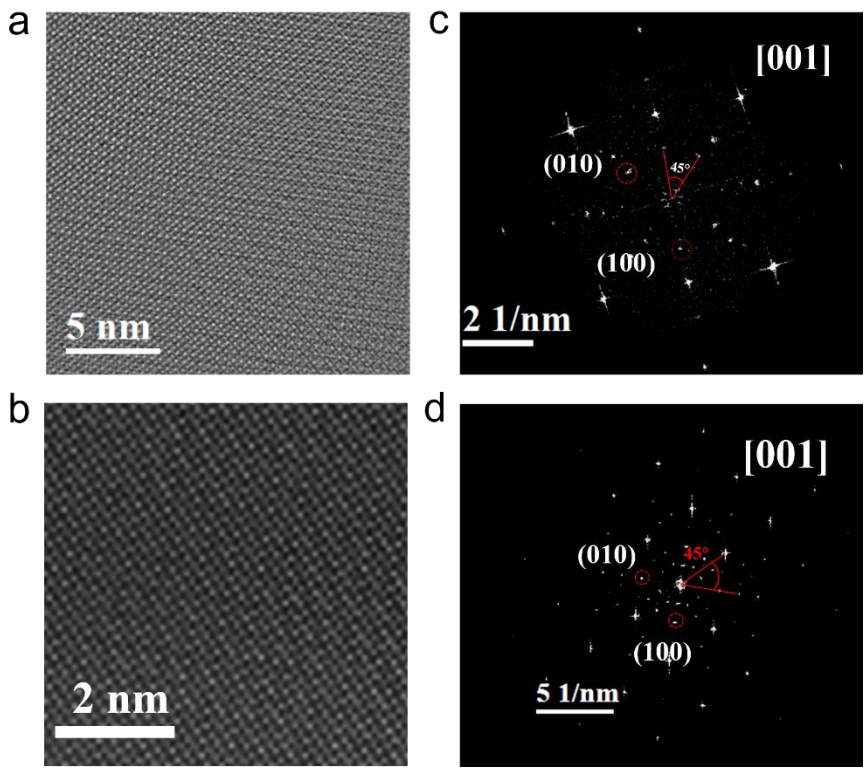

Figure A5.6: (a, b) HAADF-STEM images of (TMA)$PrNb_2O_7$ and the corresponding (c, d) FFT images after photocatalytic NH_3 synthesis reaction.

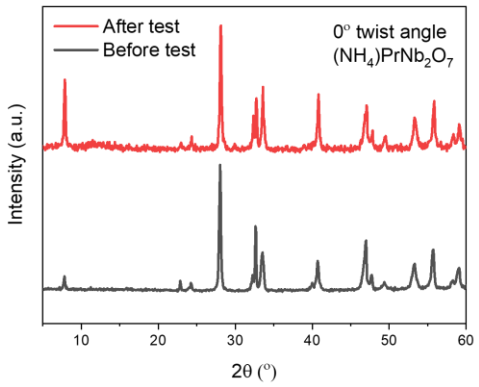

Figure A5.7: XRD pattern of $(NH_4)PrNb_2O_7$ before and after photocatalytic NH_3 synthesis measurements.

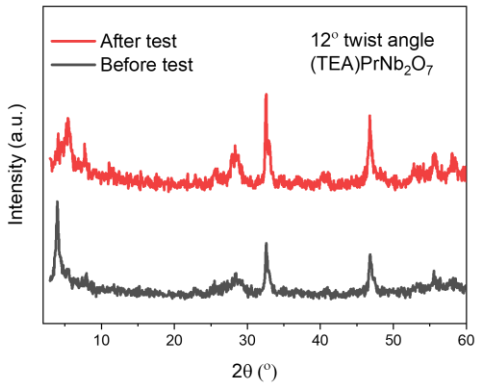

Figure A5.8: XRD pattern of $(TEA)PrNb_2O_7$ before and after photocatalytic NH_3 synthesis measurements.

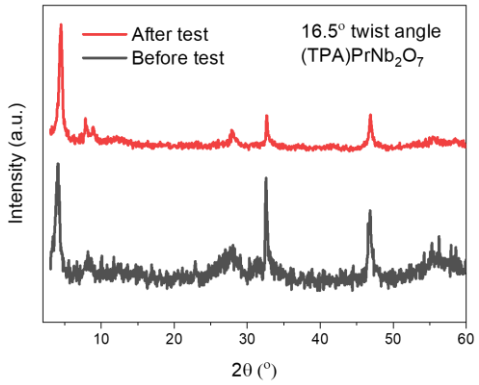

Figure A5.9: XRD pattern of $(TPA)PrNb_2O_7$ before and after photocatalytic NH_3 synthesis measurements.

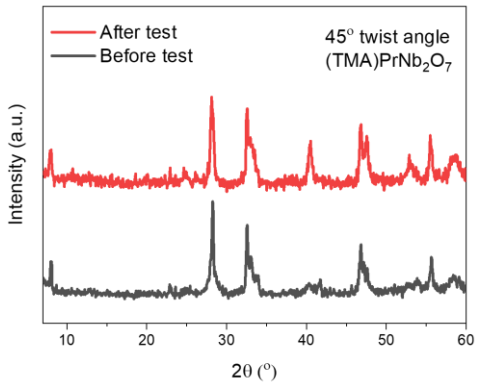

Figure A5.10: XRD pattern of (TMA)$PrNb_2O_7$ before and after photocatalytic NH_3 synthesis measurements.

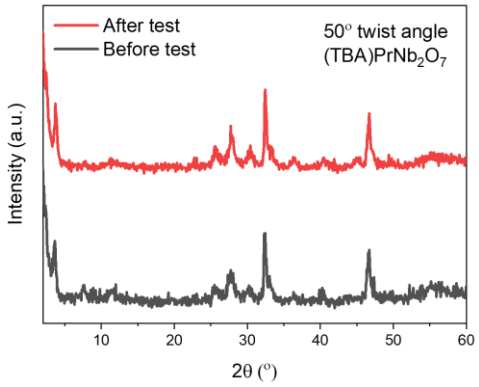

Figure A5.11: XRD pattern of (TBA)$PrNb_2O_7$ before and after photocatalytic NH_3 synthesis measurements.

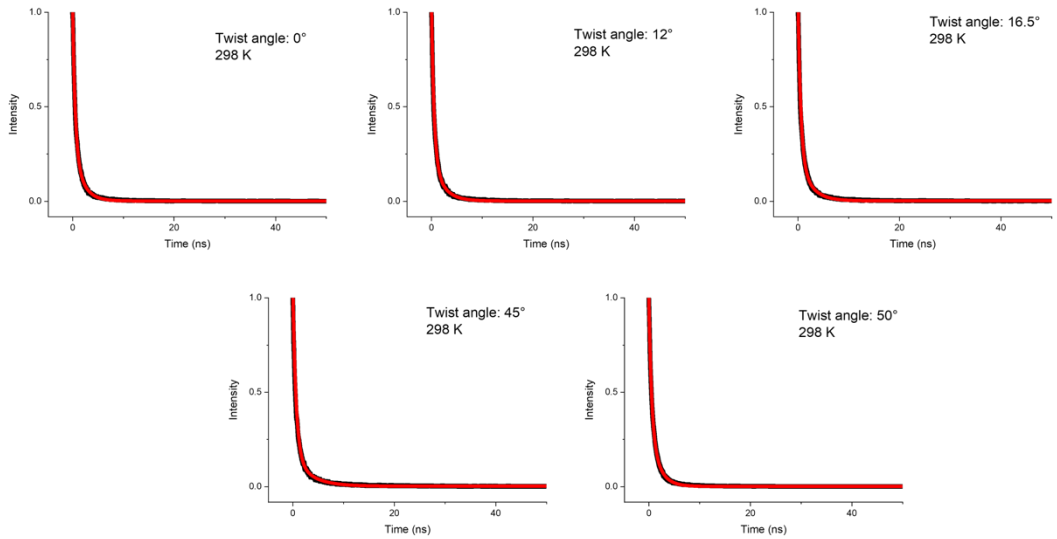

Temperature	Twist angle	t1 (ns)	A1 (%)	t2 (ns)	A2 (%)	t_{ave} (ns)
298 K	0°	0.50	75.5	1.83	24.5	0.83
298 K	12°	0.51	83.5	2.15	16.5	0.78
298 K	16.5°	0.54	84.1	2.33	15.9	0.82
298 K	45°	0.64	83.9	3.42	16.1	1.09
298 K	50°	0.52	67.5	1.75	32.5	0.92

Figure A5.12: Exponential fittings of the TRPL spectra for different twist angle at 298 K. The TRPL spectra were fitted using a biexponential decay function. The fitting parameters are listed in the table above.

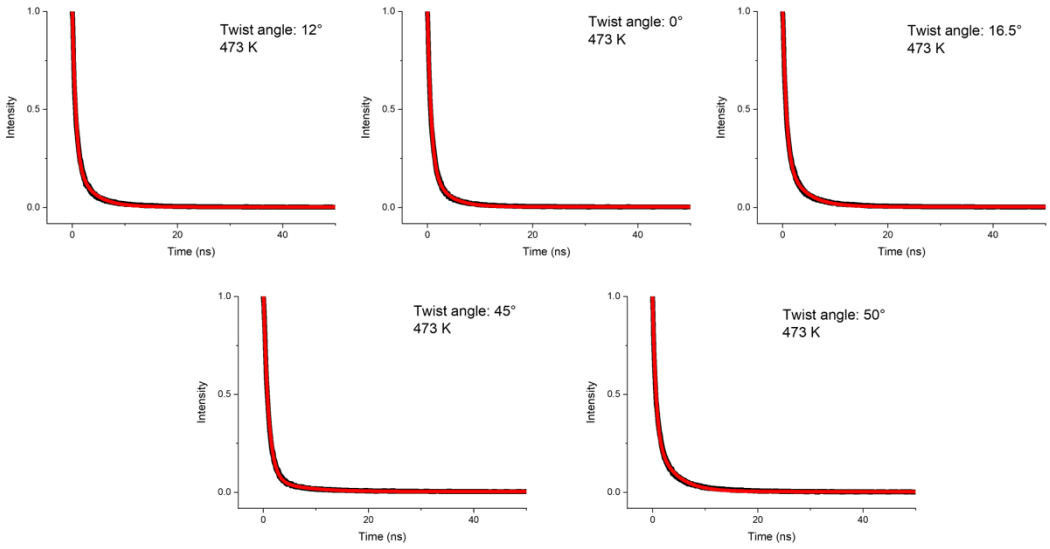

Temperature	Twist angle	t1 (ns)	A1 (%)	t2 (ns)	A2 (%)	t_{ave} (ns)
473 K	0°	0.69	83.3	3.23	16.7	1.11
473 K	12°	0.65	81.7	3.34	18.3	1.14
473 K	16.5°	0.70	79.5	3.65	20.5	1.30
473 K	45°	0.93	78.5	5.87	21.5	1.99
473 K	50°	0.64	71.4	3.70	28.6	1.52

Figure A5.13: Exponential fittings of the TRPL spectra for different twist angle at 473 K. The TRPL spectra were fitted using a biexponential decay function. The fitting parameters are listed in the table above.

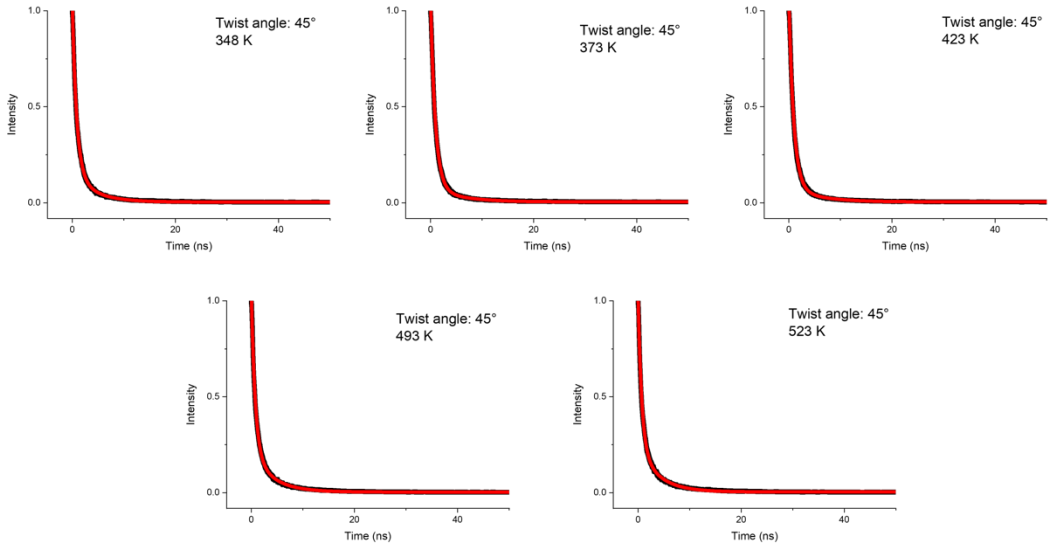

Temperature	Twist angle	t1 (ns)	t2 (ns)
348 K	45°	0.84	4.13
373 K	45°	0.92	5.45
423 K	45°	0.94	5.45
493 K	45°	0.77	4.01
523 K	45°	0.70	3.87

Figure A5.14: Exponential fittings of the TRPL spectra for 45° twist angle at different temperature. The TRPL spectra were fitted using a biexponential decay function. The fitting parameters are listed in the table above.

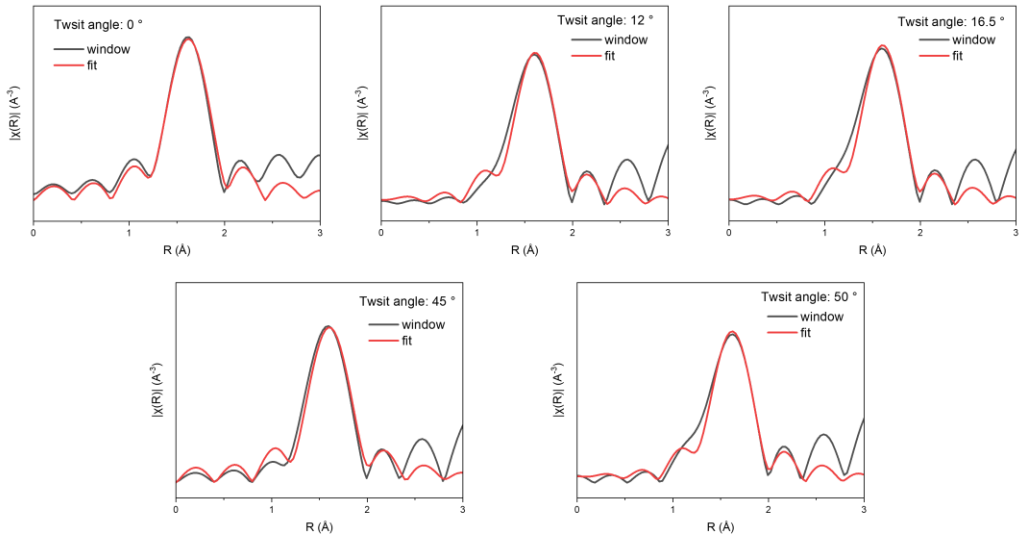

Twist angle	CN	R (Å)	σ^2 (Å^2)	ΔE_0	R-factor
0°	4.67 (0.8)	2.08 (0.01)	0.001 (0.001)	9.11 (1.85)	0.01
12°	4.89 (1.2)	2.06 (0.02)	0.002 (0.001)	6.39 (2.35)	0.02
16.5°	5.93 (1.0)	2.07 (0.02)	0.002 (0.002)	5.94 (2.34)	0.02
45°	5.89 (1.1)	2.02 (0.01)	0.002 (0.001)	7.17 (2.13)	0.02
50°	5.92 (0.9)	2.07 (0.02)	0.002 (0.002)	7.40 (1.93)	0.02

Figure A5.15: Nb K-edge EXAFS and curve fit for different twist angles shown in k^3 weighted R-space (FT magnitude).

S_0^2 was fixed as 0.71, ΔE_0 was refined as a global fit parameter. Data ranges: $1.0 \leq R \leq 2.5$ Å. The number of variable parameters is 4, out of a total of 6.2 independent data points. These coordination numbers were constrained as N(Nb-O) = 1 based on the different Nb-O paths from the different crystal structures.

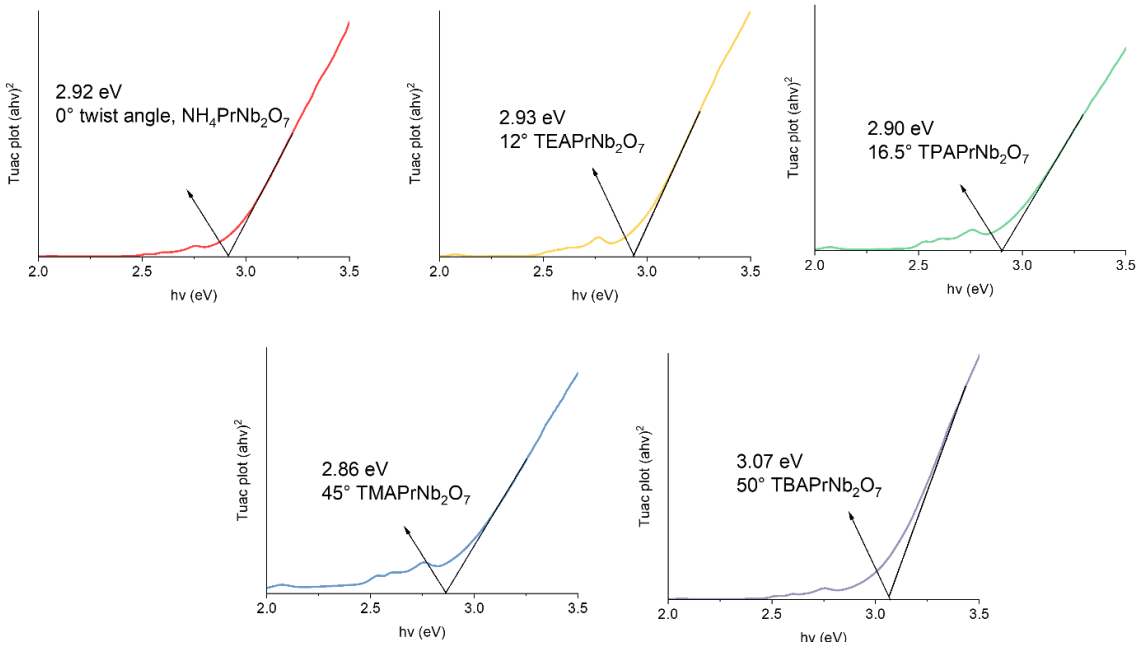

Figure A5.16: Tauc plot $(ahv)^2$ of different twist angle perovskite.

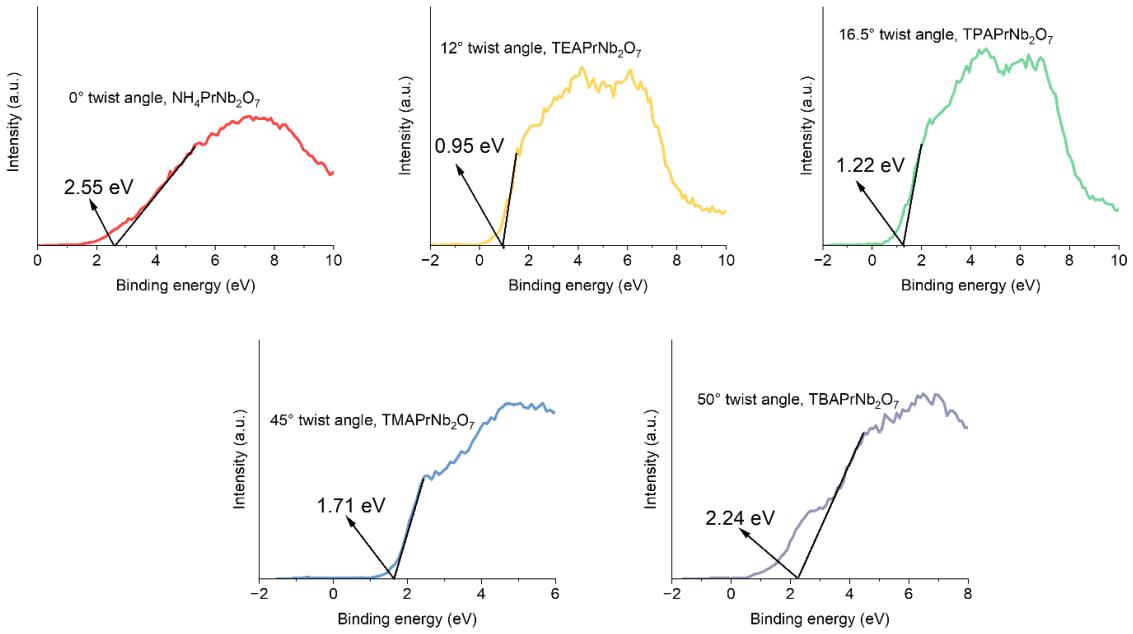

Figure A5.17: Valence band XPS of different twist angle perovskite.